

Journal of
Mechanics of
Materials and Structures

Volume 3, N° 1

January 2008

 mathematical sciences publishers

JOURNAL OF MECHANICS OF MATERIALS AND STRUCTURES

<http://www.jomms.org>

EDITOR-IN-CHIEF Charles R. Steele
ASSOCIATE EDITOR Marie-Louise Steele
Division of Mechanics and Computation
Stanford University
Stanford, CA 94305
USA

BOARD OF EDITORS

D. BIGONI University of Trento, Italy
H. D. BUI École Polytechnique, France
J. P. CARTER University of Sydney, Australia
R. M. CHRISTENSEN Stanford University, U.S.A.
G. M. L. GLADWELL University of Waterloo, Canada
D. H. HODGES Georgia Institute of Technology, U.S.A.
J. HUTCHINSON Harvard University, U.S.A.
C. HWU National Cheng Kung University, R.O. China
IWONA JASIUK University of Illinois at Urbana-Champaign
B. L. KARIHALOO University of Wales, U.K.
Y. Y. KIM Seoul National University, Republic of Korea
Z. MROZ Academy of Science, Poland
D. PAMPLONA Universidade Católica do Rio de Janeiro, Brazil
M. B. RUBIN Technion, Haifa, Israel
Y. SHINDO Tohoku University, Japan
A. N. SHUPIKOV Ukrainian Academy of Sciences, Ukraine
T. TARNAI University Budapest, Hungary
F. Y. M. WAN University of California, Irvine, U.S.A.
P. WRIGGERS Universität Hannover, Germany
W. YANG Tsinghua University, P.R. China
F. ZIEGLER Technische Universität Wien, Austria

PRODUCTION

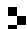
PAULO NEY DE SOUZA Production Manager
SHEILA NEWBERY Senior Production Editor
SILVIO LEVY Scientific Editor

See inside back cover or <http://www.jomms.org> for submission guidelines.

Regular subscription rate: \$500 a year.

Subscriptions, requests for back issues, and changes of address should be sent to Mathematical Sciences Publishers, 798 Evans Hall, Department of Mathematics, University of California, Berkeley, CA 94720-3840.

©Copyright 2008. Journal of Mechanics of Materials and Structures. All rights reserved.

 mathematical sciences publishers

EFFECT OF NONHOMOGENEITY ON THE CONTACT OF AN ISOTROPIC HALF-SPACE AND A RIGID BASE WITH AN AXIALLY SYMMETRIC RECESS

SAKTI PADA BARIK, MRIDULA KANORIA AND PRANAY KUMAR CHAUDHURI

We study an axially symmetric frictionless contact problem between a nonhomogeneous elastic half-space and a rigid base that has a small axisymmetric surface recess. We reduce the problem to solving Fredholm integral equations, solve these equations numerically, and establish a relationship between the applied pressure and the gap radius. We find and graph the effects of nonhomogeneity on the normal pressure, critical pressure and on the surface displacement.

1. Introduction

When two bodies are placed in contact, they touch either at a point, along a line, over a surface or in a combination thereof. While the initial contact is determined by the geometric features of the bodies, the extent generally changes when the bodies are deformed by applied forces, changes in temperature or other sources of stress. In the study of contact problems, a class of problems is considered when two bodies are in contact without a bond, so that the region of contact is not known. Here, determining the contact region, which depends on geometric features as well the load distribution, presents an additional task for finding the stress distribution. Contact problems have been studied extensively in the literature, but in most cases the study was confined to isotropic and homogeneous solids. With the increasing use of functionally graded materials or anisotropic materials in industry, the study needs to be extended to these materials also.

A comprehensive list of work by earlier investigators has been provided in [Sneddon and Lowengrub 1969] and also [Gladwell 1980]. Among the recent works on the contact problems, notable are the works of Civelek et al. [1978], Schmuesre et al. [1980], Gecit [1981], Selvanduri [1983], Loboda and Tauchert [1985], Martynyak [1985], Fabrikant [1986], Li and Dempsey [1988], Wu and Yen [1994], Shvets et al. [1996], Argatov [2000], Brock and Georiadis [2001], Kit and Monastyrsky [2001], Argatov [2004], and Barik et al. [2006].

The very important class of contact problems known as receding contact problems is the subject of study for many investigators. If the contact area diminishes as the load is applied, the contact is called receding. The analytical studies involving receding contact in homogeneous and graded media can be found in [Hussain et al. 1968; Noble and Hussain 1969; Weitsman 1969; Pu and Hussain 1970; Keer et al. 1972; Gecit 1986; Nowell and Hills 1988; Chaudhuri and Ray 1998; Birinci and Erdol 1999; Chaudhuri and Ray 2003; Comez et al. 2004; El-Borgi et al. 2006]. Numerical studies based either on the finite element method or on the boundary element method can be found in [Jing and Liao 1990; Garrido et al. 1991; Paris et al. 1995; Satish Kumar et al. 1996; Garrido and Lorenzana 1998].

Keywords: Hankel transform, dual integral equation, Fredholm integral equation, elastic nonhomogeneity.

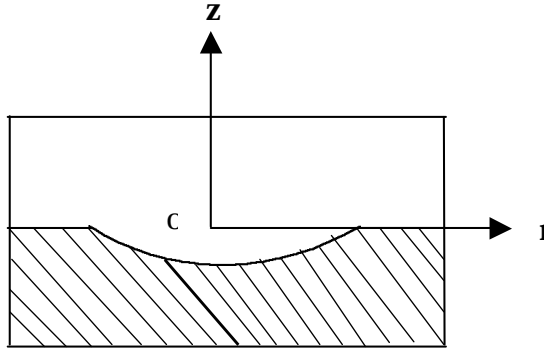


Figure 1. The semiinfinite solid with recess considered here.

In a recent paper, Kit and Monastyrsky [2001] discussed an axially symmetric problem of frictionless contact between an elastic half space and a rigid base with a small surface recess. The elastic material considered was isotropic and homogeneous. The present investigation aims at studying a similar problem, but in a nonhomogeneous elastic medium.

The nonhomogeneity arises because the rigidity modulus varies with distance in the medium. Although in the homogeneous case the displacement components are expressible in terms of potential functions, the solution of the governing equations is not so simple here, because of the nonhomogeneous modulus. Following the technique discussed in [Ozturk and Erdogan 1993], we have found the displacement components and, using the boundary conditions, have obtained a pair of dual integral equations. Further manipulation yields Fredholm integral equations, which we solve numerically. We have done numerical computations to show the effect of the nonhomogeneity. Finally, we have checked that results of [Kit and Monastyrsky 2001] are recovered from ours by zeroing the nonhomogeneous parameter.

2. Formulating the problem

Let a semiinfinite solid of nonhomogeneous isotropic material with a flat surface lie on a semiinfinite solid of rigid material. The boundary of the solid of rigid material is everywhere planar except for a geometrical defect, which is shallow axisymmetric recess, as seen in Figure 1. We put the origin at the common boundary of the half spaces and point the z_1 -axis of the cylindrical coordinate system (r_1, θ, z_1) into the elastic medium along the recess's axis of symmetry. We represent the bounding surface of the rigid base containing the recess by the equations

$$z_1 = f_1(r_1) = \begin{cases} -h_0 \left(1 - \frac{r_1^2}{b^2}\right)^{3/2}, & 0 < r_1 \leq b, \\ 0, & r_1 > b. \end{cases}$$

We shall assume that contact is smooth. In the absence of applied pressure on the solids, contact is made along the plane $z_1 = 0$, except for the central area $|r_1| < b$. Applying the normal pressure p at infinity will cause the contact surface to increase. Let $a_1(p)$ be the radius of the gap, that is, the region in which there is no contact, as an as-yet unknown function of p , as shown in Figure 2. Before proceeding, it will be convenient to adopt dimensionless variables by rescaling all lengths by the problem's only length

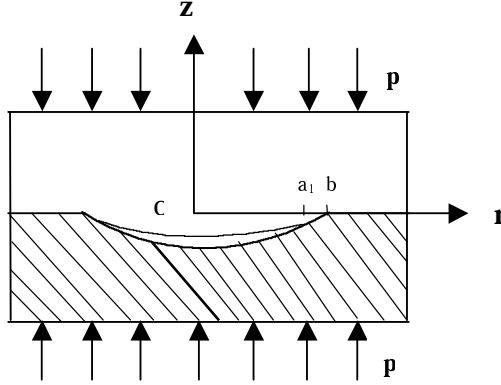


Figure 2. The first contact point a_1 moves inward as the pressure p increases.

scale b :

$$r = \frac{r_1}{b}, \quad z = \frac{z_1}{b}, \quad h = \frac{h_0}{b}, \quad a = \frac{a_1}{b}, \quad \hat{\sigma}_{i,j} = \frac{\sigma_{i,j}}{\mu_0}, \quad \hat{u}_i = \frac{u_i}{b},$$

where here and in the following $i, j = r, \theta, z$. In the dimensionless variables, the surface with recess becomes

$$z = f(r) = \begin{cases} -h(1-r^2)^{3/2}, & r \leq 1, \\ 0, & r > 1. \end{cases} \quad (1)$$

In the analysis below, for notational convenience, we shall use only dimensionless variables and politely remove their hats $\hat{}$.

We suppose that the elastic material is nonhomogeneous by assuming the rigidity modulus μ varies along the z -axis as

$$\mu = \mu_0 e^{\alpha z}, \quad (2)$$

where α is the nonhomogeneity parameter. Because of axisymmetry, the field variables are independent of θ and the displacement vector $(u, 0, w)$ is a function of r and z only. Using the strain displacement relations

$$\begin{aligned} e_{rr} &= \frac{\partial u}{\partial r}, & e_{\theta\theta} &= \frac{u}{r}, \\ e_{zz} &= \frac{\partial w}{\partial z}, & 2e_{rz} &= \frac{\partial u}{\partial z} + \frac{\partial w}{\partial r}, \end{aligned}$$

and Hooke's law

$$\sigma_{ij} = \frac{\lambda}{\mu_0} e_{kk} \delta_{ij} + 2 \frac{\mu}{\mu_0} e_{ij},$$

where λ and μ are the Lamé's constants and δ_{ij} is the Kronecker delta, the equations of equilibrium

$$\begin{aligned} 0 &= \frac{\partial \sigma_{rr}}{\partial r} + \frac{\partial \sigma_{rz}}{\partial z} + \frac{\sigma_{rr} - \sigma_{\theta\theta}}{r}, \\ 0 &= \frac{\partial \sigma_{rz}}{\partial r} + \frac{\partial \sigma_{zz}}{\partial z} + \frac{\sigma_{rz}}{r}, \end{aligned} \quad (3)$$

may be expressed in terms of displacements components u and w as:

$$\begin{aligned}
0 &= (\kappa + 1) \left(\frac{\partial^2 u}{\partial r^2} + \frac{1}{r} \frac{\partial u}{\partial r} - \frac{u}{r^2} \right) + 2 \frac{\partial^2 w}{\partial r \partial z} + (\kappa - 1) \frac{\partial^2 u}{\partial z^2} + (\kappa - 1) \alpha \left(\frac{\partial u}{\partial z} + \frac{\partial w}{\partial r} \right), \\
0 &= (\kappa + 1) \frac{\partial^2 w}{\partial z^2} + \frac{2}{r} \frac{\partial u}{\partial z} + 2 \frac{\partial^2 u}{\partial r \partial z} + (\kappa - 1) \left(\frac{\partial^2 w}{\partial r^2} + \frac{1}{r} \frac{\partial w}{\partial r} \right) \\
&\quad + (3 - \kappa) \alpha \left(\frac{\partial u}{\partial r} + \frac{u}{r} \right) + (\kappa + 1) \alpha \frac{\partial w}{\partial z},
\end{aligned} \tag{4}$$

where $\kappa = 3 - 4\nu$ and ν is Poisson's ratio.

The boundary conditions for the problem are

$$\begin{aligned}
\lim_{z \rightarrow -\infty} \sigma_{zz}(r, z) &= -\frac{P}{\mu_0}, \\
\lim_{z \rightarrow -\infty} \sigma_{rz}(r, z) &= 0,
\end{aligned} \tag{5}$$

$$\begin{aligned}
\sigma_{zz}(r, 0) &= 0, & 0 < r < a, \\
\sigma_{rz}(r, 0) &= 0, & 0 < r < \infty, \\
w(r, 0) &= f(r), & a < r < \infty,
\end{aligned} \tag{6}$$

In addition to conditions Equation (6) we should have the condition

$$\sigma_{zz}(a, 0) = 0, \quad 0 \leq a \leq 1 \tag{7}$$

which follows from the smoothness of $f(r) \in [0, 1)$.

The boundary condition of Equations (5) and (7) can also be written as

$$\begin{aligned}
\sigma_{zz}(r, 0)[w(r, 0) - f(r)] &= 0, \\
\sigma_{zz}(r, 0) &\leq 0, & w(r, 0) &\leq f(r), \quad 0 \leq r \leq 1 \\
\sigma_{rz}(r, 0) &= 0, & & 0 \leq r < \infty, \\
w(r, 0) &= f(r), & & 1 \leq r < \infty.
\end{aligned}$$

3. Solving the problem

Now we will describe the strained state of the elastic body and the relation between the gap geometry and ambient pressure. We will also find the critical value at which the gap disappears. To this end, we divide the solutions into two parts:

$$\sigma = \sigma^{(1)} + \sigma^{(2)}, \quad u = u^{(1)} + u^{(2)}. \tag{8}$$

The first terms, $\sigma^{(1)}$ and $u^{(1)}$, are solutions of the problem of the contact of an elastic body and rigid base with flat surface. The second terms correspond to the perturbed stressed-strained state caused by geometric nonhomogeneity of the surface.

Because the perturbations are local, we can write

$$\lim_{(r,z) \rightarrow \infty} \sigma^{(2)}(r, z) = 0, \quad \lim_{(r,z) \rightarrow \infty} u^{(2)}(r, z) = 0.$$

The first solution may be obtained in the form

$$\begin{aligned} \sigma_{zz}^{(1)} &= -\frac{P}{\mu_0}, & \sigma_{rr}^{(1)} &= 0, & \sigma_{rz}^{(1)} &= 0, \\ u^{(1)} &= \frac{\nu}{E} pr, & w^{(1)} &= \frac{\nu}{\alpha E} pz. \end{aligned} \quad (9)$$

Using the boundary conditions of Equations (5) and (6) and using Equations (8) and (9), the boundary conditions for the perturbed fields become

$$\begin{aligned} \lim_{z \rightarrow \infty} \sigma_{zz}^{(2)}(r, z) &= 0 \\ \lim_{z \rightarrow \infty} \sigma_{rz}^{(2)}(r, z) &= 0, \\ \sigma_{zz}^{(2)}(r, 0) &= \frac{P}{\mu_0}, & 0 < r < a, \\ \sigma_{rz}^{(2)}(r, 0) &= 0, & 0 < r < \infty, \\ w^{(2)}(r, 0) &= f(r), & a < r < \infty \end{aligned} \quad (10)$$

To solve for the perturbed field, we assume the solution of Equation (3) in the form

$$\begin{aligned} u^{(2)}(r, z) &= \int_0^\infty d\rho F_1(z, \rho) \rho J_1(r\rho), \\ w^{(2)}(r, z) &= \int_0^\infty d\rho F_2(z, \rho) J_0(r\rho), \end{aligned} \quad (11)$$

where J_0 and J_1 are Bessel functions of first kind of orders zero and one, respectively. Substituting Equation (11) into Equation (4) and inverting the related Hankel transforms, we find

$$\begin{aligned} [(\kappa - 1)D^2 + \alpha(\kappa - 1)D - (\kappa + 1)\rho^2] F_1 - [2D + \alpha(\kappa - 1)] F_2 &= 0 \\ [(\kappa + 1)D^2 + \alpha(\kappa + 1)D - (\kappa - 1)\rho^2] F_2 + \rho^2 [2D + \alpha(3 - \kappa)] F_1 &= 0, \end{aligned} \quad (12)$$

where $D = \frac{d}{dz}$. In deriving this, the following relationships have been used:

$$\begin{aligned} \left(\frac{\partial^2}{\partial r^2} + \frac{1}{r} \frac{\partial}{\partial r} - \frac{1}{r^2} \right) J_1(r\rho) &= -\rho^2 J_1(r\rho), \\ \left(\frac{\partial}{\partial r} + \frac{1}{r} \right) J_1(r\rho) &= \rho J_0(r\rho), \\ \frac{\partial^2}{\partial r^2} J_0(r\rho) &= \frac{\rho}{r} J_1(r\rho) - \rho^2 J_0(r\rho). \end{aligned}$$

The solutions of the system of differential equations (12) are found to be

$$\begin{aligned} F_1(z, \rho) &= \sum_{k=1}^4 A_k(\rho) e^{m_k z}, \\ F_2(z, \rho) &= \sum_{k=1}^4 a_k(\rho) A_k(\rho) e^{m_k z}, \end{aligned} \quad (13)$$

where the functions A_k , $k = 1, \dots, 4$, are unknowns, and m_k , $k = 1, \dots, 4$, are the roots of the characteristic equation

$$m^4 + 2\alpha m^3 + (\alpha^2 - 2\rho^2)m^2 - 2\alpha\rho^2 m + \alpha^2\rho^2 \frac{3-\kappa}{1+\kappa} + \rho^4 = 0, \quad (14)$$

and the coefficients a_k , $k = 1, \dots, 4$, are given by

$$a_k(\rho) = -\rho^2 \frac{2m_k + \alpha(3-\kappa)}{(1+\kappa)m_k^2 + (1+\kappa)\alpha m_k - (\kappa-1)\rho^2}. \quad (15)$$

The characteristic Equation (14) may easily be rewritten as

$$(m^2 + \alpha m - \rho^2)^2 + \alpha^2 \rho^2 \frac{3-\kappa}{1+\kappa} = 0,$$

from which it follows that

$$m_3 = \overline{m_1} = \frac{-\alpha + \beta}{2}, \quad m_4 = \overline{m_2} = -\frac{\alpha + \beta}{2}$$

where

$$\beta = \sqrt{\alpha^2 + 4\rho^2 + i4\alpha\rho\sqrt{\frac{3-\kappa}{1+\kappa}}},$$

After solving for m_k , $k = 1, \dots, 4$, the expressions for the coefficients a_k in Equation (15) may be simplified as follows:

$$\begin{aligned} a_k(\rho) &= -\rho \frac{2m_k + \alpha(3-\kappa)}{2\rho + i\alpha\sqrt{(3-\kappa)(1+\kappa)}}, \\ a_{k+2} &= \overline{a_k}, \end{aligned}$$

for $k = 1, 2$. We observe that $\Re m_1, \Re m_3 > 0$ and $\Re m_2, \Re m_4 < 0$, so, to satisfy the regularity condition at $z = \infty$ in the solution given by Equation (13), we must put $A_1 = A_3 = 0$ for $z > 0$. Thus the problem may be considered as that of an elastic upper half space with rigid base involving only two unknowns A_2 and A_4 , and, for $z > 0$, we have

$$\begin{aligned} F_1(z, \rho) &= A_2(\rho) e^{m_2 z} + A_4(\rho) e^{m_4 z}, \\ F_2(z, \rho) &= a_2(\rho) A_2(\rho) e^{m_2 z} + a_4(\rho) A_4(\rho) e^{m_4 z}. \end{aligned}$$

The unknowns A_2 and A_4 may be determined from the mixed boundary conditions of Equation (6). Hence, the dimensionless displacement and stress components can be written in terms of A_2 and A_4 as

$$\begin{aligned}
 u^{(2)}(r, z) &= \int_0^\infty d\rho (A_2 e^{m_2 z} + A_4 e^{m_4 z}) \rho J_1(r\rho) \\
 w^{(2)}(r, z) &= \int_0^\infty d\rho (a_2 A_2 e^{m_2 z} + a_4 A_4 e^{m_4 z}) J_0(r\rho) \\
 \sigma_{rz}^{(2)}(r, z) &= \frac{\mu}{\mu_0} \int_0^\infty d\rho ((m_2 - a_2) A_2 e^{m_2 z} + (m_4 - a_4) A_4 e^{m_4 z}) \rho J_1(r\rho) \\
 \sigma_{zz}^{(2)}(r, z) &= \frac{\mu}{\mu_0} \int_0^\infty d\rho \left[\frac{\kappa + 1}{\kappa - 1} (m_2 a_2 A_2 e^{m_2 z} + m_4 a_4 A_4 e^{m_4 z}) \right. \\
 &\quad \left. + \frac{3 - \kappa}{\kappa + 1} (A_2 e^{m_2 z} + A_4 e^{m_4 z}) \rho^2 \right] J_0(r\rho)
 \end{aligned} \tag{16}$$

Using the second boundary condition of Equation (10) yields

$$A_4(\rho) = -\frac{m_2 - a_2}{m_4 - a_4} A_2(\rho), \tag{17}$$

and the remaining two mixed boundary conditions, with the help of the last two of Equation (16) and Equation (17), give a pair of dual integral equations

$$\begin{aligned}
 \int_0^\infty d\rho A_2^*(\rho) J_0(r\rho) &= f(r), & a < r < \infty, \\
 \int_0^\infty d\rho G_1(\rho) A_2^*(\rho) J_0(r\rho) &= \frac{\kappa - 1}{\mu_0} p, & 0 < r < a,
 \end{aligned} \tag{18}$$

where

$$\begin{aligned}
 A_2^*(\rho) &= \frac{a_2 m_4 - a_4 m_2}{m_4 - a_4} A_2(\rho), \\
 G_1(\rho) &= \frac{1}{a_2 m_4 - a_4 m_2} [(\kappa + 1) (|m_2|^2 (a_2 - a_4) - |a_2|^2 (m_2 - m_4)) \\
 &\quad + (3 - \kappa) (a_2 - a_4 + m_4 - m_2) \rho^2].
 \end{aligned} \tag{19}$$

Denoting

$$\begin{aligned}
 a_2(\rho) &= A(\rho) + iB(\rho), \\
 m_2(\rho) &= -\frac{\alpha + c(\rho)}{2} - i\frac{d(\rho)}{2},
 \end{aligned}$$

we get $G_1(\rho)$ in the form

$$G_1(\rho) = \frac{(\kappa + 1) (2|m_2|^2 B(\rho) - |a_2|^2 d(\rho)) + (3 - \kappa) \rho^2 (2B(\rho) + d(\rho))}{A(\rho)d(\rho) - (\alpha + c(\rho)) B(\rho)}.$$

If we write

$$A_2^*(\rho) = C^*(\rho) + D^*(\rho),$$

where

$$D^*(\rho) = \rho \int_0^\infty dr J_0(r\rho) r f(r), \quad (20)$$

then the dual integral equations of Equation (18) transform into

$$\begin{aligned} \int_0^\infty d\rho C^*(\rho) J_0(r\rho) &= 0, & a < r < \infty, \\ \int_0^\infty d\rho G_1(\rho) C^*(\rho) J_0(r\rho) &= g(r), & 0 < r < a, \end{aligned} \quad (21)$$

where

$$g(r) = \frac{\kappa - 1}{\mu_0} p - \int_0^\infty d\rho G_1(\rho) D^*(\rho) J_0(r\rho). \quad (22)$$

Substituting the expression for $f(r)$ from Equation (1) into Equation (20) we get

$$D^*(\rho) = -3h \sqrt{\frac{\pi}{2}} \rho^{-3/2} J_{5/2}(\rho)$$

If we write

$$C^*(\rho) = \int_0^a dt \phi(t) \sin(t\rho), \quad (23)$$

where $\phi(t)$ is an unknown integrable function, then the first of Equation (21) is automatically satisfied. Substitution of Equation (23) in the second of Equation (21) leads to the equation

$$r \int_0^a dt \phi(t) \int_0^\infty d\rho \frac{G_1(\rho)}{\rho} J_1(r\rho) \sin(t\rho) = \int_0^r ds s g(s) \equiv g_1(r), \quad (24)$$

for determining the unknown function ϕ . We note that for large ρ ,

$$\frac{G_1(\rho)}{\rho} = \chi_1 + O(\rho^{-1}), \quad \text{where} \quad \chi_1 = 4 \frac{1 - \kappa}{1 + \kappa}.$$

Equation (24) may be reduced to a standard integral equation by rewriting it in the form

$$r \int_0^a dt \phi(t) \int_0^\infty d\rho J_1(r\rho) \sin(t\rho) \left[\chi_1 + \left(\frac{G_1(\rho)}{\rho} - \chi_1 \right) \right] = g_1(r). \quad (25)$$

Using the properties of Bessel function, this equation is finally reduced to a Fredholm integral equation of the second kind;

$$\chi_1 \phi(r) + \int_0^a dt K(r, t) \phi(t) = \frac{2}{\pi} \int_0^r dy \frac{y g(y)}{\sqrt{r^2 - y^2}}, \quad 0 < r < a, \quad (26)$$

where the kernel $K(r, t)$ is given by

$$K(r, t) = \frac{2}{\pi} \int_0^\infty d\rho G_2(\rho) \sin(r\rho) \sin(t\rho), \quad (27)$$

and

$$G_2(\rho) = \frac{G_1(\rho)}{\rho} - \chi_1.$$

We shall discuss the integral equation (26) and its kernel $K(r, t)$ in the next section.

Equations (16), (17), (19), (23), and (26) determine that the deformed state of the elastic half-space, the normal displacement $w^{(2)}$, and the pressure on its surface are given by

$$w^{(2)}(r, 0) = \begin{cases} \int_0^a dt \phi(t) H_2(t, r) + f(r), & 0 < r < a, \\ f(r), & r > a, \end{cases} \quad (28)$$

where

$$H_2(t, r) = \int_0^\infty d\rho \sin(t\rho) J_0(r\rho)$$

and

$$\sigma_{zz}^{(2)}(r, 0) = \begin{cases} \frac{p}{\mu_0}, & 0 < r < a, \\ \frac{1}{\kappa-1} \left[H_1(r) - \frac{3h\pi\chi_1}{4} \left(1 - \frac{3}{2}r^2 \right) \right], & a < r \leq 1, \\ \frac{1}{\kappa-1} \left[H_1(r) + \frac{h\chi_1}{5r^3} {}_2F_1 \left(\frac{3}{2}, \frac{3}{2}; \frac{7}{2}, \frac{1}{r^2} \right) \right], & r > 1, \end{cases} \quad (29)$$

where

$$H_1(r) = \int_0^a dt \phi(t) \int_0^\infty d\rho G_2(\rho) J_0(\rho) \sin(t\rho) - 3h\sqrt{\frac{\pi}{2}} \int_0^\infty d\rho \rho^{-1/2} G_2(\rho) J_0(\rho) J_{5/2}(\rho) - \chi_1 \frac{\phi(a)}{\sqrt{r^2 - a^2}} + \chi_1 \frac{\phi(0)}{r} + \chi_1 \phi'(a) \sin^{-1}(a/r) - \chi_1 \int_0^a dt \phi''(t) \sin^{-1}(t/r). \quad (30)$$

Finally, putting Equations (9), (28), and (29) into Equation (8), we get the expressions for $w(r, 0)$ and $\sigma_{zz}(r, 0)$:

$$w(r, 0) = \begin{cases} \int_0^a dt \phi(t) H_2(t, r) + f(r), & 0 < r < a, \\ f(r), & r > a, \end{cases} \quad (31)$$

$$\sigma_{zz}(r, 0) = \begin{cases} \frac{p}{\mu_0} & 0 < r < a \\ \frac{1}{\kappa-1} \left[H_1(r) - \frac{3h\pi\chi_1}{4} \left(1 - \frac{3}{2}r^2 \right) \right], & a < r \leq 1 \\ \frac{1}{\kappa-1} \left[H_1(r) + \frac{h\chi_1}{5r^3} {}_2F_1 \left(\frac{3}{2}, \frac{3}{2}; \frac{7}{2}, \frac{1}{r^2} \right) \right], & r > 1. \end{cases} \quad (32)$$

The boundary condition Equation (7) demands that

$$\phi(a) = 0. \quad (33)$$

Putting this and Equation (22) into Equation (26) yields

$$\frac{p}{\mu_0} = \frac{1}{a(\kappa-1)} \left[\frac{\pi}{2} \int_0^a dt K(a, t) \phi(t) + \int_0^\infty d\rho \frac{G_1(\rho)}{\rho} D^*(\rho) \sin(a\rho) \right]. \quad (34)$$

This equation gives a relationship between the dimensionless applied pressure p/μ_0 and the dimensionless radius a of the gap. For a given p/μ_0 , the equation determining a is nonlinear. From this equation,

it is easy to obtain the critical pressure p^* at which gap disappears, that is, at which $a = 0$. The value of p^* is obtained as

$$\frac{p^*}{\mu_0} = \frac{1}{\kappa - 1} \int_0^\infty d\rho G_1(\rho) D^*(\rho). \quad (35)$$

It should be noted as an important check on our results that if we take $\alpha = 0$ —that is, if we assume the upper half space is homogeneous and isotropic—then the expressions for p and p^* reduce to those obtained by Kit and Monastyrsky [2001].

4. Determining $\phi(r)$

The infinite integral $K(r, t)$ in Equation (27) is smooth except possibly at $\rho = 0$ and $\rho = \infty$. We may check that

$$G_2(\rho) = \frac{\psi(\rho)}{\rho^2} - \chi_1 \quad \text{as} \quad \rho \rightarrow 0, \quad (36)$$

where $\psi(\rho)$ is regular in the neighborhood of $\rho = 0$. This implies that

$$\lim_{\rho \rightarrow 0} G_2(\rho) \sin(t\rho) \sin(r\rho) = \text{a finite quantity}, \quad (37)$$

so $\rho = 0$ is not a singularity for that integral.

Now, for large ρ , $G_2(\rho) = O(\rho^{-1})$. From Gradshteyn and Ryzhik [1963],

$$\int_0^\infty d\rho \frac{\sin(t\rho) \sin(r\rho)}{\rho} = \frac{1}{2} \log \left| \frac{r+t}{r-t} \right|, \quad r \neq t, \quad (38)$$

and it follows that the behavior of the integral as $\rho \rightarrow \infty$ is not smooth for $r = t$, so determination of $\phi(r)$ from Equation (26) could be a problem. However, this difficulty may be easily overcome by writing Equation (25) in the form

$$\int_0^a dt \left[\frac{1}{t-r} + L(r, t) \right] \phi(t) = g_1(r) \quad (39)$$

where

$$\begin{aligned} L(r, t) &= \chi_1 L_0(r, t) + L_1(r, t) - \frac{1}{t-r}, \\ L_0(r, t) &= r \int_0^\infty d\rho J_1(r\rho) \sin(t\rho) = \begin{cases} \frac{t}{\sqrt{r^2 - t^2}}, & t < r, \\ 0, & t \geq r, \end{cases} \\ L_1(r, t) &= r \int_0^\infty d\rho \left(\frac{G_1(\rho)}{\rho} - \chi_1 \right) J_1(r\rho) \sin(t\rho), \end{aligned} \quad (40)$$

Using the rescalings

$$t(u) = \frac{a}{2}(1+u), \quad r(x) = \frac{a}{2}(1+x), \quad (41)$$

and the notations

$$\phi^*(u) = \phi(t(u)), \quad g^*(x) = g(r(x)), \quad (42)$$

Equation (39) is transformed into a singular integral equation

$$\int_{-1}^1 du \phi^*(u) \left[\frac{1}{u-x} + \frac{a}{2} L^*(u, x) \right] du = g_1^*(x), \quad \text{where } L^*(u, x) = L\left(\frac{a}{2}(1+u), \frac{a}{2}(1+x)\right). \quad (43)$$

This integral equation can be evaluated by using Gauss–Chebyshev method. It may be noted that $u = -1$ corresponds to $t = 0$ and $u = 1$ corresponds to $t = a$. Since the contact is smooth, neither the point $t = 0$ (that is, $u = -1$) nor the point $t = a$ (that is, $u = 1$) is a singularity of the function ϕ . Following [Erdogan and Gupta 1972], we take the solution $\phi^*(u)$ of integral equation Equation (43) in the form

$$\phi^*(u) = \sqrt{1-u^2} G(u), \quad -1 \leq u \leq 1,$$

where $G(u)$ is a bounded unknown function. Now, using Gauss–Chebyshev formula, we express the integral equation (43) in discretized form as

$$\sum_{k=1}^N \frac{\pi \sqrt{1-u_k^2}}{N+1} G(u_k) \left[\frac{1}{u_k-x_j} + \frac{a}{2} L^*(u_k, x_j) \right] = g_1(x_j), \quad (44)$$

where $j = 1, \dots, N+1$, and u_k and x_j are given by

$$u_k = \cos\left(\frac{k\pi}{N+1}\right) \quad \text{and} \quad x_j = \cos\left(\pi \frac{j-1/2}{N+1}\right).$$

Equation (44) gives a set of $(N+1)$ linear equations—one for each collocation point x_j —in the N unknowns $G(u_1), \dots, G(u_N)$. To determine the $G(u_k)$, we may ignore one collocation point, say the midpoint $x_{N/2+1}$ when N is even, and let the remaining N equations determine $G(u_k)$. This linear algebraic system can be solved by gaussian eliminations.

We note here that although Equation (26) is not quite suitable for numerical evaluation of $\phi(r)$, it is very much useful for determining the applied pressures p and p^* in relatively simple forms (see Equations (34) and (35)). Also, evaluating the integral

$$\int_0^a dt K(a, t) \phi(t) \quad (45)$$

in Equation (34) will not pose any problem here, since $\phi(a) = 0$.

5. Numerical results and discussions

We have noted that zero is not a singularity for the infinite integrals in Equations (27) and (30), and, because the integrals are regular for finite ρ , we will, in numerically evaluating these integrals, study only their behavior at infinity. We find that $G_2(\rho)$ can be asymptotically represented for large ρ as

$$G_2(\rho) = \frac{\chi_2}{\rho} + \frac{\chi_3}{\rho^2} + \frac{\chi_4}{\rho^3} + \dots \quad (46)$$

The coefficients χ_2 , χ_3 , and χ_4 are given in Appendix A.

To examine the convergence of the improper integrals in Equations (27) and (30), let us take any one, say, the improper integral

$$\int_0^{\infty} d\rho G_2(\rho) J_0(\rho) \sin(t\rho) \quad (47)$$

in Equation (30). We write

$$\int_0^{\infty} d\rho G_2(\rho) J_0(\rho) \sin(t\rho) = \lim_{A \rightarrow \infty} \int_0^A d\rho G_2(\rho) J_0(\rho) \sin(t\rho). \quad (48)$$

For large ρ , we write the integral

$$\int_0^A d\rho G_2(\rho) J_0(\rho) \sin(t\rho) \quad (49)$$

as the sum of two integrals I_1 and $I_2(A)$ such that

$$\begin{aligned} I_1 &= \int_0^{\zeta} d\rho G_2(\rho) J_0(\rho) \sin(t\rho), \\ I_2(A) &= \int_{\zeta}^A d\rho G_2(\rho) J_0(\rho) \sin(t\rho), \end{aligned} \quad (50)$$

where ζ is a suitably chosen cutoff point. The first integral I_1 is numerically evaluated using gaussian quadratures. Noting the asymptotic behavior of $G_2(\rho)$ from Equation (46) and shown in Figure 3, it is expected that for sufficiently large A , the integral I_2 should converge. This is numerically checked and shown in Table 1.

Thus, for a given tolerance ϵ , the upper limit A can be determined numerically, and the value of the integral $I_2(\infty)$ can then be approximated as $I_2(A)$ at tolerance level ϵ . For example, from Table 1, for $\zeta = 25$ and $\epsilon = 10^{-5}$, we have $A = 205$.

We can then determine ϕ numerically by the method described in Section 4. Finally, we find $w(r, 0)$, $\sigma_{zz}(r, 0)$, p/μ_0 , and p^*/μ_0 from Equations (31), (32), (34), and (35).

The dimensionless gap radius a depends on p/μ_0 as well as on the nonhomogeneity parameter α . From Equation (2), it is clear that as α increases, the material becomes harder. This implies in turn that if α is larger, a larger pressure p/μ_0 will be required to produce same change in a . Also, it is expected that

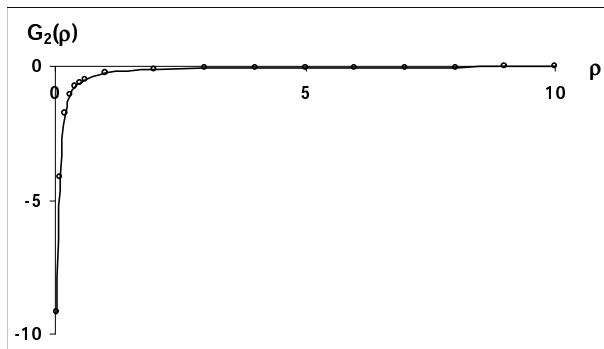


Figure 3. A plot of $G_2(\rho)$.

A	$I_2(A)$	A	$I_2(A)$	A	$I_2(A)$	A	$I_2(A)$
30	-0.00077027	75	-0.00162461	120	-0.00093715	165	-0.00105215
35	-0.00056793	80	-0.00095082	125	-0.00103405	170	-0.00096191
40	-0.00162461	85	-0.00084971	130	-0.00098509	175	-0.00101668
45	-0.00070269	90	-0.00118899	135	-0.00090544	180	-0.00099818
50	-0.00114482	95	-0.00090935	140	-0.00107440	185	-0.00093061
55	-0.00090488	100	-0.00105012	145	-0.00095260	190	-0.00103696
60	-0.00077959	105	-0.00097268	150	-0.00102384	195	-0.00096784
65	-0.00129027	110	-0.00088441	155	-0.00099292	200	-0.00101127
70	-0.00085225	115	-0.00110913	160	-0.00091986	205	-0.00100183

Table 1. $I_2(A)$ for $t = 0.5$ and cutoff point $\zeta=25$.

as p/μ_0 increases, a should decrease. To check the expected behavior we have computed from Equation (34), we compute p/μ_0 for different a and α . The results are graphed in Figure 4. In Figure 5, we show how dimensionless critical pressure p^*/μ_0 varies with nonhomogeneity parameter α . As expected, the critical pressure increases with α .

From Equation (1), we find that the function $f(r)$ is not differentiable at $r = 1$. Because the geometrical structure of the recess is expected to contribute to the behavior of surface stress distribution, we have evaluated the surface stress $\sigma_{zz}(r, 0)$ as $r \rightarrow 1$. We find that there is a finite discontinuity in the normal stress $\sigma_{zz}(r, 0)$ in the neighborhood of $r = 1$. The values of $\sigma_{zz}(r, 0)$ have been plotted against the nonhomogeneity parameter α and the gap radius a in Figures 6 and 7, respectively. In Figures 8 and 9, we show how $w(r, 0)$ varies with a and α .

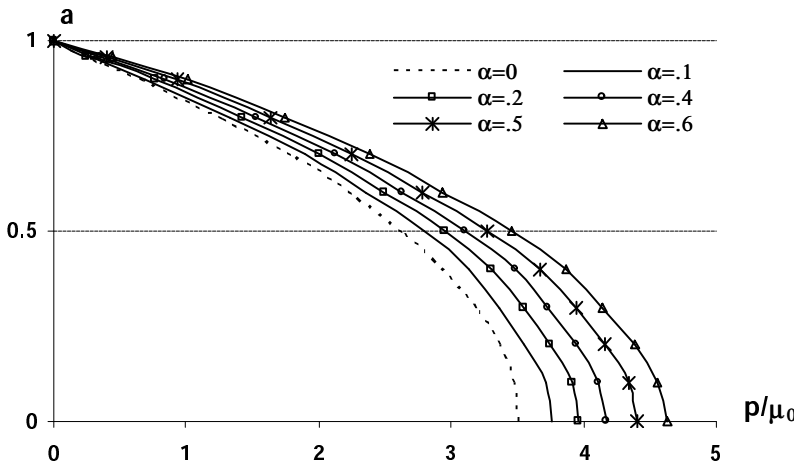


Figure 4. Variation of ambient pressure p/μ_0 with the first contact radius a for different values of the nonhomogeneity parameter α .

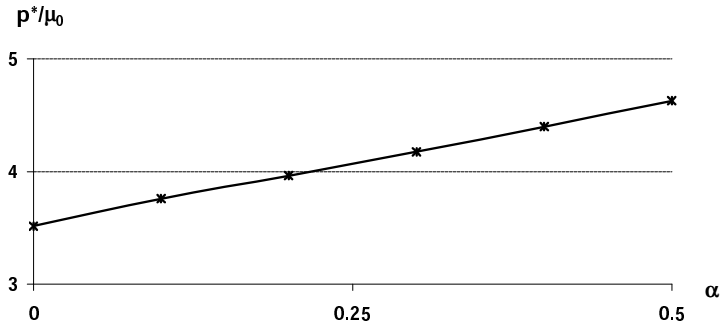


Figure 5. Variation of dimensionless critical pressure p^*/μ_0 for different values of the nonhomogeneity parameter α .

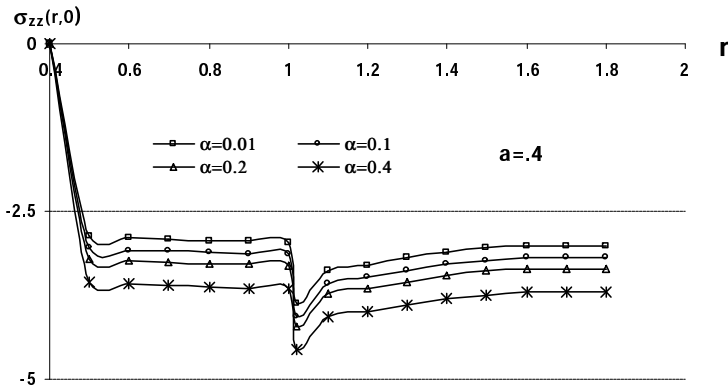


Figure 6. Variation of dimensionless normal stress $\sigma_{zz}(r, 0)$ with $r (> a)$ for various values of the nonhomogeneity parameter α .

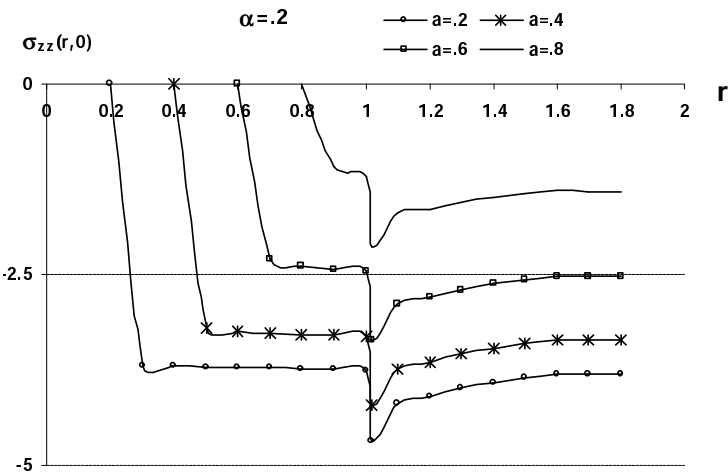


Figure 7. Variation of dimensionless normal stress $\sigma_{zz}(r, 0)$ with $r (> a)$ for different values of a .

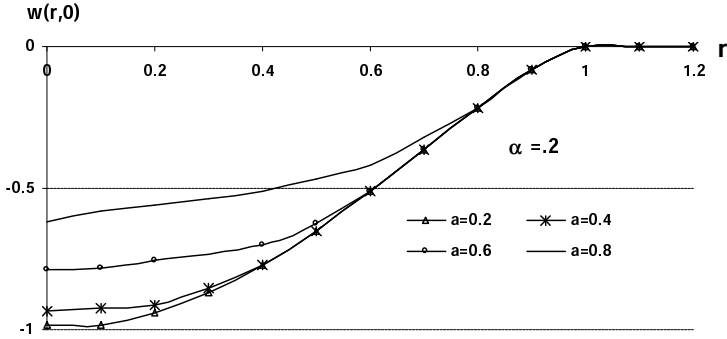


Figure 8. Variation of dimensionless normal displacement $w(r, 0)$ with r for different values of a .

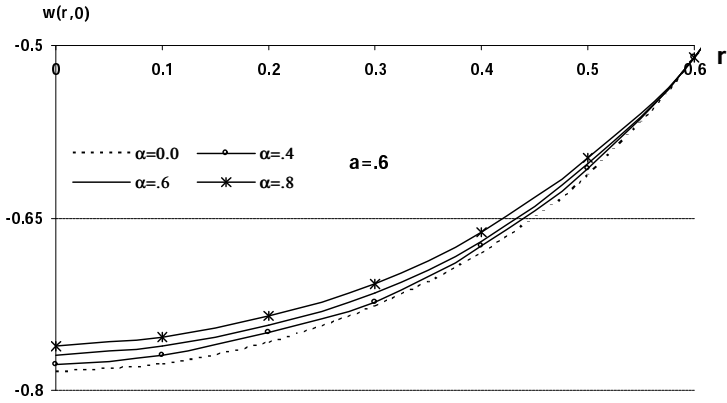


Figure 9. Variation of dimensionless normal displacement $w(r, 0)$ with $r < a$ for various values of the nonhomogeneity parameter α .

Appendix A

$$\chi_2 = 2 \frac{b_1 \alpha (\chi_1 + 2(\kappa + 1)) + 2b_2 (\chi_1 + 2(\kappa - 1)) + A_1 d_1 (2(\kappa + 1) - \chi_1)}{\alpha \sqrt{(3 - \kappa)(\kappa + 1)}},$$

$$\chi_3 = \frac{1}{p_2} \left[\frac{4d_1 \alpha^2 (1 - \kappa - \kappa^2)}{\kappa + 1} - 4A_2 \alpha \sqrt{(3 - \kappa)(\kappa + 1)} - 2\alpha(\kappa + 1)b_2 \right. \\ \left. + (\kappa + 1)d_1 (A_1^2 + 2A_2 + b_1^2) \right] + \frac{1}{p_2^2} (p_1 p_2 \chi_2 - p_1^2 \chi_1 + p_2 p_3 \chi_1), \quad (\text{A.1})$$

$$\chi_4 = \frac{1}{p_2^2} [(\kappa + 1) (p_2 (u_4 + w_4) - p_1 (u_1 + w_1)) + (3 - \kappa) (2p_2 b_4 - p_1 (2b_3 - d_2))],$$

where

$$\begin{aligned} 2p_1/d_1 &= \kappa^2 + \kappa - 4)\alpha, & A_1 &= \frac{\alpha(\kappa - 2)}{2}, \\ p_2/d_1 &= \kappa + 1, & A_2 &= \frac{\alpha^2}{4(\kappa + 1)} (2 - \kappa(\kappa + 1)(3 - \kappa)), \\ p_3/d_1 &= \frac{(\kappa^3 - \kappa - 2)\alpha}{4(\kappa + 1)} + (\kappa + 2)A_2, & A_3 &= \frac{\alpha^3}{8} (2 - \kappa)(\kappa + 1)(3 - \kappa), \end{aligned}$$

$$\begin{aligned} u_1 &= \frac{4b_1}{\kappa + 1}\alpha^2 + 2\alpha b_2 + 2b_3, & w_1/d_1 &= (A_1^2 + 2A_2 + b_1^2) - \frac{\alpha^2}{2(\kappa + 1)}, \\ u_4 &= \frac{4b_2}{\kappa + 1}\alpha^2 + 2\alpha b_3 + 2b_4 + \frac{\alpha^3 b_1}{\kappa + 1}, & w_4/d_1 &= (2A_1 A_2 + 2A_3 + 2b_1 b_2) - 2A_1 \frac{\alpha^2}{2(\kappa + 1)}, \end{aligned}$$

$$\begin{aligned} b_1 &= -\frac{\kappa d_1}{2}, & b_3 &= -\frac{\alpha}{2} A_2 \sqrt{(3 - \kappa)(\kappa + 1)} + \frac{\alpha^2}{4(\kappa + 1)} d_1, & d_1 &= \alpha \sqrt{\frac{3 - \kappa}{\kappa + 1}}, \\ b_2 &= -\frac{(\kappa + 1)A_1 d_1}{2}, & b_4 &= \frac{\alpha^4}{16} (\kappa - 2) \sqrt[3]{(\kappa + 1)(3 - \kappa)}, & d_2 &= -\frac{\alpha^2}{2(\kappa + 1)} d_1. \end{aligned}$$

Acknowledgement

The authors express sincere thanks to the reviewers for valuable comments.

References

- [Argatov 2000] I. I. Argatov, "Asymptotic modelling of the contact interaction between a system of rigidly connected punches and an elastic base", *Sib. Zh. Ind. Math.* **3:2** (2000), 10–22.
- [Argatov 2004] I. I. Argatov, "The method of averaging in a contact problem for a system of punches", *J. Appl. Math. Mech.* **68:1** (2004), 93–104.
- [Barik et al. 2006] S. P. Barik, M. K. Kanoria, and P. K. Chaudhuri, "Contact problem for an anisotropic elastic layer lying on an anisotropic elastic foundation under gravity", *J. Indian Acad. Math.* **28:1** (2006), 205–223.
- [Birinci and Erdol 1999] A. Birinci and R. Erdol, "Frictionless contact between a rigid stamp and an elastic layered composite resting on simple supports", *Math. Comput. Appl.* **4** (1999), 261–272.
- [Brock and Georiadis 2001] L. M. Brock and H. G. Georiadis, "An illustration of sliding contact at any constant speed on highly elastic half-spaces", *J. Appl. Math.* **66** (2001), 551–566.
- [Chaudhuri and Ray 1998] P. K. Chaudhuri and S. Ray, "Receding contact between an orthotropic layer and an orthotropic half-space", *Arch. Mech.* **50** (1998), 743–755.
- [Chaudhuri and Ray 2003] P. K. Chaudhuri and S. Ray, "Receding axisymmetric contact between a transversely isotropic layer and a transversely isotropic half-space", *Bull. Am. Math. Soc.* **95** (2003), 151–164.
- [Civelek et al. 1978] M. B. Civelek, F. Erdogan, and A. O. Cakiroglu, "Interface separation for an elastic layer loaded by a rigid stamp", *Int. J. Eng. Sci.* **16:9** (1978), 669–679.
- [Comez et al. 2004] I. Comez, A. Birinci, and R. Erdol, "Double receding contact problem for a rigid stamp and two elastic layers", *Eur. J. Mech. A Solid.* **23:2** (2004), 301–309.
- [El-Borgi et al. 2006] S. El-Borgi, R. Abdelmoula, and L. Keer, "A receding contact plane problem between a functionally graded layer and a homogeneous substrate", *Int. J. Solids Struct.* **43:3-4** (2006), 658–674.

- [Erdogan and Gupta 1972] F. Erdogan and G. D. Gupta, "On the numerical solution of singular integral equations", *J. Appl. Math.* **29** (1972), 525–534.
- [Fabrikant 1986] V. I. Fabrikant, "Flat punch of arbitrary shape on an elastic half-space", *Int. J. Eng. Sci.* **24**:11 (1986), 1731–1740.
- [Garrido and Lorenzana 1998] J. A. Garrido and A. Lorenzana, "Receding contact problem involving large displacements using the BEM", *Eng. Anal. Bound. Elem.* **21**:4 (1998), 295–303.
- [Garrido et al. 1991] J. A. Garrido, A. Foces, and F. Paris, "B.E.M. applied to receding contact problems with friction", *Math. Comput. Model.* **15**:3-5 (1991), 143–153.
- [Gecit 1981] M. R. Gecit, "Axisymmetric contact problem for an elastic layer and an elastic foundation", *Int. J. Eng. Sci.* **19**:6 (1981), 747–755.
- [Gecit 1986] M. R. Gecit, "Axisymmetric contact problem for a semiinfinite cylinder and a half space", *Int. J. Eng. Sci.* **24**:8 (1986), 1245–1256.
- [Gladwell 1980] G. M. L. Gladwell, *Contact problems in the classical theory of elasticity*, Sijthoff and Noordhoff, Alphen aan den Rijn, The Netherlands, 1980.
- [Gradshteyn and Ryzhik 1963] I. S. Gradshteyn and I. M. Ryzhik, *Table of integrals, series, and products*, Academic Press, New York, 1963.
- [Hussain et al. 1968] M. A. Hussain, S. L. Pu, and M. A. Sadowsky, "Cavitation at the ends of an elliptic inclusion inside a plane under tension", *J. Appl. Mech. (Trans. ASME)* **35** (1968), 505–509.
- [Jing and Liao 1990] H.-S. Jing and M.-L. Liao, "An improved finite element scheme for elastic contact problems with friction", *Comput. Struct.* **35**:5 (1990), 571–578.
- [Keer et al. 1972] L. M. Keer, J. Dundurs, and K. C. Tasi, "Problem involving receding contact between a layer and a half-space", *J. Appl. Mech. (Trans. ASME)* **39** (1972), 1115–1120.
- [Kit and Monastyrsky 2001] G. S. Kit and B. E. Monastyrsky, "A contact problem for a half-space and a rigid base with an axially symmetric recess", *J. Math. Sci.* **107**:1 (2001), 3545–3549.
- [Li and Dempsey 1988] H. Li and J. Dempsey, "Unbonded contact of a square plate on an elastic half-space or a winkler foundation", *J. Appl. Mech. (Trans. ASME)* **55** (1988), 430–435.
- [Loboda and Tauchert 1985] V. V. Loboda and T. R. Tauchert, "The elastic contact problem for dissimilar orthotropic semi-infinite and infinite strips", *Int. J. Eng. Sci.* **23**:12 (1985), 1337–1349.
- [Martynyak 1985] R. M. Martynyak, "The interaction of elastic half-planes under an incomplete mechanical contact", *Mat. Met. Fiz.-Mekh. Polya.* **22** (1985), 89–92.
- [Noble and Hussain 1969] B. Noble and M. A. Hussain, "Exact solution of certain dual series for indentation and inclusion problems", *Int. J. Eng. Sci.* **7**:11 (1969), 1149–1161.
- [Nowell and Hills 1988] D. Nowell and D. A. Hills, "Contact problems incorporating elastic layers", *Int. J. Solids Struct.* **24**:1 (1988), 105–115.
- [Ozturk and Erdogan 1993] M. Ozturk and F. Erdogan, "The axisymmetric crack problem in a non-homogeneous medium", *J. Appl. Mech. (Trans. ASME)* **60** (1993), 406–413.
- [Paris et al. 1995] F. Paris, A. Blazquez, and J. Canas, "Contact problems with nonconforming discretizations using boundary element method", *Comput. Struct.* **57**:5 (1995), 829–839.
- [Pu and Hussain 1970] S. L. Pu and M. A. Hussain, "Note on the unbonded contact between plates and an elastic half-space", *J. Appl. Mech. (Trans. ASME)* **37** (1970), 859–861.
- [Satish Kumar et al. 1996] K. Satish Kumar, B. Dattaguru, T. S. Ramamurthy, and K. N. Raju, "Elasto-plastic contact stress analysis of joints subjected to cyclic loading", *Comput. Struct.* **60**:6 (1996), 1067–1077.
- [Schmuesre et al. 1980] D. Schmuesre, M. Comminou, and J. Dundrus, "Separation and slip between a layer and substrate caused by tensile load", *Int. J. Eng. Sci.* **18**:9 (1980), 1149–1155.
- [Selvanduri 1983] A. P. S. Selvanduri, "The body force inducing separation at a frictionless precompressed transversely isotropic interface", *T. Can. Soc. Mech. Eng.* **7** (1983), 154–157.

- [Shvets et al. 1996] R. M. Shvets, R. M. Martynyak, and A. A. Kryshthafovych, “Discontinuous contact of an anisotropic half-plane and a rigid base with disturbed surface”, *Int. J. Eng. Sci.* **34**:2 (1996), 183–200.
- [Sneddon and Lowengrub 1969] I. N. Sneddon and M. Lowengrub, *Crack problems in the classical theory of elasticity*, Wiley, New York, 1969.
- [Weitsman 1969] Y. Weitsman, “On the unbonded contact between plates and an elastic half-space”, *J. Appl. Mech. (Trans. ASME)* **36** (1969), 198–202.
- [Wu and Yen 1994] E. Wu and C. S. Yen, “The contact behavior between laminated composite plates and rigid spheres”, *J. Appl. Mech. (Trans. ASME)* **61** (1994), 60.

Received 7 Mar 2007. Accepted 7 Mar 2007.

SAKTI PADA BARIK: spbarik@yahoo.com

Department of Applied Mathematics, University Calcutta, 92, A.P.C. Road, Kolkata 700 009, India

MRIDULA KANORIA: k_mri@yahoo.com

Department of Applied Mathematics, University Calcutta, 92, A.P.C. Road, Kolkata 700 009, India

PRANAY KUMAR CHAUDHURI: pranay_chaudhuri@yahoo.co.in

Department of Applied Mathematics, University Calcutta, 92, A.P.C. Road, Kolkata 700 009, India

ESTIMATING LEVER-TYPE ACTIVE MULTIPLE TUNED MASS DAMPERS FOR STRUCTURES UNDER HARMONIC EXCITATION

CHUNXIANG LI AND BINGKANG HAN

Lever-type active multiple tuned mass dampers (LT-AMTMD) consisting of several lever-type active tuned mass damper (LT-ATMD) units with a uniform distribution of natural frequencies have been proposed here for the vibration control of long-span bridges under the excitation directly acting on the structure, rather than through the base. The main purpose of selecting this form of excitation is to present guidelines for the buffeting control design of long-span bridges under wind loads. Estimations have been made on the performance of the LT-AMTMD with identical stiffness and damping coefficient and unequal masses for the reduction of harmonically forced vibrations by resorting to the defined evaluation criteria. The LT-AMTMD with the actuator set at the mass block is found to have better effectiveness and higher robustness in alleviating the vibrations of structures in comparison with the LT-AMTMD with the actuator set at any other location. A new major result is that both the spring static and dynamic stretching of the LT-AMTMD with the actuator set at the mass block may be freely adjusted in accordance with the practical requirements by changing the support locations within the viable range while practically maintaining the same performance. Numerical results demonstrate that the LT-AMTMD with the actuator set at the mass block can highly improve the performance of the LT-MTMD (that is, the passive counterpart of the LT-AMTMD) and provide better effectiveness than a single LT-ATMD. Estimations have also been simultaneously carried out on the LT-AMTMD (a single LT-ATMD) with respect to the hanging-type AMTMD (a single hanging-type ATMD) as well as on the LT-MTMD (a single LT-TMD) with reference to the hanging-type MTMD (a single hanging-type TMD), so as to highlight the improved performance of the proposed control system.

1. Introduction

The tuned mass damper (TMD) has been theoretically and experimentally corroborated to be effective in reducing the buffeting response of long-span bridges subjected to wind loads [Gu and Xiang 1992; Gu et al. 1994; Lin et al. 2000]. However, both large static and dynamic stretching of the spring in the hanging-type tuned mass damper (hanging-type TMD) may cause the spring to operate nonlinearly and the hanging-type TMD may not be fitted into the space available for installation within the bridge deck, consequently downgrading the performance and limiting the practical implementation of the hanging-type TMD. To overcome these shortcomings, the lever-type tuned mass damper (LT-TMD) has been proposed to deal with large static stretch of the spring in the hanging-type TMD [Gu et al. 1999]. In terms of the numerical results to be provided later on, the LT-TMD and the hanging-type TMD can approximately achieve the same effectiveness and mass block stroke. With respect to the hanging-type TMD, the LT-TMD, designed in accordance with the hypothesis-1 to be introduced later on, needs smaller

Keywords: damping, mass dampers, vibration control, harmonically forced vibrations, lever-type active multiple tuned mass dampers (LT-AMTMD), static and dynamic stretching of the spring, long-span bridges.

optimum damping ratio but significantly higher optimum tuning frequency ratio. However, the optimum parameters, effectiveness, and mass block stroke of the LT-TMD designed according to the hypothesis-2 to be introduced later on are approximately equal to those of the hanging-type TMD. As such, the LT-TMD can also not surmount the main disadvantage of the TMD (hanging-type TMD); that is, the sensitivity problem due to the fluctuation in tuning the natural frequency of the TMD (hanging-type TMD) to the controlled natural frequency of structures and (or) the offset in the optimum damping ratio of the hanging-type TMD. Furthermore, it has been demonstrated that both the dynamic responses and dynamic parameters of long-span bridges in terms of field measurements and wind tunnel tests and theoretical analyses are usually different from each other due in large part to the fact that the phenomenon of the wind-induced vibrations of long-span bridges is very complex [Diana et al. 1992; Conti et al. 1996].

In view of the above mentioned reasons, a more robust control device, such as the multiple tuned mass dampers (MTMD), which is able to control structural vibrations with variable natural frequencies, is needed for attaining a satisfying reduction of the buffeting response of long-span bridges under wind loads. As is well known, the MTMD with distributed natural frequencies were proposed by [Xu and Igusa 1992] and also investigated by many investigators such as [Yamaguchi and Harnpornchai 1993; Abe and Fujino 1994; Igusa and Xu 1994; Kareem and Kline 1995; Jangid 1995; Li 2000; Park and Reed 2001; Gu et al. 2001; Chen and Wu 2003; Kwon and Park 2004; Yau and Yang 2004; Hoang and Warnitchai 2005; Wang and Lin 2005; Lee et al. 2006]. The MTMD is confirmed to be capable of rendering better effectiveness and higher robustness in the mitigation of the oscillations of structures in comparison with a single TMD. Nevertheless, we note that if the hanging-type multiple tuned mass dampers (hanging-type MTMD) are directly used to suppress the buffeting response of long-span bridges, then each hanging-type TMD will possess both large static and dynamic stretching of the spring. Quantitatively, the static stretching of the spring of the j th hanging-type TMD in the hanging-type MTMD, h_j , can be determined in terms of the equation

$$h_j = g/(\omega_{Tj}^2),$$

where ω_{Tj} is the circular frequency of each hanging-type TMD and g refers to the acceleration due to gravity. Likewise, the maximum static stretching of the spring in the hanging-type MTMD is larger than the static stretching of a single hanging-type TMD with equal total mass ratio. Each LT-TMD in the lever-type multiple tuned mass dampers (LT-MTMD), proposed by the first author [Li and Li 2005], has the static stretching of the spring

$$h_j^* = \alpha[g/(\omega_{Tj}^2)] = \alpha h_j,$$

when the rigid arm is in a horizontal state. The numerical results to be stated later on demonstrate that the LT-MTMD designed in terms of the hypothesis-2 and the hanging-type MTMD have the approximately same effectiveness, robustness, and mass block stroke; but when the hanging-type MTMD is extended in terms of the hypothesis-1 to the LT-MTMD, the optimum tuning frequency ratio will change significantly while the optimum average damping ratio will show minor variations. A new basic result is that both the static and dynamic stretching of the spring in the LT-MTMD may be freely adjusted in accordance with the practical requirements through changing the support locations while approximately maintaining the same effectiveness, robustness, and mass block stroke.

Recently, a single lever-type active tuned mass damper (LT-ATMD) for mitigating harmonically forced vibrations has been recommended by [Li 2004] to acquire a control system with high effectiveness, in

which both the static and dynamic stretching of the spring may be freely adjusted to meet the practical requirements. The numerical results to be given next demonstrate that the LT-ATMD with the actuator set at the mass block can practically reach the same optimum damping ratio, optimum tuning frequency ratio, effectiveness, and mass block stroke as a single hanging-type ATMD. The LT-ATMD with the actuator set at the mass block is found to have much better effectiveness than the LT-TMD. More importantly, both the static and dynamic stretching of the spring in the LT-ATMD with the actuator set at the mass block may be freely adjusted in accordance with the practical requirements through changing the support locations, while approximately maintaining the same control performance (including the same mass block stroke). Further, the multiple active lever-type tuned mass dampers (MALTTMD), consisting of several active lever-type tuned mass damper (ALTTMD) units with a uniform distribution of natural frequencies, have been developed with the objective of attenuating the vibration control of long-span bridges under the ground acceleration, namely the external excitation acting on structures through the base [Li and Zhou 2004]. Taking into account that the probability of great drift of the controlled natural frequency may occur due to the complexity of the wind-induced vibrations of long-span bridges, a beforehand well-designed optimum LT-MTMD may result in the unsatisfactory effectiveness. This drawback can be surmounted by using the lever-type active multiple tuned mass dampers (LT-AMTMD). Therefore, there is a need for making an estimation of the LT-AMTMD with the aim of the external excitation directly acting on the structure, rather than through the base. Such a form of excitation is suitable for the buffeting control design of long-span bridges under wind loads, thereby giving guidelines for the buffeting control design of long-span bridges under wind loads.

The objective of this paper then is to evaluate the performance of the LT-AMTMD, including assessing the mass block stroke of the LT-AMTMD, in order to verify that the LT-AMTMD may also be a good candidate for the reduction of the buffeting response of long-span bridges with the consequence of not requiring both large static and dynamic stretching of the spring with respect to the hanging-type active multiple tuned mass dampers (hanging-type AMTMD) and possessing a desirable robustness in comparison with a single LT-ATMD. Estimations will also be simultaneously made on the LT-AMTMD / a single LT-ATMD with the actuator set at the mass block with respect to the hanging-type AMTMD / a single hanging-type ATMD, as well as on the LT-MTMD / a single LT-TMD with reference to the hanging-type MTMD / a single hanging-type TMD, so as to highlight both the improved performance and conspicuous feature of the proposed control system.

Nomenclature

ALTTMD	active lever-type tuned mass damper
c_s	mode-generalized damping coefficient of structures
c_T	constant damping coefficient of the LT-AMTMD
c_{Tj}	damping coefficient of the j th LT-ATMD in the LT-AMTMD
c_{ij}	velocity feedback gain of the j th LT-ATMD in the LT-AMTMD
DMF	dynamic magnification factors of the structure with the LT-AMTMD
DMF_j	dynamic magnification factors of the j th LT-ATMD in the LT-AMTMD
$F_{cj}(t)$	resultant force to act between the structure and j th LT-ATMD in the LT-AMTMD
F_s	frequency spacing of the LT-AMTMD, used for measuring its robustness

$F_{sj}(t)$	interaction force between the structure and support point of the j th LT-ATMD in the LT-AMTMD
f	tuning frequency ratio of the LT-AMTMD
$f(t)$	external excitation directly acting on the structure, rather than through the base
Hanging-type AMTMD	hanging-type active multiple tuned mass dampers
Hanging-type ATMD	Hanging-type active tuned mass damper
Hanging-type MTMD	hanging-type multiple tuned mass dampers
Hanging-type TMD	hanging-type tuned mass damper
$H_{ys}(-i\omega)$	transfer function of the structure with the LT-AMTMD
$H_{yTj}(-i\omega)$	transfer function of the j th LT-ATMD in the LT-AMTMD
h_j	static stretching of the spring in the j th hanging-type TMD in the hanging-type MTMD
h_j^*	static stretching of the spring in the j th LT-TMD in the LT-AMTMD
$\text{Im}(\omega)[\overline{\text{Im}}(\omega)]$	imaginary part of a complex function, such as the transfer function of the structure with the LT-AMTMD
I_{Tj}	mass moment of inertia of the j th lever in the j th LT-ATMD
k_s	mode-generalized stiffness of structures
k_T	constant spring stiffness of the LT-AMTMD
k_{Tj}	spring stiffness of the j th LT-ATMD in the LT-AMTMD
k_{ij}	displacement feedback gain of the j th LT-ATMD in the LT-AMTMD
LT-AMTMD	lever-type active multiple tuned mass dampers
LT-ATMD	lever-type active tuned mass damper
LT-MTMD	lever-type multiple tuned mass dampers
LT-TMD	lever-type tuned mass damper
L_{T1j}	distance between the mass block and support point of the j th LT-ATMD
L_{T2j}	distance between the spring and support point of the j th LT-ATMD
L_{T3j}	distance between the active control force and mass block of the j th LT-ATMD
MALTTMD	multiple active lever-type tuned mass dampers
min . min . max . DMF	minimization of the minimum values of the maximum dynamic magnification factors of the structure with the LT-AMTMD
MTMD	multiple tuned mass dampers
m_j	lever mass of the j th LT-ATMD in the LT-AMTMD
m_s	mode-generalized mass of structures
m_{Tj}	mass of the j th LT-ATMD mass block
m_{tj}	acceleration feedback gain of the j th LT-ATMD in the LT-AMTMD
n	number of the LT-ATMD units in the LT-AMTMD
R_I	minimization of the minimum values of the maximum dynamic magnification factors (DMF) of the structure with the LT-AMTMD
$\text{Re}(\omega)[\overline{\text{Re}}(\omega)]$	real part of a complex function, such as the transfer function of the j th LT-ATMD in the LT-AMTMD

R_{m1}	ratio of the inertial force due to lever mass to that of block mass
R_{m2}	ratio of the moment of inertial force due to lever mass to that of block mass around the horizontal axis through the support point of the lever
R_{IIj}	maximum dynamic magnification factors (DMF) of the j th LT-ATMD (that is, mass block stroke)
R_{IIj}^*	spring stroke of the j th LT-ATMD in the LT-AMTMD
r_{Tj}	ratio of the natural frequency of the j th LT-ATMD to the structural natural frequency
r_{ij}	normalized acceleration feedback gain factor, NAFGF
r	constant normalized acceleration feedback gain factor, NAFGF
SDOF	single degree of freedom
TMD	tuned mass damper
y_{Tsj}	dynamic stretching of the spring in the j th LT-ATMD
y_s	displacement of the structure with respect to the ground
y_{Tj}	displacement of the j th LT-ATMD with reference to the structure
α	constant ratio of the distance between the spring and support point to that between the mass block and support point
α_j	ratio of the distance between the spring and support point to that between the mass block and support point
β	constant ratio of the distance between the active control force and mass block to that between the spring and mass block, $L_{T1j} + L_{T2j}$
β_j	ratio of the distance between the active control force and mass block to that between the spring and mass block, $L_{T1j} + L_{T2j}$
η_j	normalized mass moment of inertia of the j th lever
λ	ratio of the external excitation frequency to the structural frequency corresponding to the vibration mode being controlled, which is set within the range from 0.4 to 3.4
ξ_s	structural damping ratio, which is set in this paper equal to 0.02
ξ_T	average damping ratio of the LT-AMTMD
ξ_{Tj}	damping ratio of the j th LT-ATMD in the LT-AMTMD
μ	constant ratio of the lever mass to block mass of the LT-AMTMD
μ_j	lever mass to block mass ratio of the j th LT-ATMD in the LT-AMTMD
μ_T	total mass ratio of the LT-AMTMD
μ_{Tj}	mass ratio of the j th LT-ATMD in the LT-AMTMD
ω	external excitation frequency
ω_s	structural natural frequency corresponding to the vibration mode being controlled
ω_T	average natural frequency of the LT-AMTMD
ω_{Tj}	natural frequency of the j th LT-ATMD in the LT-AMTMD

2. Transfer functions (TFs) of the LT-AMTMD structure system

In the present paper, the LT-AMTMD is taken into account for the control of the specific vibration mode of a structure. Likewise, only the translation degree of freedom for the dynamic response of the structure

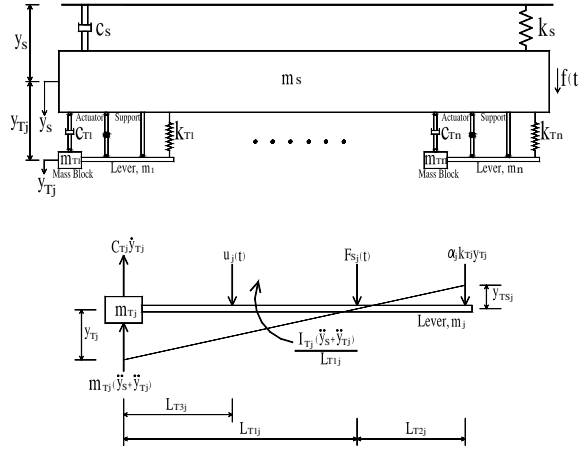


Figure 1. Schematic diagram of the lever-type active multiple tuned mass dampers (LT-AMTMD) structure system under the external excitation directly acting on the structure rather than through the base.

is taken into consideration. The structure is modeled as a single degree of freedom (SDOF) system, generally referred to as the main system, characterized by the mode-generalized dynamic parameters. Each LT-ATMD, with different dynamic characteristics, is also modeled as an SDOF system. Further, the lever is supposed to be a rigid arm. As a result, the total number of degrees of freedom of this combined system is $n + 1$, as shown in Figure 1, in which n denotes the total number of the LT-ATMD units in the LT-AMTMD. Introducing the nondimensional parameters

$$\alpha_j = \frac{L_{T2j}}{L_{T1j}} \quad \text{and} \quad \beta_j = \frac{L_{T3j}}{L_{T1j} + L_{T2j}},$$

in which L_{T1j} represents the distance between the mass block and support point of the j th LT-ATMD in the LT-AMTMD, L_{T2j} denotes the distance between the spring and support point of the j th LT-ATMD in the LT-AMTMD, and L_{T3j} is the distance between the active control force and mass block of the j th LT-ATMD in the LT-AMTMD, the dynamic stretching of each spring and the location of each active control force in the LT-AMTMD can be, respectively, determined by

$$y_{TSj} = \alpha_j y_{Tj}, \quad (1a)$$

$$L_{T3j} = [(1 + \alpha_j)\beta_j]L_{T1j}, \quad (1b)$$

in which y_{Tj} is the displacement of each LT-ATMD in the LT-AMTMD with reference to the structure.

Each LT-ATMD spring stroke, namely the dynamic stretching, can be calculated using Equation (1a), consequently meaning that $R_{IIj}^* = \alpha_j R_{IIj}$, in which R_{IIj}^* represents the spring stroke of the j th LT-ATMD in the LT-AMTMD and R_{IIj} denotes the mass block stroke of the j th LT-ATMD in the LT-AMTMD to

be defined next. The equations of motion of the LT-AMTMD structure system can be given by

$$\begin{aligned}
& I_{Tj}[(\ddot{y}_s + \ddot{y}_{Tj})/L_{T1j}] + [m_{Tj}(\ddot{y}_s + \ddot{y}_{Tj}) + c_{Tj}\dot{y}_{Tj}]L_{T1j} \\
& \quad + \alpha_j k_{Tj} y_{Tj} L_{T2j} = u_j(t)(L_{T1j} - L_{T3j}), \\
& \alpha_j k_{Tj} y_{Tj} + F_{sj}(t) + u_j(t) = c_{Tj}\dot{y}_{Tj} + m_{Tj}(\ddot{y}_s + \ddot{y}_{Tj}), \\
& m_s \ddot{y}_s + c_s \dot{y}_s + k_s y_s = f(t) + \sum_{j=1}^n F_{cj}(t),
\end{aligned} \tag{2}$$

$$F_{cj}(t) = c_{Tj}\dot{y}_{Tj} - u_j(t) - F_{sj}(t) - \alpha_j k_{Tj} y_{Tj} = -m_{Tj}(\ddot{y}_s + \ddot{y}_{Tj}).$$

An active control algorithm is required to use the measured displacement, velocity, and acceleration responses of the LT-AMTMD structure system to calculate the active control forces to drive the levers or the mass blocks during the design process of the LT-AMTMD. In the present paper, the frequency domain design method [Chang and Yang 1995; Ankireddi and Yang 1996; Yan et al. 1999] is employed for designing the LT-AMTMD. In this method, the optimum LT-MTMD, as obtained earlier, is utilized. For designing the LT-AMTMD, choices are displacement feedback, velocity feedback, and acceleration feedback. Such a LT-AMTMD control system, if properly designed, can be used to bring the system performance to another optimum state. Therefore, the active force $u_j(t)$ is calculated from the displacement, velocity, and acceleration of the mass block of the j th LT-ATMD in the following form:

$$u_j(t) = -m_{tj}\ddot{y}_{Tj} - c_{tj}\dot{y}_{Tj} - k_{tj}y_{Tj}, \tag{3}$$

where m_s , c_s , and k_s are, respectively, the mode-generalized stiffness, damping coefficient, and mass of structures; m_{Tj} , c_{Tj} , and k_{Tj} are the mass, damping coefficient, and stiffness of the j th LT-ATMD in the LT-AMTMD, respectively; y_s is the structural displacement relative to the ground; $F_{sj}(t)$ is the interaction force between the structure and the support point of each LT-ATMD in the LT-AMTMD;

$$I_{Tj} = \frac{[3(1 - \alpha_j)^2 + (1 + \alpha_j)^2]m_j L_{T1j}^2}{12}$$

is the mass moment of inertia of each lever in the LT-AMTMD, where m_j is the mass of each lever; $f(t)$ is the external excitation; m_{tj} is the acceleration feedback gain of the j th LT-ATMD in the LT-AMTMD; c_{tj} is the velocity feedback gain of the j th LT-ATMD in the LT-AMTMD; and k_{tj} is the displacement feedback gain of the j th LT-ATMD in the LT-AMTMD.

It is pointed out herein that this is the external excitation directly acting on the structure, rather than through the base. The main purpose of selecting this form of excitation is to give guidelines for the buffeting control design of long-span bridges under wind loads.

It is assumed that the stiffness and damping coefficient of each LT-ATMD in the LT-AMTMD are kept same and the natural frequencies of the LT-AMTMD are uniformly distributed around their average natural frequency. As a result, the LT-AMTMD is manufactured by keeping constant stiffness and damping and unequal masses (that is, $k_{T1} = k_{T2} = \dots = k_{Tn} = k_T$; $c_{T1} = c_{T2} = \dots = c_{Tn} = c_T$;

$m_{T1} \neq m_{T2} \neq \dots \neq m_{Tn}$). Likewise, the nondimensional parameter α_j and β_j are, respectively, assumed to be maintained constant (that is, $\alpha_1 = \alpha_2 = \dots = \alpha_n = \alpha$; $\beta_1 = \beta_2 = \dots = \beta_n = \beta$).

In the formulation of the transfer functions (TFs), the following parameters are introduced:

$$\eta_j = \frac{3(1 - \alpha_j)^2 + (1 + \alpha_j)^2}{12},$$

(in physical terms $\eta_1 = \eta_2 = \dots = \eta_n = \eta$);

$$\omega_s = \sqrt{\frac{k_s}{m_s}}, \quad \xi_s = \frac{c_s}{2m_s\omega_s}, \quad \omega_{Tj} = \sqrt{\frac{\alpha_j^2 k_{Tj} + k_{tj}(1 - \beta_j - \alpha_j\beta_j)}{m_{Tj}}},$$

$$\xi_{Tj} = \frac{c_{Tj} + c_{tj}(1 - \beta_j - \alpha_j\beta_j)}{2m_{Tj}\omega_{Tj}}, \quad r_j = \frac{m_{tj}}{m_{Tj}}, \quad (4)$$

(normalized acceleration feedback gain factor, referred to as NAFGF, letting $r_1 = r_2 = \dots = r_n = r$); $\mu_{Tj} = \frac{m_{Tj}}{m_s}$ (mass ratio of each LT-ATMD in the LT-AMTMD); $\mu_j = \frac{m_j}{m_{Tj}}$ (lever mass to block mass ratio of each LT-ATMD in the LT-AMTMD). Let it be supposed that the lever mass to block mass ratio of each LT-ATMD in the LT-AMTMD is held constant (that is, $\mu_1 = \mu_2 = \dots = \mu_n = \mu$).

Letting $f(t) = m_s[e^{-i\omega t}]$, $y_{Tj} = [H_{y_{Tj}}(-i\omega)][e^{-i\omega t}]$ and $y_s = [H_{y_s}(-i\omega)][e^{-i\omega t}]$, and setting these in Equation (2), the transfer functions (TFs) of the LT-AMTMD structure system can then be given by

$$\omega_s^2 [H_{y_s}(-i\omega)] = \frac{1}{[\text{Re}(\omega) + i \text{Im}(\omega)]}, \quad (5)$$

$$\omega_s^2 [H_{y_{Tj}}(-i\omega)] = \frac{(1 + \eta_j \mu_j)[\omega^2 / \omega_s^2]}{[\text{Re}(\omega) + i \overline{\text{Im}}(\omega)][\text{Re}(\omega) + i \text{Im}(\omega)]}, \quad (6)$$

in which $H_{y_s}(-i\omega)$ refers to the transfer function (TF) of the structure with the LT-AMTMD; $H_{y_{Tj}}(-i\omega)$ signifies the transfer function (TF) of the j th LT-ATMD in the LT-AMTMD; and $\text{Re}(\omega)$, $\text{Im}(\omega)$, $\overline{\text{Re}}(\omega)$, and $\overline{\text{Im}}(\omega)$ will be given next.

Lastly, it is pointed out that [Li and Wang 2003] have performed numerical simulations of the lever-type multiple tuned dampers (LT-MTMD) in the case of ignoring the lever mass effect. Recently, [Li and Li 2005] have again evaluated the optimal performance of the LT-MTMD under the circumstances of taking the lever moment effect into consideration and ignoring both the inertial force and corresponding moment due to the lever mass. The numerical simulations demonstrate that the lever mass may be set equal to zero in designing the LT-AMTMD. For the LT-AMTMD, the ratio of the inertial force due to lever mass to that of block mass may be given by

$$R_{m1} = \frac{\mu_j [\ddot{y}_s + 0.5(1 - \alpha_j)\ddot{y}_{Tj}]}{(\ddot{y}_s + \ddot{y}_{Tj})},$$

whereas the ratio of the moment of inertial force due to lever mass to that of block mass around the horizontal axis through the support point of the lever can be determined by

$$R_{m2} = \frac{\mu_j [0.5(1 - \alpha_j) \ddot{y}_s + 0.25(1 - \alpha_j)^2 \ddot{y}_{Tj}]}{(\ddot{y}_s + \ddot{y}_{Tj})}.$$

Therefore, both the inertial force and corresponding moment due to lever mass are also ignored in the present paper according to recommendations of the foregoing literatures [Li and Li 2005; Li and Wang 2003] and considering aforementioned two ratios.

3. Optimum criteria of the LT-AMTMD

Let ω_T be the average frequency of the LT-AMTMD, that is,

$$\omega_T = \sum_{k=1}^n \frac{\omega_{Tk}}{n}.$$

The natural frequency of each LT-ATMD in the LT-AMTMD can be derived as follows:

$$\omega_{Tj} = \omega_T \left[1 + \left[j - \frac{n+1}{2} \right] \frac{F_S}{n-1} \right], \quad (7)$$

in which the nondimensional parameter F_S is defined to be the frequency spacing of the LT-AMTMD (used for estimating the robustness of the LT-AMTMD) determined by

$$F_S = \left[\frac{\omega_{Tn} - \omega_{T1}}{\omega_T} \right].$$

Then, the ratio of the natural frequency of each LT-ATMD in the LT-AMTMD to the controlled frequency of the structure can be written as follows:

$$r_{Tj} = \frac{\omega_{Tj}}{\omega_s} = f \left[1 + \left[j - \frac{n+1}{2} \right] \frac{F_S}{n-1} \right], \quad (8)$$

in which f is defined to be the tuning frequency ratio of the LT-AMTMD calculated by $f = \frac{\omega_T}{\omega_s}$.

The average damping ratio of the LT-AMTMD is defined as follows:

$$\xi_T = \sum_{j=1}^n \frac{\xi_{Tj}}{n}. \quad (9)$$

The ratio of the total mass of the LT-AMTMD to the mode-generalized mass of the structure is referred to as the total mass ratio of the LT-AMTMD, which has the form

$$\mu_T = \sum_{j=1}^n \frac{m_{Tj}}{m_s} = \sum_{j=1}^n \mu_{Tj}. \quad (10)$$

Employing the above assumptions and derived expressions, the total mass ratio of the LT-AMTMD and the damping ratio of each LT-ATMD in the LT-AMTMD can be, respectively, determined as [Li

2000]

$$\mu_T = [\mu_{Tj} r_{Tj}^2] \left[\sum_{j=1}^n r_{Tj}^{-2} \right], \quad (11)$$

$$\xi_{Tj} = \frac{r_{Tj} \xi_T}{f}. \quad (12)$$

Defining the ratio of the external excitation frequency to the controlled frequency of the structure (that is, $\lambda = \omega/\omega_s$) and taking advantage of Equation (5) and (6), the dynamic magnification factors (DMF) of the structure with the LT-AMTMD and each LT-ATMD in the LT-AMTMD can then be respectively calculated by

$$\text{DMF} = |\omega_s^2 [H_{y_s}(-i\lambda)]| = \frac{1}{\sqrt{[\text{Re}(\lambda)]^2 + [\text{Im}(\lambda)]^2}},$$

$$\text{DMF}_j = |\omega_s^2 [H_{y_{Tj}}(-i\lambda)]| = \frac{(1 + \eta_j \mu_j) \lambda^2}{\sqrt{[\text{Re}(\lambda)]^2 + [\text{Im}(\lambda)]^2} \sqrt{[\overline{\text{Re}}(\lambda)]^2 + [\overline{\text{Im}}(\lambda)]^2}},$$

in which

$$\text{Re}(\lambda) = 1 - (1 + \mu_T) \lambda^2 - \sum_{j=1}^n \frac{[\mu_{Tj} (1 + \eta_j \mu_j) \lambda^4] \overline{\text{Re}}(\lambda)}{[\text{Re}(\lambda)]^2 + [\text{Im}(\lambda)]^2},$$

$$\text{Im}(\lambda) = -2\xi_s \lambda + \sum_{j=1}^n \frac{[\mu_{Tj} (1 + \eta_j \mu_j) \lambda^4] \overline{\text{Im}}(\lambda)}{[\text{Re}(\lambda)]^2 + [\text{Im}(\lambda)]^2},$$

$$\overline{\text{Re}}(\lambda) = r_{Tj}^2 - [1 + \eta_j \mu_j + r_j (1 - \beta_j - \alpha_j \beta_j)] \lambda^2,$$

$$\overline{\text{Im}}(\lambda) = -2\xi_{Tj} r_{Tj} \lambda.$$

Estimation can now be conducted on the optimum parameters and effectiveness of the LT-AMTMD through the implementation of the following optimum criterion:

$$R_I = \min . \min . \max . \text{DMF}(F_s, f, \xi_T). \quad (13)$$

Equation (13) means that the examination of the optimum parameters is conducted through the minimization of the minimum values of the maximum dynamic magnification factors (DMF) of structures with the LT-AMTMD. They can be explicitly explained in the following steps. First of all, for a fixed value of λ (set in the present paper within the range from 0.4 to 3.4) and a fixed tuning frequency ratio, the maximum amplitudes for different average damping ratios and frequency spacings are found, and the minimum amplitudes are selected from the maximum amplitudes, which is the minimax amplitude for that tuning frequency ratio. Then the above procedure is repeated for different tuning frequency ratios to find the minimax of each tuning frequency ratio. Finally, the smallest minimaxes are selected and the corresponding tuning frequency ratio, average damping ratio, and frequency spacing are optimum values.

Control systems	Units comprising the control systems				
LT-AMTMD	LT-ATMD1	LT-ATMD2	LT-ATMD3	LT-ATMD4	LT-ATMD5
Hanging-type AMTMD	Hanging-type ATMD1	Hanging-type ATMD2	Hanging-type ATMD3	Hanging-type ATMD4	Hanging-type ATMD5
LT-MTMD	LT-TMD1	LT-TMD2	LT-TMD3	LT-TMD4	LT-TMD5
Hanging-type MTMD	Hanging-type TMD1	Hanging-type TMD2	Hanging-type TMD3	Hanging-type TMD4	Hanging-type TMD5

Table 1. The control systems and units comprising these control systems

Estimation on the mass block stroke the LT-AMTMD can be simultaneously performed in terms of the maximum dynamic magnification factor ($\text{Max} \cdot \text{DMF}_j$) of each LT-ATMD using the obtained optimum parameters of the LT-AMTMD based on Equation (13), which has the following form:

$$R_{IIj} = \text{Max} \cdot \text{DMF}_j . \quad (14)$$

It is further pointed out here that in this study, a frequency domain analysis is conducted to demonstrate the performance of the LT-AMTMD, thus implying that the aforesaid R_I and R_{IIj} can be considered as the formal indices.

4. Numerical simulation study

Displayed in Figures 2–8 are the numerical results of the present research, in which the structural damping ratio is set equal to 0.02 and the ratio (λ) of the external excitation frequency to the structural controlled frequency is set within the range from 0.4 to 3.4. The superscript *opt* represents the optimum values of the LT-AMTMD system parameters. By optimizing R_I , the optimum frequency spacing, tuning frequency ratio, and average damping ratio of the LT-AMTMD will be obtained. It is worth mentioning that the numerical analysis may be carried out of the LT-AMTMD with 5 LT-ATMD units, due to economical reasons that the number of LT-ATMD units should be as low as possible. However, to disclose the performance of the LT-AMTMD more clearly, the present paper will display the charts of the LT-AMTMD with up to 31 LT-ATMD units. For the sake of clarity, Table 1 presents the control systems and units comprising these control systems.

4.1. Estimating the optimum locations of the actuator in the LT-AMTMD. It is interesting in observing Figure 2 [(a1) and (b1)] to note that changing the locations of the actuator makes little difference in the optimum average damping ratio of the LT-AMTMD. It is seen that the optimum average damping ratio of the LT-AMTMD is greater than that of the LT-MTMD, but is significantly lower than the optimum damping ratio of a single LT-ATMD. From Figure 2 [(a2) and (b2)], it is important to note that the LT-AMTMD with the actuator set at the mass block offers higher robustness in comparison to the LT-AMTMD with the actuator set at any other locations. Likewise, this LT-AMTMD with the actuator set at

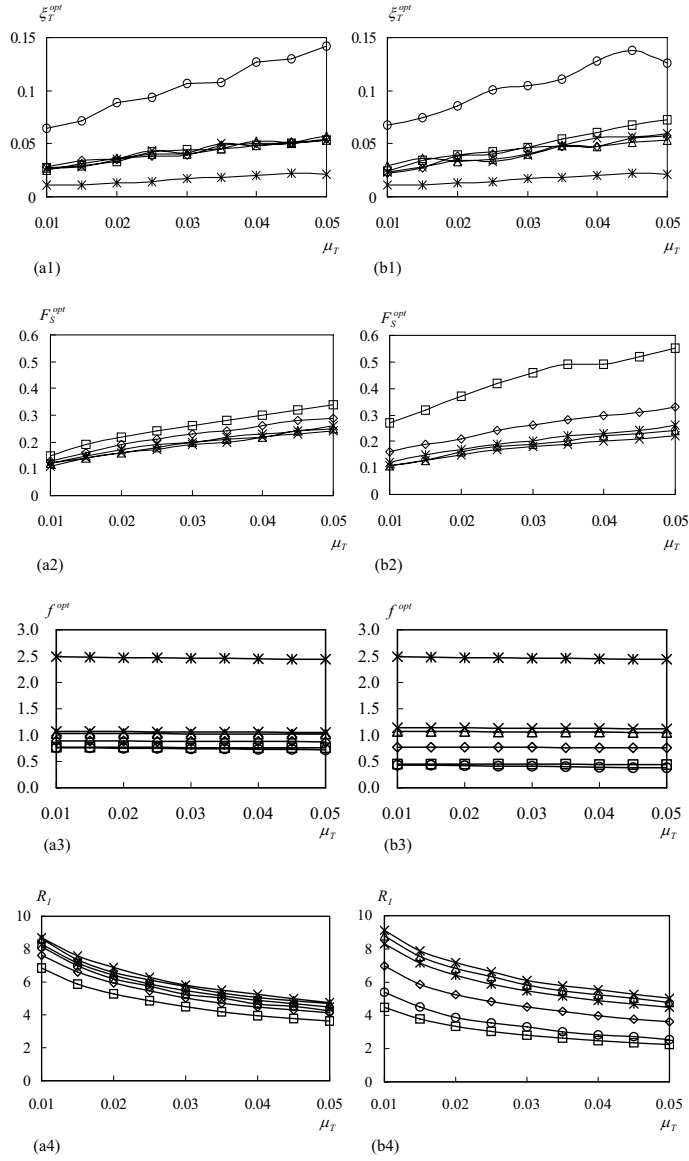


Figure 2. Variation of the optimum parameters and effectiveness of the LT-AMTMD / LT-MTMD (the passive counterpart of the LT-AMTMD) / a single LT-ATMD. (a1) ξ_T^{opt} for $r = -0.4$; (b1) ξ_T^{opt} for $r = -0.8$; (a2) F_S^{opt} for $r = -0.4$; (b2) F_S^{opt} for $r = -0.8$; (a3) f^{opt} for $r = -0.4$; (b3) f^{opt} for $r = -0.8$; (a4) R_I for $r = -0.4$; (b4) R_I for $r = -0.8$ with respect to total mass ratio with $n = 5$, $\alpha = 0.4$, $\mu = 0.01$, and several β values (considering the changes of actuator locations). Legend: \square = LT-AMTMD ($\beta = 0.0$); \diamond = LT-AMTMD ($\beta = 0.36$); \triangle = LT-AMTMD ($\beta = 0.86$); \times = LT-AMTMD ($\beta = 1.0$); $*$ = LT-MTMD; \circ = LT-ATMD ($\beta = 0$).

the mass block renders higher robustness in comparison with the LT-MTMD. It is seen from Figure 2 [(a3) and (b3)] that the influence of the locations of the actuator is not insignificant on the optimum tuning frequency ratio of the LT-AMTMD. Further, the optimum tuning frequency ratio of the LT-AMTMD is considerably close to that of a single LT-ATMD when both actuators are all set at the mass block, but is remarkably lower than that of the LT-MTMD. Figure 2 [(a4) and (b4)] clearly demonstrates that the LT-AMTMD with the actuator set at the mass block results in higher effectiveness compared to the LT-AMTMD with the actuator set at any other locations. The LT-AMTMD with the actuator set at the mass block can provide better effectiveness in comparison with the LT-MTMD and a single LT-ATMD. Therefore, it is preferable to choose to use the LT-AMTMD with the actuator set at the mass block.

4.2. Estimating the optimum parameters and effectiveness of the LT-AMTMD with the actuator set at the mass block. It is interesting in observing Figure 3 to find that the locations of the support makes little difference in the optimum parameters and effectiveness of the LT-AMTMD, corresponding to the respective NAFGF. This observation effectively means that both the static and dynamic stretching of the spring in the LT-AMTMD may be freely adjusted in accordance with the practical requirements through changing the locations of the support while practically maintaining the same optimum average damping ratio, frequency spacing, tuning frequency ratio, and effectiveness. It is clear from Figure 4 that the lever mass to block mass ratio makes little difference in the optimum parameters and effectiveness of the LT-AMTMD. This effectively means the influences of the lever mass are rather negligible on the optimum parameter and effectiveness of the LT-AMTMD.

4.3. Estimating the mass block stroke of the LT-AMTMD with the actuator set at the mass block. Figure 5 [(a1) and (b1)] clearly illustrates that the influence of the α value within the range from 0.3 to 0.7 is rather negligible on the R_{IIj} value of the LT-AMTMD, but not insignificant out of the range. Thus, both the static and dynamic stretching of the spring in the LT-AMTMD may be freely adjusted in accordance with the practical requirements through changing the location of the support within the range from $\alpha = 0.3$ to $\alpha = 0.7$ while practically maintaining the same mass block stroke. This character is very useful for the implementation of the LT-AMTMD for long-span bridges. It is seen from Figure 5 [(a2) and (b2)] that the influence of the μ value is rather negligible on the R_{IIj} value of the LT-AMTMD at smaller NAFGF such as $r = -0.8$, but not insignificant at higher NAFGF such as $r = -0.4$. In order to more accurately estimate the mass block stroke, the lever mass thus needs to be accounted for. It is seen from Figure 5 [(a3) and (b3)] that the R_{IIj} value of the LT-AMTMD decreases rapidly with the increase of the total mass ratio, which implies that the mass block stroke of the LT-AMTMD is greatly reduced at higher total mass ratio. However, the gradient of mass block stroke reduction becomes small in the case where the total mass ratio is beyond 0.03. It is important to emphasize that the NAFGF makes little difference in the mass block stroke of the LT-AMTMD.

4.4. Estimating the frequency response functions (FRFs) of the structures with the LT-AMTMD with the actuator set at the mass block. It is seen from Figure 6 that the FRFs of the structures with the LT-AMTMD for different α values are very consistent with each other, thus meaning that changing the support locations practically has no influence on the FRFs of the structures with the LT-AMTMD. Likewise the FRFs of the structures with the LT-AMTMD are very consistent with those of the hanging-type AMTMD. Figure 7 is presented to take into account the effects of the mass ratio (μ) on the FRFs

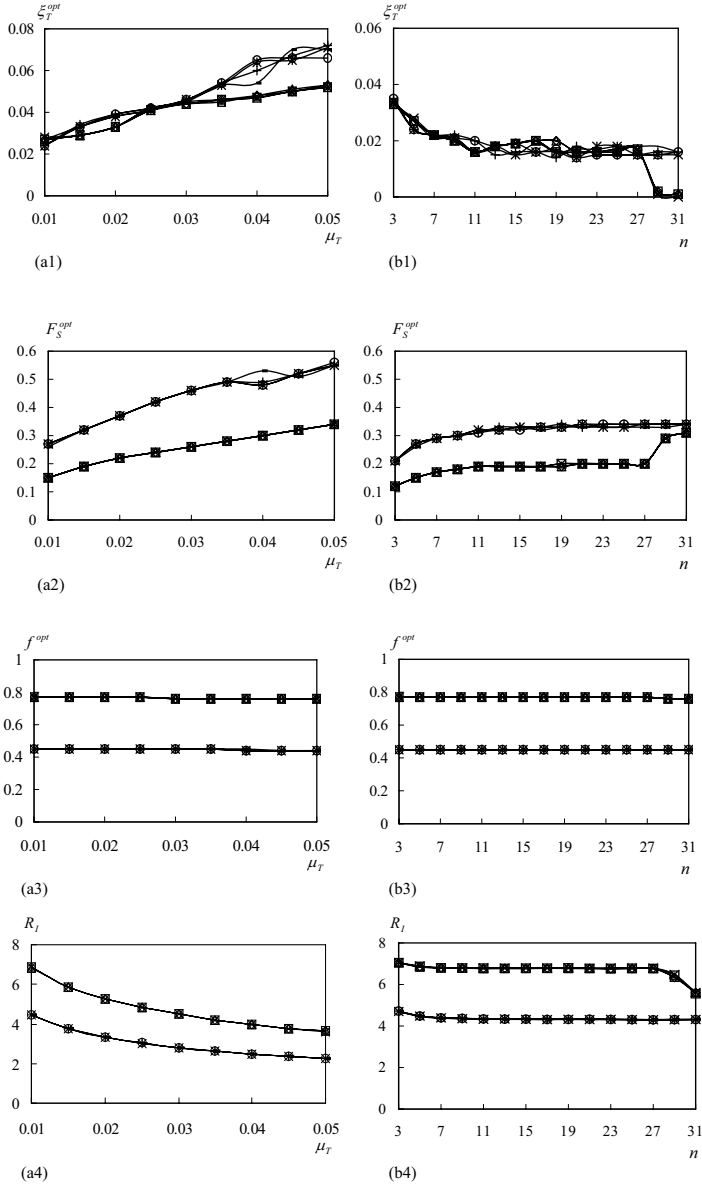


Figure 3. Variation of the optimum parameters and effectiveness of the LT-AMTMD with the actuator set at the mass block with respect to total mass ratio with $n = 5$ and $\mu = 0.01$. (a1) ξ_T^{opt} ; (a2) F_S^{opt} ; (a3) f^{opt} ; (a4) R_I and total number with $\mu_T = 0.01$ and $\mu = 0.01$ (b1) ξ_T^{opt} ; (b2) F_S^{opt} ; (b3) f^{opt} ; (b4) R_I . Legend: \square = LT-AMTMD ($\alpha = 0.1, \gamma = -0.4$); \diamond = LT-AMTMD ($\alpha = 0.3, \gamma = -0.4$); \triangle = LT-AMTMD ($\alpha = 0.5, \gamma = -0.4$); \times = LT-AMTMD ($\alpha = 1.0, \gamma = -0.4$); $*$ = LT-AMTMD ($\alpha = 0.1, \gamma = -0.8$); \circ = LT-AMTMD ($\alpha = 0.3, \gamma = -0.8$); \cdot = LT-AMTMD ($\alpha = 0.5, \gamma = -0.8$); $-$ = LT-AMTMD ($\alpha = 1.0, \gamma = -0.8$).

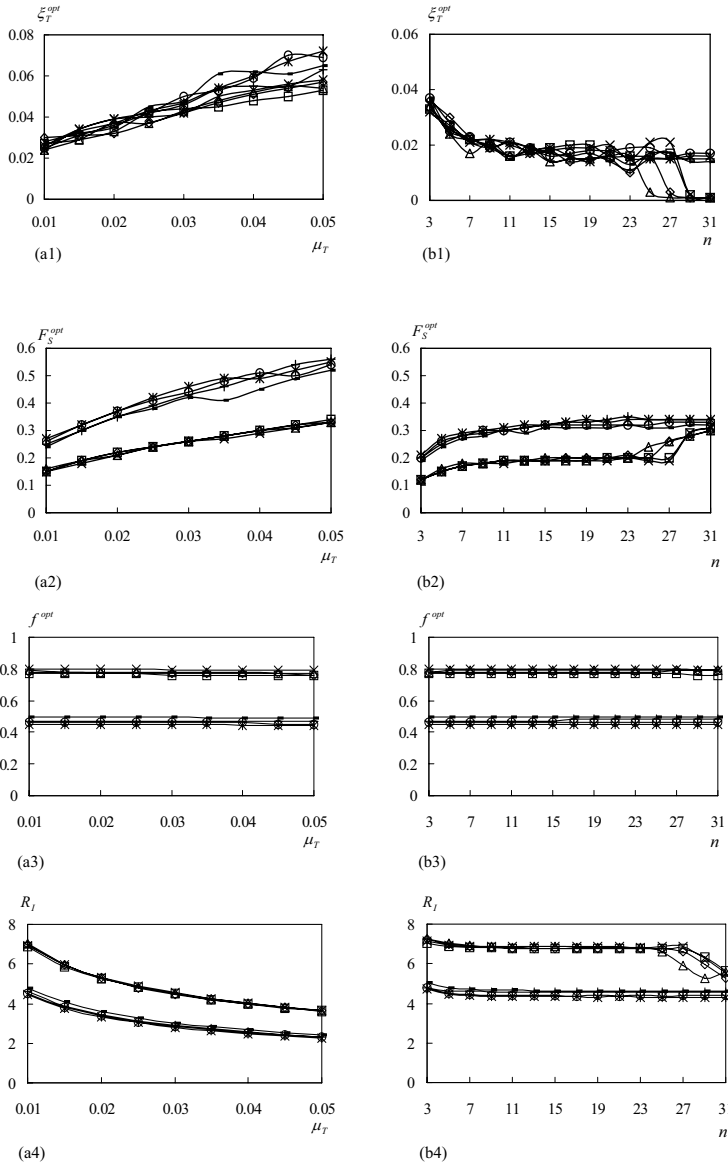


Figure 4. Variation of the optimum parameters and effectiveness of the LT-AMTMD with the actuator set at the mass block with respect to total mass ratio with $n = 5$ and $\alpha = 0.4$ (a1) ξ_T^{opt} ; (a2) F_S^{opt} ; (a3) f^{opt} ; (a4) R_I and total number with $\mu_T = 0.01$ and $\alpha = 0.4$ (b1) ξ_T^{opt} ; (b2) F_S^{opt} ; (b3) f^{opt} ; (b4) R_I . Legend: \square = LT-AMTMD ($\mu = 0.01$, $\gamma = -0.4$); \diamond = LT-AMTMD ($\mu = 0.05$, $\gamma = -0.4$); \triangle = LT-AMTMD ($\mu = 0.1$, $\gamma = -0.4$); \times = LT-AMTMD ($\mu = 0.2$, $\gamma = -0.4$); $*$ = LT-AMTMD ($\mu = 0.01$, $\gamma = -0.8$); \circ = LT-AMTMD ($\mu = 0.05$, $\gamma = -0.8$); \dagger = LT-AMTMD ($\mu = 0.1$, $\gamma = -0.8$); $-$ = LT-AMTMD ($\mu = 0.2$, $\gamma = -0.8$).

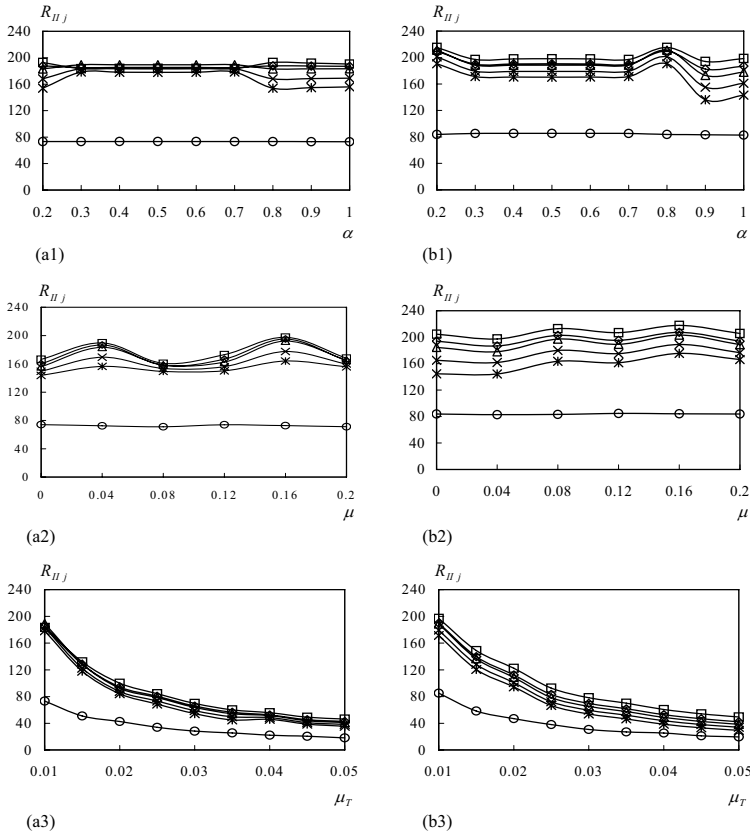


Figure 5. Variation of the R_{IIj} value of the LT-AMTMD / a single LT-ATMD with the actuator set at the mass block with respect to the α value with $n = 5$ and $\mu_T = 0.01$ and $\mu = 0.03$. (a1) $r = -0.4$; (b1) $r = -0.8$ and the μ value with $n = 5$ and $\mu_T = 0.01$ and $\alpha = 0.3$; (a2) $r = -0.4$; (b2) $r = -0.8$ and the μ_T value with $n = 5$ and $\alpha = 0.3$ and $\mu = 0.03$; (a3) $r = -0.4$; (b3) $r = -0.8$. Legend: $\square =$ LT-ATMD1; $\diamond =$ LT-ATMD2; $\triangle =$ LT-ATMD3; $\times =$ LT-ATMD4; $*$ = LT-ATMD5; $\circ =$ LT-ATMD.

of the structures with the LT-AMTMD. For smaller NAFGF, the FRFs of the structures with the LT-AMTMD are almost identical to each other for different μ values even though greater total mass ratio, such as $\mu_T = 0.03$. For greater NAFGF, the mass ratio (μ) has an effect on the FRFs of the structures with the LT-AMTMD, but not significant as well. Figure 8 exhibits the effects of the actuator locations (β) on the FRFs of the structures with the LT-AMTMD. It is seen that the actuator locations significantly affects the FRFs of the structures with the LT-AMTMD. With the increase in the β value, the FRFs of the structures with the LT-AMTMD are getting worse. Therefore, the LT-AMTMD with the actuator set at the mass block will yield the best performance.

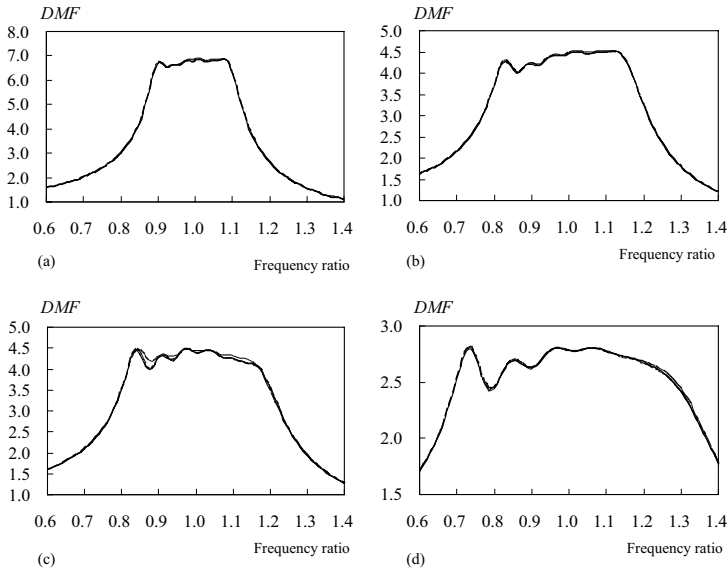


Figure 6. FRFs of the structures with the LT-AMTMD with the actuator set at the mass block with $n = 5$, $\mu = 0.01$, and several α values (considering the changes of the support locations) and with (a) $r = -0.4$ and $\mu_T = 0.01$; (b) $r = -0.4$ and $\mu_T = 0.03$; (c) $r = -0.8$ and $\mu_T = 0.01$; and (d) $r = -0.8$ and $\mu_T = 0.03$. Legend:— $\alpha = 0.1$; -- $\alpha = 0.3$; --- $\alpha = 0.5$; -.- $\alpha = 1.0$

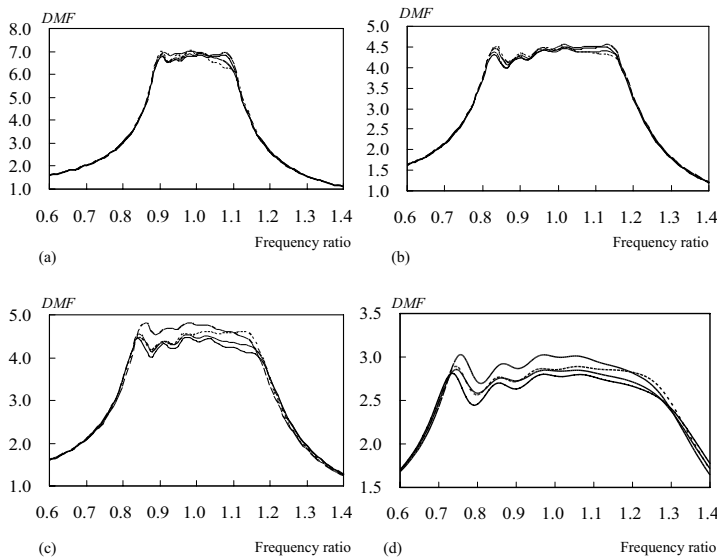


Figure 7. FRFs of the structures with the LT-AMTMD with the actuator set at the mass block with $n = 5$, $\alpha = 0.4$, and several μ values (considering the changes of lever mass) and with (a) $r = -0.4$ and $\mu_T = 0.01$; (b) $r = -0.4$ and $\mu_T = 0.03$; (c) $r = -0.8$ and $\mu_T = 0.01$; and (d) $r = -0.8$ and $\mu_T = 0.03$. Legend:— $\mu = 0.01$; -- $\mu = 0.05$; --- $\mu = 0.10$; -.- $\mu = 0.20$.

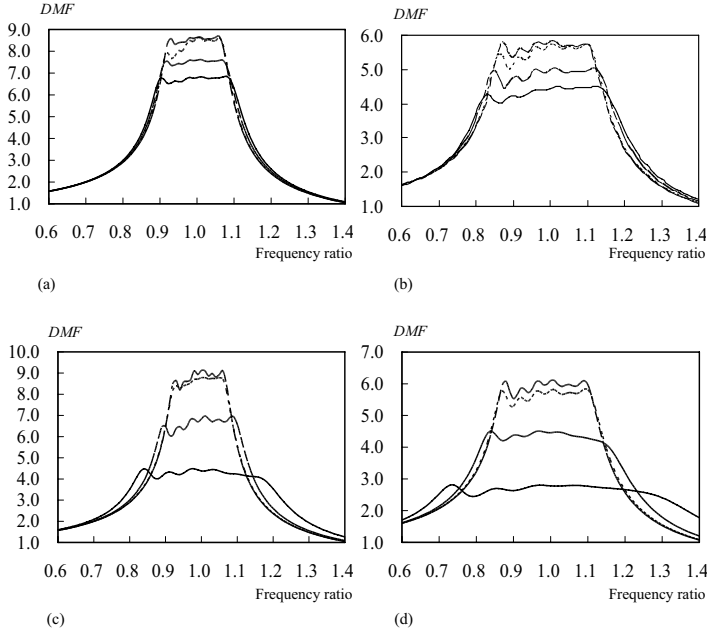


Figure 8. FRFs of the structures with the LT-AMTMD with $n = 5$, $\alpha = 0.4$, $\mu = 0.01$, and several β values (considering the changes of actuator locations) and with (a) $r = -0.4$ and $\mu_T = 0.01$; (b) $r = -0.4$ and $\mu_T = 0.03$; (c) $r = -0.8$ and $\mu_T = 0.01$; and (d) $r = -0.8$ and $\mu_T = 0.03$. Legend: — $\beta = 0.0$; - - $\beta = 0.36$; - - - $\beta = 0.86$; - - - - $\beta = 1.0$.

4.5. Estimating the performance of the LT-AMTMD / a single LT-ATMD with respect to the hanging-type AMTMD / a single hanging-type ATMD. From Tables 2 and 3, the LT-AMTMD / a single LT-ATMD has approximately the same performances as the hanging-type AMTMD / a single hanging-type ATMD. The mass block stroke of the LT-AMTMD is slightly greater than that of the LT-MTMD, but is significantly larger than that of a single ATMD. Thus, in comparison to a single LT-ATMD, this is a disadvantage of the LT-AMTMD.

4.6. Estimating the performance of the LT-MTMD (passive counterpart of the LT-AMTMD) / a single LT-TMD designed in terms of two hypotheses with respect to the hanging-type MTMD / a single hanging-type TMD. Here, it is pointed out that in this research the natural frequency of each LT-TMD in the LT-MTMD (that is, passive counterpart of the LT-AMTMD) takes the forms:

$$\omega_{Tj} = \sqrt{k_{Tj}/m_{Tj}}$$

(designated in this paper as the hypothesis-1). If

$$\omega_{Tj} = \sqrt{\alpha_j^2 k_{Tj}/m_{Tj}}$$

(similarly designated as the hypothesis-2), which can be derived from the natural frequency expression of the LT-AMTMD by setting both $1 - \beta_j - \alpha_j \beta_j = 0$ and $r_j = 0$, then the optimum tuning frequency

NAFGF (r)	LT-ATMD1	LT-ATMD2	LT-ATMD3	LT-ATMD4	LT-ATMD5
Computational results with the total mass ratio (μ_T) equal to 0.01					
-0.2	158.67	153.22	149.81	144.34	140.82
-0.4	168.76	163.08	161.27	155.64	151.56
-0.6	204.26	197.14	195.25	185.55	177.80
-0.8	221.75	209.48	203.36	185.88	168.76
Computational results with the total mass ratio (μ_T) equal to 0.03					
-0.2	65.40	61.81	59.96	57.11	54.63
-0.4	68.81	65.64	64.59	61.27	58.42
-0.6	79.49	74.48	71.54	64.72	57.79
-0.8	80.93	72.42	67.56	59.82	51.51
NAFGF (r)	Hanging-type ATMD1	Hanging-type ATMD2	Hanging-type ATMD3	Hanging-type ATMD4	Hanging-type ATMD5
Computational results with the total mass ratio (μ_T) equal to 0.01					
-0.2	159.90	145.10	142.00	135.86	129.65
-0.4	166.42	160.18	155.99	149.60	143.67
-0.6	194.25	187.14	183.07	171.01	160.08
-0.8	204.57	194.07	184.63	165.02	144.54
Computational results with the total mass ratio (μ_T) equal to 0.03					
-0.2	64.43	60.93	59.05	55.83	52.93
-0.4	70.96	67.13	65.57	62.01	58.88
-0.6	76.09	70.92	68.94	64.73	61.15
-0.8	78.56	69.31	64.52	59.22	54.56

Table 2. The R_{Ij} value, used for estimating the mass block stroke, of the LT-AMTMD with the actuator set at the mass block / hanging-type AMTMD with $n = 5$, $\alpha = 0.4$, and $\mu = 0.01$ and with different total mass ratio and NAFGF

ratio of the LT-MTMD can be approximately calculated by $f^{opt} = \alpha$ (that of the LT - MTMD computed in terms of the hypothesis -1), whereas the optimum average damping ratio of the LT-MTMD can be approximately determined by

$$\xi_T^{opt} = \frac{[\text{that of the LT - MTMD computed in terms of the hypothesis - 1}]}{\alpha},$$

from the computational results listed in Table 4.

Obviously, the LT-MTMD designed in terms of the two hypotheses practically maintains the same optimum stiffness (k_T^{opt}) and optimum damping coefficient (c_T^{opt}). Likewise, the computational results

Total mass ratio	Tuning frequency ratio	Damping ratio	R_I value	R_{II} value
Computational results of a single LT-ATMD in the case of NAFGF (r) = -0.40				
0.010	0.76	0.064	8.1430	73.1342
0.015	0.76	0.071	6.9885	54.5700
0.020	0.75	0.089	6.1971	40.4935
0.025	0.75	0.094	5.7432	34.6001
0.030	0.74	0.107	5.2518	28.5802
Computational results of a single LT-ATMD in the case of NAFGF (r) = -0.80				
0.010	0.43	0.067	5.3907	82.9899
0.015	0.43	0.074	4.5075	60.2846
0.020	0.42	0.086	3.8713	45.7221
0.025	0.41	0.101	3.5444	36.6465
0.030	0.41	0.105	3.3100	32.0467
Computational results of a single hanging-type ATMD in the case of NAFGF (r) = -0.40				
0.010	0.76	0.061	8.0113	74.1981
0.015	0.76	0.080	7.0768	51.8164
0.020	0.75	0.089	6.1191	40.5152
0.025	0.74	0.102	5.7826	33.3100
0.030	0.74	0.104	5.2222	29.0629
Computational results of a single hanging-type ATMD in the case of NAFGF (r) = -0.80				
0.010	0.43	0.063	5.2078	83.8189
0.015	0.42	0.078	4.4928	58.6995
0.020	0.42	0.085	3.9432	46.4770
0.025	0.41	0.095	3.4822	37.5096
0.030	0.40	0.110	3.2442	31.1189

Table 3. The optimum parameters and R_{II} value of a single LT-ATMD with the actuator set at the mass block / a single hanging-type ATMD and the R_I value of the structures with the LT-ATMD / hanging-type ATMD with $\alpha = 0.4$ and $\mu = 0.01$ and with different total mass ratio and NAFGF

also shows that the two hypotheses will practically provide the same optimum frequency spacing (identical to the same robustness), same R_I value (identical to the same effectiveness), and same R_{IIj} value (identical to the same mass block stroke) (Refer to Tables 4 and 5). It is seen from Table 6 that a single LT-TMD takes on the identical behaviors with the LT-MTMD for these two hypotheses. It is interesting in observing Tables 4–6 to note that the LT-MTMD (passive counterpart of the LT-AMTMD) / a single

Total mass ratio	Tuning frequency ratio	Average damping ratio	Frequency spacing	R_I value
Computational results of the LT-MTMD in terms of the hypothesis –1				
0.010	2.49	0.011	0.12	8.3019
0.015	2.48	0.011	0.15	7.1540
0.020	2.47	0.013	0.17	6.4203
0.025	2.47	0.014	0.19	5.8833
0.030	2.46	0.017	0.20	5.4793
Computational results of the LT-MTMD in terms of the hypothesis –2				
0.010	0.99	0.029	0.12	8.4505
0.015	0.99	0.028	0.15	7.1852
0.020	0.99	0.033	0.17	6.4101
0.025	0.99	0.037	0.19	5.9350
0.030	0.99	0.039	0.21	5.5650
Computational results of the hanging-type MTMD				
0.010	0.99	0.028	0.12	8.3754
0.015	0.99	0.035	0.14	7.1324
0.020	0.99	0.034	0.17	6.4332
0.025	0.99	0.039	0.19	5.9641
0.030	0.98	0.046	0.20	5.5414

Table 4. The optimum parameters of the LT-MTMD (the passive counterpart of the LT-AMTMD) / hanging-type MTMD and the R_I value of the structures with the LT-MTMD / hanging-type MTMD with $n = 5$, $\alpha = 0.4$, and $\mu = 0.01$ and with different total mass ratio obtained in terms of the two hypotheses

LT-TMD designed in terms of the hypotheses-2 has approximately the same performances (including the same mass block stroke) as the hanging-type MTMD / a single hanging-type TMD with equal total mass ratio.

5. Conclusions

In the present paper, the location of the mass block is not movable; only the location of the support is movable. The LT-AMTMD proposed herein is aimed to attenuate the vibration of long-span bridges under the excitation directly acting on the structure, rather than through the base. The main purpose of selecting this form of excitation is to offer guidelines for the buffeting control design of long-span bridges under wind loads. Another important objective is to carry out the numerical estimations on the LT-AMTMD / a single LT-ATMD with respect to the hanging-type AMTMD / a single hanging-type ATMD as well as on the LT-MTMD (that is, passive counterpart of the LT-AMTMD) / a single LT-TMD with reference to the hanging-type MTMD / a single hanging-type TMD. It is worth pointing out that the locations of both the mass block and support in the MALTMD proposed by [Li and Zhou 2004] are

Total mass ratio	LT-TMD1	LT-TMD2	LT-TMD3	LT-TMD4	LT-TMD5
Computational results in terms of the hypothesis –1					
0.010	154.01	150.66	148.34	141.62	135.23
0.015	129.20	125.98	126.57	120.26	115.60
0.020	99.56	95.84	96.14	91.96	88.48
0.025	86.16	82.66	81.58	76.79	73.28
0.030	67.94	64.04	62.84	59.84	57.86
Computational results in terms of the hypothesis –2					
0.010	140.87	141.62	143.71	140.86	137.63
0.015	125.99	123.84	124.82	119.04	115.12
0.020	99.46	95.82	95.19	90.15	85.94
0.025	82.98	79.55	78.28	72.89	68.50
0.030	73.88	70.42	69.08	63.78	58.75
Total mass ratio	Hanging-type TMD1	Hanging-type TMD2	Hanging-type TMD3	Hanging-type TMD4	Hanging-type TMD5
0.010	147.03	146.32	147.67	144.03	140.40
0.015	107.02	102.59	101.23	97.03	95.04
0.020	97.12	94.10	92.90	87.42	82.70
0.025	79.39	76.36	75.06	69.59	64.41
0.030	62.09	59.82	59.25	56.81	54.68

Table 5. The R_{IIj} value, used for estimating the mass block stroke, of the LT-MTMD (the passive counterpart of the LT-AMTMD) / hanging-type MTMD with $n = 5$, $\alpha = 0.4$, and $\mu = 0.01$ and with different total mass ratio obtained in terms of the two hypotheses

all movable. Likewise, the MALTTMD is aimed to suppress the vibration of long-span bridges under the ground motions, namely the excitation through the base. From the numerical results presented, the following main conclusions can be drawn:

- (1) The LT-AMTMD with the actuator set at the mass block can provide better effectiveness and higher robustness in reducing the vibrations of long-span bridges with respect to the LT-AMTMD with the actuator set at any other locations. The actuator locations significantly affect the FRFs of the structures with the LT-AMTMD and the LT-AMTMD with the actuator set at the mass block will render the best FRFs. The FRFs of the structures with the LT-AMTMD with the actuator set at the mass block are very consistent with those of the hanging-type AMTMD. Likewise, changing the support locations practically has no influence on the FRFs of the structures with the LT-AMTMD with the actuator set at the mass block.
- (2) A new basic result is that both the static and dynamic stretching of the spring in the LT-AMTMD with the actuator set at the mass block may be freely adjusted in accordance with the practical requirements through changing the locations of the support within the range from $\alpha = 0.3$ to $\alpha = 0.7$ while practically maintaining the same performance (including the same mass block stroke).

Total mass ratio	Tuning frequency ratio	Damping ratio	R_I value	R_{II} value
Computational results of a single LT-TMD in terms of the hypothesis –1				
0.010	2.47	0.025	9.4510	67.7894
0.015	2.46	0.032	8.3178	47.7892
0.020	2.44	0.036	7.5204	37.7196
0.025	2.43	0.040	6.8651	31.3496
0.030	2.42	0.042	6.4355	27.4125
Computational results of a single LT-TMD in terms of the hypothesis –2				
0.010	0.99	0.066	9.5663	66.5275
0.015	0.98	0.080	8.3924	47.6999
0.020	0.98	0.090	7.5680	38.0642
0.025	0.97	0.098	6.9489	31.6057
0.030	0.97	0.104	6.5137	27.6807
Computational results of a single hanging-type TMD				
0.010	0.99	0.065	9.6623	67.0634
0.015	0.98	0.080	8.3198	47.5598
0.020	0.98	0.090	7.6252	38.1530
0.025	0.97	0.098	6.8943	31.5617
0.030	0.97	0.103	6.5625	27.8820

Table 6. The optimum parameters and R_{II} value of a single LT-TMD (the passive counterpart of the LT-ATMD) / a single hanging-type TMD and the R_I value of the structures with the LT-TMD / hanging-type TMD with $\alpha = 0.4$ and $\mu = 0.01$ and with different total mass ratio obtained in terms of the two hypotheses

- (3) The LT-AMTMD with the actuator set at the mass block can largely enhance the robustness and effectiveness of the LT-MTMD and can offer higher effectiveness in comparison to a single LT-ATMD. The mass block stroke of the LT-AMTMD with the actuator set at the mass block is slightly greater than that of the LT-MTMD, but is significantly larger than that of a single LT-ATMD.
- (4) The LT-MTMD designed using the two hypotheses practically maintains the same optimum stiffness and optimum damping coefficient. The two hypotheses will practically lead to the same robustness, effectiveness, and mass block stroke. Likewise, a single LT-TMD possesses the identical behaviors to the LT-MTMD corresponding to these two hypotheses.

In fact, any type of single-degree-of-freedom oscillators can be employed as the tuned mass dampers. However, the major advantage of the LT-AMTMD is that the dynamic stretching of spring (spring stroke) can be freely adjusted while practically maintaining the performance of the LT-AMTMD unchanged. The present paper is concerned with wind-induced harmonic vibrations of long span bridges. The focus is on the (vertical) flexural mode of the bridge deck. Usually under wind there are problems with the dominant flexural and torsional modes of vibration of long span bridges. It may be necessary to reduce at least two

or even more modes. Therefore, there is a need for further estimating the behaviors of the LT-AMTMD for the dominant flexural and torsional modes of vibration of long span bridges.

Acknowledgements

The authors would like to acknowledge the financial contributions received from the National Natural Science Foundation of China (No. 50578092).

References

- [Abe and Fujino 1994] M. Abe and Y. Fujino, “Dynamic characterization of multiple tuned mass dampers and some design formulas”, *Earthquake Eng. Struc.* **23**:8 (1994), 813–835.
- [Ankireddi and Yang 1996] S. Ankireddi and H. T. Y. Yang, “Simple ATMD control methodology for tall buildings subject to wind loads”, *J. Struct. Eng. ASCE* **122**:1 (1996), 83–91.
- [Chang and Yang 1995] C. C. Chang and H. T. Y. Yang, “Control of buildings using active tuned mass dampers”, *J. Eng. Mech. ASCE* **121**:3 (1995), 355–66.
- [Chen and Wu 2003] G. Chen and J. Wu, “Experimental study on multiple tuned mass dampers to reduce seismic responses of a three-storey building structure”, *Earthquake Eng. Struc.* **32**:5 (2003), 793–810.
- [Conti et al. 1996] E. Conti, G. Grillaud, J. Jacob, and N. Cohen, “Wind effects on the Normandie cable-stayed bridge: comparison between full aeroelastic model tests and quasi-steady analytical approach”, *J. Wind Eng. Ind. Aerod.* **65**:1-3 (1996), 189–201.
- [Diana et al. 1992] G. Diana, F. Cheli, A. Zasso, A. Collina, and J. Brownjohn, “Suspension bridge parameter identification in full scale test”, *J. Wind Eng. Ind. Aerod.* **41**:1-3 (1992), 165–176.
- [Gu and Xiang 1992] M. Gu and H. F. Xiang, “Optimization of TMD for suppressing buffeting responses of long-span bridges”, *J. Wind Eng. Ind. Aerod.* **42**:1-3 (1992), 1383–1392.
- [Gu et al. 1994] M. Gu, H. F. Xiang, and A. R. Chen, “A practical method of passive TMD for suppressing wind-induced vertical buffeting of long-span cable-stayed bridges and its application”, *J. Wind Eng. Ind. Aerod.* **51**:2 (1994), 203–213.
- [Gu et al. 1999] M. Gu, S. R. Chen, and C. C. Chang, “Buffeting control of the Yangpu bridge using multiple tuned mass dampers”, pp. 893–8 in *Proceedings of the 10th international conference on wind engineering*, edited by A. Larsem et al., A. A. Balkema, Rotterdam, 1999.
- [Gu et al. 2001] M. Gu, S. R. Chen, and C. C. Chang, “Parametric study on multiple tuned mass dampers for buffeting control of Yangpu bridge”, *J. Wind Eng. Ind. Aerod.* **89**:11-12 (2001), 987–1000.
- [Hoang and Warnitchai 2005] N. Hoang and P. Warnitchai, “Design of multiple tuned mass dampers by using a numerical optimizer”, *Earthquake Eng. Struc.* **34**:2 (2005), 125–144.
- [Igusa and Xu 1994] T. Igusa and K. Xu, “Vibration control of using multiple tuned mass dampers”, *J. Sound Vib.* **175**:4 (1994), 491–503.
- [Jangid 1995] R. S. Jangid, “Dynamic characteristics of structures with multiple tuned mass dampers”, *Struct. Eng. Mech.* **3**:5 (1995), 497–509.
- [Kareem and Kline 1995] A. Kareem and S. Kline, “Performance of multiple mass dampers under random loading”, *J. Struct. Eng. ASCE* **121**:2 (1995), 348–361.
- [Kwon and Park 2004] S.-D. Kwon and K.-S. Park, “Suppression of bridge flutter using tuned mass dampers based on robust performance design”, *J. Wind Eng. Ind. Aerod.* **92**:11 (2004), 919–934.
- [Lee et al. 2006] C.-L. Lee, Y.-T. Chen, L.-L. Chung, and Y.-P. Wang, “Optimal design theories and applications of tuned mass dampers”, *Eng. Struct.* **28**:1 (2006), 43–53.
- [Li 2000] C. Li, “Performance of multiple tuned mass dampers for attenuating undesirable oscillations of structures under the ground acceleration”, *Earthquake Eng. Struc.* **29**:9 (2000), 1405–1421.

- [Li 2004] C. Li, “Evaluation of the lever-type active tuned mass damper for structures”, *Struct. Control Health Monit.* **11**:4 (2004), 259–271.
- [Li and Li 2005] C. Li and Q. S. Li, “Evaluation of the lever-type multiple tuned mass dampers for mitigating harmonically forced vibration”, *Int. J. Struct. Stab. Dyn.* **5**:4 (2005), 641–664.
- [Li and Wang 2003] C. Li and Z. Wang, “Dynamic characteristics of lever-type multiple tuned mass dampers”, *Acta Mech. Solida Sin.* **24**:4 (2003), 451–455. Chinese.
- [Li and Zhou 2004] C. Li and D. Zhou, “Evaluation of multiple active lever-type tuned mass dampers for structures under ground acceleration”, *Eng. Struct.* **26**:3 (2004), 303–317.
- [Lin et al. 2000] Y.-Y. Lin, C.-M. Cheng, and C.-H. Lee, “A tuned mass damper for suppressing the coupled flexural and torsional buffeting response of long-span bridges”, *Eng. Struct.* **22**:9 (2000), 1195–1204.
- [Park and Reed 2001] J. Park and D. Reed, “Analysis of uniformly and linearly distributed mass dampers under harmonic and earthquake excitation”, *Eng. Struct.* **23**:7 (2001), 802–814.
- [Wang and Lin 2005] J.-F. Wang and C.-C. Lin, “Seismic performance of multiple tuned mass dampers for soil-irregular building interaction systems”, *Int. J. Solids Struct.* **42**:20 (2005), 5536–5554.
- [Xu and Igusa 1992] K. Xu and T. Igusa, “Dynamic characteristics of multiple substructures with closely spaced frequencies”, *Earthquake Eng. Struct.* **21**:12 (1992), 1059–1070.
- [Yamaguchi and Harnpornchai 1993] H. Yamaguchi and N. Harnpornchai, “Fundamental characteristics of multiple tuned mass dampers for suppressing harmonically forced oscillations”, *Earthquake Eng. Struct.* **22**:1 (1993), 51–62.
- [Yan et al. 1999] N. Yan, C. M. Wang, and T. Balendra, “Optimal damper characteristics of atmd for buildings under wind loads”, *J. Struct. Eng. ASCE* **125**:12 (1999), 1376–83.
- [Yau and Yang 2004] J.-D. Yau and Y.-B. Yang, “A wideband MTMD system for reducing the dynamic response of continuous truss bridges to moving train loads”, *Eng. Struct.* **26**:12 (2004), 1795–1807.

Received 8 Jul 2006. Accepted 25 Mar 2007.

CHUNXIANG LI: li-chunxiang@vip.sina.com

Department of Civil Engineering, Shanghai University, No. 149 Yanchang Rd., Shanghai 200072, China

BINGKANG HAN: College of Civil Engineering, Tongji University, No. 1239 Si Ping Rd., Shanghai 200092, China

FLEXURE OF BEAMS WITH AN INTERLAYER — SYMMETRIC BEAMS WITH ORTHOTROPIC ADHERENDS

K. S. ALFREDSSON, T. A. BOGETTI, L. A. CARLSSON, J. W. GILLESPIE, JR. AND A. YIOURNAS

Analysis of the three-point flexure loading of a symmetric beam configuration consisting of two identical adherends joined by a flexible layer is presented. A closed-form solution is presented in the form of a layer-wise approach, and shows excellent agreement with finite element results. Particular emphasis is given to the global beam compliance. The results show that a thin, shear deformable layer may effectively decouple the responses of the two beams. Furthermore, in contrast to ordinary beams, the presence of an overhang reduces the beam compliance. These effects are quantified and discussed. Experiments on aluminum adherends joined by a rubber layer were conducted over a range of overhang lengths in a three-point flexure fixture, and very good agreement between measured and predicted beam compliance was noted.

Introduction

Sandwich structures are commonly designed in an effort to mimic the I-beam concept where the web supports shear loads and the flanges bending loads. In certain structural applications, however, it may be desirable to utilize a highly shear deformable layer sandwiched between more rigid adherends, such as in structures utilizing shear thickening fluids to control the vibration response; see [Fischer et al. 2006], and in mechanical shielding of brittle layers; see for example [Mahdi et al. 2003].

The design of such structures is greatly benefited by an improved understanding of the role of the thickness and stiffness of the rubber layer in its ability to interact with the upper and lower layers of the structure. Most analysis of such structures to date is based on finite element analysis [Davila and Chen 2000; Mahdi and Gillespie 2004], because it is widely recognized that the large local shear deformation of the layer prohibits the use of ordinary beam and plate theories [Timoshenko and Woinowsky-Kreiger 1959; Gere and Timoshenko 1984] and first order shear deformation theory [Whitney 1973]. Sandwich beams and panels with shear-deformable compliant core materials have been considered by numerous researchers since the pioneering work of Reissner [1947, 1948]; see, for example, [Zenkert 1997]. Such analysis, however, is applicable to structures with thin faces over a thick core, while the present work considers thick adherends over a thin flexible layer.

In this paper we will present a layer-wise analytical beam approach to the mechanics of symmetric beam configurations with a flexible interlayer. Use of the simplest possible formulation that can capture the global bending behavior allows us to obtain a closed form solution. The approach shares several

Keywords: flexure, interlayer, shear deformation.

The authors would like to acknowledge funding from the Army Research Laboratory (Cooperative Agreement # DAAD19-01-2-0005) and the Composite Materials Center of Excellence program at the University of Delaware Center for Composite Materials.

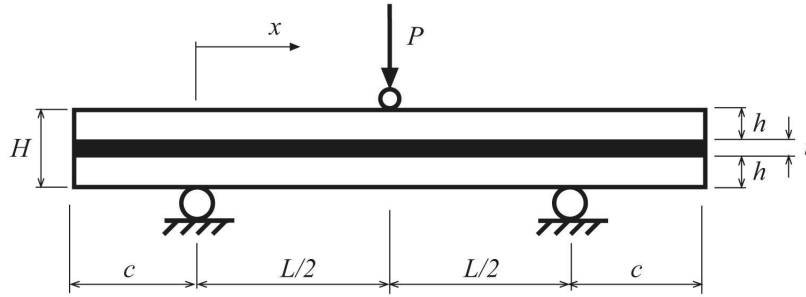


Figure 1. Three-point flexure loading of a layered beam with symmetric overhangs.

elements with the layer-wise approach developed for sandwich beams with a flexible core by [Frostig and Baruch \[1990\]](#), although they considered a thick core between thin faces and addressed local indentation at load introduction and support regions, while the main focus of our approach is on the global beam response and shear transfer effects. [Alfredsson \[2004\]](#) examined adhesively bonded end-notch flexure (ENF) fracture test specimens, but his analysis is valid only for infinitely thin layers. The analysis will be compared to finite element (FE) results and to experimental compliance data determined for beams with a rubber layer tested in three-point flexure loading.

Problem description

A multilayer symmetric beam structure consisting of two stiff and thick orthotropic adherends separated by a flexible isotropic interlayer loaded in three-point flexure is considered ([Figure 1](#)). In this initial study, the adherends are assumed to be of identical thickness. The solution is simplified to isotropic adherends to facilitate correlation with the experimental compliance data. A major objective here is to determine the global beam deflection. As will be shown, the overhang length c influences the compliance, and the role of this parameter will be examined.

For the symmetrical beam configuration considered ([Figure 1](#)), the loading may be divided into symmetric and antisymmetric parts ([Figure 2](#)), and each solution is superimposed to obtain the solution to the original problem. It is recognized that the symmetric part of the loading produces extensional (tensile or compressive) deformation of the interlayer, while the antisymmetric part produces shear deformation of the interlayer and bending of the layered beam. The symmetric part of the loading will not contribute to the global bending of the layered beam, and for this reason, only the antisymmetric part of the loading is considered here.

Derivation of governing equations

The adherends are considered to be Euler–Bernoulli beams. Considering only the antisymmetric part of the loading means that the resulting displacement field is also antisymmetric. Hence, the two adherends will have equal deflection, which is denoted w . The longitudinal displacements of the midplanes of the adherends are of equal magnitude, but of opposite sign. The displacement in the x direction ([Figure 1](#)) of the midplane of the lower adherend is denoted by u ; see [Figure 3](#).

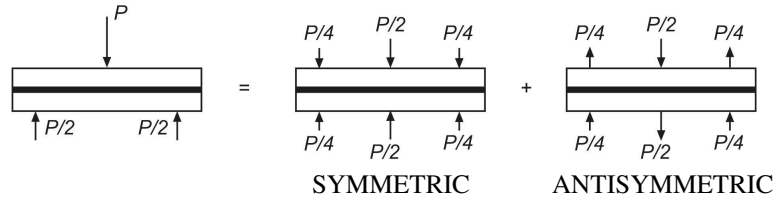


Figure 2. Superposition of symmetric and antisymmetric loadings.

The deformation of the interlayer is defined as the relative displacements of the lower and upper adherend/interlayer interfaces. According to classical beam theory, the cross sections of the adherends are assumed to undergo translation and rotation only. Hence, the deformation of the interlayer is defined with respect to the midplane of each adherend. As shown in Figure 3, both the axial displacement of each adherend, u , and the rotation of the beam, w' , contribute to the total shear deformation v of the flexible layer

$$v(x) = 2u(x) + (h + t)w'(x). \quad (1)$$

Longitudinal equilibrium of the flexible interlayer is assumed to be fulfilled by a shear stress, τ , which is constant throughout the thickness of the layer; see Figure 4. This means that the longitudinal normal stress in the flexible layer is neglected, which is justified since it is much smaller than the longitudinal normal stresses in the adherends and the shear stress in the flexible layer. The antisymmetric condition implies that there are no transverse normal stresses at the symmetry line passing through the middle of the interlayer. However, at the interface between the interlayer and the adherends, a normal stress σ may be present; see Figure 4.

Vertical equilibrium of the flexible layer requires that

$$2\sigma(x) = t\tau'(x), \quad (2)$$

where t is the thickness of the flexible layer; see Figure 1.

The adherends transmit normal forces, N , bending moments, M , and transversal shear forces, V . The positive directions of these stress resultants are shown in Figure 4 for the antisymmetric loading case.

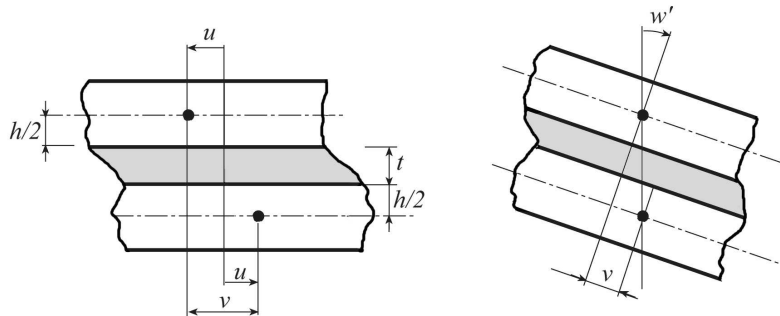


Figure 3. Shear deformation of a flexible layer due to longitudinal displacements, u (left), and slope, w' (right).

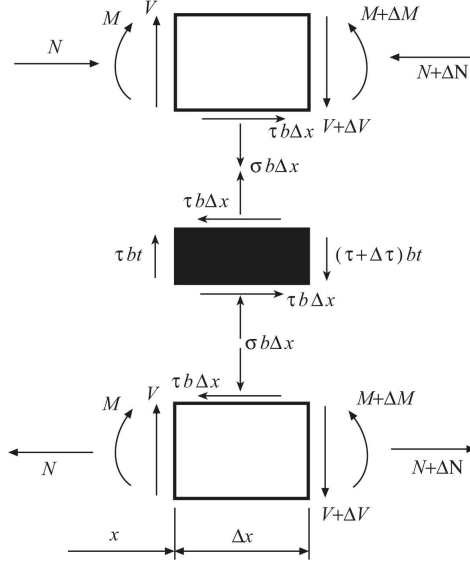


Figure 4. Positive direction of adhesive stresses and sectional loads.

Equilibrium of the adherends requires that

$$N'(x) = b\tau[v(x)], \quad (3a)$$

$$V'(x) = -b\sigma(x), \quad (3b)$$

$$V(x) = M'(x) + \frac{1}{2}bh\tau[v(x)], \quad (3c)$$

where b is the specimen width and h is the adherend thickness.

Assuming that the adherends deform elastically according to the Euler–Bernoulli beam theory, the normal force and the bending moment are given by

$$N(x) = Au'(x), \quad (4a)$$

$$M(x) = -Dw''(x), \quad (4b)$$

where $A = b \int E_1(z) dz$ and $D = b \int E_1(z) z^2 dz$ are the extensional and flexural stiffnesses of the adherends. E_1 is the Young's modulus in the longitudinal direction of the adherends. Furthermore, z is a coordinate in the thickness direction. For isotropic adherends with a Young's modulus E , integration yields

$$A = Ebh \quad \text{and} \quad D = Ebh^3/12.$$

In order to define a boundary value problem which involves only the shear deformation, the longitudinal displacement and the deflection are eliminated from the governing equations. Combination of Equations (2) and (3b) yields

$$2V'(x) + bt\tau'(x) = 0.$$

Integration yields

$$2V(x) + bt\tau(x) = \bar{V}, \quad (5)$$

where \bar{V} is the total shear force transmitted by the sandwich beam; see Figure 5. This equation can also be obtained directly from Figures 4 and 5. Substitution of Equation (3c) into Equation (5) yields the following differential equation:

$$2M'(x) + b(h+t)\tau[v(x)] = \bar{V}, \quad (6)$$

where the shear stress in the layer, τ , is a function of the shear deformation, v . Next, τ is substituted from Equation (3a) into Equation (6). With N and M expressed in terms of the displacements u and w according to Equation (4), the result is,

$$2w'''(x) - \frac{A}{D}(h+t)u''(x) = -\frac{\bar{V}}{D}. \quad (7)$$

Differentiating Equation (1) twice and combining the result with Equation (7) yields a relation between the second derivatives of u and v ,

$$\left[2 + \frac{A}{2D}(h+t)^2\right]u''(x) = v''(x) + \frac{\bar{V}}{2D}(h+t). \quad (8)$$

Substitution of the second derivative of u from Equation (8) into the equation obtained by combining Equations (3a) and (4a), the following differential equation relating shear deformation and shear stress is found:

$$v''(x) = \frac{b}{A} \left[2 + \frac{A}{2D}(h+t)^2\right] \{\tau[v(x)] - \bar{\tau}\}, \quad (9)$$

where

$$\bar{\tau} = \frac{\bar{V}}{bh} \frac{1 + \frac{t}{h}}{\frac{4D}{Ah^2} + (1 + \frac{t}{h})^2} = \frac{3}{4} \frac{\bar{V}}{bh} \frac{1 + \frac{t}{h}}{1 + \frac{3}{2} \frac{t}{h} + \frac{3}{4} (\frac{t}{h})^2}. \quad (10)$$

Here, $\bar{\tau}$ is the constant shear stress in the interlayer predicted by ordinary beam theory, [Gere and Timoshenko 1984]. For a small deformation of the interlayer, a linear constitutive relation applies. Thus, for the shear deformation,

$$\tau(x) = kv(x), \quad k = \frac{G}{t}, \quad (11)$$

where G is the shear modulus of the layer. Due to the assumed antisymmetric loading (Figures 2, and 4), no transverse deformation of the interlayer will take place since the transverse stress in the interlayer

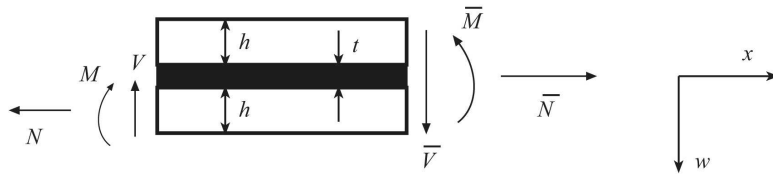


Figure 5. Sectional loads for entire beam sections; \bar{N} , \bar{M} , and \bar{V} , and for adherends N , M , and V .

varies linearly with a zero average. Substitution of Equation (11) into Equation (9) yields a linear differential equation of second order:

$$v''(x) - \kappa^2 v(x) = -\kappa^2 \bar{\tau}/k, \quad (12)$$

with

$$\kappa = \sqrt{\left[2 + \frac{A}{2D}(h+t)^2\right] \frac{bG}{At}} = \sqrt{\frac{8G}{Eht} \left[1 + \frac{3t}{2h} + \frac{3}{4}\left(\frac{t}{h}\right)^2\right]}. \quad (13)$$

As will be further discussed in this paper, κ constitutes an inverse length scale of the solution. The general solution to Equation (12) is

$$v(x) = A_1 e^{\kappa x} + A_2 e^{-\kappa x} + \frac{\bar{\tau}}{k}, \quad (14)$$

where A_1 and A_2 are integration constants determined by boundary conditions on v or v' .

The following relation, obtained from Equation (1) and Equation (4), can be used to transform boundary conditions on N and M into boundary conditions on v' ,

$$v'(x) = \frac{2}{A}N(x) - \frac{h+t}{D}M(x). \quad (15)$$

From this equation it also follows that not only v but also v' are continuous when no concentrated longitudinal forces or moments are applied to the adherends. Specific solutions will be discussed for beams without and with overhang.

Beams without overhang

Consider first a beam without overhang, that is, $c = 0$ in Figure 1. Due to symmetry, only one half of the specimen, here the left part, $0 \leq x \leq L/2$, must be analyzed. At the left end, $x = 0$, the adherends are unloaded, with $N(0) = 0$ and $M(0) = 0$. From Equation (15), the boundary conditions on N and M can be translated to a boundary condition on v' . Since the shear stress in the flexible layer is antisymmetric with respect to the loading point, $x = L/2$, the shear deformation is zero at $x = L/2$. Thus, the boundary conditions are:

$$v'(0) = 0, \quad v(L/2) = 0. \quad (16)$$

Subjecting the general solution, Equation (14), to these conditions, the shear stress takes the form

$$\tau(x) = \bar{\tau} \left[1 - \frac{\cosh(\kappa x)}{\cosh(\kappa L/2)} \right], \quad 0 \leq x \leq L/2, \quad (17)$$

where $\bar{\tau}$ is given by Equation (10) with $\bar{V} = P/2$. The distribution of interlayer shear stress along the beam is shown in Figure 6 for three span lengths. The results are normalized by $\bar{\tau}$. For long beams ($L = 2.0$ m) the shear stress is close to the ordinary beam theory result ($\bar{\tau}$) everywhere except near the loading point where a sign change takes place. This can also be deduced from Equation (17); that is, for large values of L the second term inside the parentheses is negligible except when x is close to $L/2$. Hence, with respect to the shear stress distribution in the interlayer, the present theory degenerates into ordinary beam theory for large span lengths. The shear stress decreases with decreasing span length.

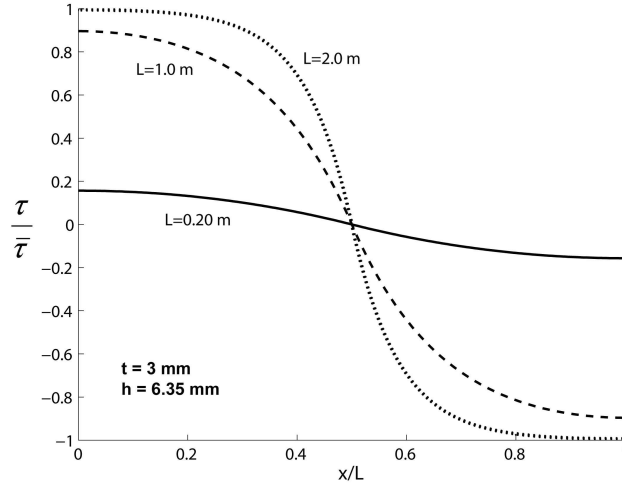


Figure 6. Shear stress distribution along the beam for three span lengths, $L = .2, 1$ and 2 m, $E = 70$ GPa, $G = 3.1$ MPa, $h = 6.35$ mm, $t = 3$ mm. The shear stress is normalized by the value obtained from ordinary beam theory.

For a short span length ($L = 0.2$ m), the maximum shear stress is only about 20% of the ordinary beam theory value.

The normal force in the adherends is determined by integration of [Equation \(3a\)](#),

$$N(x) = b \int_0^x \tau[v(\tilde{x})]d\tilde{x} = \frac{b\bar{\tau}}{\kappa} \left[\kappa x - \frac{\sinh(\kappa x)}{\cosh(\kappa L/2)} \right]. \quad (18)$$

The bending moment in the adherends is determined from the equilibrium of a free body element of the beam cut at a distance x from the left end:

$$M(x) = \frac{1}{4}Px - \frac{1}{2}(h+t)N(x) = \frac{bh\bar{\tau}}{2\kappa(1+t/h)} \left[\frac{4D}{Ah^2}\kappa x + \left(1 + \frac{t}{h}\right)^2 \frac{\sinh(\kappa x)}{\cosh(\kappa L/2)} \right],$$

where $P = 2\bar{V}$ and [Equations \(10\)](#) and [\(18\)](#) have been used to obtain the final expression for $M(x)$ above. Notice that for isotropic adherends, $Ah^2/(12D) = 1$.

The deflection, $w(x)$, is determined by integrating [Equation \(4b\)](#) and using the boundary conditions, $w(0) = 0$ and $w'(L/2) = 0$. The beam compliance, $C = w(L/2)/P$ takes the form,

$$\frac{C}{C_{bt}} = 1 + \frac{Ah^2}{12D} \left(1 + \frac{t}{h}\right)^2 \left[\frac{36}{\kappa^2 L^2} - \frac{72}{\kappa^3 L^3} \tanh\left(\frac{\kappa L}{2}\right) \right], \quad (19)$$

where C_{bt} is the compliance according to ordinary beam theory,

$$C_{bt} = \frac{L^3}{96D + 24A(h+t)^2} = \frac{L^3}{32Ebh^3} \left[1 + \frac{3t}{2h} + \frac{3}{4}\left(\frac{t}{h}\right)^2 \right]^{-1}. \quad (20)$$

It is seen from [Equation \(19\)](#) that for large values of L we have $C \approx C_{bt}$, which implies that with respect to the compliance, the present theory degenerates into ordinary beam theory for large span lengths.

In an attempt to clarify the implications of Equation (19), two definitions referring to the effects of introducing a flexible layer, *thickness effect* and *flexibility effect*, are introduced. The thickness effect refers to the increase in flexural stiffness (decrease of compliance) due to the thickness of the flexible layer. If only the thickness effect is accounted for, the compliance equals C_{bt} (Equation (20)), the compliance predicted by ordinary beam theory.

The flexibility effect refers to the decoupling of the two adherends due to shear deformation of the layer, but disregards the increased thickness. To isolate this effect, it is assumed that $t/h \ll 1$, and Equation (19) becomes

$$\frac{C_f}{C_0} = 1 + \frac{Ah^2}{12D} \left[\frac{36}{\bar{k}^2 L^2} - \frac{72}{\bar{k}^3 L^3} \tanh\left(\frac{\bar{k}L}{2}\right) \right], \quad \frac{t}{h} \ll 1, \quad (21)$$

where

$$\bar{k} = \sqrt{\left[2 + \frac{Ah^2}{2D} \right] \frac{bG}{At}} = \sqrt{\frac{8G}{Eht}}, \quad (22a)$$

$$C_0 = \frac{L^3}{96D + 24Ah^2} = \frac{L^3}{32Ebh^3}, \quad (22b)$$

in which C_0 is the compliance when the two outer beams are fully coupled by an interlayer of zero thickness.

Figure 7 illustrates the influences of the two effects on the beam compliance, here normalized by C_0 (Equation (22b)). The dotted curve shows the monotonic decrease of the compliance according to ordinary beam theory, C_{bt} in Equation (20), due to the increased interlayer thickness. The dashed curve shows the monotonic increase of C_f (Equation (21)) due to the increase of the flexibility, $k^{-1} = t/G$, with increasing interlayer thickness. The solid curve represents the actual compliance, C , predicted by

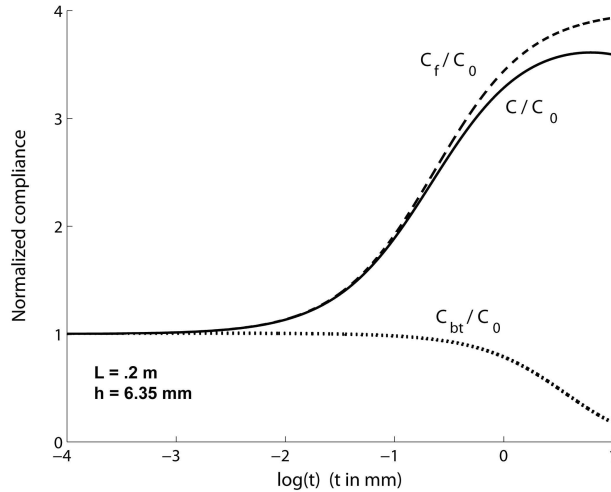


Figure 7. Compliance as a function of layer thickness. $E = 70$ GPa, $G = 3.1$ MPa, $h = 6.35$ mm, $L = 0.2$ m.

Equation (19). It is seen that the actual compliance C is bounded by C_{bt} and C_f . That is, when only the thickness effect is accounted for (ordinary beam theory) the compliance is underestimated, and when only the flexibility effect is accounted for, the compliance is overestimated. It can be shown mathematically that this is always the case, that is, $C_{bt} \leq C \leq C_f$.

Figure 8 shows the compliance calculated from Equation (19), normalized by C_0 , as a function of layer thickness for span lengths of .2, 1, and 2 m. For the shortest span ($L = .2$ m), the compliance increases with increasing layer thickness over the entire interval studied. This means that for large layer thicknesses, the two adherends are practically decoupled and bend independently of one another, that is, the flexibility effect dominates. Such beams actually have two neutral planes with each plane on the geometrical center of each adherend. For a beam with a large span ($L = 2.0$ m), the compliance decreases with layer thickness, that is, the thickness effect dominates the behavior. For the intermediate span length ($L = 1.0$ m), the compliance increases with layer thickness up to a critical value of $t_{cr} \approx 3.5$ mm. Below this value the flexibility effect dominates. For layer thicknesses above 3.5 mm, the thickness effect dominates and the compliance decreases with increasing layer thickness.

From the results shown in Figure 8, it becomes clear that for a specified choice of adherends and a given interlayer material, there exists a critical span length, L_{cr} , above which the addition of a thin flexible layer will not decouple the response—that is, the compliance will not increase when a thin flexible interlayer is added. The critical span length is found by making C stationary with respect to t for $t \rightarrow 0$, which yields,

$$L_{cr} = \sqrt{\frac{3Ah}{bG}} = h\sqrt{\frac{3E}{G}}.$$

For the present geometry the critical span length is 1.65 m; see Figure 8. This equation should be useful for the design of structures containing flexible interlayers.

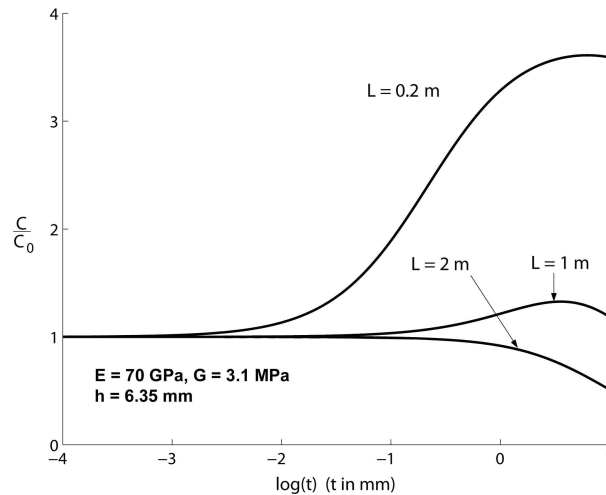


Figure 8. Compliance as a function of layer thickness for span lengths of .2, 1 and 2 m $E = 70$ GPa, $G = 3.1$ MPa, $h = 6.35$ mm.

Equation (21) can also be used to examine the behavior for beams with a very thin ($t/h \ll 1$) layer. If such a layer is very stiff, $G \rightarrow \infty$, the compliance approaches that of a homogeneous beam, and $C \rightarrow C_0$. On the other hand, if the thin layer is very flexible, $G \rightarrow 0$, $\bar{\kappa} \rightarrow 0$, then the compliance $C \rightarrow 4C_0$ for the case of isotropic adherends. This case effectively corresponds to one beam sliding on top of the other. The beams may be said to be fully decoupled if the compliance is more than 99% of the asymptotic value, $C = 4C_0$. The other extreme, *fully coupled*, may be defined when the compliance exceeds the lower limit, $C = C_0$, by less than 1%. These conditions can be quantified using Equation (21). The degree of decoupling is characterized by introduction of the following dimensionless decoupling parameter,

$$\beta = \frac{8}{\bar{\kappa}^2 L^2} = \frac{E}{G} \left(\frac{h}{L} \right)^2 \frac{t}{h}.$$

The variation of compliance with β is shown in Figure 9. The curve can be used to assess the level of decoupling by calculating β for any particular beam configuration. The curve also shows that for a very thin layer it is required that $\beta < 0.0023$ to achieve full coupling of the two beams ($C/C_0 < 1.01$). On the other hand, $\beta > 59$ gives full decoupling of the two beams ($C/(4C_0) > 0.99$).

Beams with overhang

Consider a beam with symmetric overhang, that is, $c > 0$ in Figure 1. Due to symmetry, only the left part, $-c \leq x \leq L/2$, is studied. The total shear force is discontinuous at the supports:

$$\bar{V}(x) = \begin{cases} 0, & \text{for } -c \leq x < 0 \\ P/2, & \text{for } 0 < x < L/2. \end{cases}$$

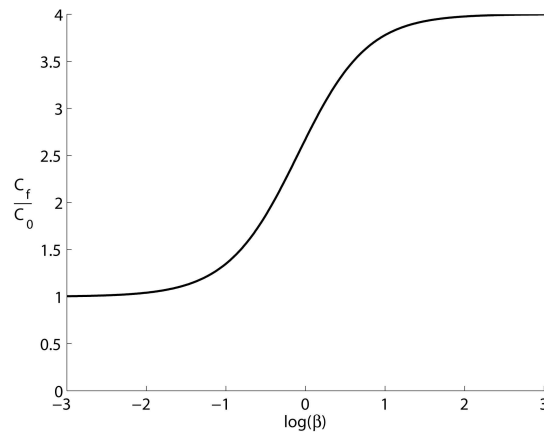


Figure 9. Compliance as a function of decoupling parameter, β , for thin interlayers, $t/h \ll 1$.

According to Equation (14), and the procedure outlined for the $c = 0$ case, this implies that the general solution for the shear deformation of the interlayer is given by

$$v(x) = \begin{cases} (A_1 e^{\kappa x} + A_2 e^{-\kappa x}) \frac{\bar{\tau}}{k}, & \text{for } -c \leq x \leq 0 \\ (A_3 e^{\kappa x} + A_4 e^{-\kappa x} + 1) \frac{\bar{\tau}}{k}, & \text{for } 0 \leq x \leq L/2, \end{cases} \quad (23)$$

where $\bar{\tau}$ is given by Equation (10) with $\bar{V} = P/2$. The absence of a constant term for the overhang portion in Equation (23) reflects the fact that the total shear force, \bar{V} , Figure 5, is zero in the overhang part of the beam. The boundary conditions at the free left end, $x = -c$, and at the midspan, $x = L/2$, are, similar to Equation (16),

$$v'(-c) = 0, \quad (24a)$$

$$v(L/2) = 0. \quad (24b)$$

Moreover, both v and v' must be continuous at the support, $x = 0$. With these four conditions, the integration constants become

$$A_1 = \frac{1}{2} \frac{e^{\kappa L/2} + e^{-\kappa L/2} - 2}{e^{\kappa L/2} + e^{-\kappa(4c+L)/2}}, \quad (25a)$$

$$A_2 = A_1 e^{-2\kappa c} = \frac{1}{2} \frac{e^{\kappa(L-4c)/2} + e^{-\kappa(4c+L)/2} - 2e^{-2\kappa c}}{e^{\kappa L/2} + e^{-\kappa(2c+L)/2}}, \quad (25b)$$

$$A_3 = A_1 - \frac{1}{2} = \frac{1}{2} \frac{e^{-\kappa L/2} - e^{-\kappa(4c+L)/2} - 2}{e^{\kappa L/2} + e^{-\kappa(4c+L)/2}}, \quad (25c)$$

$$A_4 = A_2 - \frac{1}{2} = \frac{1}{2} \frac{e^{\kappa(L-4c)/2} - e^{\kappa L/2} - 2e^{-2\kappa c}}{e^{\kappa L/2} + e^{-\kappa(4c+L)/2}}. \quad (25d)$$

The longitudinal force, N (Figure 3), is obtained by integration of Equation (3a),

$$N(x) = b \int_{-c}^x \tau[v(\tilde{x})] d\tilde{x}. \quad (26)$$

The bending moment in the adherends is determined from equilibrium:

$$M(x) = \begin{cases} -\frac{1}{2}(h+t)N(x), & \text{for } -c \leq x \leq 0 \\ \frac{1}{4}Px - \frac{1}{2}(h+t)N(x), & \text{for } 0 \leq x \leq L/2. \end{cases} \quad (27)$$

With the bending moment determined, the deflection, $w(x)$, is determined by integration of Equation (4b). With the boundary conditions, $w(0) = 0$ and $w'(L/2) = 0$, the compliance, $C_{oh} = w(L/2)/P$, takes the form,

$$\frac{C_{oh}}{C_{bt}} = 1 + \left(\frac{Ah^2}{12D}\right) \frac{36}{\kappa^3 L^3} \left(1 + \frac{t}{h}\right)^2 \left[A_3 \{e^{\kappa L/2} (2 - \kappa L) - 2\} + A_4 \{2 - e^{-\kappa L/2} (2 + \kappa L)\} \right], \quad (28)$$

where A_3 , A_4 and C_{bt} are given in Equations (25c), (25d), and (20). For zero overhang length, $c = 0$, it can be shown that C_{oh} degenerates into C according to Equation (19). When the overhang is infinitely long, the limit compliance is given by

$$\frac{C_{oh}}{C_{bt}} = 1 + \left(\frac{Ah^2}{12D}\right) \frac{36}{\kappa^3 L^3} \left(1 + \frac{t}{h}\right)^2 [\kappa L - 3 - e^{-\kappa L} + 4e^{-\kappa L/2}].$$

It will be demonstrated below that even though C_∞ is an asymptotic value for infinitely long overhangs, it is also a very good approximation for moderate values of the overhang. Figure 10 shows the compliance for beams with overhang normalized by the limiting value of the compliance. The data are plotted against the dimensionless parameter κc . It is noted that the overhang does not influence the compliance very much at longer spans. Figure 10 also shows that for $\kappa c > 3$ the limit value of the compliance, C_∞ , is a very good approximation, regardless of the span length. Hence, from Equation (13) it follows that compliance, C_{oh} , is very close to the limiting value of the compliance, C_∞ , if the overhang length exceeds the limiting overhang length, c_∞ ,

$$c_\infty = 3\sqrt{\frac{At}{bG} \left[2 + \frac{A}{2D}(h+t)^2\right]^{-1}} = 3\sqrt{\frac{Eht}{8G} \left[1 + \frac{3t}{2h} + \frac{3}{4}\left(\frac{t}{h}\right)^2\right]^{-1}}.$$

For isotropic adherends and a thin flexible layer ($t/h \ll 1$), the limiting overhang is given by

$$\bar{c}_\infty = 3\sqrt{\frac{Eht}{8G}}.$$

This expression resembles the one for the decay length of end effects for composites according to St. Venant's principle ([Horgan 1972; Choi and Horgan 1977; Horgan and Knowles 1983; Bogetti et al. 1988]) in the sense that the square root of the ratio of the Young's and shear moduli governs the length scale.

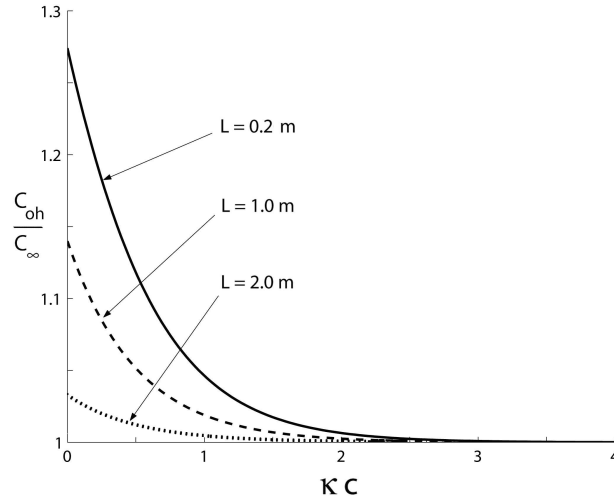


Figure 10. Compliance as a function of overhang length (κc), for span lengths, of .2, 1 and 2 m. $E = 70$ GPa, $G = 3.1$ MPa, $h = 6.35$ mm, $t = 3$ mm.

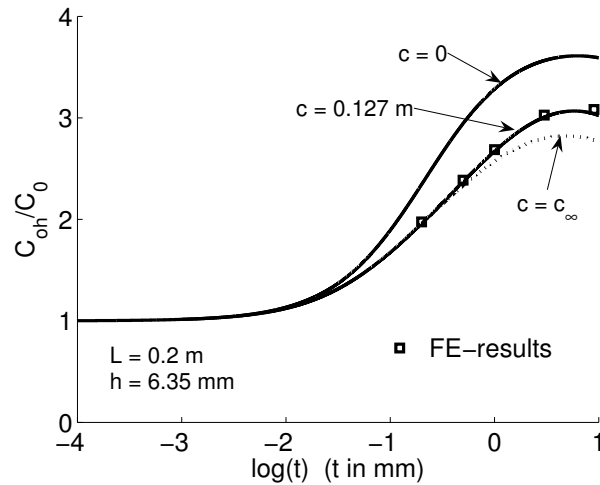


Figure 11. Compliance as a function of layer thickness for overhang lengths, c , of 0, .127 m, and c_∞ . $E = 70$ GPa, $G = 3.1$ MPa, $h = 6.35$ mm, and $L = 0.2$ m. The open squares represent results from FE analysis with Poisson's ratio $\nu = 0.4999$ for the rubber and $\nu = 0.33$ for the aluminum.

Figure 11 shows the compliance C_{oh}/C_0 as a function of the layer thickness for overhang lengths $c = 0$, .127 m, and c_∞ . The reduction of the compliance by the overhang segments is quite substantial for thick layers. A comparison with a two-dimensional continuum finite element model is also made in Figure 11 for the case of $c = .127$ m. The adherends are assumed to deform under plane stress in order to conform to the beam theory solution. The flexible interlayer is constrained in its plane by the stiff adherends, and is thus assumed to deform under plane strain. The FE code [Mechanica 2007] is used in the FE simulations. A ninth order polynomial is used for interpolation of displacements along all element edges. Sixteen elements are used along the span. The elements in the overhang regions are of the same lengths as those inside the span. One element through the thickness of each adherend and the interlayer is used. This is sufficient due to the high degree of the interpolation polynomial. The FE results are shown as squares in Figure 11. The correspondence to the analytical solution is very good. For large interlayer thicknesses a small deviation is observed, and the FE solution gives a slightly higher compliance. This is due to compression of the interlayer, an effect which is not accounted for in the analytical solution. This effect could be accounted for by also considering the symmetric part of the analytical solution; see Figure 2. For the present case however, this effect is small.

Figure 12 shows the compliance C_{oh}/C_{bt} as a function of the span length, L , for two layer thicknesses, $t = .76$ and 3 mm. For short span lengths, the overhang has a significant influence on the compliance. For large span lengths, however, C_{oh}/C_{bt} approaches unity for both layer thicknesses, which shows that ordinary beam theory is recovered.

Figure 13 shows the shear stress distribution, $\tau/\bar{\tau}$, in the layer for three overhang lengths $c = 0$, $c = 0.127$ m, and $c = c_\infty$ (0.506 m). It is seen that an overhang causes substantial changes in the shear stress close to the supports. This will also affect the distribution of the normal force and bending moments

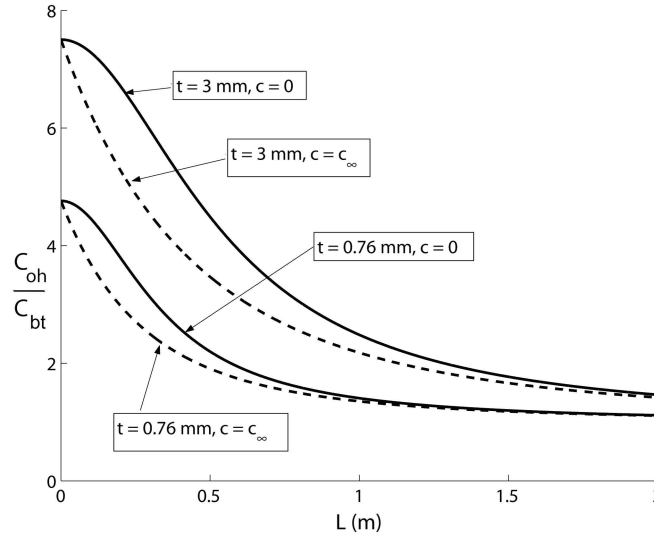


Figure 12. Compliance as a function of span length for beams without overhang (continuous lines) and limiting overhang (dashed lines). $E = 70$ GPa, $G = 3.1$ MPa, $h = 6.35$ mm, $L = 0.2$ m.

in the adherends and the deflection. For the beam with $c = c_\infty$ the shear stress in the layer decays to zero at the left end of the beam. This case represents a limiting value of the overhang. If the overhang is increased beyond this value, the stress distribution (and compliance) will not change.

Experiments

Rubber testing. The shear modulus, G , of the rubber layer was determined using the following equation derived from the statistical theory of rubber elasticity [Aklonis and MacKnight 1983],

$$\sigma = G \left(\lambda - \frac{1}{\lambda^2} \right),$$

where incompressibility has been assumed, and σ represents the tensile stress (calculated based on the original cross sectional area), and λ is the extension ratio of the rubber ($\lambda = l/l_0$, where l and l_0 are the deformed and undeformed lengths of the rubber specimen). By constructing plots of σ versus $\lambda - \lambda^{-2}$ the shear modulus, G , is the slope of the initially linear portion of the curve.

A rectangular specimen of 2.54 cm width and 3 mm thickness was cut from a flat EPDM rubber sheet. The tensile tests were conducted on specimens using a gage length of 30.5 cm at a crosshead rate of 2.5 mm/min. The extension ratio, λ , was calculated from the crosshead displacement. The rubber shear modulus was determined to be $G = 3.11 \pm .07$ MPa.

Flexure testing. Three-point flexure tests were conducted on beams with aluminum adherends connected by a rubber layer. The adherends were 6.53 mm thick and 51 mm wide, with a 3.0 mm thick rubber layer.

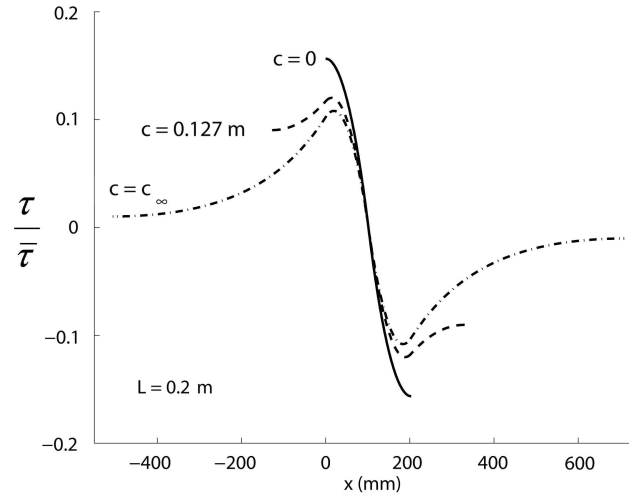


Figure 13. Shear stress distribution for beams with overhang lengths $c = 0$, $.127$ m and c_{∞} . $E = 70$ GPa, $G = 3.1$ MPa, $L = .2$ m, $h = 6.35$ mm, $t = 3$ mm. The shear stress is normalized by $\bar{\tau}$ given by [Equation \(10\)](#).

A critical test of the analytical model is to determine if the effect of the overhang on compliance is borne out experimentally. For that purpose the experiments were conducted at a constant span length, $L = 20.3$ cm, and at overhang lengths $c = 2.54, 5.08, 7.62, 10.2,$ and 12.7 cm.

The bonding surfaces of the aluminum beams were grit blasted and treated with silane for adhesive bonding to an EPDM rubber layer. The rubber layer was abraded and treated with a primer before bonding to the adherends using a two-component epoxy adhesive (Applied Poleramic SC-11). Thin scrim cloth layers were inserted between the rubber layer and the adherends to maintain a uniform bond line.

The beams were tested in an Instron 4484 load frame in a three-point flexure fixture with 19.1 mm diameter cylindrical rollers at the supports and load introduction locations. [Figure 14](#) shows a photo of the actual test setup. To achieve a more uniform load introduction, 1.6 mm thick rubber pads were inserted between the loading and support rollers and the beam. The displacement of the beams was measured on the top surface above each support, and on the bottom surface under the central load introduction line using LVDTs. The accuracy of the LVDTs was $\pm .0025$ mm, or better. The actual deflection of the lower beam surface at the center span ($x = L/2$) was determined by subtracting the average displacement at the supports from that at the central load introduction. By this procedure, it was possible to compensate for displacement contributions from the load cell and fixture as well as local deformations in the support regions. By measuring the displacement of the lower surface under the central load, local load introduction effects were eliminated.

The flexure tests were conducted at a cross head rate of 2.5 mm/min. The beam compliance was determined from the corrected central beam deflection (δ) divided by the applied load (P), $C = \delta/P$.

In order to satisfy the desired range of overhang lengths at a constant span length ($L = 20.3$ cm) without introducing multiple beam specimens, the initially 45.7 cm long beam was loaded to very small displacements in order to maintain linear elastic reversible response. Following this test, the beam was

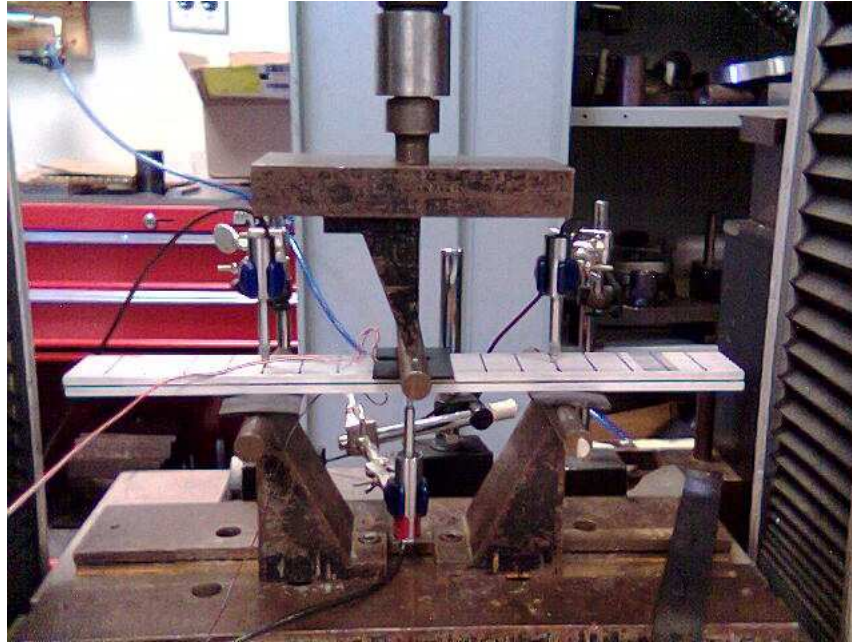


Figure 14. Experimental setup for compliance determination of three-point flexure loaded beams with rubber interlayer.

unloaded, removed from the fixture, and a 2.54 cm long section of each end was cut off in order to achieve a beam with a shorter overhang length. This procedure was repeated until the shortest (2.54 cm) overhang length was accomplished.

Figure 15 shows compliance of the beam versus overhang length. The solid circles represent experimental test data determined as described above, while the continuous curve represents predictions from Equation (28), with $E = 70$ GPa and $G = 3.1$ MPa. It is verified that the presence of an overhang reduces the compliance, and the test data are in very good agreement with the analytical predictions, lending confidence to the approach adopted in this study.

The squares in Figure 15 represent FE results according to the model used in connection with Figure 11. The comparison to the analytical solution is very good. Thus, the predicted reduction of compliance with increasing overhang length, c , is confirmed by the FE results.

Concluding remarks

The beam analysis presented here shows that beams with a flexible interlayer behave quite differently from ordinary homogeneous beams in the sense that a highly localized shear deformation substantially adds to the flexibility and decoupling characteristics of the structure. These effects are quantified through an analytical form of the compliance for the three-point flexure geometry. It is also shown and quantified how an overhang portion of the beam reduces the beam compliance. Conditions for full coupling and full decoupling are formulated for beams with thin interlayers, and expressed in the form of a dimensionless decoupling parameter. The analysis is intended as a design tool that is simpler to use and more

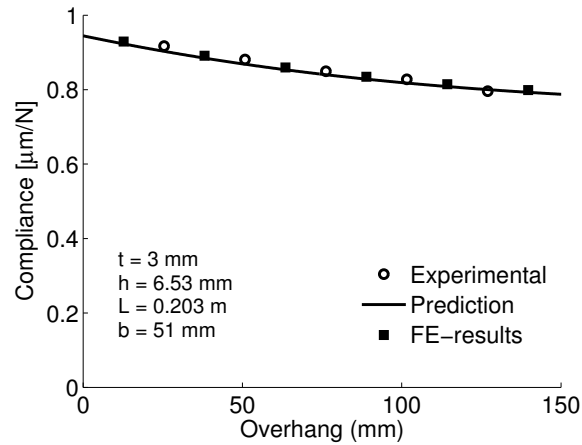


Figure 15. Compliance as a function of overhang length. $E = 70$ GPa, $G = 3.1$ MPa $h = 6.53$ mm, $b = 51$ mm, $t = 3$ mm, and $L = .203$ m. Open circles represent experimental data and the continuous line predictions using Equation (28). Solid squares represent results from FE analysis with Poisson’s ratio $\nu = 0.4999$ for the rubber and $\nu = 0.33$ for the aluminum.

computationally efficient than finite elements. Comparison of the analytical model to a continuum finite element model shows excellent agreement. Experiments on three-point flexure loaded aluminum beams with a rubber interlayer were in favorable agreement with the beam analysis predictions.

Acknowledgements

The authors would like to acknowledge Dr. John Tierney for his valuable contributions.

References

- [Aklonis and MacKnight 1983] J. J. Aklonis and W. J. MacKnight, *Introduction to polymer viscoelasticity*, 2nd ed., Wiley, New York, 1983.
- [Alfredsson 2004] K. S. Alfredsson, “On the instantaneous energy release rate of the end-notch flexure adhesive joint specimen”, *Int. J. Solids Struct.* **41**:16-17 (2004), 4787–4807.
- [Bogetti et al. 1988] T. A. Bogetti, J. W. Gillespie Jr., and R. B. Pipes, “Evaluation of the IITRI compression test method for stiffness and strength determination”, *Compos. Sci. Technol.* **32**:1 (1988), 57–76.
- [Choi and Horgan 1977] I. Choi and C. O. Horgan, “Saint-Venant’s principle and end effects in anisotropic elasticity”, *J. Appl. Mech. (Trans. ASME)* **44** (1977), 424–430.
- [Davila and Chen 2000] C. G. Davila and T.-K. Chen, “Advanced modeling strategies for the analysis of tile-reinforced composite armor”, *Appl. Compos. Mater.* **7**:1 (2000), 51–68.
- [Fischer et al. 2006] C. Fischer, S. A. Braun, P.-E. Bourban, V. Michaud, C. J. G. Plummer, and J.-A. E. Manson, “Dynamic properties of sandwich structures with integrated shear-thickening fluids”, *Smart Mater. Struct.* **15**:5 (2006), 1467–1475.
- [Frostig and Baruch 1990] Y. Frostig and M. Baruch, “Bending of sandwich beams with transversely flexible core”, *AIAA J.* **28**:3 (1990), 523–531.
- [Gere and Timoshenko 1984] J. M. Gere and S. P. Timoshenko, *Mechanics of materials*, 2nd ed., Brooks/Cole Engineering Division, Monterey, CA, 1984.

- [Horgan 1972] C. O. Horgan, "On Saint-Venant's principle in plane anisotropic elasticity", *J. Elasticity* **2**:3 (1972), 169–180.
- [Horgan and Knowles 1983] C. O. Horgan and J. K. Knowles, "Recent developments concerning Saint-Venant's principle", *Adv. Appl. Mech.* **23** (1983), 179–269.
- [Mahdi and Gillespie 2004] S. Mahdi and J. W. Gillespie, Jr., "Finite element analysis of tile-reinforced composite structural armor subjected to bending loads", *Compos. Part B Eng.* **35**:1 (2004), 57–71.
- [Mahdi et al. 2003] S. Mahdi, B. A. Gama, S. Yarlagadda, and J. W. Gillespie Jr., "Effect of the manufacturing process on the interfacial properties and structural performance of multi-functional composite structures", *Compos. Part A Appl. S.* **34**:7 (2003), 635–647.
- [Mechanica 2007] Mechanica, "Pro/MECHANICA, Mechanica Wildfire 3.0", 2007, Available at <http://www.ptc.com/partners/hardware/current/prom.htm>.
- [Reissner 1947] E. Reissner, "On bending of elastic plates", *Q. Appl. Math.* **5** (1947), 55–68.
- [Reissner 1948] E. Reissner, "Finite deflections of sandwich plates", *J. Aeronautical Sci.* **15** (1948), 435–440.
- [Timoshenko and Woinowsky-Kreiger 1959] S. Timoshenko and S. Woinowsky-Kreiger, *Theory of plates and shells*, 2nd ed., McGraw-Hill, New York, 1959.
- [Whitney 1973] J. M. Whitney, "Shear correction factors for orthotropic laminates under static load", *J. Appl. Mech. (Trans. ASME)* **40** (1973), 302–304.
- [Zenkert 1997] D. Zenkert, *An introduction to sandwich construction*, EMAS, London, 1997.

Received 24 Oct 2006. Accepted 7 May 2007.

K. S. ALFREDSSON: svante.alfredsson@his.se
University of Skövde, S-541 28 Skövde, Sweden

T. A. BOGETTI: bogetti@arl.army.mil
Army Research Laboratory, Aberdeen Proving Ground, Aberdeen, MD 21005, United States

L. A. CARLSSON: carlsson@fau.edu
Department of Mechanical Engineering, Florida Atlantic University, Boca Raton, FL 33431, United States

J. W. GILLESPIE, JR.: gillespie@udel.edu
Center for Composite Materials, University of Delaware, Newark, DE 19716, United States

A. YIOURNAS: yiournas@udel.edu
Dynamic Science Inc. DTSD, Aberdeen, MD 21001, United States

ENERGY-MINIMIZING INCLUSION IN AN ELASTIC PLATE UNDER REMOTE SHEAR

SHMUEL VIGDERGAUZ

A single foreign inclusion perfectly embedded in an elastic plate is considered as a bimaterial setup for finding the interface shape that minimizes the energy increment in a homogeneous shear stress field given at infinity. While simple in concept, this optimization problem is very hard computationally. For tractability, we limit our focus to a narrowed set of curves which can be conformally mapped onto a circle by an analytic function with only one nonzero Laurent term. The resultant one-parameter shape optimization problem with an integral objective functional is then accurately solved using an enhanced complex variable approach. This scheme, though seemingly restrictive, provides good qualitative insight into the optimal solution and bridges the gap between the limiting cases of the energy-minimal hole and the rigid inclusion solved previously.

1. Introduction

Elastostatic analysis and optimization of fiber-reinforced composites is of current interest in various fields of structural engineering, from the traditional mechanical industry [Ibrahim et al. 1991; Bull 1996] to modern nanotechnology [Ovid'ko and Sheinerman 2005] and phononics [Gazonas et al. 2006]. The fibers' shape is of much less practical importance than their volume fraction, though they do significantly influence the overall mechanical behavior. This results in an optimization problem: to maximize structural rigidity of a matrix, determine the shape of a fixed volume of fibers that minimizes the strain energy increment induced in a given homogeneous stress state.

As in other branches of continuum mechanics, the stress-strain analysis of bimaterial structures has advanced much further than the optimization of their mechanical properties. This is true even for the simplest linear two-dimensional case considered here. Closed-form optima such as the equistress inclusion shapes [Vigdergauz 1989] are extremely rare, whereas numerical schemes require a computationally difficult repetitive solution of the fourth-order elasticity equations in the phases domains with a successively modified mutual boundary. The resulting chain of direct boundary value problems becomes especially challenging in a multiconnected domain when a reinforcing phase is arranged into a set of interacting inclusions. This manifests itself in unstable, inaccurate, and too time-consuming computations. It should be pointed out that the difficulties emerge precisely from the computational repetitiveness of the optimization process even though, for any *given* inclusion shape, the stresses and strains can be effectively determined by a wide variety of methods.

Clearly, the optimization is simplified by neglecting fiber interaction. Motivated by this, we consider here the relatively simple but nontrivial case of a single inclusion perfectly embedded into an unbounded

Keywords: plane elasticity problem, Kolosov–Muskhelishvili potentials, shape optimization, effective energy, extremal elastic structures, genetic algorithm.

and homogeneous medium that maintains at infinity the elastic fields $\sigma_{xx}^\infty = P$, $\sigma_{yy}^\infty = Q$, $\sigma_{xy}^\infty = 0$. The exact formulation reads:

Given the single inclusion matrix topology, uniform static far-field loading, and the elastic properties of both materials, find from among all admissible continuous curves the interface shape that minimizes the ratio of the induced energy increment δW to the inclusion area.

For definiteness, the applied stresses are usually taken as either bulk load, that is, $P = Q$, or pure shear, that is, $P = -Q$. The first case is much simpler than the second. For the bulk load, one may use the principle of equestress boundary [Cherepanov 1974; Vigdergauz 1989] to reduce the matrix-inclusion interaction along the optimal interface to a uniform normal pressure. The energy-minimizing inclusion is then a circle regardless of elastic moduli of the phases. This principle does not apply to anisotropy induced by shear loading. Instead, one may resort to a complex variable technique to perform semianalytical optimization in the limiting cases of a hole [Vigdergauz and Cherkayev 1986; Vigdergauz 2006] and infinitely-rigid inclusion [Vigdergauz 2007]. Numerically, this approach leads to a resolving system of linear algebraic equations with closed form coefficients obtained through the following steps:

- (i) The biharmonic Airy function in the matrix region is equivalently replaced with a pair of complex-valued holomorphic functions, the Kolosov–Muskhelishvili potentials [Muskhelishvili 1975].
- (ii) This region is conformally mapped onto the exterior of a circle with the Laurent terms of the mapping function serving as the optimizing design variables. In practice, they are necessarily truncated after a small number of nonzero terms.
- (iii) As a result, the KM potentials are transformed into new holomorphic functions which are then expanded outside the circle into orthogonal Laurent series.
- (iv) Finally, satisfying the boundary conditions (zero tractions for a hole, or zero displacements for a rigid inclusion) gives the required system in the KM expansion coefficients. Due to the basis orthogonality, a finite term mapping gives *exactly* a finite size system, with the closed form entries linearly expressed through the Laurent mapping terms and integers [Vigdergauz and Cherkayev 1986; Vigdergauz 2006; 2007].

Both resulting shapes look like a slightly rounded square. For the optimal hole, the square is aligned with the main stresses P , Q , whereas, for the optimal rigid inclusion, it is rotated from them by 45 degrees.

An *elastic* inclusion involves a second pair of the KM potentials, those *inside* the inclusion. Both pairs are linked through the perfect contact conditions along the interface and hence are to be treated together. It is well known, however, that no curve can have its inner and outer domains mapped simultaneously. For this reason, the third step above becomes impossible and hence the whole scheme cannot be applied, at least straightforwardly.

Shenfeld et al. [2005] proposed an alternative approach for use with a direct FEM solver with adaptive meshing. They performed a reanalysis inside using a specially tailored conjugate gradient method. This combination appears to perform well only for a hole or for a rather rigid inclusion; otherwise, the process fails to converge. The genetic algorithm [Vigdergauz 2001], though highly effective for a hole, suffers otherwise from the same drawback. Both schemes define the shape through a large number of equally spaced nodal points, which are then taken as design variables.

This suggests reconsidering the more economical representation achieved by the above mapping scheme and adapting its third step for elastic inclusions. The untransformed potentials should be directly expanded in their *physical domains* in a nonorthogonal basis, and the conformal mapping should serve only to parameterize the shape. This modification alters the prior numerical performance in two ways, both stemming from the allowed nonorthogonality. The resolving system remains *infinite* for a finite-term mapping, but the closed forms for its coefficients now involve *infinite* sums. All other advantages of the complex-variable approach remain. It permits developing a stable and sensitive optimization scheme that is in line with the approach used for the limiting cases of a hole and a rigid inclusion. The corresponding values of the energy minimum are used as a benchmark to control the computations. Importantly, both cases converge rapidly after increasing the number of mapping terms: even the one term approximation error is less than 0.36% (see Table 1 as extracted from [Cherkaev et al. 1998] and [Vigdergauz 2006]). The error should decrease further for elastic inclusions having less contrast shear moduli. In other words, the simplest possible configuration provides acceptable accuracy at rather low computational cost. For these reason, we concentrate here on this one term scheme and obtain detailed optimization results for all admissible values of the elastic parameters.

The paper is structured as follows. Section 2 formulates the elastostatic boundary value problem for the matrix-inclusion layout. On this basis, the scheme for analytically assessing the energy increment dependence of the inclusion shape is developed in Section 3 and Section 4 with some details moved to Appendix A and Appendix B. Section 5 develops the optimization's computational framework. In Section 6, the proposed scheme is validated by comparing the simulation results with the limiting cases' exact solutions. We present and discuss the numerical results in Section 7 and summarize the main findings in Section 8.

2. Complex variable formulation of plane elasticity

2.1. The forward problem in a bimaterial structure. Figure 1 shows the two phase arrangement in an infinite plate S with an interface L enclosing the origin of the Cartesian system (x, y) . Here and throughout, we use the indexes $j = 1$ and $j = 2$ to identify the inclusion the matrix, respectively. The curve L divides the plate in two parts S_1 and $S_2 = S - S_1$. To each we associate isotropic and homogeneous phases with planar shear moduli μ_j and Poisson ratios ν_j .

To begin, remotely load the plane by an asymptotically uniform stress tensor σ^∞ with components

$$\sigma_{xx}^\infty = P, \quad \sigma_{yy}^\infty = Q, \quad \sigma_{xy}^\infty = 0. \quad (1)$$

Define $z = x + iy$ to be the complex variable in the plane S . Then the inclusion distorted field $\sigma = \{\sigma_{xx}, \sigma_{yy}, \sigma_{xy}\}$ is linearly expressed at any point $z \in S$ through the first two derivatives of the coupled KM analytical potentials $\varphi_j(z)$ and $\psi_j(z)$, which are defined in the subdomains S_j [Muskhelishvili 1975]. For $z \in S_j$,

$$\begin{aligned} \text{Tr}\{\sigma(z)\} &= \sigma_{xx}(z) + \sigma_{yy}(z) = 4\Re\varphi_j'(z), \\ \text{Dev}\{\sigma(z)\} &= \sigma_{yy}(z) - \sigma_{xx}(z) = 2\Re[\bar{z}\varphi_j''(z) + \psi_j'(z)], \\ \sigma_{xy}(z) &= \Im[\bar{z}\varphi_j''(z) + \psi_j'(z)]. \end{aligned} \quad (2)$$

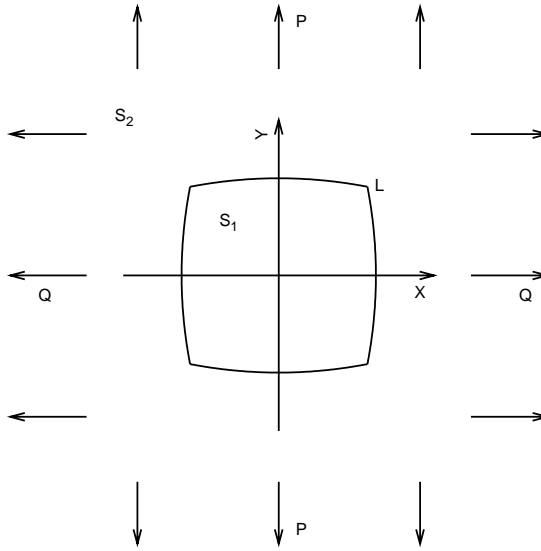


Figure 1. The problem schematic: an infinite plate with a perfectly embedded elastic inclusion under uniform stresses. The cases $P = Q$ and $P = -Q$ correspond to remote bulk and shear. The piecewise smooth hole boundary has a discrete rotational symmetry and may have a finite number of angular points.

Across the interface L , the assumed continuity of the tractions and the displacements links the boundary values of the KM potentials as [Muskhelishvili 1975]

$$\begin{aligned} \overline{\varphi_1(t)} + \bar{t}\varphi_1'(t) + \psi_1(t) &= \overline{\varphi_2(t)} + \bar{t}\varphi_2'(t) + \psi_2(t), \\ \lambda_1\overline{\varphi_1(t)} - \bar{t}\varphi_1'(t) - \psi_1(t) &= \mu_{12}[\lambda_2\overline{\varphi_2(t)} - \bar{t}\varphi_2'(t) - \psi_2(t)], \end{aligned} \quad (3)$$

where $\mu_{12} = \mu_1/\mu_2$, $\mu_2 \neq 0$, and $t \in L$. Here

$$\lambda_j = \frac{3 - \nu_j^{(\text{stress})}}{1 + \nu_j^{(\text{stress})}}, \quad \nu_j^{(\text{stress})} \in [0, 1], \quad \text{for plane stress,} \quad (4)$$

$$\lambda_j = 3 - 4\nu_j^{(\text{strain})}, \quad \nu_j^{(\text{strain})} = \frac{\nu_j^{(\text{stress})}}{1 + \nu_j^{(\text{stress})}} \in [0, 0.5], \quad \text{for plane strain.} \quad (5)$$

The unobservable negative values of ν_j are excluded from the numerical simulations (see Section 7). Then both cases $j = 1, 2$ share the interval $1 \leq \lambda_j \leq 3$. The λ_j , together with the shear moduli ratio μ_{12} , serve as unified elastic parameters of the problem.

In the limiting cases of a hole ($\mu_{12} = 0$) or an infinitely rigid inclusion ($\mu_{12} \rightarrow \infty$), the contact relations Equation (3) degenerate to one condition of zero tractions or zero displacements, respectively

[Muskhelishvili 1975]:

$$\begin{aligned}\overline{\varphi_2(t)} + \bar{t}\varphi_2'(t) + \psi_2(t) &= 0, & \text{for a hole,} \\ \lambda_2\overline{\varphi_2(t)} - \bar{t}\varphi_2'(t) - \psi_2(t) &= 0, & \text{for a rigid inclusion.}\end{aligned}$$

For reference, we note that the second goes into the first by formally putting $\lambda_2 = -1$. This is the Dundurs correspondence [Jasiuk 1995]. This fact makes it possible to express the matrix side stresses on L in a form not involving the second potential $\psi_2(t)$ [Vigdergauz 2007], as

$$\begin{aligned}\sigma_{\rho\rho}(t) &= (\lambda_2 + 1)\Re\varphi_2'(t), \\ \sigma_{\theta\theta}(t) &= (3 - \lambda_2)\Re\varphi_2'(t), \\ \sigma_{\rho\theta}(t) &= (\lambda_2 + 1)\Im\varphi_2'(t),\end{aligned}\tag{6}$$

where $t = \rho e^{i\theta} \in L$. The local von Mises equivalent stresses $\sigma_M^2 = (\sigma_{\rho\rho} + \sigma_{\theta\theta})^2 + \sigma_{\rho\theta}^2 - 3\sigma_{\rho\rho}\sigma_{\theta\theta}$ at t can also be combined from Equation (6) in similar fashion, so that

$$\begin{aligned}\sigma_M^2(t) &= D_1(\lambda)(\Re\varphi_2'(t))^2 + D_2(\lambda)(\Im\varphi_2'(t))^2, \\ D_1(\lambda) &= 7 - 6\lambda + 3\lambda^2, \\ D_2(\lambda) &= 3(1 + \lambda)^2.\end{aligned}\tag{7}$$

Of course, at $\lambda_2 = -1$ the above relations transform into the traction-free conditions $\sigma_{\rho\rho}(t) = \sigma_{\rho\theta}(t) = 0$.

Finally, homogeneous loads (1) yield the far field asymptotics

$$\begin{aligned}\varphi_2(z) &= Bz + a_1^{(2)}z^{-1} + O(|z|^{-2}), \\ \psi_2(z) &= \Gamma z + b_1^{(2)}z^{-1} + O(|z|^{-2}), \\ 4B &= \text{Tr}\{\sigma^\infty\} = P + Q, \\ 2\Gamma &= \text{Dev}\{\sigma^\infty\} = Q - P.\end{aligned}\tag{8}$$

At the chosen bimaterial topology, the initial problem of finding the local stresses and strains is equivalent to the homogeneous boundary value problem (3) in the analytic functions $\varphi_j(z)$, $\psi_j(z)$ with a nonzero right hand side given by Equation (8).

The normalized energy increment has the form (see for instance [Jasiuk 1995])

$$\delta W = 2\pi f_1^{-1} \left(2\Gamma a_1^{(2)} + B b_1^{(2)} \right),\tag{9}$$

where f_1 is the inclusion area. Because the stresses are linear in the far loading parameters P and Q , we have

$$a_1^{(2)} = B\alpha_{12} + \Gamma\alpha_{11}, \quad b_1^{(2)} = B\beta_{22} + \Gamma\beta_{21},$$

and hence δW possesses a convenient bilinear form in B , Γ given by

$$\delta W = 2\pi f_1^{-1} \left(2\Gamma^2\alpha_{11} + B\Gamma(2\alpha_{12} + \beta_{21}) + B^2\beta_{22} \right),\tag{10}$$

where α_{12} , β_{22} and α_{11} , β_{21} are computed at the unit trial loadings: for bulk $B = 1$, $\Gamma = 0$, and for pure shear $B = 0$, $\Gamma = 1$, respectively. Though they can be extracted only from the full-scale solution

to Equation (3) and Equation (8), such extraction requires less accuracy than optimizing, say, the local stresses. Next, we will exploit this numerical advantage further by developing a scheme for minimizing δW .

3. Developing the optimization scheme: analytical preliminaries

In our notation, the problem takes the following form:

Given the phase moduli λ_1, λ_2 , and μ_{12} , find the interface shape L that globally minimizes the energy increment of Equation (10) for pure shear ($B = 0, \Gamma = 1$):

$$\delta W(\lambda_1, \lambda_2, \mu_{12}, L) \xrightarrow{\{L\}} \min \equiv \delta W_{min}(\lambda_1, \lambda_2, \mu_{12}). \quad (11)$$

Its numerical treatment requires a nontrivial preliminary analysis which is performed below to the maximum extent.

3.1. Integral criterion for the analyticity of a function. The following development is based on the analyticity of the KM potentials, which can be represented in several equivalent forms. Most relevant here is the set of regular integrals along L as we derived previously in [Vigdergauz 2001]. For convenience, the result is presented here.

Let $\phi_1(z)$ and $\phi_2(z)$ be arbitrary analytic functions of z in S_1 and S_2 with $\phi_2(z)$ linearly growing at infinity, that is, $\phi_2(z) = C_1 z + O(z^{-1})$. Then their boundary values along L obey the following identities in the complementary domains [Gamelin 2001]:

$$J_1(z) \equiv \int_L \frac{\phi_1(t)}{t-z} dt = 0, \quad \text{for all } z \in S_2; \quad J_2(z) \equiv \int_L \frac{\phi_2(t) - C_1 t}{t-z} dt = 0, \quad \text{for all } z \in S_1. \quad (12)$$

By construction, Cauchy-type integrals such as Equation (12) are always analytic [Gamelin 2001]. The Cauchy identity is commonly used for transforming functions into a boundary form with a singularity

$$\begin{aligned} J_1(t_0) &= \frac{1}{2} \phi_1(t_0) + \frac{1}{2\pi i} \int_L \frac{\phi_1(t)}{t-t_0} dt = 0, \\ J_2(t_0) &= \frac{1}{2} (\phi_2(t_0) - C_1 t_0) - \frac{1}{2\pi i} \int_L \frac{\phi_2(t) - C_1 t}{t-t_0} dt = 0, \end{aligned} \quad (13)$$

where $t_0 \in L$, and L is traversed counterclockwise. When L satisfies some minimal smoothness requirements, Equation (12) and Equation (13) are equivalent [Gamelin 2001].

To avoid the boundary singularity, we can use alternatively the analyticity property that implies $J_1(z)$ and $J_2(z)$ remain zero everywhere if they vanish in the circular subdomains $|t/z| < 1$ for $z \in S_2$ and $|z/t| < 1$ for $z \in S_1$. We expand the Cauchy kernel $(t-z)^{-1}$ in the convergent powers series

$$\begin{aligned} \frac{1}{t-z} &= -\frac{1}{z} \sum_{k=0}^{\infty} \frac{t^k}{z^k}, & \left| \frac{t}{z} \right| < 1, & \quad z \in S_2, \\ \frac{1}{t-z} &= \frac{1}{t} \sum_{k=0}^{\infty} \frac{z^k}{t^k}, & \left| \frac{z}{t} \right| < 1, & \quad z \in S_1, \end{aligned} \quad (14)$$

and substitute Equation (14) into Equation (12). Requiring each term vanish yields equivalent sets of resolving identities:

$$\int_L \phi_1(t)t^k dt = 0, \quad \int_L \phi_2(t)t^{-k-1} dt = C_1 \delta_{k,1}, \quad (15)$$

where $k = 0, 1, 2, \dots$ and $\delta_{j,k}$ is the Kronecker delta.

These regular integrals have numerical advantages over their more frequently used singular counterparts of Equation (13).

3.2. Inclusion shape representation.

3.2.1. A circular inclusion. The elastostatic problem of Equation (3) and Equation (8) has a unique solution [Muskhelishvili 1975], at least for any piecewise smooth inclusion shape L . The shape is therefore the only factor influencing the overall numerical difficulty. For instance, a circle $|t| = 1$, $f_1 = \pi$ gives a finite form solution

$$\begin{aligned} \varphi_1(z) &= \frac{\mu_{12}(\lambda_2 + 1)}{2\mu_{12} + \lambda_1 - 1} Bz, & \psi_1(z) &= \frac{\mu_{12}(\lambda_2 + 1)}{1 + \mu_{12}\lambda_2} \Gamma z, \\ \varphi_2(z) &= Bz + \Gamma \alpha_{11} z^{-1}, & \psi_2(z) &= \Gamma z + B\beta_{22} z^{-1} + \Gamma \alpha_{11} z^{-3}, \\ \alpha_{11} &= \frac{\mu_{12} - 1}{1 + \mu_{12}\lambda_2}, & \beta_{22} &= \frac{\mu_{12}(\lambda_2 - 1) - \lambda_1 + 1}{2\mu_{12} + \lambda_1 - 1}, \\ & & \alpha_{21} &= \beta_{12} = 0, \end{aligned}$$

with the energy increment of Equation (10) becoming

$$\delta W_{\text{circle}} = 2B^2 \frac{\mu_{12}(\lambda_2 - 1) - \lambda_1 + 1}{2\mu_{12} + \lambda_1 - 1} + 4\Gamma^2 \frac{\mu_{12} - 1}{1 + \mu_{12}\lambda_2}. \quad (16)$$

It is worth noting that the inclusion potentials $\varphi_1(z)$ and $\psi_1(z)$ are linear in z , and hence, in view of Equation (2), both trial loadings induce a similar constant stress tensor inside a circle $|z| \leq 1$. For bulk loading,

$$\text{Tr}\{\sigma^\infty\} = B = 1, \quad \text{Dev}\{\sigma^\infty\} = \Gamma = 0, \quad (17)$$

$$\implies \text{Tr}\{\sigma(z)\} = 4 \frac{\mu_{12}(\lambda_2 + 1)}{2\mu_{12} + (\lambda_1 - 1)}, \quad \text{Dev}\{\sigma(z)\} = 0, \quad \sigma_{xy}(z) \equiv 0, \quad (18)$$

whereas, for pure shear,

$$\text{Tr}\{\sigma^\infty\} = B = 0, \quad \text{Dev}\{\sigma^\infty\} = \Gamma = 1, \quad (19)$$

$$\implies \text{Tr}\{\sigma(z)\} = 0, \quad \text{Dev}\{\sigma(z)\} = 2 \frac{\mu_{12}(\lambda_2 + 1)}{1 + \mu_{12}\lambda_2}, \quad \sigma_{xy}(z) \equiv 0. \quad (20)$$

The similarity between the remote and inclusion fields is important in the optimization context. Due to the *isotropy* of $\sigma(z)$ in Equation (17), a circle provides the global minimum for δW under *isotropic* bulk loading [Vigdergauz 1989]. In contrast, it remains unknown whether the *full anisotropy* of $\sigma(z)$ in

Equation (19) provides the energy minimum under *anisotropic* pure shear. Numerical evidence relevant to this question is discussed in Section 7.

3.2.2. A general shape. Other shapes can be treated only numerically. Within the complex variable formulation, a typical numerical scheme consists of four consecutive steps:

- (i) transforming the problem Equation (3) with (8) into singular integral equations for the complex-valued density function $\chi(t)$, $t \in L$ along the material's interface. Discussed by Greengard and Helsing [1998], the idea dates back to Sherman [1959];
- (ii) converting the equation into an infinite system of linear algebraic equations in the Fourier amplitudes of $\chi(t)$:

$$\chi(t) = \sum_{k=1}^{\infty} a_k t^k + b_k t^{-k};$$

- (iii) solving numerically the truncated system;
- (iv) restoring the finite-term approximation for the potentials by integrating $\chi(t)$ and related quantities over L . Here, the difficulties are transferred to stage (ii) because the system coefficients involve hard-to-compute integrals of rapidly oscillating functions along L .

For stage (ii), Greengard and Helsing [1998] use the fast multipole method, an adaptive quadrature technique, and other advanced procedures to achieve impressive results in computing the stress field for a generally shaped interface. Clearly, the algorithm works much faster for a smooth shape when the time-consuming integration over singularities can be simplified without loss of accuracy to the trapezoidal rule.

In numerical experiments, Greengard and Helsing [1998] parameterize the interface shape using a Fourier series over a unit circle γ :

$$t = \sum_{k=1}^{\infty} g_k \xi^k + h_k \xi^{-k}, \quad (21)$$

where $t \in L$, $\xi = e^{i\eta} \in \gamma$, and $0 \leq \eta \leq 2\pi$. This is exemplified by the *nine-armed* contour:

$$\begin{aligned} t &= 0.36(1 + 0.36 \cos 9\eta)e^{i\eta} = g_1 \xi + g_{10} \xi^{10} + h_8 \xi^{-8}, \\ g_1 &= 0.36, \quad g_{10} = h_8 = 0.18, \end{aligned} \quad (22)$$

where all other g_i and h_i vanish. Greengard and Helsing [1998] calculated numerically the integral-type coefficients of the resolving algebraic system in stage (ii). However, for on-circle parameterizations such as Equation (22), we can obtain the coefficients analytically, using the residue technique [Gamelin 2001]. This feature could save time in analyzing structures modified repeatedly. However, computations (not reported here) show the optimization process has an instability caused by the simultaneous presence of high positive and negative powers of the polar angle Fourier series such as those in Equation (22).

Matters can be substantially improved by presenting the inclusion shape through the boundary values of an analytic mapping function $\omega(\zeta)$ that behaves asymptotically as $C\zeta + o(1)$ and has only negative powers:

$$t = \omega(\theta) = C\tau + \sum_{k=1}^{\infty} d_k \tau^{-k}. \quad (23)$$

$\omega(\zeta)$ maps conformally the region $\Sigma_2 : |\zeta| \geq 1$ outside the unit circle onto the matrix domain S_2 outside L , with correspondence of the infinity point. Without loss of generality, we suppose that $C = 1$ and the coefficients $\{d_k\}$ are real.

In Equation (21) and (23) we use different notations for the circle points to clarify the following. At first glance, (23) might appear to be a only subset of (21) narrowed by dropping the coefficients g_k for $k > 1$. On the contrary, the complex analysis implies that any closed continuous curve can be written in either of the two forms even though there is no pointwise correspondence between them. Actually, both parameterizations are linked through the identity

$$t = \sum_{k=1}^{\infty} g_k \xi^k + h_k \xi^{-k} = \tau(\xi) + \sum_{k=1}^{\infty} d_k \tau(\xi)^{-k},$$

using the transformation function $\tau = \tau(\xi)$ and requiring $|\tau| = |\xi| = 1$. Unfortunately, such $\tau(\xi)$ is not easy to find, even for only one nonzero coefficient $g_k, k > 1$, as in Equation (22). However this is not our aim here. Instead, we truncate the representation (23) after M terms:

$$\omega(\zeta) = \zeta + \sum_{k=1}^M d_k \zeta^{-k},$$

where $|\zeta| \geq 1$. The expansion coefficients serve as design variables in our previous papers [Vigdergauz 2006; 2007] for the limiting cases of a hole or rigid inclusion. This leads to a novel direct problem solver which is rather fast and stable and can be repetitively used in a successive shape optimization algorithm over the set $C_M(d_1, \dots, d_M)$ of the M -term conformal images of γ . An additional computational option is a p -fold rotational symmetry of the inclusion $\omega(\exp(2i\pi/p)\zeta) = \exp(2i\pi/p)\omega(\zeta)$ in which only the coefficients $\{d_{pk-1}, k = 1, 2, \dots\}$ differ from zero. Here,

$$\omega(\zeta) = \zeta + \sum_{k=1}^M d_{pk-1} \zeta^{-(pk-1)}. \quad (24)$$

In these design variables, the mapping terms possess several useful properties that diminish the problem's computational burden. First, they are subject to successfully narrowing bilateral estimations

$$-\frac{1}{\sqrt{m}} \leq d_m \leq \frac{1}{\sqrt{m}}, \quad m = 1, 2, \dots, \quad (25)$$

that follow from the nonnegativeness of the area f_1 inside γ [Gamelin 2001]

$$f_1 = \pi \left(1 - d_1^2 - 2d_2^2 - \dots - nd_n^2 \right) \geq 0.$$

Second, they are *naturally* ordered, in that the higher the coefficient, the lesser its global impact on the inclusion shape (see Table 1). This argument parallels the fact that the set C_M contains a diverse pool of closed continuous curves even at very small values of M . For instance, the one-term mapping $\omega(\zeta) = \zeta + d_1 \zeta^{-1}$ presents the full family of axes-aligned ellipses with eccentricity $|d_1| \leq 1$, a widely modeled inclusion shape in elasticity studies. Their square symmetric counterparts are exemplified in Figure 2. Finally, as already mentioned, the residue technique routinely gives the integrals of Equation (15) in closed form.

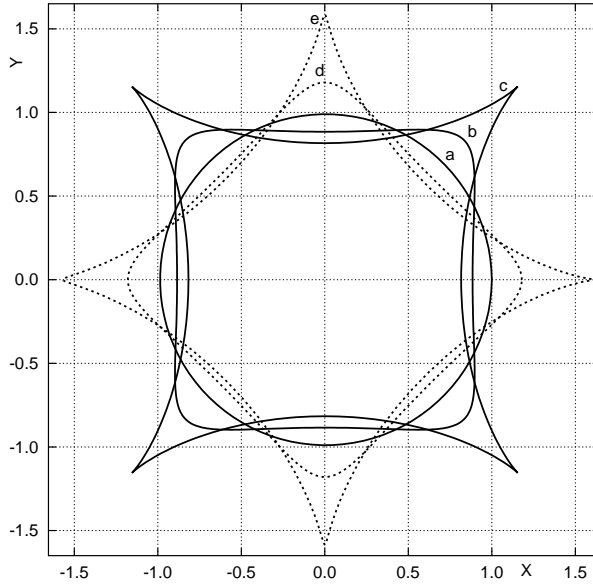


Figure 2. Square symmetric shapes generated from a circle by the one-term mapping $\omega(\zeta) = \zeta + d_3\zeta^{-3}$ for $d_3 = 0$ (a), $d_3 = \mp 0.21$ (b, d, respectively), $d_3 = \mp 1/3$ (c, e). The latter curves present the limiting case of 4-cusped hypocycloids with entrant angles.

In concluding, we note that the first derivative of a single-valued mapping can vanish only inside γ [Gamelin 2001]. For the one-term function $\omega(\zeta) = \zeta + d_m\zeta^{-m}$, that $\omega'(\zeta) = 1 - md_m\zeta^{-m-1} = 0$ only for $|\zeta| < 1$ implies that the inequalities in Equation (25) are sharpened to

$$-\frac{1}{m} \leq d_m \leq \frac{1}{m}.$$

To our knowledge, this has not yet been noticed in the literature.

	Hole [Cherkaev et al. 1998]	Rigid inclusion [Vigdergauz 2006]			
	$\lambda_2 = -1$	$\lambda_2 = 3$	$\lambda_2 = 2$	$\lambda_2 = 1.4$	$\lambda_2 = 1$
N=1	3.6E-03	1.0E-04	4.5E-04	1.5E-03	3.6E-03
N=2	7.7E-04	6.2E-06	5.3E-05	2.6E-04	7.7E-04
N=3	2.5E-04	6.9E-07	1.1E-05	7.1E-05	2.5E-04
N=4	9.6E-05	9.9E-08	2.8E-06	2.0E-05	9.6E-05
N=5	3.1E-05	1.5E-08	6.5E-07	1.7E-06	3.1E-05

Table 1. The limiting cases: the relative error $(\delta W(N)/\delta W(6) - 1)$ of the minimum energy increment versus the number of the first nonzero mapping terms, N . The value $\delta W(6)$ is nearly exact. The outside error columns coincide due to the Dundurs correspondence.

4. The one-potential solving scheme

We are now in a position propose a scheme for solving the forward elastostatic problem. First, we note that the previous section's stage (i) for deriving the singular integral equation is redundant. The contact conditions Equation (3) can be directly transformed into an infinite set of regular integrals along L that involve only the first potentials $\varphi_{1,2}(t)$. This set serves as a pattern for obtaining a resolving system algebraic equations such as those in stage (ii).

Here we use that, in contrast to $\varphi_{1,2}(z)$, the second potentials $\psi_{1,2}(z)$ appear in the boundary conditions of Equation (3), and they are neither conjugated nor differentiated. This makes it possible to separate the potentials and hence to economically find them in sequence rather than in parallel. In doing so, we first exclude $\psi_{1,2}(z)$ from consideration. Solving the algebraic relations of Equation (3) for them, we have

$$(1 - \mu_{12}) \psi_1(t) = (\lambda_1 + \mu_{12}) \overline{\varphi_1(t)} - (1 - \mu_{12}) \bar{t} \varphi_1'(t) - \mu_{12} (1 + \lambda_2) \overline{\varphi_2(t)}, \quad (26)$$

$$(1 - \mu_{12}) \psi_2(t) = (1 + \lambda_2) \varphi_1(\bar{t}) - (1 - \mu_{12}) \bar{t} \varphi_2'(t) - (1 + \lambda_2 \mu_{12}) \varphi_2(\bar{t}). \quad (27)$$

Inserting the right-hand sides of Equation (26) as integrands for the analyticity conditions in Equation (15) and making use of Equation (8), we arrive at an infinite set of identities in $\varphi_{1,2}(z)$. In the second step, we evaluate the resultant integrals involving the boundary values of $\varphi_{1,2}(z)$ and their first derivatives multiplied by powers of t . With Equation (8), we simply expand the sought-for functions in converging series inside and outside L :

$$\varphi_1(z) = \sum_{m=1}^{\infty} a_m^{(1)} z^m, \quad \varphi_2(z) = B + \sum_{m=1}^{\infty} a_m^{(2)} z^{-m}(z). \quad (28)$$

Their substitution results finally in the infinite system of algebraic equations in $a_m^{(1,2)}$, where only the unknown $a_1^{(2)}$ is required for finding the energy increment δW at pure shear when, in conformity with Equation (10),

$$\delta W = 4\pi f_1^1 \Gamma^2 \alpha_{11}. \quad (29)$$

Here again, $\alpha_{11} = a_1^{(2)}$ at $B = 0$ and $\Gamma = 1$.

Some local characteristics of the resultant stress field can be evaluated without the second potential $\psi_{1,2}(z)$. For instance, in view of Equation (2), the trace $\text{Tr}\{\sigma(t)\}$ along the inclusion-matrix interface has a form involving only the potential $\varphi_{1,2}(t)$. However, in contrast to the integral relation of Equation (29) for δW , here the remaining unknowns $a_k^{(1,2)}$ also enter in the resultant expressions through Equation (28). Numerically, this manifests in high frequency oscillations about the true values (the Gibbs phenomenon) as exemplified in Section 6.

In the optional final step, the second potential $\psi_{1,2}(z)$ can be immediately computed through Equation (26), if we are interested in the individual local stresses of Equation (2).

5. The computational framework

In computational practice, the infinite resolving system is truncated to a finite size as

$$\begin{pmatrix} -(\lambda_2 \mu_{12} + 1) A_{11}^{(0)} - (1 - \mu_{12}) A_{11}^{(1)} & (\lambda_1 + \mu_{12}) A_{12} \\ -\mu_{12} (1 + \lambda_2) A_{21} & (1 + \lambda_2) A_{22}^{(0)} - (1 - \mu_{12}) A_{22}^{(1)} \end{pmatrix} X = B, \quad (30)$$

where the A_{ij} are $N \times N$ matrices whose elements are linear in the boundary integrals

$$J_{m,n}^{(1)} = \frac{1}{2\pi i} \int_L t^m \bar{t}^n dt, \quad J_{m,n}^{(2)} = \frac{1}{2\pi i} \int_L t^{m+n} \bar{t} dt, \quad (31)$$

where $m, n = \pm 1, \pm 2, \dots$ and there are no elastic constants involved. The $(2N)$ -element vector of unknowns takes the form

$$X = (a_1^{(2)}, a_2^{(2)}, \dots, a_N^{(2)}, a_1^{(1)}, a_2^{(1)}, \dots, a_N^{(1)}).$$

For pure shear, the right-hand side B has zeroes in all places but the first, which is equal to $(1 - \mu_{12})$. When $\mu_{12} = 1$, the homogeneous system Equation (30) returns all unknowns as zero. Physically, this is because the far-field shear stress is not disturbed by any inclusion shape if both materials have the same shear modulus. Further, when the moduli are almost the same with $\mu_2 = \mu_1 + \varepsilon$, $\|\varepsilon\| \ll 1$, the first order ε -approximation of δW is independent of the inclusion shape, as proven analytically in Appendix A.

In the general case, the system Equation (30) must be treated numerically. Though only the first unknown $a_1^{(2)}$ is required for finding the energy increment, we prefer finding the full vector X for control purposes. We solve the system using the standard LU -decomposition with iterative refinement. This requires $8N^3/3 + 2N^2 + N$ operations which are performed for better accuracy in double-precision arithmetic.

However, in the entire computation, the most time-consuming stage is evaluating the integrals of Equation (31). As already mentioned, this is done analytically by summing the residues at the integrand poles. Deriving the needed expressions involves complicated algebra, especially if the mapping has multiple terms. As a technical simplification, we consider here only a one-term mapping as Equation (24) for the p -fold rotational symmetry: $\omega(\zeta) = \zeta + d_{p-1}\zeta^{-p+1}$. The optimization problem of Equation (11) then becomes

$$\delta W(\lambda_1, \lambda_2, \mu_{12}, d_{p-1}) \xrightarrow{\{d_{p-1}\}} \delta W_{min}(\lambda_1, \lambda_2, \mu_{12}), \quad (32)$$

where

$$f_1 = 1 - (p-1)d_{p-1}^2, \quad -\frac{1}{p-1} \leq d_{p-1} \leq \frac{1}{p-1}. \quad (33)$$

Single-term expressions for the integrals are given in Appendix B. The shape optimization over d_{p-1} in the interval in Equation (33) is then performed by the standard GA scheme with a 32-bit representation of random numbers.

At first glance, the problem Equation (32) with Equation (33) is disappointingly simple compared to the initial formulation in the Introduction. We emphasize again that our choice is justified quantitatively by the accurate one-term results displayed in Table 1 for the limiting cases with the most contrasting shear moduli. Though it does not capture the optimum's fine details, already this approximation leads to nontrivial results not yet reported in the literature.

6. Numerical validation of the optimization scheme

In this section, we assess the performance of the proposed approach by comparing it against the one-term exact solutions. They are known for the limiting cases of the hole and rigid inclusion [Vigdergauz 2007].

Apparently, the optimal shapes differ from circles only for square symmetry ($p = 4$):

$$\begin{aligned} \delta W_3 &= \frac{\lambda_2}{(\lambda_2 + d_3)(1 - 3d_3^2)}, & d_3^{(min)} &= \frac{\sqrt{\lambda_2^2 + 1} - \lambda_2}{3}, \\ \min_{d_3} \delta W_3 &= \frac{9\lambda_2}{2(2\lambda_2 + \sqrt{\lambda_2^2 + 1})(1 - \lambda_2^2 + \lambda_2\sqrt{\lambda_2^2 + 1})}, \\ \varphi_2(\tau) &= -\frac{\tau^2}{(\lambda_2 + d_3)(1 - d_3\tau^4)}, \quad \text{where } \tau = e^{i\theta} \in \gamma, \end{aligned} \quad (34)$$

and where the negative value of the radical $\sqrt{\lambda_2^2 + 1}$ is taken for the hole with $\lambda_2 = -1$.

We first use these analytical results to choose a compromise value for N in the truncated system of Equation (30)), so that a reasonably accurate energy assessment can be obtained at a moderate computational cost. As N increases, Table 2 shows the convergence to the exact value of $\min \delta W_3$. We take $N = 24$ for further computations. This relatively large number is the price paid for using the nonorthogonal expansions of Equation (28).

As could be expected, the local von Mises stresses Equation (7) are computed less accurately than the energy increment because of the oscillations around the exact values (see Figure 3, Figure 4). These oscillations are caused not only by the nonorthogonal expansion basis Equation (28) but also by truncating the resolving infinite system to a finite size. The net effect of the truncation on the oscillations is nicely shown in [Cherkaev et al. 1998], where the transformed KM potentials are orthogonally expanded outside a unit circle. We note that the oscillations are not eliminated completely by increasing N . Only the analytical solution of the infinite system by finite differences [Vigdergauz 2006; 2007] yields in the limiting cases the exact results of the type in Equation (34). Alternatively, the oscillations can be mitigated using filter techniques (see, for example, Laverty and Gazonas [2006]). This subject deserves a separate study.

	Hole $\lambda_2 = -1$		Rigid inclusion			
	δW	E_{rel}	$\lambda_2 = 2$	$\lambda_2 = 1.4$	δW	E_{rel}
	0.931980515		0.980355859		0.962041131	
$N = 6$	0.916266066	$< 1.7 \times 10^{-2}$	0.980330084	$< 2.6 \times 10^{-5}$	0.960521619	$< 1.6 \times 10^{-3}$
$N = 12$	0.931497017	$< 5.2 \times 10^{-4}$	0.980355816	$< 4.4 \times 10^{-9}$	0.962031339	$< 1.0 \times 10^{-5}$
$N = 18$	0.931913140	$< 7.2 \times 10^{-5}$	0.980355859	$< 1.3 \times 10^{-10}$	0.962040784	$< 3.6 \times 10^{-7}$
$N = 24$	0.931967450	$< 1.4 \times 10^{-5}$	0.980355859	$< 8.9 \times 10^{-11}$	0.962041116	$< 1.6 \times 10^{-8}$
$N = 30$	0.931977621	$< 3.1 \times 10^{-6}$	0.980355859	$< 5.0 \times 10^{-14}$	0.962041131	$< 2.4 \times 10^{-10}$

Table 2. The limiting cases of a hole and a rigid inclusion: the energy minima and their relative deviations from the exact value of Equation (34), as computed for different half-sizes of the resolving system (30) for the one-term square symmetric mapping.

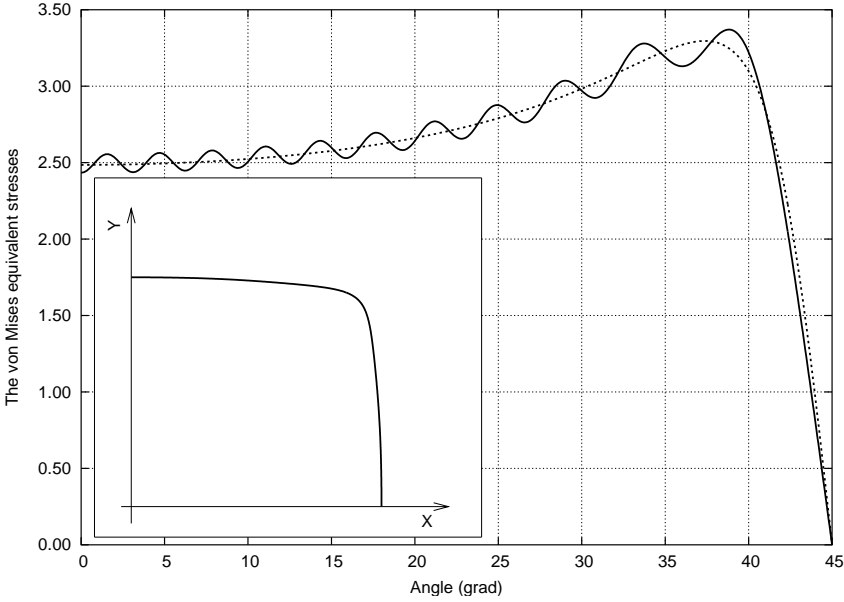


Figure 3. The angular distribution of the von Mises stresses $\sigma_M(t)$ along a quarter of the δW -optimal hole shown in the inset. The computed values stand against the exact result (the dotted line).

7. Numerical results

In the main body of the numerical simulations we detail the dependence of the energy minimum on the elastic parameters of both materials, as seen in the right hand side of Equation (32). To this end, we replace the problem Equation (32) by the three-parameter subproblems ($1 \leq \lambda_{1,2} \leq 3$)

$$\begin{aligned} \delta W(\lambda_1, \lambda_2, \mu_{12}, d_{p-1}) &\xrightarrow{\min\{\lambda_1\}, \min\{\lambda_2\}, \min\{d_{p-1}\}} \delta W_m(\mu_{12}), \\ \delta W(\lambda_1, \lambda_2, \mu_{12}, d_{p-1}) &\xrightarrow{\max\{\lambda_1\}, \max\{\lambda_2\}, \min\{d_{p-1}\}} \delta W_M(\mu_{12}), \end{aligned} \quad (35)$$

which are solved separately over the discrete set of values $0 < \mu_{12} < 1$ when the inclusion is softer than the matrix, and $0 < \mu_{21} \equiv \mu_{12}^{-1} < 1$ when the inclusion is harder than the matrix. It is of interest that the computed minima of Equation (35) are attained at the *endpoints* of the interval for $\lambda_{1,2}$. This is displayed in Table 3, together with the reference points $\delta W_{m,M}(\lambda_2, \mu_{12})$ for $\mu_{12} = 0, 1, \infty$, which are already known from Equation (34). Recall that $\lambda_{1,2} = 1$ describes an incompressible material.

	$\mu_{12} = 0$	$0 < \mu_{12} < 1$	$\mu_{12} = 1$	$\mu_{12} \geq 1$	$\mu_{12} = \infty$
δW_m	0.931980515...	$\lambda_1 = 3, \lambda_2 = 1$	0.0	$\lambda_1 = 1, \lambda_2 = 1$	0.931980515...
δW_M	0.931980515...	$\lambda_1 = 1, \lambda_2 = 3$	0.0	$\lambda_1 = 3, \lambda_2 = 3$	0.990987403...

Table 3. The parameters $\lambda_{1,2}$ at which the extrema of Equation (35) are attained versus μ_{12} .

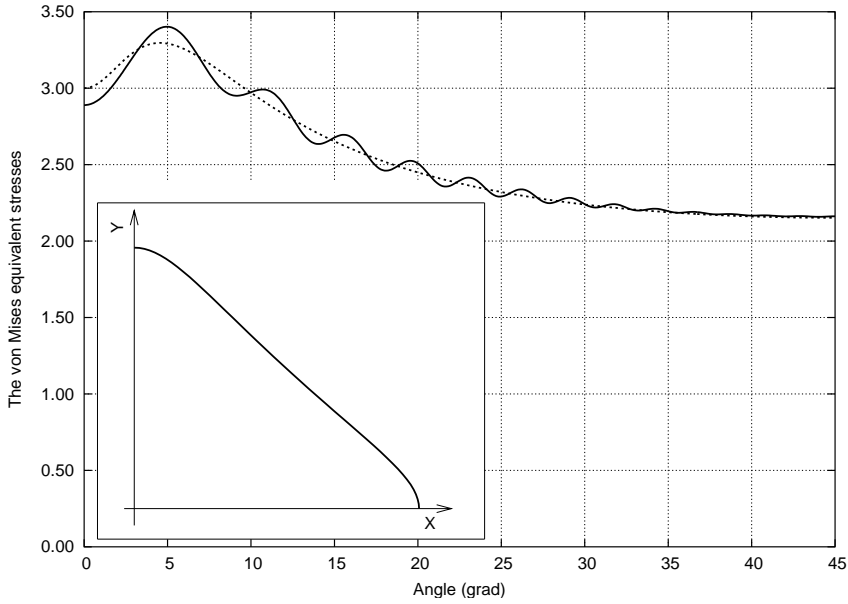


Figure 4. The angular distribution of the matrix-side von Mises stresses $\sigma_M(t)$ along a quarter of the δW -optimal rigid inclusion (shown in the inset). The computed values stand against the exact result (the dotted line).

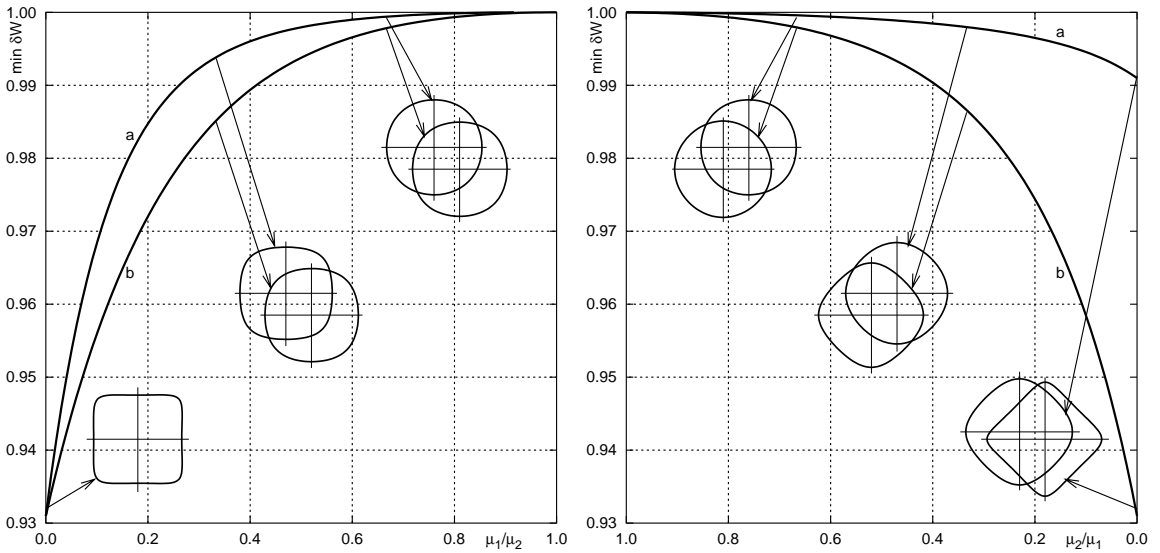


Figure 5. The attainable region of δW_{min} from Equation (36) bounded by $\delta W_M(\mu_{12})(a)$ and $\delta W_m(\mu_{12})(b)$. The evolution of the optimal inclusion shape is also shown by discrete examples.

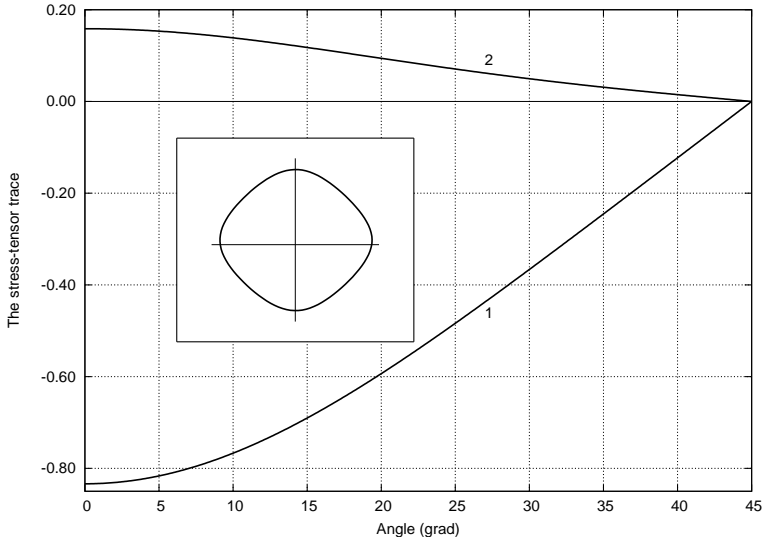


Figure 6. The angular distribution of the matrix-side (1) and inclusion-side (2) stress-tensor trace along a quarter of the δW -optimal inclusion (shown in the inset) at $\mu_{12} = 3$, $\nu_1 = \nu_2 = 0$.

The tabled information is graphed in Figure 5, which depicts the attainable region for $\delta W_{min}(\lambda_1, \lambda_2, \mu_{12})$ in the $(\delta W_{min}, \mu_{12})$ plane:

$$\delta W_m(\mu_{12}) \leq \delta W_{min}(\lambda_1, \lambda_2, \mu_{12}) \leq \delta W_M(\mu_{12}), \quad (36)$$

where $\mu_{12} \in [0, \infty)$ and $\lambda_{1,2} \in [1, 3]$. It would be interesting to know whether each point inside the bounds in Equation (36) at a given μ_{12} corresponds to a pair of Poisson ratios ν_1 and ν_2 . This question is still open, though the affirmative answer seems ‘obvious’.

Finally, Figure 6 shows the distribution of the stress-tensor trace $\text{Tr}\{\sigma(t)\}$ along the optimal inclusion shape. We note that the found local optima are extremely stable against multiple starts of the GA solver.

Three distinctive features seen in the figures support our assumption that the one-term mapping works practically for elastic inclusions.

First, Figure 5 shows that the energy bounds $\delta W_m(\mu_{12})$, $\delta W_M(\mu_{12})$ grow rapidly near the limit points $\mu_{12} = 0, \infty$. In other words, even slightly low contrast materials significantly reduce the energy optimization gain.

Next, the gain is vanishingly small in a reasonably wide vicinity of the point $\mu_{12} = 1$ of the same shear moduli so that very good accuracy is achieved with the first-order approximation of Equation (A.6) in the small parameter $(\mu_{12} - 1)$. We note that the proposed algorithm is here surprisingly stable and accurate in computing small differences between the energy values.

Finally, Figure 6 shows no oscillations in the stress distributions, as opposed to the limiting cases in Figure 3 and Figure 4. This is because the scheme converges faster for low contrast shear moduli. Hence, the local results are sufficiently accurate to conclude that the stress state inside the shear-optimal elastic inclusion has a nonzero trace, in contrast to the circular inclusion as given by Equation (19). However,

we cannot rule out that the trace gradually vanishes for multiterm mappings not considered here. Finally, we note that the optimal shape's large curvature points become less distinctive for low contrast materials (see Figure 5) and that the shape turns by 45 degrees when passing the point $\mu_{12} = 1$.

8. Concluding remarks

We present a novel numerical scheme for solving the elastic equations for a single-inclusion composite model. This scheme has distinctive features making it highly competitive against other known approaches in assessing the global strain energy and the related quantities.

First, the material interface is presented by a finite-term conformal mapping rather than by nodal points. Regardless of the elastostatic specifics, this expedient enables one to form the initial pool of shapes with a very small number of design variables and hence can be used for optimizing other physical processes in plane two-phase structures.

Next, the KM potentials are computed sequentially rather than in parallel. Finally, the boundary integrals involved are computed analytically (by the residuals) rather than numerically. This stage, though computationally effective, is the most time-consuming part of the algorithm, especially for a multiterm mapping. For this reason, repetitive calculation of the forward problem within an optimization process can be troublesome. Matters can be simplified by using the minimal one-term map which is nevertheless informative enough to provide nontrivial results not previously reported in the literature.

Appendix A: Perturbations of the energy for nearly equal shear moduli

To advance the analytical derivations, we now suppose that $\mu_1 \approx \mu_2$ or, equivalently

$$\mu_{12} = 1 + \varepsilon_\mu + \varepsilon_\mu^2 + \dots, \quad (\text{A.1})$$

where $|\varepsilon| \ll 1$. The continuous K, μ -dependence of the KM potentials allows us expand them also as perturbation series in ε_μ

$$\begin{aligned} \varphi_j(z) &= \varphi_{j,0}(z) + \varphi_{j,1}(z)\varepsilon_\mu + \dots \\ \psi_j(z) &= \psi_{j,0}(z) + \psi_{j,1}(z)\varepsilon_\mu + \dots, \end{aligned} \quad (\text{A.2})$$

where $z \in S_j$, $j = 1, 2$. Substituting (A.1) and (A.2) into Equation (3) and equating the coefficients of equal powers of ε on the left and right hand sides gives:

- (i) At zeroth order, two chained, homogeneous problems in sectionally holomorphic functions $((\lambda_1 + 1)\varphi_1(z), (\lambda_2 + 1)\varphi_2(z))$ and $(\psi_1(z), \psi_2(z))$. For $t \in L$,

$$\begin{aligned} (\lambda_1 + 1)\varphi_{1,0}(t) &= (\lambda_2 + 1)\varphi_{2,0}(t) \\ \psi_{1,0}(t) - \psi_{2,0}(t) &= \overline{\varphi_{2,0}(t)} + \bar{t}\varphi'_{2,0}(t) - \overline{\varphi_{1,0}(t)} - \bar{t}\varphi'_{1,0}(t) \end{aligned} \quad (\text{A.3})$$

with nonzero shear-type asymptotics of Equation (8). As $|z| \rightarrow \infty$,

$$\varphi_{2,0}(z) = O(|z|^{-1}), \quad \psi_{2,0}(z) = \Gamma z + O(|z|^{-1}). \quad (\text{A.4})$$

(ii) At the successive inhomogeneous higher orders, we have, for $t \in L$,

$$\begin{aligned} (\lambda_1 + 1)\varphi_{1,l}(t) - (\lambda_2 + 1)\varphi_{2,l}(t) &= F^{(l)}(t) \equiv \lambda_2\varphi_{2,l-1}(t) - \overline{t\varphi'_{2,l-1}(t)} - \overline{\psi_{2,l-1}(t)} \\ \psi_{1,l}(t) - \psi_{2,l}(t) &= \overline{\varphi_{2,l}(t)} + \overline{t\varphi'_{2,l}(t)} - \overline{\varphi_{1,l}(t)} - \overline{t\varphi'_{1,l}(t)}, \end{aligned} \quad (\text{A.5})$$

for $l = 1, 2, \dots$ and with $\varphi_{2,l}(z), \psi_{2,l}(z)$ vanishing at infinity.

In view of (A.4), the unique solution of the homogeneous problem of (A.3) is an identically vanishing $\varphi_{j,0}(z) \equiv 0$, for $z \in S_1 + S_2$ and $j = 1, 2$. Hence

$$\psi_{j,0}(z) = \Gamma z$$

for the same z and j . Substituting (A.4) into (A.5) at $l = 1$ yields the first-order boundary value problem for $\varphi_{1,2}(z)$. For $t \in L$,

$$(\lambda_1 + 1)\varphi_{1,1}(t) - (\lambda_2 + 1)\varphi_{2,1}(t) = -\Gamma\bar{t},$$

which is immediately solved through the Cauchy-type integral

$$(\lambda_j + 1)\varphi_{j,1}(z) = -\frac{\Gamma}{2\pi i} \int_L \frac{\bar{t} dt}{t - z};$$

for $z \in S_j$. This permits finding the first-order approximation for the coefficient $a_1^{(2)}$ entering into the energy increment expression Equation (9) as

$$\begin{aligned} a_{1,1}^{(2)} &= \lim_{z \rightarrow \infty} z\varphi_{2,1}(z) = \lim_{z \rightarrow \infty} \frac{\Gamma}{2\pi i(\lambda_2 + 1)} \oint_L \frac{\bar{t} dt}{1 - t/z} = \frac{\Gamma}{2\pi i(\lambda_2 + 1)} \oint_L \bar{t} dt \\ &= \frac{\Gamma}{2\pi(\lambda_2 + 1)} \oint_L (y dx + x dy) = \frac{\Gamma}{\lambda_2 + 1} f_1. \end{aligned}$$

Taking this expression into Equation (9), we see that the first-order energy increment

$$\delta W_1 = \frac{4\Gamma^2}{(\lambda_2 + 1)} (\mu_{12} - 1) \quad (\text{A.6})$$

depends neither on the inclusion shape L nor the elastic parameter λ_1 . As expected, identity (Equation (A.6)) is consistent with the asymptotic expansion δW_{circle} in Equation (16). The L -dependence of the energy thus first appears at second-order in $(\mu_{12} - 1)$.

Appendix B: Analytical evaluation of the integrals

Our aim here is show the technique for obtaining in closed form the coefficients of Equation (31) for the resolving algebraic system Equation (30). With a finite-term mapping function $t = \omega_n(\tau)$, $\tau \in \gamma$, it can be done using the binomial identities [Abramowitz 1965] to expand the integrands into convergent powers series in τ and integrating them term-by-term over a unit circle γ where the residue theorem [Gamelin 2001] gives

$$\int_{\gamma} \tau^m d\tau = 2\pi i \delta_{m,-1}, \quad (\text{B.1})$$

where $m = 0, \pm 1, \pm 2, \dots$. For concreteness, we consider next the one-term square symmetric mapping $\omega(\tau) = \tau + d_3\tau^{-3}$. Employing the generating polynomials for a nonnegative integer $m = 0, 1, \dots$ [Abramowitz 1965], we use, for $|x| < 1$,

$$(1+x)^m = \sum_{i=0}^m \binom{m}{i} x^i, \quad (1+x)^{-m-1} = \sum_{i=0}^{\infty} \binom{-m}{i} x^i,$$

where

$$\binom{m}{i} = \frac{m!}{i!(m-i)!}, \quad \binom{-m}{i} = (-1)^i \frac{(m+i)!}{m!i!}. \quad (\text{B.2})$$

We arrive at the basic expansions in powers of τ

$$(1+d_3\tau^{\pm 4})^m = \sum_{i=0}^m \binom{m}{i} d_3^i \tau^{\pm 4i}, \quad (1+d_3\tau^{\pm 4})^{-m-1} = \sum_{i=0}^{\infty} \binom{-m}{i} d_3^i \tau^{\pm 4i}. \quad (\text{B.3})$$

With Equation (B.1), substitution of (B.2)–(B.3) into Equation (31) yields separately for positive and negative indices m, n

$$\begin{aligned} J_{-m,-n}^{(1)} &= \int_L \frac{dt}{\bar{t}^{4n-3} t^{4m-2}} = \int_L \frac{\tau^{4(n-m)}(1-3d_3\tau^{-4})d\tau}{\tau(1+d_3\tau^4)^{4n-3}(1+d_3\tau^{-4})^{4m-2}} \\ &= 2\pi i (S_0 - 3d_3 S_1), \\ S_p &= \sum_{\substack{i=0,\dots,\infty \\ j=0,\dots,\infty \\ \text{s.t. } n-m+j-i=p}} \binom{-(4m-3)}{i} \binom{-(4n-4)}{j} d_3^{i+j}, \quad \text{where } p = 0, 1. \end{aligned} \quad (\text{B.4})$$

Also,

$$J_{-m,-n}^{(2)} = \int_L \frac{\bar{t} dt}{t^{4(m+n-1)}} = \int_L \frac{(1+d_3\tau^4)(1-3d_3\tau^{-4})d\tau}{\tau^{4(m+n-1)+1}(1+d_3\tau^{-4})} = 2\pi i d_3 \delta_{m+n,2}.$$

The remaining integrals are written similarly

$$\begin{aligned} J_{m,-n}^{(1)} &= \int_L \frac{t^{4m-2} dt}{\bar{t}^{4n-3}} = 2\pi i (T_0 - 3d_3 T_1), \\ T_p &= \sum_{\substack{i=0,\dots,4m-2 \\ j=0,\dots,\infty \\ \text{s.t. } m+n-i+j=p+1}} \binom{4m-2}{i} \binom{-(4n-4)}{j} d_3^{i+j}, \quad \text{where } p = 0, 1, 2, \end{aligned}$$

and

$$J_{m,n}^{(1)} = \int_L \bar{t}^{4n-1} t^{4m-2} dt = 2\pi i (V_0 - 3d_3 V_1),$$

$$U_p = \sum_{\substack{i=0, \dots, 4m-2 \\ j=0, \dots, 4n-1 \\ \text{s.t. } m-n-i+j=p}} \binom{4m-2}{i} \binom{4n-1}{j} d_3^{i+j}, \quad \text{where } p = 0, 1, 2.$$

Finally,

$$J_{m,n}^{(2)} = \int_L t^{4(m+n+1)} \bar{t} dt = 2\pi i ((1 - 3d_3^2)W_0 + d_3(W_{-1} - 3W_1)),$$

$$W_p = \sum_{\substack{i=0, \dots, 4m-2 \\ j=0, \dots, 4n-2 \\ \text{s.t. } m+n-i-j=p+1}} \binom{4m-2}{i} \binom{4n-2}{j} d_3^{i+j}, \quad \text{where } p = 0, \pm 1. \quad (\text{B.5})$$

Though seemingly cumbersome, identities (B.4)–(B.5) are easily programmed. The infinite sums involved are truncated to their first 16 terms because after that the remainder appears to be below the machine precision (16 bits). To avoid the rounding errors that can occur by using large integers, we employ double precision arithmetic and alternate multiplication with division to compute the binomial coefficients and d_3 powers.

References

- [Abramowitz 1965] M. Abramowitz, *Handbook of mathematical functions, with formulas, graphs, and mathematical tables*, edited by M. Abramowitz and I. A. Stegun, Dover, New York, 1965.
- [Bull 1996] J. W. Bull (editor), *Numerical analysis and modelling of composite materials*, edited by J. W. Bull, Blackie Academic & Professional, London, U.K., 1996.
- [Cherepanov 1974] G. P. Cherepanov, “Inverse problems of the plane theory of elasticity”, *J. Appl. Math. Mech.* **38**:6 (1974), 915–931.
- [Cherkaev et al. 1998] A. V. Cherkaev, Y. Grabovsky, A. B. Movchan, and S. K. Serkov, “The cavity of the optimal shape under shear stresses”, *Int. J. Solids Struct.* **35**:33 (1998), 4391–4410.
- [Gamelin 2001] T. W. Gamelin, *Complex analysis*, UTM series, Springer, New York, 2001.
- [Gazonas et al. 2006] G. A. Gazonas, D. S. Weile, R. Wildman, and A. Mohan, “Genetic algorithm optimization of phononic bandgap structures”, *Int. J. Solids Struct.* **43**:18-19 (2006), 5851–5866.
- [Greengard and Helsing 1998] L. Greengard and J. Helsing, “On the numerical evaluation of elastostatic fields in locally isotropic two-dimensional composites”, *J. Mech. Phys. Solids* **46**:8 (1998), 1441–1462.
- [Ibrahim et al. 1991] I. A. Ibrahim, F. A. Mohamed, and E. J. Lavernia, “Particulate reinforced metal matrix composites - a review”, *J. Mater. Sci.* **26**:5 (1991), 1137–1156.
- [Jasiuk 1995] I. Jasiuk, “Cavities vis-a-vis rigid inclusions: elastic moduli of materials with polygonal inclusions”, *Int. J. Solids Struct.* **32**:3/4 (1995), 407–422.
- [Lavery and Gazonas 2006] R. R. Lavery and G. A. Gazonas, “An improvement to the Fourier series method for inversion of Laplace transforms applied to elastic and viscoelastic waves”, *Int. J. Comput. Meth.* **3**:1 (2006), 57–69.
- [Muskhelishvili 1975] N. I. Muskhelishvili, *Some basic problems of the mathematical theory of elasticity: fundamental equations, plane theory of elasticity, torsion and bending*, 4th ed., Noordhoff, Leiden, the Netherlands, 1975.

- [Ovid'ko and Sheinerman 2005] I. A. Ovid'ko and A. G. Sheinerman, "Elastic fields of inclusions in nanocomposite solids", *Rev. Adv. Mater. Sci.* **9**:1 (2005), 17–33.
- [Shenfeld et al. 2005] V. Shenfeld, D. Givoli, and S. Vigdergauz, "Optimal shape of a grain or a fibre cross-section in a two-phase composite", *Commun. Numer. Meth. Eng.* **21**:2 (2005), 49–60.
- [Sherman 1959] D. I. Sherman, "On the problem of plane strain in non-homogeneous media", pp. 3–20 in *Non-homogeneity in elasticity and plasticity*, edited by W. Olszak, Pergamon Press, New York, 1959.
- [Vigdergauz 1989] S. B. Vigdergauz, "Piecewise-homogeneous plates of extremal stiffness", *J. Appl. Math. Mech.* **53**:1 (1989), 76–80.
- [Vigdergauz 2001] S. Vigdergauz, "Genetic algorithm perspective to identify energy optimizing inclusions in an elastic plate", *Int. J. Solids Struct.* **38**:38-39 (2001), 6851–6867.
- [Vigdergauz 2006] S. Vigdergauz, "The stress-minimizing hole in an elastic plate under remote shear", *J. Mech. Mater. Struct.* **1**:2 (2006), 387–406.
- [Vigdergauz 2007] S. Vigdergauz, "Shape optimization of a rigid inclusion in a shear-loaded elastic plane", *Journal of Mechanics of Materials and Structures = J. Mech. Mater. Struct* **2**:2 (2007), 275–292.
- [Vigdergauz and Cherkayev 1986] S. B. Vigdergauz and A. V. Cherkayev, "A hole in a plate, optimal for its biaxial extension-compression", *J. Appl. Math. Mech.* **50**:3 (1986), 401–404.

Received 10 Mar 2007. Accepted 7 May 2007.

SHMUEL VIGDERGAUZ: smuel@iec.co.il

Research and Development Division, The Israel Electric Corporation Ltd., P.O. Box 10, Haifa 31000, Israel

HOMOGENIZATION RELATIONS FOR ELASTIC PROPERTIES OF TWO-PHASE COMPOSITES USING TWO-POINT STATISTICAL FUNCTIONS

GHAZAL SAHELI, HAMID GARMESTANI AND ARUN GOKHALE

In this research we focus on studying the effect of anisotropy on the homogenization technique based on two-point statistics. We will investigate how the one-point and two-point statistical information from the microstructure can contribute in the calculation of elastic properties of isotropic and anisotropic composites. For this purpose, the homogenization relations will be studied in detail and the technique will be applied to two samples of anisotropic Al-SiC composite that were fabricated through extrusion with two different particle size ratios (PSR). The results show that two-point statistics is capable of capturing the effect of clustering of SiC particles in evaluating elastic properties for anisotropic composites. Although the two samples have the same volume fraction (difference less than 1%), the calculated elastic constants for both samples are different. The validity of the results will be investigated by direct comparison with experimental results.

1. Introduction

Materials science always looks for establishing a relationship between the internal structures of materials and their properties. In polycrystals, internal structure refers to the size and shape of crystallites (grains), the distribution of their crystallographic orientations (texture), and the spatial correlations between these geometrical and crystallographic features. However, in composites, internal structure refers to spatial correlations between geometrical features of the two phases.

The prediction of mechanical properties from details of the microstructure such as phase, crystalline grain orientation distribution, and microstructural morphology has received a special attention in the mechanics and materials community [Torquato and Stell 1982; Adams et al. 1987]. The mathematical description of heterogeneity has received some breakthroughs in the last few decades with the works [Beran 1968; Kröner 1972; 1977]. More progress has been achieved in calculating the effective properties by making simple assumptions about the microstructure distribution (random, isotropic, and periodic microstructures) or the shape of the second phase (spherical, ellipsoidal, etc.). These studies have relied primarily on the one-point probability functions (number or volume fractions of individual states within the microstructure), which ignored shape and geometric characteristics of the microstructure. It was realized that in order to use the measured materials' heterogeneity it is necessary to incorporate two and higher order probability functions. Progress was hindered due to lack of experimental techniques to obtain two and three-point correlation functions. These techniques are now available, which makes

Keywords: statistical mechanics, microstructure, elastic moduli, composite.

This work has been funded under the AFOSR grant # F49620-03-1-0011 and Army Research Lab contracts # DAAD17-02-P-0398 and DAAD 19-01-1-0742. AMG gratefully acknowledges financial support of the grant from the Air Force Office of Scientific Research (AFOSR grant number 04-NA-152).

it possible to measure individual crystalline orientation in polycrystalline materials. Extension of this effort to nonrandom microstructures requires proper definition of n -th degree statistical correlation functions. For a detailed description of the theoretical discussion and the derivations please refer to [Adams et al. 1987; 1989; Beran et al. 1996; Garmestani et al. 1998b; 2001; Garmestani and Lin 2000; Saheli et al. 2004]. A statistical continuum mechanics approach for both elastic and inelastic deformation of composites was introduced earlier [Garmestani et al. 1998b; 1998a; 2001; Garmestani and Lin 2000]. In this research, the elastic formulation for the isotropic distribution will be extended to include anisotropy.

In this work a microstructure will be represented by a set of two-point correlation functions for a variety of states. In a polycrystalline material, each orientation is considered a different state and an n -dimensional space is then formulated for the homogenization relation [Garmestani et al. 2001; Adams et al. 2002]. However, a two-phase composite that consists of only two phases and the n -dimensional space is reduced to a two-dimensional state, assuming that the anisotropy within each phase is ignored. It is clear that such a construction that uses volume fraction of the second phase can only present a limited description of the composite. In this paper, two-point correlation functions are used as additional parameters for the description of a composite. Two-point statistics can incorporate not only the distribution and interaction of the two phases but also information on the shape and morphology of each individual phase.

The orientation distribution function (ODF) is a one-point statistical distribution function that only considers volume fractions (or number fractions) of crystallites with the same orientation. Two-point statistical functions can be used as a first order correction to the average (volume fraction) representation. Two-point correlation functions [Torquato and Stell 1982; Adams et al. 1987; Garmestani et al. 1998b; 1998a; 2001; Garmestani and Lin 2000; Lin et al. 2000] provide information about near neighbor and far field effects and allow the defect sensitive properties to be incorporated in the analysis. The composite formulation will be markedly enhanced by the use of empirical or spectral form of the two-point correlations [Corson 1974a; 1974b; Torquato and Stell 1982; Garmestani et al. 1998b; 2001].

Recent improvements in electron microscopy and image analysis have led to new techniques for analyzing the structure of polycrystalline materials at the scale of the crystalline grains. Orientation imaging microscopy (OIM) provides information on the spatial arrangement of lattice orientations in polycrystalline structures and is based on Kikuchi diffractometry [Garmestani et al. 1998a]. Measurements of the local orientation and misorientation of polycrystalline materials are now possible. However, for the composite, if the orientation of each phase is ignored, the correlation functions can be measured using imaging techniques (optical, SEM, etc.). The use of OIM for the measurement of orientation for a multiphase composite can introduce a large amount of detail and complexity. Higher order statistical formulations will be needed to incorporate such information for each phase as well as the interaction of the two phases.

For two-phase composite structures, the application of two-point statistics requires two different sets of probability functions. The first set can be chosen to describe the probability distribution functions for the interaction of the two phases. This reduces the problem to a composite formulation ignoring the crystalline phase for each component. The two phases can then be taken as isotropic (or anisotropic) phases, and the effect of texture can be incorporated in the anisotropy parameters in the constitutive relations. The second set can consist of the probability distribution functions for the individual crystalline phases. This means incorporating the effect of orientation for each phase.

2. Two-point distribution functions

The statistical details of a microstructure can be represented by an n -point probability distribution function. Volume fraction v_i is a one-point probability distribution function that is usually used to give an estimate of the effective properties. The details of the shape and morphology of the microstructure, including the interaction of the second phase in the composite and orientation distribution of crystallographic grains (texture), can only be realized by using higher order distribution functions [Corson 1974a; 1974b; Torquato and Stell 1982; Mason and Adams 1999]. A two-point distribution function can be defined as a conditional probability function when the statistics of a three-dimensional vector r is investigated once attached to each set of random points in a particular microstructure (One-point and two-point statistics functions are defined in Appendix A).

The exponential form of the distribution function, as proposed by [Corson 1974a; 1974b], has been shown to be appropriate for random microstructures. It is represented as

$$P_{ij}(r) = \alpha_{ij} + \beta_{ij} \exp(-c_{ij}r^{n_{ij}}), \quad (1)$$

where α_{ij} and β_{ij} are components including volume fraction of phases. For a polycrystalline microstructure, i and j can vary from 1 to M . M is the total number of grains (or states); for a two-phase composite i and j correspond to phases 1 and 2. This reduces the number of two-point functions to four, $P_{11}(r)$, $P_{12}(r)$, $P_{21}(r)$, and $P_{22}(r)$, in the case of two-phase composites where normality relations require that only P_{11} be treated as an independent variable. The values of α_{ij} and β_{ij} are summarized for a two-phase composite in Table 1.

In this equation r can generally be a vector which has been thrown in the microstructure to measure two-point probability functions. The other constants c_{ij} and n_{ij} are also microstructure parameters: $n_{ij} = 1$ [Tewari et al. 2004], and c_{ij} is a scaling parameter representing the correlation distance. These empirical coefficients can be reformulated into an anisotropic form [Saheli et al. 2004],

$$c_{ij}(\theta, A) = c_{ij}^0(1 + (1 - A) \sin \phi), \quad (2)$$

where A is a material parameter that represents the degree of anisotropy in a microstructure, such that $A = 1$ corresponds to an isotropic microstructure and c_{ij}^0 is the reference empirical coefficient. ϕ represents the angle of the vectors thrown in the microstructures to measure two-point probabilities in different directions. The present form of Equation (1) is sufficient for a two-phase composite when the statistical information is uniform in all directions. However, a three-dimensional form of the distribution can also be introduced when the microstructure includes anisotropy. This requires data from a variety of sections through the sample.

	$i = 1; j = 1$	$i = 1; j = 2$	$i = 2; j = 1$	$i = 2; j = 2$
α_{ij}	$v_1 v_1$	$v_1 v_2$	$v_2 v_1$	$v_2 v_2$
β_{ij}	$v_1 v_2$	$-v_1 v_2$	$-v_2 v_1$	$v_1 v_2$

Table 1. The empirical coefficients in Corson's equation for a two-phase composite.

An alternative form of the probability function was suggested in [Torquato 2002] for random and homogeneous systems of impenetrable spheres:

$$\begin{aligned} P_{11} &= 1 - \rho V(r) + \rho^2 M(r), \\ P_{12} &= P_{21} = v_1 - P_{11}, \\ P_{22} &= v_2 - v_1 + P_{11}, \end{aligned} \quad (3)$$

where ρ is the number density of spheres, v_1 and v_2 are the volume fractions of phases, r is the distance between two points, and $V(r)$ and $M(r)$ are functions of r as defined in Appendix B.

In Figure 1 Corson's equation and the Torquato equation are compared to real data of two-point statistics for a random microstructure.

3. Homogenization relations for elastic properties of composites

In the following section, the full homogenization relations for an elastic medium are reviewed for a representative volume element. The equilibrium equation is defined by

$$\sigma_{ij,j} = 0, \quad (4)$$

where $\sigma_{ij}(x)$ is the local stress field. The elastic constitutive relations are satisfied locally throughout the heterogeneous medium as

$$\sigma_{ij}(x) = c_{ijkl}(x)\varepsilon_{kl}(x); \quad (5)$$

$c_{ijkl}(x)$, $\sigma_{ij}(x)$, and $\varepsilon_{ij}(x)$ are local values of stiffness, stress and strain respectively. Let us define an effective elastic modulus C_{ijkl} such that [Beran et al. 1996; Garmestani and Lin 2000],

$$\langle \sigma_{ij} \rangle = C_{ijkl} \langle \varepsilon_{kl} \rangle. \quad (6)$$

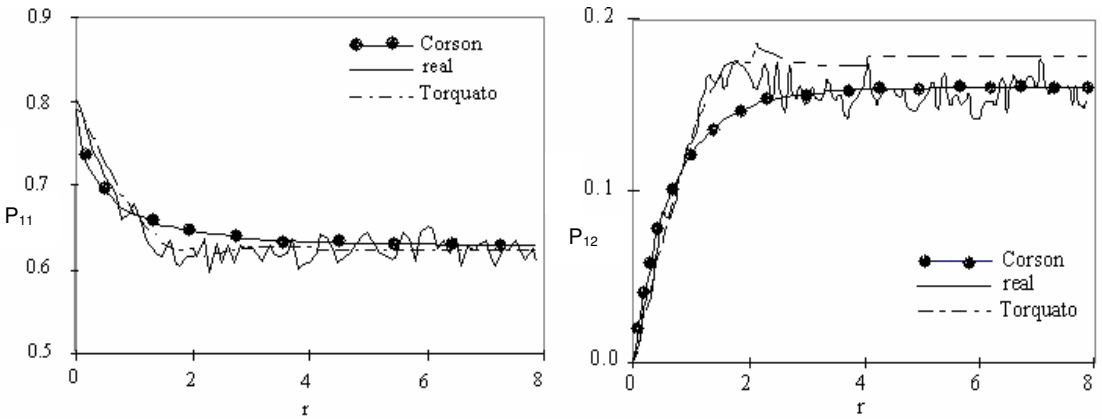


Figure 1. Comparison of different models for two-point probability functions for a two-phase composite with random distribution of the second phase. Note that c_{ij} and n_{ij} are fitted to the measured (real) data in Corson's equation.

Symbol $\langle h \rangle$ denotes the ensemble average over grains (phases, components, etc.) at state h . Assuming ergodic hypothesis, the average of the local stiffness $\langle c_{ijkl} \rangle$ is defined as [Kröner 1972]

$$\langle c_{ijkl} \rangle = \langle c_{ijkl}(x) \rangle = \frac{1}{V} \int_V c_{ijkl}(x) dV. \quad (7)$$

The same definition is applicable for stress, strain and compliance. The local moduli and compliance, as well as the local stress and strain, can be defined as a perturbation from the average values $\langle \dots \rangle$ by defining a new parameter ($\tilde{\dots}$) as in [Beran et al. 1996; Garmestani and Lin 2000]

$$\begin{aligned} c_{ijkl}(x) &= \langle c_{ijkl} \rangle + \tilde{c}_{ijkl}(x), \\ s_{ijkl}(x) &= \langle s_{ijkl} \rangle + \tilde{s}_{ijkl}(x), \end{aligned} \quad (8)$$

$$\begin{aligned} \sigma_{ij}(x) &= \langle \sigma_{ij} \rangle + \tilde{\sigma}_{ij}(x), \\ \varepsilon_{ij}(x) &= \langle \varepsilon_{ij} \rangle + \tilde{\varepsilon}_{ij}(x), \end{aligned} \quad (9)$$

where $\tilde{c}_{ijkl}(x)$, $\tilde{s}_{ijkl}(x)$, $\tilde{\sigma}_{ij}(x)$, and $\tilde{\varepsilon}_{ij}(x)$ are, respectively, the deviation from the mean value at each point of stiffness, compliance, stress and strain. Therefore, the following are satisfied:

$$\begin{aligned} \langle \tilde{c}_{ijkk}(x) \rangle &= 0, & \langle \tilde{s}_{ijkl}(x) \rangle &= 0, \\ \langle \tilde{\sigma}_{ij}(x) \rangle &= 0, & \langle \tilde{\varepsilon}_{ij}(x) \rangle &= 0. \end{aligned} \quad (10)$$

In the following, statistical continuum mechanics analysis is applied to a two-phase composite for the prediction of elastic properties. A theoretical framework has already been developed for isotropic distributions in composites, by [Garmestani et al. 1998b; Garmestani and Lin 2000], and for a textured polycrystalline material, by [Beran et al. 1996]. Here, a brief discussion is provided for the calculation of the effective elastic constants for isotropic distribution and will be extended to anisotropic distributions in later sections.

Substituting local moduli (Equation (9)) in the equilibrium equations (Equation (4)) and rewriting the equation as a function of displacement, the following equations will be obtained:

$$\langle c_{ijkm} \rangle \frac{\partial^2 \tilde{u}_k}{\partial x_j \partial x_m} + \frac{\partial}{\partial x_j} [\tilde{c}_{ijkm}(x) \varepsilon_{km}(x)] = 0. \quad (11)$$

The solution for this PDE can be written as an integral equation using the Green's function, defined by the PDE

$$\langle c_{ijkm} \rangle \frac{\partial^2 G_{kp}(x, x')}{\partial x_j \partial x_m} + \delta_{ip} \delta(x - x') = 0, \quad (12)$$

where $\delta(x - x')$ is the Dirac's delta function for the vector relating any two points in the microstructure, and the term $\delta_{ip} \delta(x - x')$ represents the i -th component of a unit force acting parallel to the direction p for a fixed point, p [Kröner et al. 1987; Willis 1965]. Green's function in the case of isotropy can be defined by a closed form, and for the case of anisotropy has to be calculated numerically. The details of the calculations of Green's functions for both cases are presented in Appendix C [Bacon et al. 1980; Mason and Adams 1999]. Substituting the values of local stress and strain in Equation (5), after some

manipulation, the effective elastic constants (in Equation (6)) can be calculated as (for details see paper by [Garmestani and Lin 2000])

$$C_{ijkl} = \langle c_{ijkl} \rangle + \langle \tilde{c}_{ijmn}(x) a_{mnkl}(x) \rangle, \quad (13)$$

where a_{mnkl} is a matrix defined to show the heterogeneity in the strain field as [Garmestani and Lin 2000, Equation (4)]

$$\tilde{\varepsilon}_{kl} = a_{mnkl} \langle \varepsilon_{kl} \rangle. \quad (14)$$

By substituting local stress from Equation (5) into the equilibrium Equation (4) an equation for displacement is obtained. Differentiating this equation and multiplying the result by c_{ijkl} , the second term in Equation (13) can be derived as [Saheli 2006], (details in Appendix D)

$$\begin{aligned} \langle \tilde{c}_{ijku}(x) a_{kurs}(x) \rangle = & \int_V \frac{\partial [K_{kpu}(x, x') \langle \tilde{c}_{ijku}(x) \tilde{c}_{pmrs}(x') \rangle]}{\partial x'_m dX'} \\ & - \int_V K_{kpum}(x, x') \langle \tilde{c}_{ijku}(x) \tilde{c}_{pmrs}(x') \rangle dX', \quad (15) \end{aligned}$$

where x and x' are two different positions in the media, dX' is the volume integral on the volume element around position x' , and K_{kpu} and K_{kpum} are calculated through

$$\begin{aligned} K_{kpu} &= \frac{(G_{kp,u} + G_{up,k})}{2}, \\ K_{kpum} &= \frac{(G_{kp,um} + G_{up,km})}{2}. \end{aligned} \quad (16)$$

$G_{kp,u}$ and $G_{up,km}$ are, respectively, the first and the second derivative of the Green's function that solves Equation (12).

The two-point correlation function is defined through the equation

$$\langle \tilde{c}_{ijku}(x) \tilde{c}_{pmrs}(x') \rangle = \iint \tilde{c}_{ijku}(x) \tilde{c}_{pmrs}(x') P_2(x|h, x'|h') dh dh', \quad (17)$$

where P_2 is a correlation function for two states of h and h' , and is defined in Appendix A. Equation (17) can be derived for composites by the relationship

$$\langle \tilde{c}_{ijku}(x) \tilde{c}_{pmrs}(x') \rangle = \tilde{c}_{ijku}^1 \tilde{c}_{pmrs}^1 P_{11} + \tilde{c}_{ijku}^1 \tilde{c}_{pmrs}^2 P_{12} + \tilde{c}_{ijku}^2 \tilde{c}_{pmrs}^1 P_{21} + \tilde{c}_{ijku}^2 \tilde{c}_{pmrs}^2 P_{22}, \quad (18)$$

where c^1, c^2 are the local elastic moduli for the two individual phases.

4. Analytical procedure

It was shown earlier that the effective modulus C can be calculated through Equation (13), which includes the correlation term (Equation (15)). This term will be analyzed analytically in this section to observe the effect of one-point and two-point statistics. This term is composed of two parts, or

$$\langle \tilde{c}_{ijku}(x) a_{kurs}(x) \rangle = I_{ijrs}^1 + I_{ijrs}^2, \quad (19)$$

where the first term is

$$I_{ijrs}^1 = \int_V \frac{\partial [K_{kpu}(x, x') \langle \tilde{c}_{ijk}(x) \tilde{c}_{pmrs}(x') \rangle]}{\partial x'_m dX'} \quad (20)$$

and can be converted to a surface integral by applying Gauss' theorem (for additional information see mathworld.wolfram.com/DivergenceTheorem.html). Gauss' theorem converts the volume integral in a sphere with infinite radius to a surface integral with the boundary of this sphere. The resulting surface integral requires evaluation on a surface at infinity and on a surface enclosing the singularity of K_{kpu} at $x = 0$.

Choosing both surfaces as spheres and applying Gauss' theorem, the following integral is obtained:

$$I_{ijrs}^1 = \left(\int_{x-x' \rightarrow 0} \langle \tilde{c}_{ijkl}(x) \tilde{c}_{pmrs}(x') \rangle K_{kpu} d\hat{A}_m \right) + \left(\int_{x-x' \rightarrow \infty} \langle \tilde{c}_{ijkl}(x) \tilde{c}_{pmrs}(x') \rangle K_{kpu} d\hat{A}_m \right) \quad (21)$$

To calculate the two surface integrals, the correlation term shown by $\langle \tilde{c}_{ijk}(x) \tilde{c}_{pmrs}(x') \rangle$ has to be evaluated when $x - x' \rightarrow 0$ and $x - x' \rightarrow \infty$. When $x - x' \rightarrow 0$, then the correlation will be a constant and independent of x , and when $x - x' \rightarrow \infty$ there will be no correlation between two points. This can be proven for the case of a two-phase composite using Equation (18)

$$\begin{aligned} x - x' \rightarrow 0 &\implies \begin{cases} P_{11} \rightarrow v_1 \\ P_{12} \rightarrow 0 \\ P_{22} \rightarrow v_2 \end{cases} \implies \langle \tilde{c}_{ijk}(x) \tilde{c}_{pmrs}(x') \rangle \rightarrow \text{constant}, \\ x - x' \rightarrow \infty &\implies \begin{cases} P_{11} \rightarrow v_1^2 \\ P_{12} \rightarrow v_1 v_2 \\ P_{22} \rightarrow v_2^2 \end{cases} \implies \langle \tilde{c}_{ijk}(x) \tilde{c}_{pmrs}(x') \rangle \rightarrow 0. \end{aligned} \quad (22)$$

Therefore the second term in Equation (21) will be equal to zero, and the components of the first integral, I_{ijrs}^1 , can be calculated by

$$I_{ijrs}^1 = (\tilde{c}_{ijk}^1 \tilde{c}_{pmrs}^1 v_1 + \tilde{c}_{ijk}^2 \tilde{c}_{pmrs}^2 v_2) K_{kcpum}, \quad (23)$$

where

$$K_{kcpum} = \int K_{kpu} d\hat{A}_m, \quad (24)$$

and is evaluated as

$$\begin{aligned} K_{c_{iiii}} &= -\frac{(16/15\bar{K})}{8\bar{\mu}}, \\ K_{c_{ijij}} = K_{c_{jiji}} &= \frac{(4/3 - 4/5\bar{K})}{8\bar{\mu}}, \\ K_{c_{ijji}} = K_{c_{jii j}} = K_{c_{iijj}} = K_{c_{jjii}} &= -\frac{(2/3 + 2/15\bar{K})}{8\bar{\mu}}, \end{aligned} \quad (25)$$

where \bar{K} is the average property of two phases

$$\bar{K} = \frac{\bar{\lambda} + \bar{\mu}}{\bar{\lambda} + 2\bar{\mu}}. \quad (26)$$

Note that i and j can vary from 1 to 3, but there is no summation on the indices in Equation (25). Although a two-point correlation function shows up in the integral I_{ijrs}^1 , this integral is the result of the contribution of one-point statistics since the only variables contributed in the calculations of Equations (25) and (26) are volume fractions of two phases.

The second term in Equation (19) can also be found using

$$I_{ijrs}^2 = - \int_V K_{kpum}(x, x') \langle \tilde{c}_{ijk}(x) \tilde{c}_{pmrs}(x') \rangle dX'. \quad (27)$$

This integral can be shown to be zero for isotropic composites. In isotropic composites the correlation term will be only a function of r ($F(r)$). On the other hand, by assuming the definition of isotropic Green's function [Kröner et al. 1987], K_{kpum} is derived as

$$\begin{aligned} K_{kpum} = & \frac{1}{8\pi\bar{\mu}} \left\{ [\bar{K} \delta_{uk} \delta_{pm} + (\bar{K} - 1)(\delta_{pu} \delta_{km} + \delta_{um} \delta_{pk})] / |r|^3 \right. \\ & + [(3 - 3\bar{K})(r_m r_k \delta_{pu} + r_m r_u \delta_{kp}) \delta_{uk} \delta_{pm} - 3\bar{K}(r_m r_p \delta_{ku} + r_n r_p \delta_{km} + r_k r_p \delta_{um} + r_k r_n \delta_{pm})] / |r|^5 \\ & \left. + [15\bar{K}(r_p r_m r_u r_k)] / |r|^7 \right\}. \quad (28) \end{aligned}$$

Therefore, the integrand of the Equation (27) can be integrated with respect to r , separately. Some components of the integral of I_{ijrs}^2 are evaluated here as an example:

$$\begin{aligned} I_{1111}^2 &= \frac{1}{8\pi\bar{\mu}} \int_r \int_\theta \int_\phi F(r) \left[(3\bar{K} - 2) \sin \phi + (6 - 18\bar{K}) \cos^2 \theta \sin^3 \phi + 15\bar{K} \cos^4 \theta \sin^5 \phi \right] / r dr d\theta d\phi = 0, \\ I_{1212}^2 &= \frac{1}{8\pi\bar{\mu}} \int_r \int_\theta \int_\phi F(r) \left[\bar{K} \sin \phi - 3\bar{K} \sin^3 \phi + 15\bar{K} \sin^2 \theta \cos^2 \theta \sin^5 \phi \right] / r dr d\theta d\phi = 0, \\ I_{1122}^2 &= \frac{1}{8\pi\bar{\mu}} \int_r \int_\theta \int_\phi F(r) \left[(\bar{K} - 1) \sin \phi + (3 - 3\bar{K}) \sin^2 \theta \sin^3 \phi - 3\bar{K} \cos^2 \theta \sin^3 \phi \right. \\ & \quad \left. + 15\bar{K} \sin^2 \theta \cos^2 \theta \sin^5 \phi \right] / r dr d\theta d\phi = 0. \end{aligned}$$

For more details on the integration please refer to [Saheli 2006]. This can be shown in a general form

$$I_{iii}^2 = I_{ijij}^2 = I_{iijj}^2 = 0, \quad (29)$$

where i and j vary from 1 to 3, indicating the three directions in spherical coordinates. Note that there is no summation on the indices in Equation (29). Therefore I_{ijrs}^2 has been shown analytically to be zero for isotropic distributions found in [Beran 1968] and [Kröner 1977]. This is in agreement with the numerical results that Beran et al. [1996] obtained in their work. In this work, as the oxygen free electronic (OFE) alloy 101 copper plates were nearly isotropic, it was observed numerically that the contribution of the second integral is almost zero in the calculation of elastic properties. Hence the effect of spatial arrangement of the crystals was not observed.

Also note that in the previous works by Garmestani and Lin [2000] only an isotropic composite was considered. Therefore the effect of morphology and spatial arrangement of the features in the microstructure on properties was not completely evident; however, in the following section of this research, it will be shown that the contribution of two-point statistics is very significant in anisotropic composites.

5. Numerical analysis

In the last section it was shown that I_{ijrs}^2 is zero for isotropic composites; however, it is nonzero and should be evaluated by Equation (27) in anisotropic composites. The numerical integration has been done using Simpson’s rule (see mathworld.wolfram.com/SimpsonsRule.html). For this purpose, a sphere is divided into $n_r \times n_\theta \times n_\varphi$ units, where n_r is the number of sections for variable r (radius) and n_θ and n_φ are the number of sections for variables $0 < \theta < 2\pi$ and $0 < \varphi < \pi$, respectively, in spherical coordinates. The variable r also changes between 0 and ∞ . There are two issues to be taken into account to perform the integration. One is the singularity of the Green’s function at $r = 0$ and the other is the definition of ∞ for r in the integration. Empirical forms of the probability density functions were introduced earlier. It can be shown that for all physically realizable forms of the probability density functions for a random media, they merge to a constant value at large r (as shown schematically in Figure 2).

The correlation function defined in Equation (18) becomes zero when the probabilities P_{11} , P_{12} , P_{21} , and P_{22} reach their limits. Therefore the coherence radius, (R_c), is defined as the limiting value of the probability functions. This value should be used as an upper limit (or ∞) for r in the volume integral (I_{ijrs}^2). Since the Green’s function is undefined at $r = 0$, the integral can be divided into two parts with respect to variable r , (0 to r_{min}) and (r_{min} to R_c). For infinitesimally small values of r (0 to r_{min}) the correlation does not change, so the correlation term can be taken out of the integral, and therefore the term

$$\int_V K_{kpum}(x, x')dX'$$

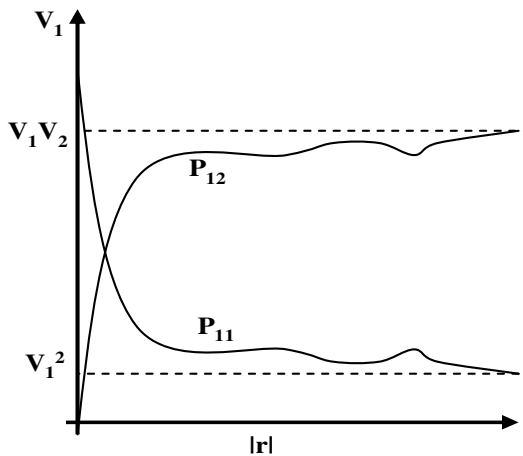


Figure 2. Schematic representation of two-point probability functions (P_{11} and P_{12} merge to their limiting values as the dimension of vector r increases).

has to be calculated. Similar to the case of isotropic composites, this integral can be shown to be zero. Therefore the integral, I_{ijrs}^2 , needs to be evaluated between r_{\min} and R_c for anisotropic composites. On the other hand, r_{\min} should be chosen as a small nonzero value in such a way as to be small enough to bring the contribution of two-point correlations for small radius and large enough to pass the singularity. For this purpose, a numerical procedure should be adopted that calculates a r_{\min} by reducing r until a saturation is reached for the value of the integral, not reaching infinity. Therefore the volume integral needs to be calculated from r_{\min} to R_c . Furthermore, time of operation is another aspect that has to be considered. For instance, in the case of Al-Pb composites [Saheli et al. 2004], if $r_{\min} = 0.03$ and $\Delta r = 0.1$ it takes about 20 minutes for the codes to calculate one elastic constant in a Pentium IV machine, 2.4 MHZ. However, if r_{\min} is chosen the same and $\Delta r = 0.01$ then it takes about 2 hours and 35 minutes to calculate one elastic constant. The difference between the two results is about 0.04 percent. In contrast, for $r_{\min} = 0.003$, $\Delta r = 0.01$ it takes about 20 hours, where the difference in the calculation compared to the first case is less than 0.5 percent.

6. Applications

It was shown that two-point statistics does not contribute in the evaluation of elastic properties of isotropic composites. However, it has a considerable effect in the case of anisotropy. The key to this approach is the correct representation of the microstructure. In the previous works [Garmestani and Lin 2000; Saheli et al. 2004] a simplified empirical form of the two-point probability function was used for the microstructure representation, whereas in this work the statistical information has been measured directly from the microstructure and used as a database.

In this section, the statistical continuum mechanics model presented earlier as a homogenization technique will be studied in anisotropic composite materials. For this purpose, elastic properties of Al-SiC composite will be calculated by using the two-point statistical homogenization technique, and the contribution of two-point statistics will be discussed. The results of the simulation will be compared with experiments to validate the theory.

6.1. Al-SiC samples. An Al-SiC composite was fabricated by extrusion by varying the distribution of two different sizes of Al particles mixed with SiC particles. The difference in the initial particle sizes of SiC reinforcement phases and Al-alloy matrix results in the heterogeneity of the microstructure. The micrographs of the two samples with different PSR are shown in Figures 3 and 4. The particles of SiC are clustered in the sample with $\text{PSR} = 8:1$, therefore they introduce more anisotropy in the extrusion direction. However, the microstructure with $\text{PSR} = 2:1$ seems to have a smaller anisotropy. The validity of this interpretation will be studied by computing the elastic properties of the two samples. Note that the anisotropy of the microstructure has been considered in 1-3 or 2-3 plane (Figure 5). The distribution of the two-point correlation functions in these microstructures is symmetric with respect to the extrusion axis (Figure 5). Therefore the extrusion axis is chosen as the vertical axis. The probability distribution function changes with orientation φ and the magnitude of the vector r in each section. However, these probabilities are the same for all planes with different θ which include extrusion (vertical) axis. Therefore the measurements of this composite on any section including the vertical axis provides the same statistical information within which the statistics may be anisotropic and would be sufficient for the simulation (θ

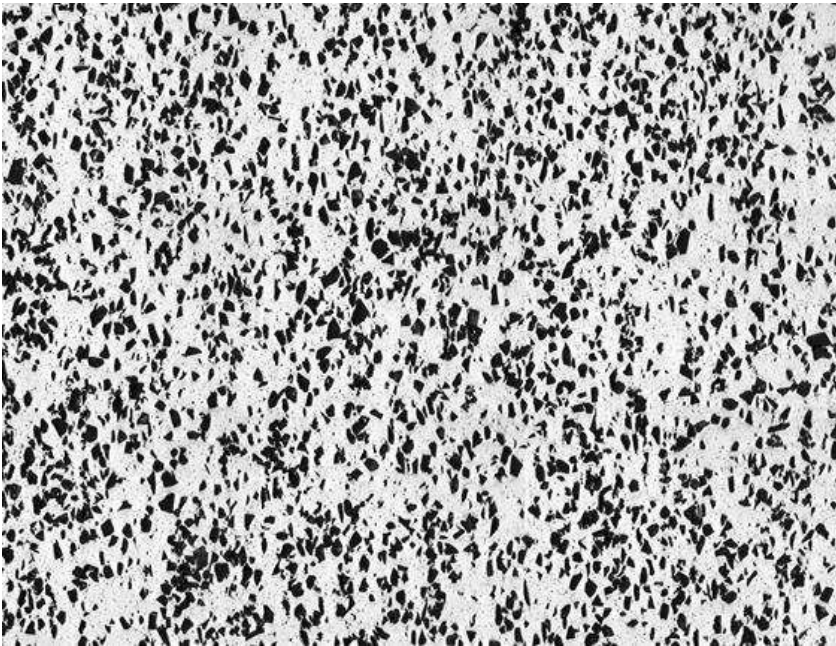


Figure 3. Micrograph of Al-SiC composite, PSR = 2:1.

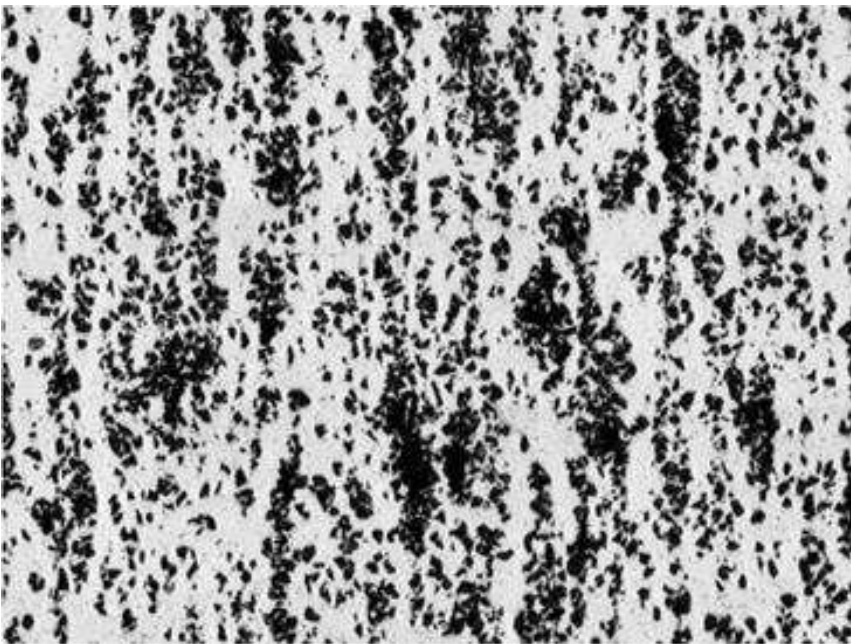


Figure 4. Micrograph of Al-SiC composite, PSR = 8:1.

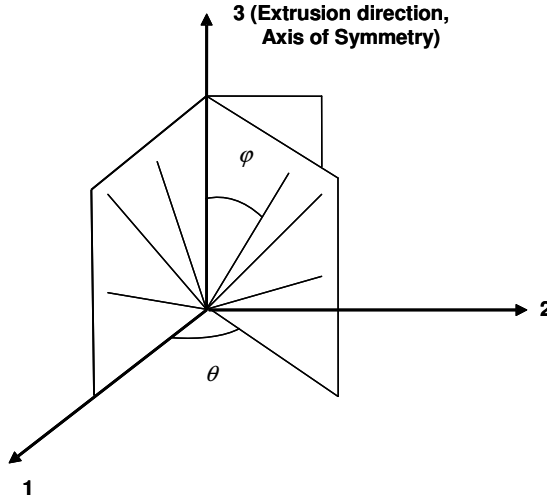


Figure 5. Representation of symmetry in samples of Al-SiC.

and φ are respectively the angles with axis 1 and axis 3 in spherical coordinates). Therefore the two-point probability functions are measured directly from the microstructure for a different range of φ on any plane including extrusion axis, which can be averaged as [Tewari et al. 2004]

$$\langle P_{ij}(r) \rangle = \frac{\int_{\varphi_1}^{\varphi_2} [P_{ij}(r, \varphi)] v d\varphi}{\int_0^{2\pi} d\varphi} \tag{30}$$

As an example the measured values of P_{11} are shown in Figure 6 as a function of r and φ in each section containing extrusion (shown in Figure 5). In addition, Corson’s equation is used to measure values of P_{11} in Figure 7. It is observed that the measured values show an exponential trend which follows Corson’s equation (Equation (1)), and empirical factor n in Corson’s equation is calculated near 1, in agreement

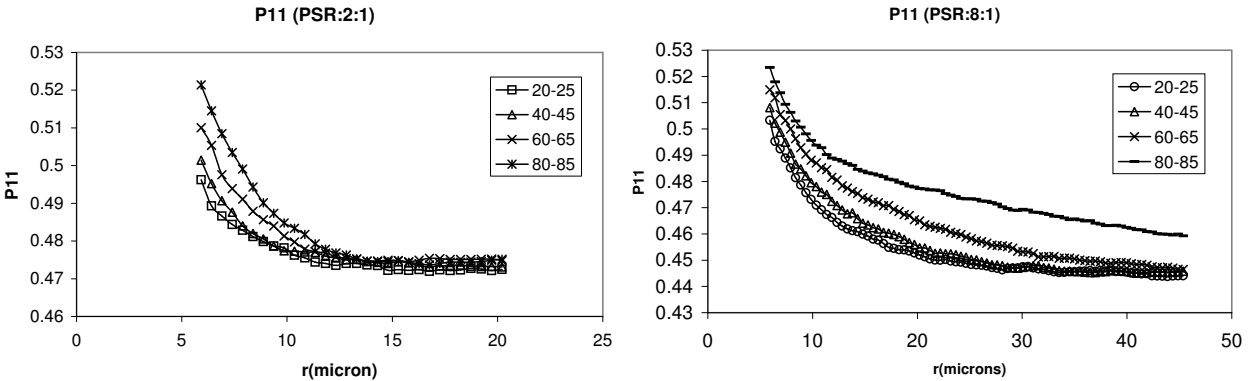


Figure 6. Measurement of two-point statistics in a vertical section (P_{11}) of two samples for different angles.

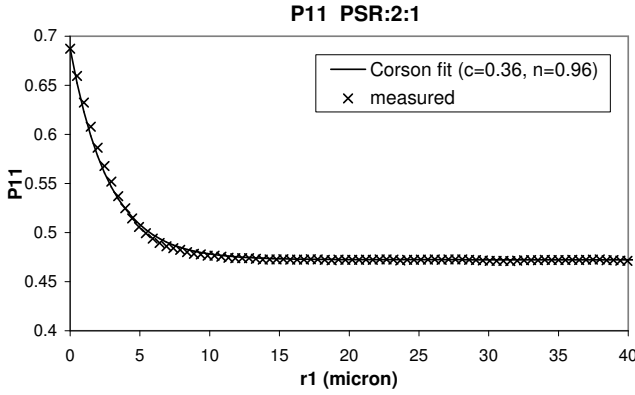


Figure 7. Fitted curve to the measured values of P_{11} .

with results by Tewari et al. [2004]. P_{11} for two samples at $40 < \varphi < 45$ are shown in Figure 8. The value of P_{11} (defined in Equation (1)) reaches its limit $v_1^2 = 0.4761$ for the case of PSR = 2:1 faster than it reaches its limit $v_1^2 = 0.4489$ for the case of PSR = 8:1.

Using the measured two-point probabilities and preparing the simulation code based on the homogenization relations described in previous sections, one can calculate elastic stiffness matrices for each sample. The mechanical properties of each phase are assumed as (based on previous experimental data)

$$E(\text{Al}) = 69 \text{ GPa}, \quad \nu(\text{Al}) = 0.33, \quad (31)$$

$$E(\text{SiC}) = 393 \text{ GPa}, \quad \nu(\text{SiC}) = 0.19. \quad (32)$$

In this simulation both integrals in Equation (19) are calculated, as the samples are considered anisotropic. Therefore the effect of anisotropy as introduced by clustering is studied in the estimation of elastic properties of these two samples.

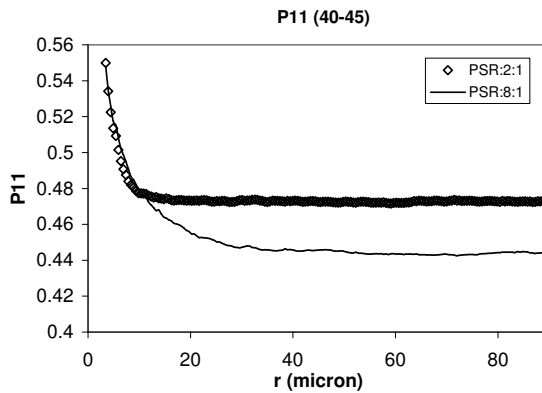


Figure 8. Measured P_{11} for two samples.

C	Upper Bound	C (statistical model)	One-point	Two-point	Lower Bound
C_{1111}	229.86	205.08	-15.85	8.92	139.81
C_{1313}	72.43	71.95	-2.70	-2.23	36.18

Table 2. Contribution of one-point (Equation (19)) and two-point (Equation (26)) statistics in calculation (Equation (13)) of elastic constants of Al-SiC sample (PSR = 8:1).

6.2. Results. Calculating both integrals in Equation (19), the results show that the contribution of the second integral is about 30 and 50 percent in the calculation of C_{iiii} and C_{ijij} respectively. 1 and 3 indicate transverse and longitudinal (extrusion) directions. For example, when $i = 1$, C_{iiii} refers to C_{1111} . Some of the components of effective elastic constants for an 8:1 sample are shown in Table 2.

Using the simulated values of the longitudinal elastic modulus, the linear behavior of the stress-strain curve in the elastic region is shown in Figures 9 and 10. The enlarged elastic region of stress strain curves obtained through mechanical testing is also shown in the graphs. In addition, upper bound [Voigt 1889] and lower bound [Reuss 1929], Hashin–Shtrikman upper and lower bound [Hashin and Shtrikman 1962; 1963], and self-consistent approximation [Hill 1965] are calculated and shown in the figure as well as in Table 3 for comparison to the simulation and experimental results. The linear elastic modulus calculated from the statistical simulations represented the best slope for the experimental stress-strain curves in the elastic region.

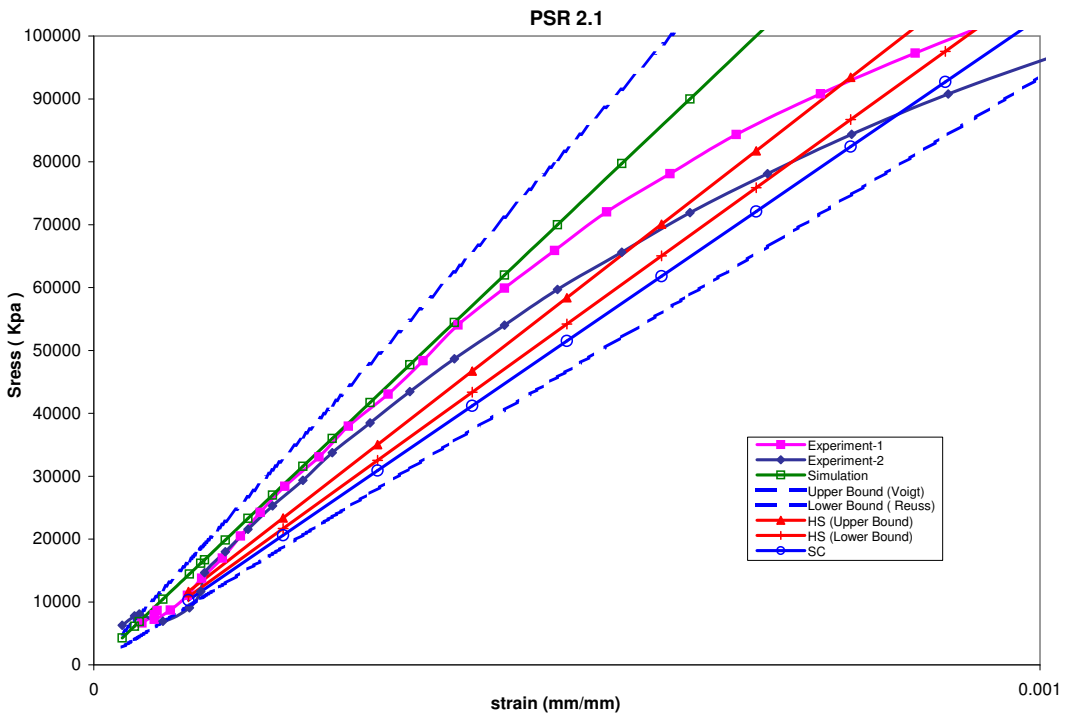


Figure 9. Stress-strain curve for Al-SiC PSR = 2:1.

E	REUSS	HS-LB	Statistics	Experiment	SC	HS-UB	VOIGT
PSR = 2:1	95.67	175.2	143.12	151.51	102.99	175.61	176.72
PSR = 8:1	98.43	185.65	161.29	156.82	106.63	186.04	184.07

Table 3. Comparison of calculated longitudinal elastic modulus of two samples with different models.

The error is estimated to be between 0.07% and 20%, where 20% error relates to the points that have the largest deviation from experimental data in elastic region. The elastic moduli in two different directions (longitudinal and transverse) are shown for two samples in Figure 11. It was observed from the micrographs that clustering in the sample with PSR = 8:1 introduces more anisotropy in the elastic modulus than the other sample. This verifies the results of the simulation in Figure 11.

The volume fraction of the second phase (SiC) in two microstructures with PSR = 2:1 and PSR = 8:1 is estimated to be 31% and 33%, respectively. Although the volume fractions are very close, it shows a different degree of anisotropy (about 15% in the two samples). The upper Hashin–Shtrikman bounds for the two samples shown in this figure are not able to represent the anisotropy in the system properly. It shows an identical slope for the two cases, whereas the statistical calculations predict different elastic properties in the two directions.

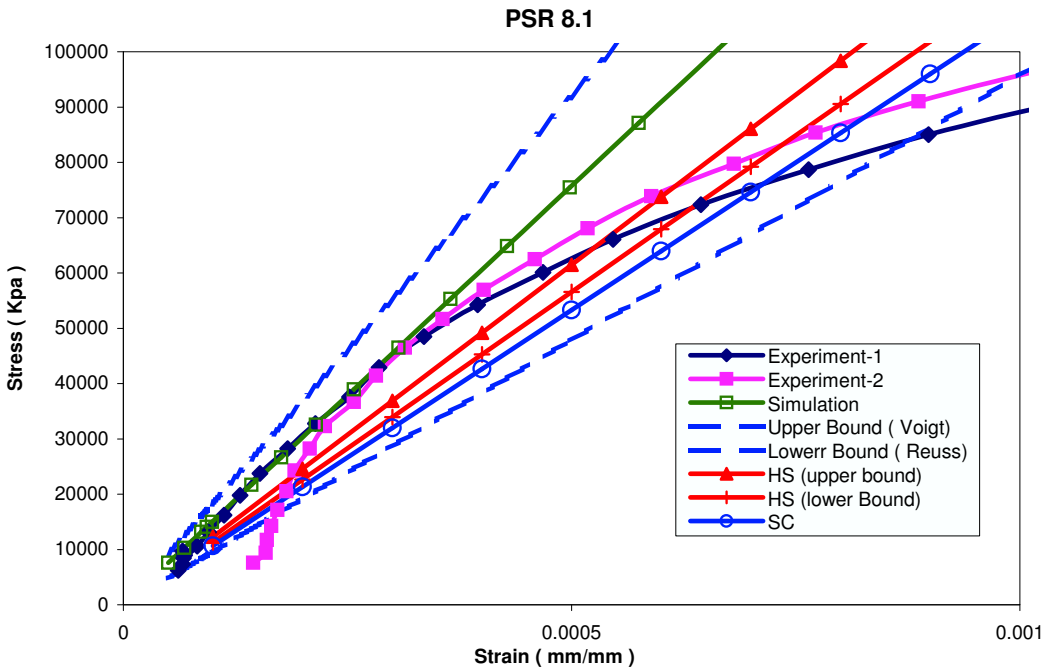


Figure 10. Stress-strain curve for Al-SiC PSR = 8:1.

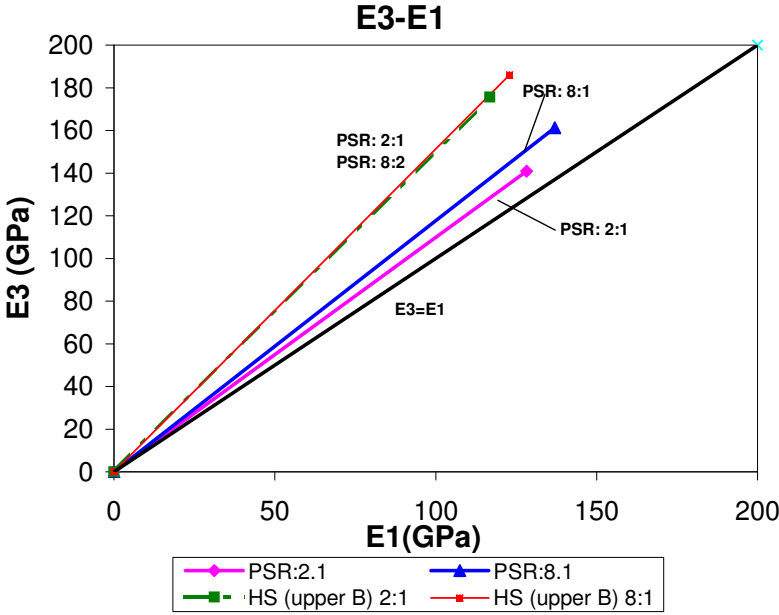


Figure 11. Comparison of longitudinal elastic modulus and transverse elastic modulus for two samples.

7. Summary

Statistical continuum mechanics modeling has been extended to include anisotropy in the calculation of elastic properties of composites. The effect of one-point and two-point statistics on the calculation of elastic properties of composites was studied in detail. It was shown analytically that two-point statistical information does not contribute in the calculation of elastic properties of isotropic composites, whereas it plays a major role for anisotropic materials. The homogenization technique was then applied to an Al-SiC composite with two different PSR’s. In this simulation two-point statistical functions were measured directly from the microstructures, and the statistical formulation uses the two-point probability functions to incorporate the effect of the microstructure distribution. Applying statistical continuum mechanics analysis, the effective properties of the two samples of Al-SiC composite were estimated and compared with the experimental data, the upper (Voigt) and lower bounds (Reuss), Hashin–Shtrikman bounds, and self-consistent approximations. Although the microstructures of the two composite samples have very similar volume fractions, this analysis results in different values of the effective elastic properties and predicts different anisotropy levels for them. Therefore the results show that the statistical analysis can provide a good estimate for the elastic effective properties, considering the spatial distribution of the phases.

Appendix A: Definition of one-point and two-point statistics functions

One-point probability functions. To measure a one-point probability function, a random number of points (N) have to be inserted in the microstructure (Figure 12). The number of points located in one

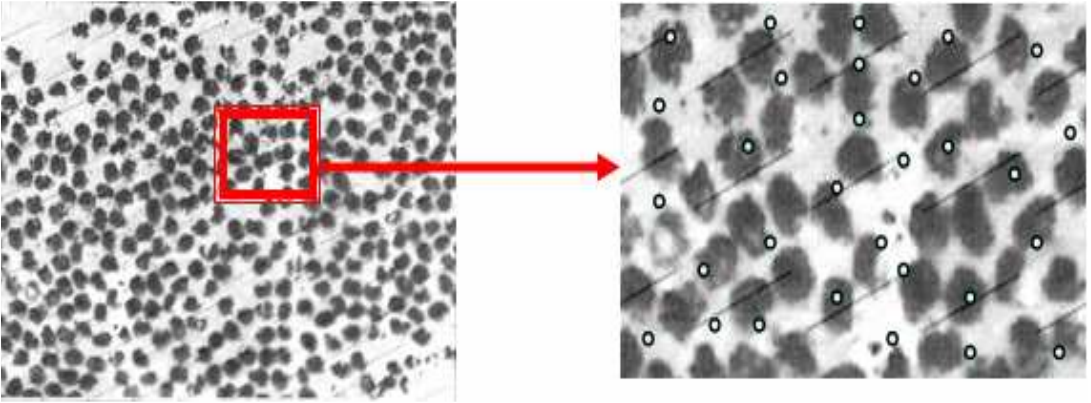


Figure 12. Schematic representations of one-point statistics measurement in a two-phase composite microstructure.

phase with respect to the total number of points (N) indicates a one-point probability

$$\begin{aligned} P(\phi_1) &= P_1 = \frac{n_1}{N} = v_1 \\ P(\phi_2) &= P_2 = \frac{n_2}{N} = v_2, \end{aligned} \quad (\text{A.1})$$

where phase one and phase two have been considered as matrix and particles respectively, and the normalization relationship

$$P(\phi_1) + P(\phi_2) = 1. \quad (\text{A.2})$$

is always satisfied.

Two-point probability functions. A two-point probability function can be defined as a conditional probability function when the statistics of a three-dimensional vector r are investigated once attached to each set of the random points in a particular microstructure (Figure 13). Two-point statistics can be calculated by the probability of a specific phase at the head of the vector given the phase at the tail of the vector, and can be shown by $P(r \mid \{1, 2\}, \{1, 2\})$.

The following normalization relationship is valid for all the functions:

$$\begin{aligned} P_{11} + P_{12} &= v_1 \\ P_{22} + P_{21} &= v_2 \\ P_{11} + P_{12} + P_{21} + P_{22} &= 1. \end{aligned} \quad (\text{A.3})$$

As it is observed from the above normalization relationship, P_{11} is the only independent variable.

Appendix B: Torquato probability functions

Functions $V(r)$ and $M(r)$ in Equation (3) are defined as

$$\begin{aligned} V(r) &= \frac{4\pi}{3} \left[1 + \frac{3r}{4} - \frac{r^3}{16} \right], & r < 2, \\ V(r) &= \frac{8\pi}{3}, & r > 2, \end{aligned} \quad (\text{B.1})$$

and

$$\begin{aligned} M(r) &= \left[-\frac{16}{9} + \frac{r^3}{3} - \frac{r^4}{10} + \frac{r^6}{1260} \right] \pi^2 + \frac{16\pi^2}{9}, & 0 \leq r < 2, \\ M(r) &= \left[\frac{256}{35r} - \frac{128}{9} + \frac{32r}{5} - \frac{5r^3}{9} + \frac{r^4}{10} - \frac{r^6}{1260} \right] \pi^2 + \frac{16\pi^2}{9}, & 2 \leq r < 4, \\ M(r) &= \frac{16\pi^2}{9}, & r \geq 4. \end{aligned} \quad (\text{B.2})$$

Note that r in general is a vector; however, for an isotropic two-phase composite, r is considered to be a scalar.

Appendix C: Green's function definition

Green's function for the case of isotropic materials is defined by the closed form equation as in [Kröner et al. 1987]

$$G_{kp}(x, x') = \frac{1}{8\bar{\mu}\pi|r_{12}|} \left\{ 2\delta_{kp} - \frac{\bar{\lambda} + \bar{\mu}}{\bar{\lambda} + 2\bar{\mu}} \left(\delta_{kp} - \frac{r_{12k}r_{12p}}{|r_{12}|^2} \right) \right\}, \quad (\text{C.1})$$

where $\bar{\lambda}$ and $\bar{\mu}$ are the average values of Lamé's Constants in the composite.

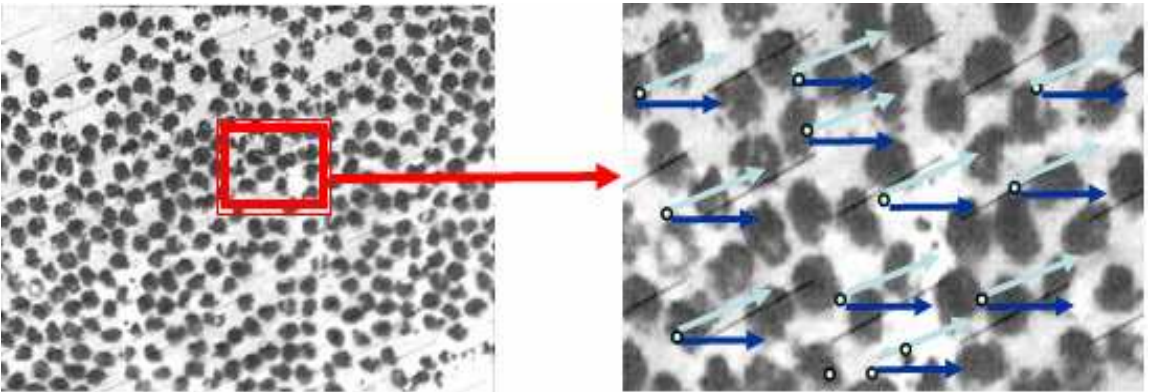


Figure 13. Schematic representations of two-point statistics measurement in a two-phase composite microstructure.

However in the case of anisotropy and texture, there is no closed form equation, and it can be written in the numerical form [Bacon et al. 1980]

$$G_{ij}(x - x') = \frac{1}{8\pi^2|x - x'|} \oint_{|z|=1} (zz)_{ij}^{-1} ds, \quad (\text{C.2})$$

where

$$(zz)_{ij} = C_{kijl} z_k z_l, \quad (\text{C.3})$$

$$(z_{ij})^{-1} = \frac{\varepsilon_{ism} \varepsilon_{jrw} (zz)_{sr} (zz)_{mw}}{2\varepsilon_{pgn} (zz)_{1p} (zz)_{2g} (zz)_{3n}}. \quad (\text{C.4})$$

T is the unit vector in the direction of the line connecting two position x and x' . The general expression for the n -th derivative of the Green's function is given by

$$G_{ij,s_1 \dots s_n} = (x - x') = \frac{(-1)^N T_{k_1} \dots T_{k_N}}{8\pi^2|x - x'|^{N+1}} \times \oint_{|z|=1} \frac{\partial^N [(zz)_{ij}^{-1} z_{s_1} \dots z_{s_N}]}{\partial z_{k_1} \dots \partial z_{k_N}} ds, \quad (\text{C.5})$$

$$G_{ij,s}(x - x') = \frac{1}{8\pi^2|x - x'|^2} \times \oint_{|z|=1} [T_s (zz)_{ij}^{-1} - z_s F_{ij}] ds, \quad (\text{C.6})$$

$$G_{ij,sr}(x - x') = \frac{1}{8\pi^2|x - x'|^3} \times \oint [2T_s T_r (zz)_{ij}^{-1} - 2(z_s T_r + z_r T_s) F_{ij} + z_s z_r E_{ij}] ds, \quad (\text{C.7})$$

where

$$F_{ij} = (zz)_{im}^{-1} (zz)_{kj}^{-1} [(zT)_{mk} + (Tz)_{mk}], \quad (\text{C.8})$$

$$E_{ij} = [(zT)_{mk} + (Tz)_{mk}] [F_{im} (zz)_{kj}^{-1} + (zz)_{im}^{-1} F_{kj}] - 2(zz)_{im}^{-1} (zz)_{kj}^{-1} (TT)_{mk}. \quad (\text{C.9})$$

The resulting integral is a line integral on a circle defined in a perpendicular plane to T with a unit radius (Figure 14).

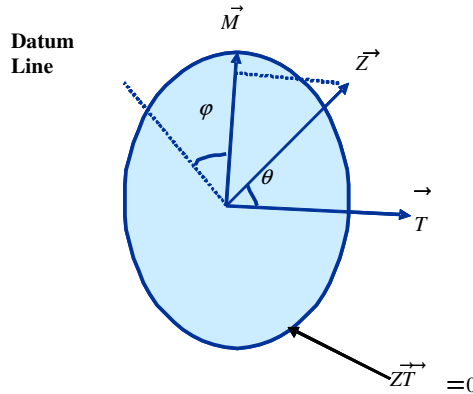


Figure 14. Schematic representation of different vectors in calculating Green's function for anisotropic case ($\vec{T} \equiv \vec{r}$).

Appendix D: Derivation of homogenization relations

Substituting the stress definition from Equation (5) into Equation (4), using the definition of local stress and strain, and finally substituting strain field by displacement field, the equilibrium equation can be solved by Equation (10). For this purpose the Green's function was used to solve the PDE. The strain field is finally obtained as

$$\tilde{u}_k(x) = \int_V G_{kp}(x, x') \frac{\partial[\tilde{c}_{plrs}(x')\varepsilon_{rs}(x')]}{\partial x'_l} dX', \quad (D.1)$$

where dX' is the volume integral on the volume element around position x' ,

By differentiating the above equation, $\tilde{\varepsilon}_{ku}(x)$ is calculated by

$$\tilde{u}_{k,u}(x) = \int_V G_{kp,u}(x, x') \frac{\partial[\tilde{c}_{plrs}(x')\varepsilon_{rs}(x')]}{\partial x'_l} dX' + \overbrace{\int_V G_{kp}(x, x') \frac{\partial[\tilde{c}_{plrs}(x')\varepsilon_{rs}(x')]}{\partial x'_l \partial x_u} dX'}^0. \quad (D.2)$$

It is observed that the second term is zero, since the term $[\tilde{c}_{plrs}(x')\varepsilon_{rs}(x')]$ is just a function of x' , whereas the derivative is with respect to x . Therefore, the strain can be calculated as

$$\tilde{\varepsilon}_{ku} = \int_V \frac{1}{2} [G_{kp,u}(x, x') + G_{up,k}(x, x')] \frac{\partial[\tilde{c}_{plrs}(x')\varepsilon_{rs}(x')]}{\partial x'_l} dX'. \quad (D.3)$$

Defining the first derivative of the Green's function as

$$K_{kpu} = \frac{(G_{kp,u} + G_{up,k})}{2}, \quad (D.4)$$

multiplying the strain in Equation (D.3) by the value of the local moduli $\tilde{c}_{ijk}(x)$, and averaging with respect to x ,

$$\langle \tilde{c}_{ijk}(x) \tilde{\varepsilon}_{ku}(x) \rangle = \int_V \int_{V'} K_{kpu} \tilde{c}_{ijk}(x) \frac{\partial[\tilde{c}_{plrs}(x')\varepsilon_{rs}(x')]}{\partial x'_l} dX' dX, \quad (D.5)$$

is found, where dX is the volume integral on the volume element around position x . Substituting the local strain field from Equation (8), the above equation can be rewritten by

$$\begin{aligned} \langle \tilde{c}_{ijk}(x) \tilde{\varepsilon}_{ku}(x) \rangle &= \int_V \int_{V'} K_{kpu} \frac{\partial[\tilde{c}_{ijk}(x) \tilde{c}_{plrs}(x')]}{\partial x'_l} dX' dX \langle \varepsilon_{rs}(x) \rangle \\ &\quad + \int_V \int_{V'} K_{kpu} \frac{\partial[\tilde{c}_{ijk}(x) \tilde{c}_{plrs}(x') \tilde{\varepsilon}_{rs}(x')]}{\partial x'_l} dX' dX. \end{aligned} \quad (D.6)$$

Showing the integral over the variable x as an ensemble average, the above equation is reduced to

$$\begin{aligned} \langle \tilde{c}_{ijk}(x) \tilde{\varepsilon}_{ku}(x) \rangle &= \int_V K_{kpu} \frac{\partial \langle \tilde{c}_{ijk}(x) \tilde{c}_{plrs}(x') \rangle}{\partial x'_l} \langle \varepsilon_{rs} \rangle dX' \\ &\quad + \int_V K_{kpu} \frac{\partial [\langle \tilde{c}_{ijk}(x) \tilde{c}_{plrs}(x') \tilde{\varepsilon}_{rs}(x') \rangle]}{\partial x'_l} dX'. \end{aligned} \quad (D.7)$$

In the above equation $\langle \tilde{c}_{ijk}(x)\tilde{c}_{pmrs}(x') \rangle$ is called a two-point correlation function, and can be calculated using Equation (18). It is observed that the second term is a three-point correlation function. At this time the calculation is truncated up to a two-point probability function. For this research the second term is neglected. Therefore to get the microstructural information and correlate them to properties, one needs to calculate the first integral in Equation (D.7). A fourth rank tensor $\langle a \rangle$ was introduced as the deviation in the strain field,

$$\langle \tilde{\varepsilon}_{ku} \rangle = \langle a_{kurs} \rangle \langle \varepsilon_{rs} \rangle. \quad (\text{D.8})$$

Substituting the above equation in Equation (D.7) and omitting $\langle \varepsilon_{ku} \rangle$ from both sides, the equation is reduced to

$$\langle \tilde{c}_{ijk}(x)a_{kurs} \rangle = \int_V K_{kpu} \frac{\partial \langle \tilde{c}_{ijk}(x)\tilde{c}_{plrs}(x') \rangle}{\partial x'_l} dX'. \quad (\text{D.9})$$

Applying integration by parts to the above equation, it can be rewritten as

$$\langle \tilde{c}_{ijk}(x)a_{kurs}(x) \rangle = \int_{V'} \frac{\partial [K_{kpu} \langle \tilde{c}_{ijk}(x)\tilde{c}_{plrs}(x') \rangle]}{\partial x'_l} dX' - \int_{V'} K_{kpul}(x, x') \langle \tilde{c}_{ijk}(x)\tilde{c}_{plrs}(x') \rangle dX'. \quad (\text{D.10})$$

References

- [Adams et al. 1987] B. L. Adams, P. R. Morris, T. T. Wang, K. S. Willden, and S. I. Wright, "Description of orientation coherence in polycrystalline materials", *Acta Metall.* **35**:12 (1987), 2935–2946.
- [Adams et al. 1989] B. L. Adams, G. R. Canova, and A. Molinari, "A statistical formulation of viscoplastic behavior in heterogeneous polycrystals", *Texture Microstruct.* **11**:1 (1989), 57–71.
- [Adams et al. 2002] B. L. Adams, M. Lyon, B. Henrie, S. R. Kalidindi, and H. Garmestani, "Spectral integration of microstructure and design", *Mater. Sci. Forum* **408-412** (2002), 487–492.
- [Bacon et al. 1980] D. J. Bacon, D. M. Barnett, and R. O. Scattergood, "Anisotropic continuum theory of lattice defects", *Prog. Mater. Sci.* **23** (1980), 51–262.
- [Beran 1968] M. J. Beran, *Statistical continuum theories*, Interscience Publishers, New York, 1968.
- [Beran et al. 1996] M. J. Beran, T. A. Mason, B. L. Adams, and T. Olsen, "Bounding elastic constants of an orthotropic polycrystal using measurements of the microstructure", *J. Mech. Phys. Solids* **44**:9 (1996), 1543–1563.
- [Corson 1974a] P. B. Corson, "Correlation functions for predicting properties of heterogeneous materials, I: experimental measurement of spatial correlation functions in multiphase solids", *J. Appl. Phys.* **45**:7 (1974), 3159–3164.
- [Corson 1974b] P. B. Corson, "Correlation functions for predicting properties of heterogeneous materials, II: empirical construction of spatial correlation functions for two-phase solids", *J. Appl. Phys.* **45**:7 (1974), 3165–3170.
- [Garmestani and Lin 2000] H. Garmestani and S. Lin, "Statistical continuum mechanics analysis of an elastic two-isotropic-phase composite material", *Compos. B Eng.* **31**:1 (2000), 39–46.
- [Garmestani et al. 1998a] H. Garmestani, P. Kalu, and D. Dingley, "Characterization of Al-8090 superplastic materials using orientation imaging microscopy", *Mater. Sci. Eng. A* **242**:1-2 (1998), 284–291.
- [Garmestani et al. 1998b] H. Garmestani, S. Lin, and B. L. Adams, "Statistical continuum theory for inelastic behavior of a two-phase medium", *Int. J. Plasticity* **14**:8 (1998), 719–731.
- [Garmestani et al. 2001] H. Garmestani, S. Lin, B. Adams, and S. Ahzi, "Statistical continuum theory for large deformation of polycrystalline materials", *J. Mech. Phys. Solids* **49**:3 (2001), 589–607.
- [Hashin and Shtrikman 1962] Z. Hashin and S. Shtrikman, "On some variational principles in anisotropic and nonhomogeneous elasticity", *J. Mech. Phys. Solids* **10**:4 (1962), 335–342.
- [Hashin and Shtrikman 1963] Z. Hashin and S. Shtrikman, "A variational approach to the theory of the elastic behavior of multiphase materials", *J. Mech. Phys. Solids* **11**:2 (1963), 127–140.

- [Hill 1965] R. Hill, “A self-consistent mechanics of composite materials”, *J. Mech. Phys. Solids* **13**:4 (1965), 213–222.
- [Kröner 1972] E. Kröner, *Statistical continuum mechanics: course held at the Department of General Mechanics*, Springer-Verlag, Wien, 1972.
- [Kröner 1977] E. Kröner, “Bounds for effective elastic moduli of disordered materials”, *J. Mech. Phys. Solids* **25**:2 (1977), 137–155.
- [Kröner et al. 1987] E. Kröner, J. Gittus, and J. Zarka, *Modeling small deformations of polycrystals*, Elsevier Applied Science, New York, 1987. 229–230.
- [Lin et al. 2000] S. Lin, H. Garmestani, and B. Adams, “The evolution of probability functions in an inelastically deforming two-phase medium”, *Int. J. Solids Struct.* **37**:3 (2000), 423–434.
- [Mason and Adams 1999] A. T. Mason and B. L. Adams, “Use of microstructural statistics in predicting polycrystalline material properties”, *Metall. Mater. Trans. A* **30**:4 (1999), 969–977.
- [Reuss 1929] A. Reuss, “Berechnung der fließgrenze von mischkristallen auf grund der plastizitätsbedingung für einkristalle”, *Math. Mech.* **9** (1929), 49–58.
- [Saheli 2006] G. P. Saheli, *Homogenization relations for elastic properties based on two-point statistical functions*, PhD dissertation, Georgia Institute of Technology, 2006, Available at <http://smartech.gatech.edu/handle/1853/14492>.
- [Saheli et al. 2004] G. Saheli, H. Garmestani, and B. L. Adams, “Microstructure design of a two phase composite using two-point correlation functions”, *J. Comput. Aided Mater.* **11**:2-3 (2004), 103–115.
- [Tewari et al. 2004] A. Tewari, A. M. Gokhale, J. E. Spowart, and D. B. Miracle, “Quantitative characterization of spatial clustering in three-dimensional microstructures using two-point correlation functions”, *Acta Mater.* **52**:2 (2004), 307–319.
- [Torquato 2002] S. Torquato, *Random heterogeneous materials: microstructure and macroscopic properties*, Springer, New York, 2002.
- [Torquato and Stell 1982] S. Torquato and G. Stell, “Microstructure of two-phase random media, I: the n -point probability functions”, *J. Chem. Phys.* **77**:4 (1982), 2071–2077.
- [Voigt 1889] W. Voigt, “Über die Beziehung zwischen den beiden elastizitätskonstanten isotroper Körper”, *Wied. Ann.* **38** (1889), 573–587.
- [Willis 1965] J. R. Willis, “The elastic interaction energy of dislocation loops in anisotropic media”, *Q. J. Mech. Appl. Math.* **18**:4 (1965), 419–433.

Received 17 Jan 2006. Accepted 8 May 2007.

GHAZAL SAHELI: saheli@gatech.edu

School of Materials Science and Engineering, Georgia Institute of Technology, Atlanta, GA, United States

HAMID GARMESTANI: hamid.garmestani@mse.gatech.edu

School of Materials Science and Engineering, Georgia Institute of Technology, Atlanta, GA, United States

ARUN GOKHALE: arun.gokhale@mse.gatech.edu

School of Materials Science and Engineering, Georgia Institute of Technology, Atlanta, GA, United States

DYNAMIC ANALYSIS OF BANANA FIBER REINFORCED HIGH-DENSITY POLYETHYLENE/POLY (ϵ -CAPROLACTONE) COMPOSITES

RAGHVENDRA KUMAR MISRA, SANDEEP KUMAR, KUMAR SANDEEP AND ASHOK MISRA

Banana fiber reinforced HDPE/PCL (high-density polyethylene/poly (ϵ -caprolactone)) composites have been prepared in the laboratory for the evaluation of mechanical properties. The tensile strength and Young's modulus of the HDPE/PCL blend attains saturation at approximately 20% by weight of PCL addition. Therefore, the 80:20 blend of HDPE/PCL has been selected as the matrix material. It has also been observed that the ductility of the HDPE/PCL blend drops rapidly by addition of more than 15% by weight of PCL. Reinforcement of the banana fiber in an 80:20 HDPE/PCL blend matrix shows improvement in ductility, tensile strength and Young's modulus. In order to study the dynamic response of this banana fiber reinforced HDPE/PCL composite plate, a multiquadric radial basis function (MQRBF) is developed. MQRBF is applied for spatial discretization and a Newmark implicit scheme is used for temporal discretization. The discretization of the differential equations generates a greater number of algebraic equations than the unknown coefficients. To overcome this ill-conditioning, the multiple linear regression analysis, based on the least square error norm, is employed to obtain the coefficients. Simple supported and clamped boundary conditions are considered. Numerical results are compared with those obtained by other analytical methods.

1. Introduction

Fiber reinforced composites are used extensively in various industries such as automobiles, aerospace, and defence and are replacing various metallic structures because of many advantages, such as high strength to weight ratio, enhanced corrosion resistance, and longer fatigue life. In this context, banana fiber reinforced composites have recently gained importance. Banana fibers are mainly used for light-weight composites and green composites in agricultural industries. These composites can also be used for door panels, room partitions, wall cladding, food packaging, home appliances, automotive parts, building and construction, and electrical housing.

Banana fibers are a waste product of banana cultivation, are easily available, and may be reinforced in thermosets and thermoplastics. Fabrication of banana fiber reinforced low-density polyethylene/poly-caprolactone composites has been reported recently by [Sandeep and Misra \[2007\]](#). When the quantity of banana fibers is increased, tensile and flexural properties of the resin matrix [\[Joseph et al. 2002\]](#) is also increased. Addition of banana fibers to brittle phenol formaldehyde resin makes the matrix ductile. The interfacial shear strength indicates a strong adhesion between the lignocellulosic banana fibers and the phenol formaldehyde resin. Reinforcement of bamboo and sisal fibers in thermoplastic resin has also been reported [\[Chen et al. 1998; Ali et al. 2003\]](#).

Keywords: banana fiber, multiquadric radial basis function, eigenvalue.

However, the theoretical analysis of banana fiber reinforced composite plates by conventional methods poses some problems. Generally, finite elements and finite difference methods are used for analysis of composites. The finite element method is not very suitable as it consumes more time in mesh generation than in execution. The vast applications of composite plates in industries have emphasized the development of new efficient numerical technique for the analysis of composite plates. Therefore, to avoid these problems, new methods known as meshless methods have been developed recently. These methods are the meshless local Petrov–Galerkin (MLPG) method [Atluri and Zhu 1998], partition of unity method [Babuska and Melenk 1997], element free Galerkin method (EFGM) [Belystcho et al. 1994], method of finite spheres [De and Bathe 2000], and wavelet Galerkin method [Qian and Weiss 1993]. Kansa [1990] and Franke and Schaback [1997] developed the concept of solving PDEs using radial basis functions (RBF). Fedoseyev et al. [2002] improved the accuracy of the solution by placing the interior knots. Hardy [1971] used the multiquadric radial basis function method (MQRBF) for the interpolation of geographically scattered data. The discretization process in MQRBF is based on the employment of a set of randomly distributed boundary and internal nodes. Coleman [1996] employed RBFs in the analysis of elliptic boundary value problems. Chen et al. [2004] studied the free vibration analysis of circular and rectangular plates by employing the RBF in the imaginary-part fundamental solution. Misra et al. [2007] have recently presented the static and dynamic analysis of anisotropic plates by using the MQRBF method and the multiple linear regression analysis technique.

In light of the above discussion, it appears that some experimental and theoretical investigations on banana fiber reinforced composites could offer some interesting results. This paper reports the fabrication, chemical treatment, and evaluation of properties of banana fiber reinforced high-density polyethylene/polycaprolactone composites. High-density polyethylene (HDPE) and poly (ϵ -caprolactone) (PCL) in 80:20 ratios were selected to make a matrix material. Since the melting point of PCL is 60° C, it could help in the processing of HDPE. With the properties thus obtained, a collocation method based on the MQRBF method is employed for the dynamic analysis of banana fiber reinforced HDPE/PCL composites due to self-weight.

Notation

a, b	Dimension of plates
h	Thickness of plates
R	Aspect ratio (a/b)
ν_{LT}	Major Poisson's ratio
ρ	Mass density of plates
m	Mass of the plate
C_v^*, C_v	Viscous damping, dimensionless viscous damping
$D_{11}, D_{22}, D_{12}, D_{66}$	Flexural rigidity of plates
E_L, E_T	Young's modulus in x^* , y^* direction respectively
G_{LT}	Shear modulus relative to $x^* - y^*$ direction
q, Q	Transverse load, dimensionless transverse load
t^*, t	Time, dimensionless time
w^*	Displacement in z^* direction

w	Dimensionless displacement in z direction
ω	Natural frequency of vibration
ρ_0	Surface density ($\rho_0 = \rho h$)
λ	Eigen value

2. Materials and methods

2.1. Materials. The banana fibers were obtained from Regional Research Laboratory (CSIR) Jorhat, India. Sodium hydroxide and HDPE (HD50MA 180) were obtained from Indian Petrochemicals Corporation Limited, Vadodara. PCL was obtained from Union Carbide Company, USA.

The melt flow index of HDPE was 17.3 (at 190° C/2.16 Kg), the density was 0.98 g/cm³ and the melting temperature was 130° C. PCL is a low melting aliphatic polyester, which is biodegradable and miscible with many polymers. The properties of PCL were as follows: melt flow index 2.2 gm/10 min (at 125° C/2.16 Kg), density 1.145 g/cm³, melting temperature 60° C.

2.2. Chemical treatment of banana fibers. Organic solvents were used to separate the fibers. Better separation of fibers was achieved by using toluene followed by washing with petroleum ether. After separation, the fibers were dipped in sodium hydroxide for achieving better mechanical properties. Banana fibers were pale yellowish brown. When treated with NaOH the color became dark brown.

2.3. Fabrication of composites. A Klockner Windsor single screw extruder having an L/D ratio of 21:1 and screw diameter of 30 mm was used for blending HDPE and PCL. For proper mixing of these polymers, the following optimum parameters were used: screw speed, 35 rpm; barrel zone temperature, 135, 140 and 150° C; die zone temperature, 150° C. After mixing, the mixture was quenched in water. Banana fibers were separated and dried in oven for 3 hours at 80° C. These banana fibers were used for composite fabrication. The untreated and 10% alkali treated banana fibers are designated by UB and TB respectively in the present paper. A prefix indicating the weight % of banana fibers is appended to these letter designations. For example, 9 UB and 13 TB represent blends with 9 weight % untreated banana fibers and 13 weight % alkali treated banana fibers respectively.

2.4. Evaluation of properties. A 10 KN capacity Zwick tensile testing machine model Z010 was used to determine the mechanical properties of these banana fiber reinforced composites. The tex and denier of the fibers were determined by measuring the weight of fibers of known length. The diameter of the fibers was calculated from the density and denier of the fibers. Properties of the banana fibers have been

Treatment with	Designation	% Wt. Loss	Density (g/cm ³)	Tex (g/1000 m)	Denier (g/9000 m)	Diameter (mm)
Untreated	UB	—	1.4	14.2	127.8	0.113
5% NaOH	AIB5	20.31	1.45	13.1	117.9	0.107
10% NaOH	AIB10	25.4	1.48	13.0	117	0.105

Table 1. Properties of banana/modified banana fibers.

Sample designation	HDPE (g)	PCL (g)	Banana Fiber (g)	Wt % of Banana Fibers
M	160	40	0	0
5UB	160	40	10 (untreated)	4.76
5TB	160	40	10 (treated)	4.76
9UB	160	40	20 (untreated)	9.1
9TB	160	40	20 (treated)	9.1
13UB	160	40	30 (untreated)	13
13TB	160	40	30 (treated)	13

Table 2. Composition of the banana fiber reinforced composites.

shown in Table 1. The compositions of banana fiber reinforced composites are given in Table 2. The resulting tensile strength, tensile modulus, and percentage elongation at tensile fracture are presented in Table 3. The matrix (HDPE:PCL, 80:20) has been designated as M , while ML and MT represent the longitudinal and transverse fibers composites respectively.

3. Theoretical analysis

3.1. The multiquadric radial basis function method. Consider a general differential equation:

$$Aw = f(x, y) \quad \text{in } \Omega, \quad (1)$$

$$Bw = g(x, y) \quad \text{on } \partial\Omega. \quad (2)$$

The governing equation for a free flexural vibration of a uniform thin plate is written as follows [Chen et al. 2004]:

$$\nabla^4 w = \lambda^4 w(x), \quad x \in \Omega,$$

where w is the lateral displacement, $\lambda^4 = \omega^2 \rho_0 h / D$, λ is the frequency parameter, ω is the circular frequency, ρ_0 is the surface density, D is the flexural rigidity of the isotropic plate, and h is the thickness of the plate.

In the present work, it is assumed that the banana fiber reinforced composite plate behaves as an orthotropic plate because the diameter of each banana fiber is so small that its contribution to the strength is predominantly along its longitudinal direction. In such a case, Equations (1) and (2) for a uniform thin

Sample designation	Tensile strength (GPa)	Tensile modulus (GPa)	Elongation at break (%)
M	21.4	11.41	4.50
ML	80.8	18.0	7.23
MT	32.9	8.0	6.78

Table 3. Mechanical properties of composites.

orthotropic composite plate can be reduced to

$$Aw = \lambda^4 w, \quad (3)$$

$$Bw = 0, \quad (4)$$

where A is a linear differential operator, B is a linear boundary operator imposed on boundary conditions for the orthotropic plate, and λ is an eigenvalue.

Let $\{P_i = (x_i, y_i)\}_{i=1}^N$ be N collocation points in the domain Ω of which $\{(x_i, y_i)\}_{i=1}^{N_I}$ are interior points and $\{(x_i, y_i)\}_{i=N_I+1}^N$ are boundary points. In the MQRBF method, the approximate solution for the differential Equation (1) with boundary conditions Equation (2) can be expressed as:

$$w(x, y) = \sum_{j=1}^N w_j \varphi_j(x, y),$$

with a multiquadric radial basis:

$$\varphi_j = \sqrt{(x - x_j)^2 + (y - y_j)^2 + c^2} = \sqrt{r_j^2 + c^2},$$

where $\{w_j\}_{j=1}^N$ are the unknown coefficients to be determined, and $\varphi_j(x_j, y_j)$ is a basis function. Other widely used radial basis functions are:

$\varphi(r) = r^3,$	cubic,
$\varphi(r) = r^2 \log(r),$	thin plate splines,
$\varphi(r) = (1 - r)^m + p(r),$	Wendland functions,
$\varphi(r) = e^{-(cr)^2},$	Gaussian,
$\varphi(r) = (c^2 + r^2)^{-1/2},$	inverse multiquadrics.

Here $r = \|P - P_j\|$ is the Euclidean norm between points $P = (x, y)$ and $P_j = (x_j, y_j)$. The Euclidian distance r is real and nonnegative, and c is a positive and constant shape parameter. c is smaller in the domain and larger at the boundary [Ling and Kansa 2004].

3.2. Calculation of eigenvalues. Let N_B be the total number of points on the boundary $\partial\Omega$, N_I is the total number of points inside Ω , and $N = N_I + N_B$. Applying the RBF in Equation (3) gives

$$\sum_{j=1}^N w_j A\varphi\|P_i - P_j\| = \lambda^4 \sum_{j=1}^N w_j \varphi\|P_i - P_j\|, \quad (5)$$

where $i = 1, 2, \dots, N_I$.

Define

$$\mathbf{L} = [A\varphi(\|P_i - P_j\|)]_{N_I \times N},$$

$$\mathbf{M} = [\varphi\|P_i - P_j\|]_{N_I \times N}.$$

Applying the multiquadric radial basis functions (MQRBF) in Equation (4) gives

$$\sum_{j=1}^N w_j B\phi(\|P_i - P_j\|) = 0,$$

where $i = N_{I+1}, N_{I+2}, \dots, N$, and

$$\begin{aligned} \mathbf{K} &= [B\phi(\|P_i - P_j\|)]_{N_B \times N}, \\ \mathbf{w} &= [w_1 w_2 w_3 \cdots w_N]^T. \end{aligned} \quad (6)$$

Equations (5) and (6) can be written as:

$$\begin{aligned} \mathbf{L}\mathbf{w} &= \lambda^4 \mathbf{M}\mathbf{w}, \\ \mathbf{K}\mathbf{w} &= 0. \end{aligned}$$

The general eigenvalue problem becomes (in matrix form):

$$\begin{bmatrix} \mathbf{L} \\ \mathbf{K} \end{bmatrix} \mathbf{w} = \lambda^4 \begin{bmatrix} \mathbf{M} \\ 0 \end{bmatrix} \mathbf{w}.$$

The algorithm of Ferreira et al. [2005] for solving this standard eigenvalue problem has been used in the present analysis as follows:

$$\mathbf{L}^1 \mathbf{w}^2 = \lambda^4 \mathbf{w}^2,$$

where

$$\mathbf{L}^1 = \mathbf{L}\mathbf{D}^{-1} \begin{bmatrix} \mathbf{I}_{N_I \times N_I} & \mathbf{0}_{N_B \times N_I} \end{bmatrix}, \quad \mathbf{w}^2 = [w_1 w_2 w_3 \cdots w_N]^T, \quad \mathbf{D} = [\mathbf{M}\mathbf{K}].$$

4. Results and discussion

The effect of PCL addition on the mechanical properties of the HDPE matrix is shown in Figures 1 and 2. It is apparent that both the tensile modulus and tensile strength increase with percent of PCL addition, and attain almost saturation at about 20% PCL addition by weight. The modulus increases by 41% and the tensile strength by 29% on introducing 20% by weight of PCL into the HDPE matrix. This may be attributed to the higher degree of crystallinity of PCL than HDPE, and better room temperature mechanical properties. It was for this reason that HDPE/PCL blend in 80:20 ratios was selected for the preparation of the banana fiber reinforced composite.

Figures 3 and 4 show the improvement of the tensile modulus and tensile strength of the NaOH treated banana fiber reinforced HDPE/PCL (80:20) blend composite plates. There is an increase of 11% in the tensile modulus and 15% in the tensile strength at 15% volume fraction of fibers.

Figure 5 offers an interesting result. There is a sharp drop in the percentage elongation between 15 and 20% of PCL addition in the HDPE/PCL blend. This shows that the characteristic of the blend changes drastically from ductile to brittle in this interval. However, when the banana fibers were introduced into this blend, the ductile characteristics were improved appreciably, as shown in Figure 6.

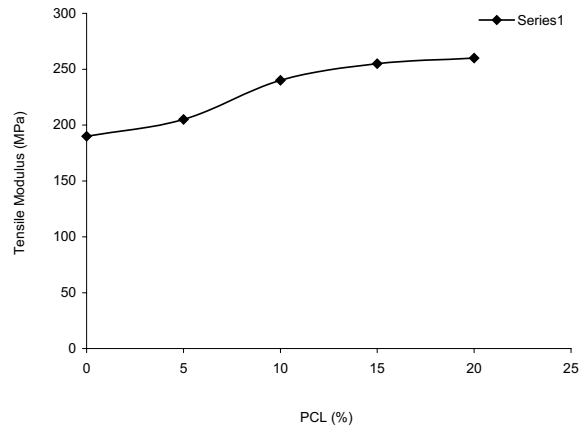


Figure 1. Effect of PCL content on tensile modulus of HDPE/PCL blend.

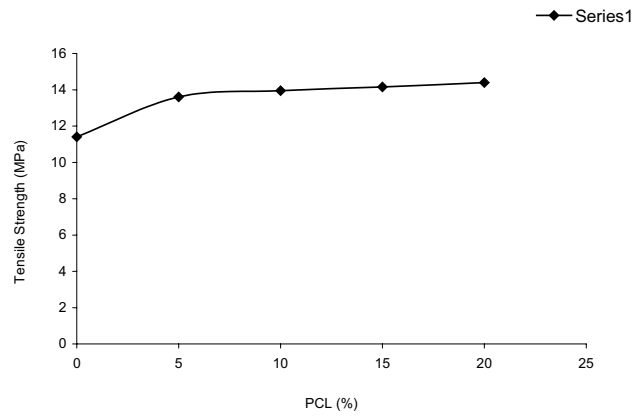


Figure 2. Effect of PCL content on tensile strength of HDPE/PCL blend.

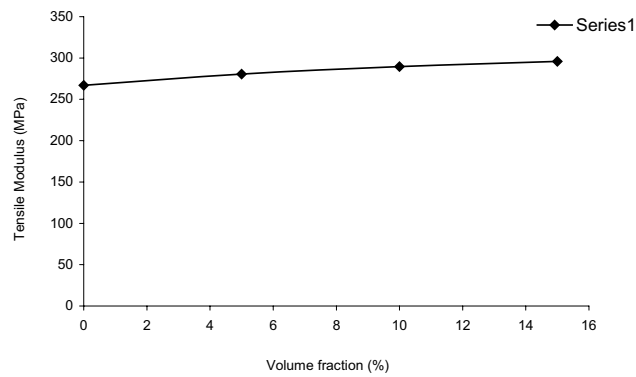


Figure 3. Effect of weight fraction of NaOH treated banana fibers on tensile modulus of HDPE/PCL (80:20) blend.

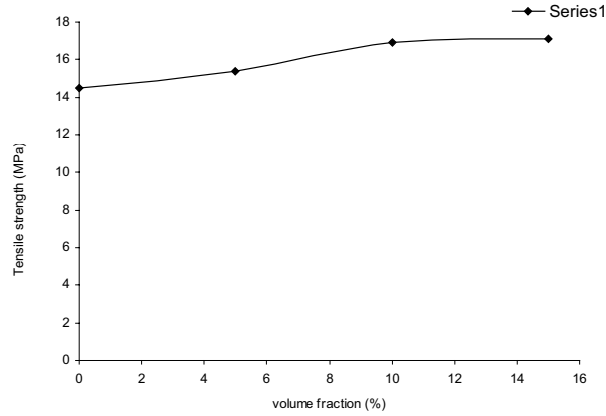


Figure 4. Effect of weight fraction of NaOH treated banana fibers on tensile strength of HDPE/PCL (80:20) blend.

Using the MQRBF method, the dynamic response and natural frequencies of banana fiber reinforced HDPE/PCL composites are obtained. Parameters of the composite plate are as follows:

$$E_L = 18 \text{ GPa}, \quad E_T = 8 \text{ GPa}, \quad G_{LT} = 6.6176 \text{ GPa}, \quad \nu_{LT} = 0.36.$$

The subscripts L and T denote the normal and transverse directions of the fiber.

4.1. Case study 1: dynamic response of composites. Figure 7 shows the geometry, coordinate system, and loading in banana fiber reinforced composites. Neglecting the transverse shear and rotary inertia, the equation describing the banana fiber reinforced composites is expressed in nondimensional form as:

$$(w_{xxxx} + 2R^2\eta w_{xxyy} + R^4\psi w_{yyyy}) + w_{tt} + c_v w_t - Q(x, y, t) = 0, \quad (7)$$

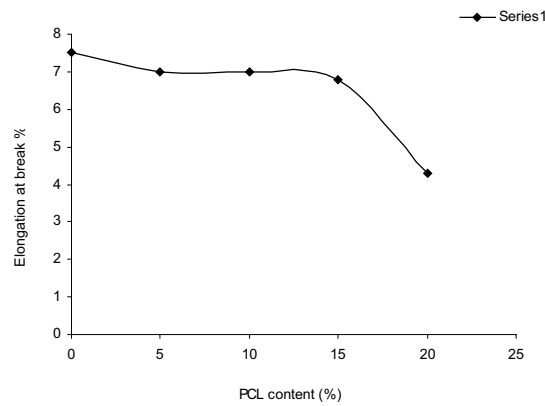


Figure 5. Effect of PCL content on elongation at break of HDPE/PCL blend.

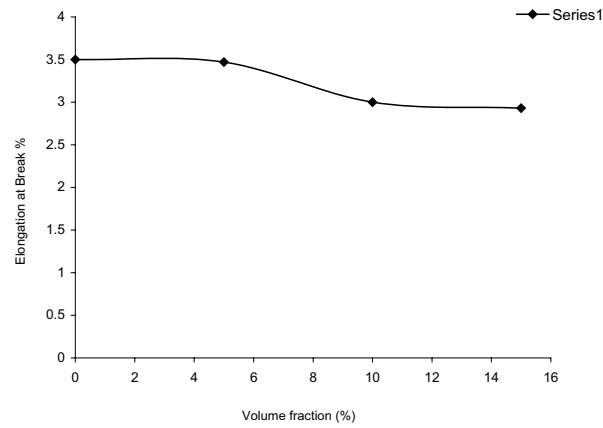


Figure 6. Effect of weight fraction of NaOH treated banana fibers on elongation at break of HDPE/PCL blend.

where the subscript denotes the partial derivative with respect to the variables. The nondimensional quantities are defined by

$$w = w^*/h,$$

$$x = x^*/a,$$

$$y = y^*/b,$$

$$R = a/b,$$

$$t = t^* \sqrt{D_{11}/(\rho a^4 h)},$$

$$Q = qa^4/(D_{11}h),$$

$$C_v = (C_v^*/M) \sqrt{(\rho a^4 h)/D_{11}},$$

$$M = \rho abh,$$

$$\eta = (D_{12} + 2D_{66})/D_{11},$$

$$\psi = D_{22}/D_{11}.$$

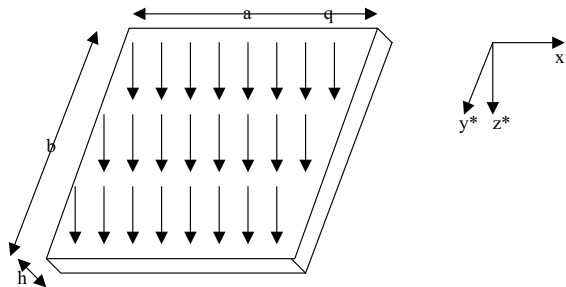


Figure 7. Geometry of the rectangular plate.

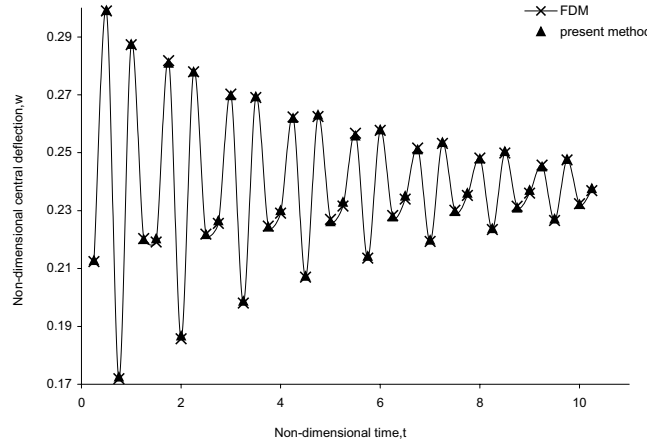


Figure 8. Damped response of a simple supported banana fiber reinforced square orthotropic plate for $C_v = 1.25$.

Boundary conditions for the plate simply supported at all four edges are:

$$\begin{aligned}
 x = 0, 1, \quad w &= 0, \\
 x = 0, 1, \quad w_{xx} &= 0, \\
 y = 0, 1, \quad w &= 0, \\
 y = 0, 1, \quad w_{xx} &= 0.
 \end{aligned} \tag{8a}$$

Boundary conditions for the clamped edge plate are:

$$\begin{aligned}
 x = 0, 1, \quad w &= 0, \\
 x = 0, 1, \quad w_x &= 0, \\
 y = 0, 1, \quad w &= 0, \\
 y = 0, 1, \quad w_y &= 0.
 \end{aligned} \tag{9a}$$

The governing Equation (7) is solved using the multiquadric radial basis function and boundary conditions, Equations (8) and (9), for simply supported and clamped edge plates respectively, and has been presented in Appendix A. In this collocation method, the domain is discretized into $n \times n$ grid points. Inside the domain, there are $(n - 2) \times (n - 2)$ grid points and the remaining grid points are at the boundaries. There are eight boundary conditions: four boundary conditions for x and four for y . The governing equations generate $(n - 2)^2$ equations and every boundary condition creates n equations. Therefore, the total number of equations becomes $(n - 2)^2 + 8n$. Since the total number of unknown coefficients is n^2 , the number of equations is more than the number of unknown coefficients. Hence, this method creates ill-conditioning. To overcome this ill-conditioning, multiple linear regression analysis (Appendix B) based on least-square error norms is employed. A computer program based on the finite difference method (FDM) proposed by Chandrashekhara [2001] is also developed.

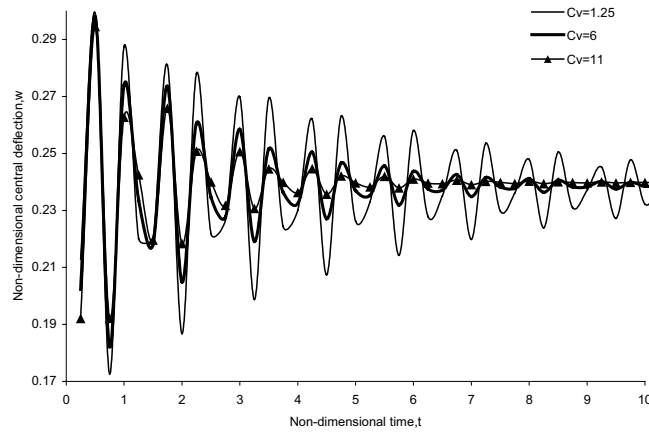


Figure 9. Damped response of a simple supported banana fiber reinforced orthotropic plate for aspect ratio $R = 1$.

The damped response of the simple supported composite plates obtained by the present method and finite difference method has been compared and shown in Figure 8 for nondimensional load $Q = 100$ and nondimensional viscous damping factor $C_v = 1.25$. There is good agreement within the results. According to the present method, at an aspect ratio of 1.0 the maximum deflections at $C_v = 1.25, 6.0,$ and 11.0 are $0.2992, 0.298,$ and $0.2946,$ respectively. However, the fluctuations in deflection with $C_v = 6.0$ and $11.0,$ decay rapidly after the nondimensional time $8.0,$ as shown in Figure 9. Furthermore, at an aspect ratio of 2.0 the maximum deflections at $C_v = 1.25, 6.0,$ and 11.0 are $0.0556, 0.0553,$ and $0.0549,$ respectively (Figure 10). As aspect ratio increases from 1.0 to $2.0,$ nondimensional deflection decreases as shown in Figures 9 and 10. Figure 11 shows the damped response of the simple supported pure HDPE/PCL (80:20) blend orthotropic plate for $R = 1$ and $Q = 100.$ The following features are observed after analyzing Figures 9 and 11, and Table 4 for the simple supported boundary condition:

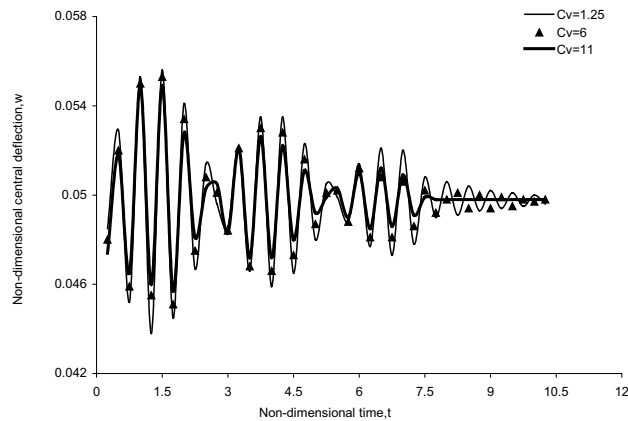


Figure 10. Damped response of a simple supported banana fiber reinforced orthotropic plate for aspect ratio $R = 2$.

Material	$Cv = 1.25$		$Cv = 6.0$		$Cv = 11.0$	
	Maximum Deflection	Stability Time	Maximum Deflection	Stability Time	Maximum Deflection	Stability Time
Pure HDPE/PCL (80:20) blend	0.9665	Did not stabilize after non-dimensional time 10	0.9159	Stabilize after 5.75	0.8602	Stabilize after 3.75
Banana fibers-reinforced high density polyethylene polycaprolactone composites	0.2992	Did not stabilize after non-dimensional time 10	0.298	Stabilize after 10	0.2946	Stabilize after 7.25

Table 4. Damped response of a simple supported orthotropic plate.

- When the damping coefficient increases from 1.25–11, nondimensional maximum deflection decreases in the banana fiber reinforced composite plate and HDPE/PCL blend orthotropic plate.
- At damping coefficients $Cv = 1.25, 6$ and 11 , nondimensional maximum deflections are $0.2992, 0.298, 0.2946$, and $0.9665, 0.9159, 0.8602$ in the banana fiber reinforced composite plate and HDPE/PCL blend orthotropic plate respectively.
- The HDPE/PCL blend orthotropic plate stabilized early compared to the banana fiber reinforced composite plate.

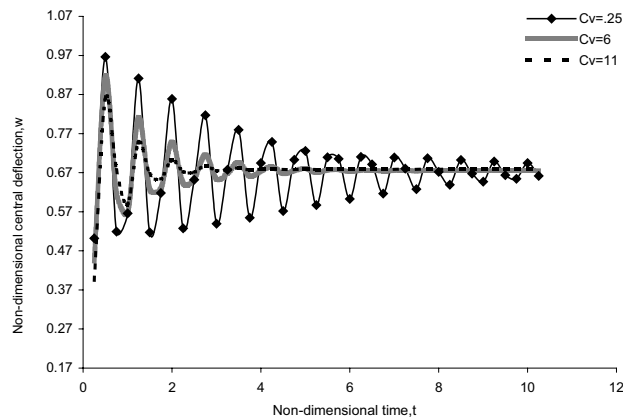


Figure 11. Damped response of a simple supported pure HDPE/PCL (80:20) blend orthotropic plate for $R = 1$ and $Q = 100$.

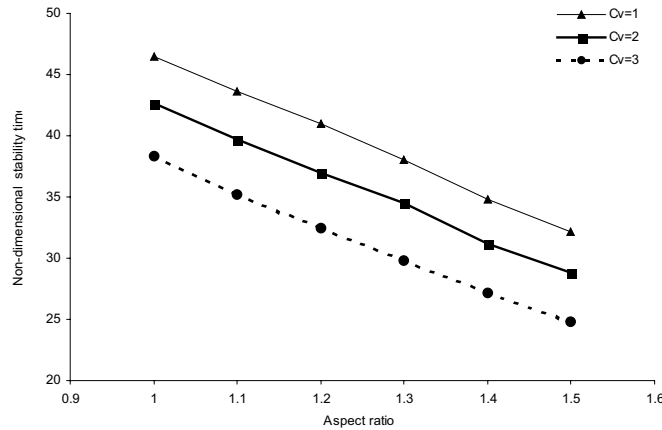


Figure 12. Nondimensional stability time at various aspect ratios for a simple supported banana fiber reinforced orthotropic plate.

It may be noted here that after introducing the banana fibers, the tensile strength of the composite increases. Therefore, the maximum nondimensional deflection decreases in the banana fiber reinforced composite plate compared to HDPE/PCL blend orthotropic plate.

Amash and Zugenmaier [2000] have reported that by incorporation of cellulose fiber, the damping properties of a polypropylene/cellulose composite decreases and stiffness improves. Pothan et al. [2003] reported that in a composite system, damping is affected through the incorporation of fibers. This is due mainly to shear stress concentrations at the fiber ends in association with the additional viscoelastic energy dissipation in the matrix material. Another contributing factor could be the elastic nature of the fiber. When interfacial bonding improves, damping property decreases.

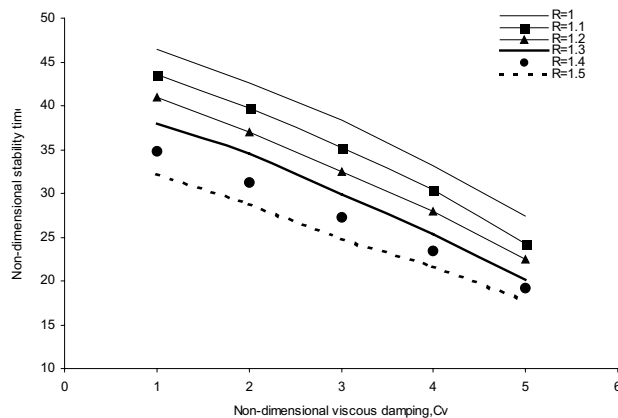


Figure 13. Nondimensional stability time at various nondimensional viscous damping ratios for a simple supported banana fiber reinforced orthotropic plate.

Material	$C_v = 1.25$		$C_v = 6.0$		$C_v = 11.0$	
	Maximum Deflection	Stability Time	Maximum Deflection	Stability Time	Maximum Deflection	Stability Time
Pure HDPE/PCL (80:20) blend	0.2551	Did not stabilize after nondimensional time 10	0.2548	Stabilize after 8	0.254	Stabilize after 6.75
Banana fibers-reinforced high density polyethylene polycaprolactone composites	0.0908	Did not stabilize after nondimensional time 10	0.0904	Stabilize after 10.5	0.0899	Stabilize after 10.25

Table 5. Damped response of a clamped edge orthotropic plate.

Figure 12 shows that as the aspect ratio increases, nondimensional stability time decreases. This may be due to the fact that for a constant load per unit area, the stiffness of the plate increases with an increase in the aspect ratio.

Figure 13 shows the variation of nondimensional stability time with nondimensional viscous damping factor for various aspect ratios. It is observed that as the nondimensional viscous damping factor increases, nondimensional stability time decreases. Furthermore, the effect of C_v on the nondimensional

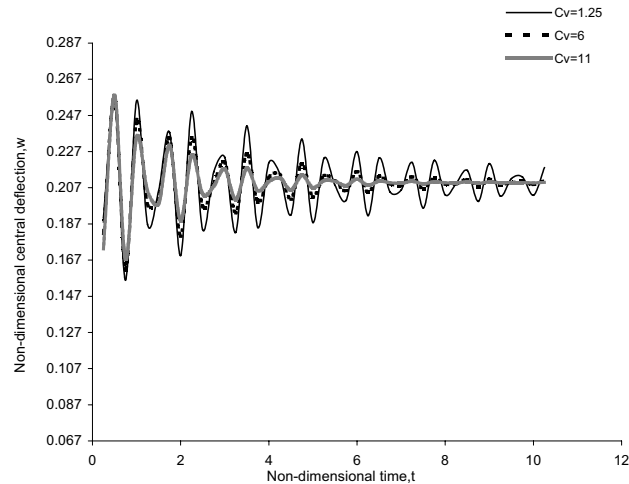


Figure 14. Damped response for a clamped edges pure HDPE/PCL (80:20) blend orthotropic plate for $R = 1$ and $Q = 100$.

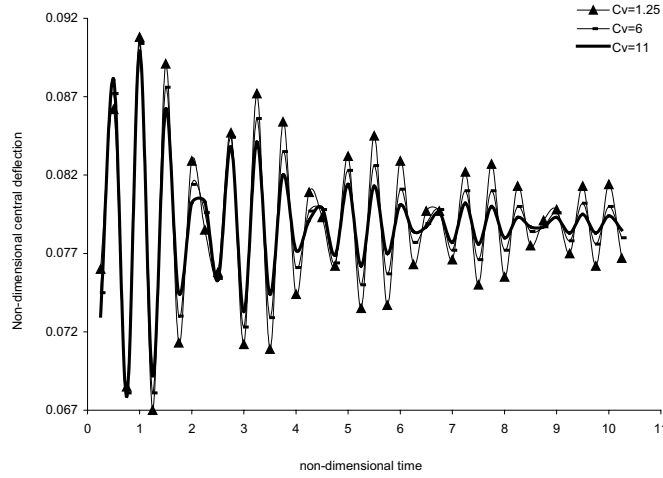


Figure 15. Damped response of a clamped supported banana fiber reinforced orthotropic plate for aspect ratio, $R = 1$.

stability time is more pronounced than the effect of the aspect ratio, as seen in Figures 12 and 13. Similarly, Figures 14, 15 and Table 5 show the damped responses for the clamped edges pure HDPE/PCL (80:20) blend and composite orthotropic plates, at $R = 1$ and $Q = 100$. The pure HDPE/PCL (80:20) blend orthotropic plate behaves identically under the clamped edge boundary conditions and the simple supported boundary conditions, but in the clamped edge boundary conditions the HDPE/PCL blend orthotropic plate stabilizes more slowly than the simple supported boundary conditions. The maximum deflections in the clamped edges composite plate are 0.0908, 0.0904, and 0.0899 at $C_v = 1.25$, 6.0, and 11.0, respectively, as shown in Figure 15. It should be noted that the deflections in clamped edge conditions are much less than those in simple supported edge conditions.

4.2. Case study 2: natural frequency of banana fiber reinforced with high-density polyethylene / polycaprolactone composites. The equation governing the free vibration of orthotropic plates is:

$$(D_{11}/D_{22})w_{xxxx} + 2(H/D_{22})w_{xxyy} + w_{yyyy} = \lambda^4 w(x, y), \quad (10)$$

where $\lambda^4 = \omega^2 \rho_0 h / D_{22}$ and $H = (D_{12} + 2x D_{66})$. The natural frequency of the simply supported orthotropic plate is obtained by [Ashton and Whitney 1970] as:

$$\omega_{mn} = \frac{\pi^2}{R^2 b^2} \frac{1}{\sqrt{\rho}} \sqrt{D_{11} m^4 + 2(D_{12} + 2D_{66}) m^2 n^2 R^2 + D_{22} n^4 R^4},$$

where m and n are integers. Different natural frequencies are obtained at different combinations of m and n . On the other hand, Hearmon [1959] has expressed the natural frequencies of a clamped supported plate as:

$$\omega_{mn} = \frac{1}{a^2 \sqrt{\rho}} \sqrt{D_{11} \alpha_1^4 + 2(D_{12} + 2D_{66}) \alpha_2 R^2 + \alpha_3^4 D_{22} R^4},$$

where α_1 , α_2 , and α_3 are the coefficients, and their values have been given in Table 6. Substituting the property values of banana fiber reinforced high-density polyethylene/polycaprolactone composites,

α_1	α_3	α_2	m	n
4.730	4.730	151.3	1	1
4.730	$(n + 0.5)\pi$	$12.30\alpha_3(\alpha_3 - 2)$	1	2, 3, 4
$(m + 0.5)\pi$	4.730	$12.30\alpha_1(\alpha_1 - 2)$	2, 3, 4	1
$(m + 0.5)\pi$	$(n + 0.5)\pi$	$(\alpha_1\alpha_3(\alpha_1 - 2)(\alpha_3 - 2))$	2, 3, 4	2, 3, 4

Table 6. Coefficients for natural frequency calculations.

The natural frequencies of free vibration at simple supported and clamped edge boundary conditions have been evaluated by the present method and by the [Ashton and Whitney 1970] and [Hearmon 1959] methods. The results are presented in Tables 7 and 8 respectively, which show a good agreement.

5. Conclusions

Preparation of banana fiber reinforced HDPE/PCL composite plates, evaluation of their mechanical properties, and theoretical dynamic analyses under self-weight of the composite plate have been presented in this work. The tensile strength and Young's modulus of the HDPE/PCL blend attain saturation at approximately 20% by weight of PCL addition. Therefore, the 80:20 blend of HDPE/PCL has been selected for the matrix materials. It has also been observed that the ductility of the HDPE/PCL blend drops rapidly by addition of more than 15% by weight of PCL. Reinforcement of banana fibers into the 80:20 HDPE/PCL blend matrix shows improvement in ductility, tensile strength and Young's modulus.

Furthermore, the MQRBF method is used to analyze the dynamic behavior of the HDPE/PCL blend orthotropic plate and the banana fiber reinforced HDPE/PCL composite plate due to self-weight. This method is more advantageous than the finite element and finite difference methods because it does not

a/b	Mode	m	n	k^\dagger	k (Present)
1	1st	1	1	2.6624	2.6731
	2nd	1	2	5.7968	5.8102
	3rd	1	3	10.8533	10.8624
	4th	2	1	7.2355	7.2541
2	1st	1	1	1.4492	1.4498
	2nd	1	2	4.4698	4.4735
	3rd	1	3	9.4751	9.4902
	4th	2	1	2.6624	2.6731
3	1st	1	1	1.2059	1.2261
	2nd	1	2	4.2111	4.2109
	3rd	1	3	9.2123	9.2345
	4th	2	1	1.7749	1.7830

Table 7. The normalized fundamental frequency $\omega = \frac{k\pi^2}{b^2} \sqrt{\frac{D_{22}}{\rho}}$ of a simple supported banana fiber reinforced orthotropic plate. \dagger [Ashton and Whitney 1970].

<i>a/b</i>	ω_{mn}	<i>m</i>	<i>n</i>	Hearmon <i>k</i>	Present <i>k</i>
1	ω_{11}	1	1	46.9840	48.1430
	ω_{12}	1	2	84.2114	85.4823
	ω_{13}	1	3	142.7529	142.8692
	ω_{21}	2	1	105.8893	106.9134
	ω_{22}	3	1	194.9038	195.6231
	ω_{14}	1	4	221.5417	223.4689
2	ω_{11}	1	1	107.0414	108.0613
	ω_{12}	1	2	265.6229	266.8829
	ω_{13}	1	3	503.1788	503.6571
	ω_{21}	2	1	158.8229	158.9673
	ω_{22}	3	1	243.9031	245.0341
	ω_{14}	1	4	819.3282	820.5245
3	ω_{11}	1	1	216.5571	217.6572
	ω_{12}	1	2	572.9067	572.8692
	ω_{13}	1	3	1106.70	1107.48
	ω_{21}	2	1	261.9165	261.4561
	ω_{22}	3	1	339.6262	341.3216
	ω_{14}	1	4	1817.40	1819.51

Table 8. The normalized fundamental frequency $\omega = \frac{k}{a^2} \sqrt{\frac{D_{22}}{\rho}}$ of a clamped supported banana fiber reinforced orthotropic plate.

require generation of a mesh. In this collocation method, the number of equations generated is more than the number of unknowns. Therefore, multiple regression analysis is used to overcome this incompatibility. The present results are compared with those obtained by the finite difference method as well as the results available in the literature. The banana fiber reinforced composite plate shows less deflection due to high tensile strength but takes more time to stabilize compared to HDPE/PCL blend orthotropic plate. After the incorporation of fibers, the damping properties of the banana fiber reinforced composite plate decrease and stiffness increases. The natural frequencies are determined for the self-weight of the composite plate. This method is found to be effective in the dynamic response studies of the composite plates.

Appendix A: Multiquadric method for governing differential equation

Substitution of the radial basis functions in Equation (9) gives

$$\left(\sum_{j=1}^N w_j \frac{\partial^4}{\partial x^4} \varphi_j + 2\lambda^2 \eta \sum_{j=1}^N w_j \frac{\partial^4}{\partial x^2 \partial y^2} \varphi_j + \sum_{j=1}^n \lambda^4 \psi w_j \frac{\partial^4}{\partial y^4} \varphi_j \right) + \sum_{j=1}^N w_j \frac{\partial^2}{\partial t^2} \varphi_j - C_v w_j \frac{\partial}{\partial t} \varphi_j - Q = 0.$$

Substitution of the radial basis functions in Equation (10) gives

$$\left(D_{11}/D_{22} \sum_{j=1}^N w_j \frac{\partial^4}{\partial x^4} \varphi_j + 2H/D_{22} \sum_{j=1}^N w_j \frac{\partial^4}{\partial x^2 y^2} \varphi_j + \sum_{j=1}^N w_j \frac{\partial^4}{\partial y^4} \varphi_j \right) = \lambda^4 \sum_{j=1}^N w_j \varphi_j.$$

Boundary conditions for simple supported edges:

$$\begin{aligned} x = 0, 1 \quad \sum_{j=1}^N w_j \varphi_j &= 0, & y = 0, 1 \quad \sum_{j=1}^N w_j \varphi_j &= 0, \\ x = 0, 1 \quad \sum_{j=1}^N w_j \frac{\partial^2}{\partial x^2} \varphi_j &= 0, & y = 0, 1 \quad \sum_{j=1}^N w_j \frac{\partial^2}{\partial y^2} \varphi_j &= 0. \end{aligned}$$

Boundary conditions for clamped edges:

$$\begin{aligned} x = 0, 1 \quad \sum_{j=1}^N w_j \varphi_j &= 0, & y = 0, 1 \quad \sum_{j=1}^N w_j \varphi_j &= 0, \\ x = 0, 1 \quad \sum_{j=1}^N w_j \frac{\partial}{\partial x} \varphi_j &= 0, & y = 0, 1 \quad \sum_{j=1}^N w_j \frac{\partial}{\partial y} \varphi_j &= 0. \end{aligned}$$

Appendix B: Multiple regression analysis

$A \cdot a = p$, where A is an $(l \times k)$ coefficient matrix, a is a $(k \times 1)$ vector, and p is a $(l \times 1)$ load vector. Approximating the solution by introducing the error vector e , one gets $p = Aa + e$, where e is an $(l \times 1)$ vector. To minimize the error norm, function S is defined as $S(a) = e^T e = (p - Aa)^T (p - Aa)$. The least-square norm must satisfy $(\partial S / \partial a)_a = -2A^T p + 2A^T Aa = 0$. This can be expressed as $a = (A^T A)^{-1} A^T P$ or $a = B \cdot p$. The matrix B is evaluated once and stored for subsequent usages.

References

- [Ali et al. 2003] R. Ali, S. Iannace, and L. Nicolais, "Studies on sisal reinforced thermoplastic", *composites J. Appl. Polym. Sci.* **88** (2003), 1637.
- [Amash and Zugenmaier 2000] A. Amash and P. Zugenmaier, "Morphology and properties of isotropic and oriented samples of cellulose fiber-polypropylene composites", *Polymer* **41** (2000), 1589-96.
- [Ashton and Whitney 1970] J. E. Ashton and J. M. Whitney, *Theory of laminated plates*, Technomic Publishing Co., Inc, 1970.
- [Atluri and Zhu 1998] S. N. Atluri and T. Zhu, "A new meshless local Petrov-Galerkin (MLPG) approach in computational mechanics", *Comput. Mech.* **22** (1998), 117-27.
- [Babuska and Melenk 1997] I. Babuska and J. M. Melenk, "The partition of unity method", *Int. J. Numer. Meth. Eng.* **40** (1997), 727-758.
- [Belystcho et al. 1994] T. Belystcho, Y. Lu, and L. Gu, "Element free Galerkin methods", *Int. J. Numer. Meth. Eng.* **37** (1994), 229-256.
- [Chandrashekhara 2001] K. Chandrashekhara, *Theory of plates*, Universities Press, India, 2001. Limited.
- [Chen et al. 1998] X. Chen, Q. Guo, and Y. Mi, "Studies on bamboo reinforced thermoplastic composites", *J. Appl. Polym. Sci.* **69** (1998), 1891.

- [Chen et al. 2004] J. T. Chen, I. L. Chen, K. H. Chen, Y. T. Lee, and Y. T. Yeh, "A meshless method for free vibration analysis of circular and rectangular clamped plates using radial basis function", *Eng. Anal. Bound. Elem.* **28** (2004), 535–545.
- [Coleman 1996] C. J. Coleman, "On the use of radial basis functions in the solution of elliptic boundary value problems", *Comput. Mech.* **17**:6 (1996), 418–422.
- [De and Bathe 2000] S. De and K. J. Bathe, "The method of finite spheres", *Comput. Mech.* **25** (2000), 329–345.
- [Fedoseyev et al. 2002] A. I. Fedoseyev, M. J. Friedman, and E. J. Kansa, "Improved multiquadric method for elliptic partial differential equations via PDE collocation on the boundary", *Comput. Math. Appl.* **43**:3–5 (2002), 491–500.
- [Ferreira et al. 2005] A. J. M. Ferreira, C. M. C. Roque, and R. M. N. Jorge, "Free vibration analysis of symmetric laminated composite plates by FSDT and radial basis functions", *Comput. Methods Appl. Mech. Eng.* **194** (2005), 4265–4278.
- [Franke and Schaback 1997] C. Franke and R. Schaback, "Solving partial differential equations by collocation using radial basis functions", *Appl. Math. Comput.* **93** (1997), 73–82.
- [Hardy 1971] R. L. Hardy, "Multiquadric equations of topography and other irregular surfaces", *Geophys. Res.* **176** (1971), 1905–1915.
- [Hearmon 1959] R. F. S. Hearmon, "The frequency of flexural vibration of rectangular orthotropic plates with clamped or supported edges", *J. Appl. Mech. (Trans. ASME)* **12** (1959), 537–540.
- [Joseph et al. 2002] S. Joseph, M. S. Sreekala, and S. Thomas, "Studies on resol matrix resin", *Composites* **62** (2002), 1857.
- [Kansa 1990] E. J. Kansa, "Multiquadrics—a scattered data approximation scheme with applications to computational fluid dynamics, i: Surface approximations and partial derivative estimates", *Comput. Math. Appl.* **19**:8/9 (1990), 127–145.
- [Ling and Kansa 2004] L. Ling and E. J. Kansa, "Preconditioning for radial basis functions with domain decomposition methods", *Math. Comput. Model.* **40** (2004), 1413–1427.
- [Misra et al. 2007] R. K. Misra, K. Sandeep, and A. Misra, "Analysis of anisotropic plate using multiquadric radial basis function", *Eng. Anal. Bound. Elem.* **31** (2007), 28–34.
- [Poathan et al. 2003] L. A. Poathan, Z. Oommen, and S. Thomas, "Dynamic mechanical analysis of banana fiber reinforced polyester composites", *Composit. Sci. Tech.* **63** (2003), 283–293.
- [Qian and Weiss 1993] S. Qian and J. Weiss, "Wavelet and the numerical solution of partial differential equations", *J. Comput. Phys.* **106** (1993), 155–175.
- [Sandeep and Misra 2007] K. Sandeep and R. K. Misra, "Analysis of banana fibers reinforced low-density polyethylene/ poly (ϵ -caprolactone) composites", *Int. J. Soft mater.* **4**:1 (2007), 1–13.

Received 30 Oct 2006. Accepted 8 May 2007.

RAGHVENDRA KUMAR MISRA: mishrark_kanpur@yahoo.com

Department of Mechanical Engineering, Birla Institute of Technology, Mesra, Ranchi 835215 Jharkhand, India

SANDEEP KUMAR: sandeepasom@yahoo.com

Department of Polymer Engineering, Birla Institute of Technology, Mesra, Ranchi 835215 Jharkhand, India

KUMAR SANDEEP: sandeepkumar333@yahoo.com

Department of Mechanical Engineering, Institute of Technology, Banaras Hindu University, Varanasi 221005, India

ASHOK MISRA: dr_ashok_misra@rediffmail.com

Department of Mechanical Engineering, Birla Institute of Technology, Mesra, Ranchi 835215 Jharkhand, India

GRADIENT REPRODUCING KERNEL PARTICLE METHOD

ALIREZA HASHEMIAN AND HOSSEIN M. SHODJA

This paper presents an innovative formulation of the RKPM (reproducing kernel particle method) pioneered by Liu. A major weakness of the conventional RKPM is in dealing with the derivative boundary conditions. The EFGM (element free Galerkin method) pioneered by Belytschko shares the same difficulty. The proposed RKPM referred to as GRKPM (gradient RKPM), incorporates the first gradients of the function in the reproducing equation. Therefore in three-dimensional space GRKPM consists of four independent types of shape functions. It is due to this feature that the corrected collocation method can be readily generalized and combined with GRKPM to enforce the EBCs (essential boundary conditions), involving both the field quantity and its first derivatives simultaneously. By considering several plate problems it is observed that GRKPM yields solutions of higher accuracy than those obtained using the conventional approach, while for a desired accuracy the number of particles needed in GRKPM is much less than in the traditional methodology.

1. Introduction

Boundary value problems (BVPs) often have essential boundary conditions (EBCs) that involve derivatives, for example, in beams and plates, where slopes are commonly enforced at the boundaries. Such problems are solved numerically using meshless techniques like the reproducing kernel particle method (RKPM) and the element free Galerkin method (EFGM), pioneered by Liu et al. [1995] and Belytschko et al. [1994b], respectively. However, both methods require an often awkward auxiliary method for enforcing the EBCs. Li and Liu [2002] gives a useful review of the previous methodologies.

We summarize the major contributions specifically aimed at remedying the issue of EBCs. The method of Lagrange multipliers is a classic approach [Belytschko et al. 1994b]. However, it is unattractive because it increases the number of unknowns, causes a loss of positive definiteness, and leads to an awkward system of linear equations. Another method is a modified variational principle [Lu et al. 1994] that interprets the Lagrange multipliers and replaces them by physical quantities. Although it leads to a banded set of equations, the coefficient matrix is not necessarily positive definite and the results are less accurate than those obtained by using Lagrange multipliers. The penalty method [Belytschko et al. 1994a; Zhu and Atluri 1998] is a very simple and effective approach which does not increase the number of unknowns. However, it does not satisfy the EBCs exactly, and its accuracy depends on the penalty factor. Yet another approach couples EFGM and finite element method (FEM) [Krongauz and Belytschko 1996; Liu et al. 1997] by using FEM for the boundaries and their neighboring domains and using EFGM elsewhere. This technique dramatically simplifies enforcing the EBCs. However, it loses the advantage of the meshfree technology near the boundaries. Another idea uses the singular kernel function to enforce the Kronecker delta property [Lancaster and Salkauskas 1981]. It enforces the EBCs

Keywords: meshfree, RKPM, gradient, mixed boundary conditions, plates.

efficiently, but it works only when the dilation parameter falls within a limited range. When it is too large, the convergence rate deteriorates rapidly. Finally, the transformation technique, first proposed by Chen et al. [1996], can efficiently impose the EBCs for meshless methods. However, it cannot be applied when the EBCs involve derivatives.

Liu et al. [1996a] took advantage of the Hermite polynomials and proposed the Hermite reproducing kernel method (HRKM), which incorporates the derivative terms into the reproducing equation. In the one-dimensional formulation, four admissible forms were presented for selecting the modified kernels associated with the derivative terms. However, they claimed that the only form that can be generalized to higher dimensions violates the second order reproducing condition. As a result, it reconstructs the function less accurately than the standard RKPM. Moreover, the EBCs were enforced by an auxiliary method which was not stated explicitly. Atluri et al. [1999] extended the conventional moving least squares (MLS) interpolant, first presented by Lancaster and Salkauskas [1981], to Hermite-type interpolation and called it generalized MLS (GMLS). For illustration, Atluri et al. [1999] considered a one-dimensional thin beam and imposed the EBC using the penalty method. Later, Tiago and Leitão [2004] used GMLS to solve the isotropic Kirchhoff plate. They enforced the EBCs using Lagrange multipliers. Li et al. [2003] and Lam et al. [2006] employed the Hermite theorem to construct the Hermite–Cloud method based on the classical RKPM but used a fixed kernel instead of a moving one. They chose the strong form of governing partial differential equations; that is, they used the point collocation technique to discretize the governing partial differential equations. Liu et al. [2004] combined a meshfree and a finite element interpolant by introducing a hybrid fundamental equation that incorporates the concepts of both RKPM and FEM. In this manner, they generated a class of hybrid interpolation functions that may achieve a higher order of smoothness in multiple dimensions. They called this technology the reproducing kernel element method (RKEM) and pointed out that it has a great advantage over the traditional FEM. Li et al. [2004] proposed that, by extending the RKEM interpolant to a Hermite-type interpolant, one can obtain higher order Kronecker delta properties suitable for solving BVPs involving higher order partial differential equations. It should be emphasized that RKEM is a mesh-based technique which requires element defining and mapping.

In 1999, we were working on a Master's thesis that studied solving beam-column problems by meshless methods, particularly RKPM. During our work, we found it difficult to enforce the EBCs associated with the deflection and rotation of beam-columns. As the work progressed, we realized that the usual transformation method, however efficient, cannot apply to the derivative type of EBCs. We generalized the transformation technique so that it could accommodate not only the function but also the derivative type of EBCs. In so doing, we modified the RKPM formulation extensively and successfully linked it to the generalized transformation technique. We added a gradient term to the reproducing equation, and, for this reason, we called the new approach the gradient RKPM (GRKPM). The advantage of GRKPM over RKPM is that, in addition to exactly enforcing the EBCs without resorting to the penalty method or Lagrange multipliers, it gives more accurate results and converges faster. Moreover, it gives a banded set of equations with a positive definite matrix [Hashemian 2000].

The one-dimensional formulation of GRKPM of [Hashemian 2000] is not extended straightforwardly to multiple dimensions. In three dimensions, a major difficulty is in choosing the correction functions to produce a well-conditioned system. However, once that has been done, the formulation can be reduced easily back to one or two dimensions. In this work, we present GRKPM in three dimensions, and

hence one and two as well. Besides affirming its accuracy and good convergence, we establish that the approach enforces mixed EBCs by reexamining several thin plate problems solved previously by other methods. Next, we further demonstrate the method's efficacy by considering more complex and physically important problems that are poorly solved by the existing meshless techniques (RKPM and EFGM).

2. Formulating the GRKPM

2.1. Reproducing equation. The starting point for the conventional RKPM is that a given function $u(\mathbf{x})$ in the three-dimensional space (with coordinates x_k) can be expressed by the reproducing formula

$$u^R(\mathbf{x}) = \int_{\Omega} \bar{\phi}_a^0(\mathbf{x}; \mathbf{x} - \mathbf{y})u(\mathbf{y})d\Omega,$$

where $u^R(\mathbf{x})$ is the reproduced function, a is a dilation parameter, and $\bar{\phi}_a^0(\mathbf{x}; \mathbf{x} - \mathbf{y})$ is the modified kernel function associated with the function. We propose expressing $u^R(\mathbf{x})$ as

$$u^R(\mathbf{x}) = \int_{\Omega} \bar{\phi}_a^0(\mathbf{x}; \mathbf{x} - \mathbf{y})u(\mathbf{y})d\Omega + \sum_{k=1}^3 \int_{\Omega} \bar{\phi}_a^k(\mathbf{x}; \mathbf{x} - \mathbf{y})u_{,k}(\mathbf{y})d\Omega. \quad (1)$$

In Equation (1), $u_{,k}(\mathbf{y}) = \partial u(\mathbf{y})/\partial y_k$ and $\bar{\phi}_a^k(\mathbf{x}; \mathbf{x} - \mathbf{y})$ for $k \neq 0$ is the modified kernel function associated with $u_{,k}(\mathbf{y})$. For $k = 0, 1, 2, 3$, we define

$$\bar{\phi}_a^k(\mathbf{x}; \mathbf{x} - \mathbf{y}) = C^k(\mathbf{x}; \mathbf{x} - \mathbf{y})\phi_a(\mathbf{x} - \mathbf{y}),$$

where $\phi_a(\mathbf{x} - \mathbf{y})$ is the kernel function and $C^k(\mathbf{x}; \mathbf{x} - \mathbf{y})$ are correction functions, which are derived from a reference function

$$C(\mathbf{x}; \mathbf{x} - \mathbf{y}) = b_0(\mathbf{x}) + \sum_{i=1}^3 b_i(\mathbf{x})(x_i - y_i) + \frac{1}{2} \sum_{i=1}^3 \sum_{j=1}^3 b_{ij}(\mathbf{x})(x_i - y_i)(x_j - y_j),$$

by the relations

$$\begin{aligned} C^0(\mathbf{x}; \mathbf{x} - \mathbf{y}) &= b_0(\mathbf{x}) + \sum_{i=1}^3 b_i(\mathbf{x})(x_i - y_i), \\ C^k(\mathbf{x}; \mathbf{x} - \mathbf{y}) &= -\frac{\partial C(\mathbf{x}; \mathbf{x} - \mathbf{y})}{\partial y_k}, \quad k = 1, 2, 3. \end{aligned} \quad (2)$$

In the reference function, b_i and b_{ij} ($b_{ij} = b_{ji}$) are unknown coefficients to be determined by the completeness conditions. It should be noted that $C^0(\mathbf{x}; \mathbf{x} - \mathbf{y})$ is just the part of $C(\mathbf{x}; \mathbf{x} - \mathbf{y})$ affine in \mathbf{y} .

Using the previous three equations, one obtains

$$\begin{aligned}\bar{\phi}_a^0(\mathbf{x}; \mathbf{x} - \mathbf{y}) &= \left[b_0(\mathbf{x}) + \sum_{i=1}^3 b_i(\mathbf{x})(x_i - y_i) \right] \phi_a(\mathbf{x} - \mathbf{y}), \\ \bar{\phi}_a^k(\mathbf{x}; \mathbf{x} - \mathbf{y}) &= \left[b_k(\mathbf{x}) + \sum_{i=1}^3 b_{ki}(\mathbf{x})(x_i - y_i) \right] \phi_a(\mathbf{x} - \mathbf{y}), \quad k = 1, 2, 3.\end{aligned}$$

In this result, note that the forms chosen in Equation (2) for the correction functions assure the linear independence of the modified kernels.

2.2. Completeness. Consider the Taylor's series of $u(\mathbf{y})$ around point \mathbf{x} up to second order:

$$u(\mathbf{y}) \cong u(\mathbf{x}) - \sum_{i=1}^3 (x_i - y_i) u_{,i}(\mathbf{x}) + \frac{1}{2} \sum_{i=1}^3 \sum_{j=1}^3 (x_i - y_i)(x_j - y_j) u_{,ij}(\mathbf{x}),$$

Upon substituting this into Equation (1), it follows that

$$u^R(\mathbf{x}) = u(\mathbf{x}) R_0(\mathbf{x}) - \sum_{m=1}^3 u_{,m}(\mathbf{x}) R_m(\mathbf{x}) + \frac{1}{2} \sum_{m=1}^3 \sum_{n=1}^3 u_{,mn}(\mathbf{x}) R_{mn}(\mathbf{x}) + \text{Err}, \quad (4)$$

where Err denotes the cumulative truncation error and

$$\begin{aligned}R_0(\mathbf{x}) &= \int_{\Omega} \bar{\phi}_a^0(\mathbf{x} - \mathbf{y}) d\Omega, \\ R_m(\mathbf{x}) &= \int_{\Omega} (x_m - y_m) \bar{\phi}_a^0(\mathbf{x} - \mathbf{y}) d\Omega - \int_{\Omega} \bar{\phi}_a^m(\mathbf{x} - \mathbf{y}) d\Omega, \quad m = 1, 2, 3, \\ R_{mn}(\mathbf{x}) = R_{nm}(\mathbf{x}) &= \int_{\Omega} (x_m - y_m)(x_n - y_n) \bar{\phi}_a^0(\mathbf{x} - \mathbf{y}) d\Omega \\ &\quad - \int_{\Omega} (x_m - y_m) \bar{\phi}_a^n(\mathbf{x} - \mathbf{y}) d\Omega - \int_{\Omega} (x_n - y_n) \bar{\phi}_a^m(\mathbf{x} - \mathbf{y}) d\Omega, \quad m, n = 1, 2, 3.\end{aligned}$$

In view of Equation (4), the completeness condition on $u^R(\mathbf{x})$ leads to 10 independent conditions [Liu et al. 1996b; Liu et al. 1996a]. Introducing the ijk th moment at the point \mathbf{x} with respect to the kernel function $\phi_a(\mathbf{x} - \mathbf{y})$ as

$$m_{ijk}(\mathbf{x}) = \int_{\Omega} (x_1 - y_1)^i (x_2 - y_2)^j (x_3 - y_3)^k \phi_a(\mathbf{x} - \mathbf{y}) d\Omega, \quad (5)$$

it follows that

$$\mathbf{M}(\mathbf{x}) \boldsymbol{\beta}(\mathbf{x}) = \mathbf{H}, \quad (6)$$

in which $\mathbf{M}(\mathbf{x})$ is

$$\begin{bmatrix} m_{000} & m_{100} & m_{010} & m_{001} & 0 & 0 & 0 & 0 & 0 & 0 \\ m_{100} & m_{200} - m_{000} & m_{110} & m_{101} & -m_{100} & -m_{010} & -m_{001} & 0 & 0 & 0 \\ m_{010} & m_{110} & m_{020} - m_{000} & m_{011} & 0 & -m_{100} & 0 & -m_{010} & -m_{001} & 0 \\ m_{001} & m_{101} & m_{011} & m_{002} - m_{000} & 0 & 0 & -m_{100} & 0 & -m_{010} & -m_{001} \\ m_{200} & m_{300} - 2m_{100} & m_{210} & m_{201} & -2m_{200} & -2m_{110} & -2m_{101} & 0 & 0 & 0 \\ m_{110} & m_{210} - m_{010} & m_{120} - m_{100} & m_{111} & -m_{110} & -m_{020} - m_{200} & -m_{011} & -m_{110} & -m_{101} & 0 \\ m_{101} & m_{201} - m_{001} & m_{111} & m_{102} - m_{100} & -m_{101} & -m_{011} & -m_{200} - m_{002} & 0 & -m_{110} & -m_{101} \\ m_{020} & m_{120} & m_{030} - 2m_{010} & m_{021} & 0 & -2m_{110} & 0 & -2m_{020} & -2m_{011} & 0 \\ m_{011} & m_{111} - m_{001} & m_{021} & m_{012} - m_{010} & 0 & -m_{101} & -m_{110} & -m_{011} & -m_{020} - m_{002} & -m_{011} \\ m_{002} & m_{102} & m_{012} & m_{003} - 2m_{001} & 0 & 0 & -2m_{101} & 0 & -2m_{011} & -2m_{002} \end{bmatrix},$$

the vector containing the unknown coefficients

$$\boldsymbol{\beta}^T(\mathbf{x}) = [b_0(\mathbf{x}) \ b_1(\mathbf{x}) \ b_2(\mathbf{x}) \ b_3(\mathbf{x}) \ b_{11}(\mathbf{x}) \ b_{12}(\mathbf{x}) \ b_{13}(\mathbf{x}) \ b_{22}(\mathbf{x}) \ b_{23}(\mathbf{x}) \ b_{33}(\mathbf{x})],$$

and

$$\mathbf{H}^T = [1 \ 0 \ 0 \ 0 \ 0 \ 0 \ 0 \ 0 \ 0 \ 0].$$

The unknown b_i and b_{ij} are readily determined by solving Equation (6). We compute the first derivatives of $\boldsymbol{\beta}(\mathbf{x})$ by differentiating Equation (6)

$$\mathbf{M}(\mathbf{x})\boldsymbol{\beta}_{,m}(\mathbf{x}) = -\mathbf{M}_{,m}(\mathbf{x})\boldsymbol{\beta}(\mathbf{x}), \quad m = 1, 2, 3,$$

and compute the second derivatives by differentiating the above, as

$$\begin{aligned} \mathbf{M}(\mathbf{x})\boldsymbol{\beta}_{,mn}(\mathbf{x}) &= -\mathbf{M}_{,mn}(\mathbf{x})\boldsymbol{\beta}(\mathbf{x}) \\ &\quad - \mathbf{M}_{,m}(\mathbf{x})\boldsymbol{\beta}_{,n}(\mathbf{x}) \\ &\quad - \mathbf{M}_{,n}(\mathbf{x})\boldsymbol{\beta}_{,m}(\mathbf{x}), \quad m, n = 1, 2, 3, \end{aligned}$$

in the order shown above.

2.3. Shape functions. To extract the shape functions and their associated derivatives, one must discretize the integral in Equation (1). In this paper, we use the trapezoidal rule, and the equation becomes

$$u^R(\mathbf{x}) = \sum_{i=1}^{\text{NP}} \psi_i^0(\mathbf{x})u^i + \sum_{k=1}^3 \sum_{i=1}^{\text{NP}} \psi_i^k(\mathbf{x})u_{,k}^i, \quad (7)$$

where NP is the number of particles,¹ $u^i = u(\mathbf{y}^i)$, $u_{,k}^i = \partial u(\mathbf{y})/\partial y_k|_{\mathbf{y}=\mathbf{y}^i}$, and

$$\begin{aligned} \psi_i^0(\mathbf{x}) &= \left[b_0(\mathbf{x}) + \sum_{j=1}^3 b_j(\mathbf{x})(x_j - y_j^i) \right] \phi_a(\mathbf{x} - \mathbf{y}^i) \Delta \mathbf{y}^i, \\ \psi_i^k(\mathbf{x}) &= \left[b_k(\mathbf{x}) + \sum_{j=1}^3 b_{kj}(\mathbf{x})(x_j - y_j^i) \right] \phi_a(\mathbf{x} - \mathbf{y}^i) \Delta \mathbf{y}^i, \end{aligned} \quad (8)$$

¹ Smooth particle hydrodynamics (SPH) is a meshfree method which was first proposed by Lucy [1977]. Utilizing this method, he modeled the collective behavior of a discrete set of physical particles in astrophysics. For this reason, in RKPM [Liu et al. 1995] and in the present work, the \mathbf{y}^i are called particles rather than nodes.

in which $\psi_i^k(\mathbf{x})$ is the k th shape function for the i th particle evaluated at \mathbf{x} , and $\Delta \mathbf{y}^i$ is the area belonging to the i th particle.

Many authors, for example Donning and Liu [1998] and Liu [2003], have extensively studied various window functions and their effects. In the present work, we use the cubic spline

$$\phi(z) = \begin{cases} \frac{2}{3} - 4z^2 + 4z^3, & 0 \leq |z| \leq \frac{1}{2}, \\ \frac{4}{3} - 4z + 4z^2 - \frac{4}{3}z^3, & \frac{1}{2} < |z| \leq 1, \\ 0, & \text{otherwise,} \end{cases}$$

and construct the three-dimensional window function by multiplying the one-dimensional window functions:

$$\phi_a(\mathbf{x} - \mathbf{y}) = \prod_{i=1}^3 \frac{1}{a_i} \phi\left(\frac{x_i - y_i}{a_i}\right),$$

in which a_i is the dilation parameter associated with the x_i -direction.

Numerically evaluating the unknowns b_i , b_{ij} , and their derivatives requires discretizing the integral in Equation (5) and subsequently calculating the moment $m_{ijk}(\mathbf{x})$. To satisfy the consistency condition, the technique used for discretizing the reproducing equation must be used also for the moment equation [Chen et al. 1996].

The first derivatives of the shape functions are obtained by differentiating Equation (8):

$$\begin{aligned} [\psi_i^0(\mathbf{x})]_{,m} &= \left\{ [b_0(\mathbf{x})]_{,m} + \sum_{j=1}^3 [b_j(\mathbf{x})]_{,m} (x_j - y_j^i) + b_m(\mathbf{x}) \right\} \phi_a(\mathbf{x} - \mathbf{y}^i) \Delta \mathbf{y}^i \\ &\quad + \left\{ b_0(\mathbf{x}) + \sum_{j=1}^3 b_j(\mathbf{x}) (x_j - y_j^i) \right\} [\phi_a(\mathbf{x} - \mathbf{y}^i)]_{,m} \Delta \mathbf{y}^i, \\ [\psi_i^k(\mathbf{x})]_{,m} &= \left\{ [b_k(\mathbf{x})]_{,m} + \sum_{j=1}^3 [b_{kj}(\mathbf{x})]_{,m} (x_j - y_j^i) + b_{km}(\mathbf{x}) \right\} \phi_a(\mathbf{x} - \mathbf{y}^i) \Delta \mathbf{y}^i \\ &\quad + \left\{ b_k(\mathbf{x}) + \sum_{j=1}^3 b_{kj}(\mathbf{x}) (x_j - y_j^i) \right\} [\phi_a(\mathbf{x} - \mathbf{y}^i)]_{,m} \Delta \mathbf{y}^i, \quad k = 1, 2, 3, \end{aligned}$$

with $i = 1, 2, \dots, NP$ and $m = 1, 2, 3$. Differentiating again leads to the shape functions' second derivatives:

$$\begin{aligned} [\psi_i^0(\mathbf{x})]_{,mn} &= \left\{ [b_0(\mathbf{x})]_{,mn} + \sum_{j=1}^3 [b_j(\mathbf{x})]_{,mn}(x_j - y_j^i) + [b_n(\mathbf{x})]_{,m} + [b_m(\mathbf{x})]_{,n} \right\} \phi_a(\mathbf{x} - \mathbf{y}^i) \Delta \mathbf{y}^i \\ &+ \left\{ [b_0(\mathbf{x})]_{,n} + \sum_{j=1}^3 [b_j(\mathbf{x})]_{,n}(x_j - y_j^i) + b_n(\mathbf{x}) \right\} [\phi_a(\mathbf{x} - \mathbf{y}^i)]_{,m} \Delta \mathbf{y}^i \\ &+ \left\{ [b_0(\mathbf{x})]_{,m} + \sum_{j=1}^3 [b_j(\mathbf{x})]_{,m}(x_j - y_j^i) + b_m(\mathbf{x}) \right\} [\phi_a(\mathbf{x} - \mathbf{y}^i)]_{,n} \Delta \mathbf{y}^i \\ &+ \left\{ b_0(\mathbf{x}) + \sum_{j=1}^3 b_j(\mathbf{x})(x_j - y_j^i) \right\} [\phi_a(\mathbf{x} - \mathbf{y}^i)]_{,mn} \Delta \mathbf{y}^i, \end{aligned}$$

$$\begin{aligned} [\psi_i^k(\mathbf{x})]_{,mn} &= \left\{ [b_k(\mathbf{x})]_{,mn} + \sum_{j=1}^3 [b_{kj}(\mathbf{x})]_{,mn}(x_j - y_j^i) + [b_{kn}(\mathbf{x})]_{,m} + [b_{km}(\mathbf{x})]_{,n} \right\} \phi_a(\mathbf{x} - \mathbf{y}^i) \Delta \mathbf{y}^i \\ &+ \left\{ [b_k(\mathbf{x})]_{,n} + \sum_{j=1}^3 [b_{kj}(\mathbf{x})]_{,n}(x_j - y_j^i) + b_{kn}(\mathbf{x}) \right\} [\phi_a(\mathbf{x} - \mathbf{y}^i)]_{,m} \Delta \mathbf{y}^i \\ &+ \left\{ [b_k(\mathbf{x})]_{,m} + \sum_{j=1}^3 [b_{kj}(\mathbf{x})]_{,m}(x_j - y_j^i) + b_{km}(\mathbf{x}) \right\} [\phi_a(\mathbf{x} - \mathbf{y}^i)]_{,n} \Delta \mathbf{y}^i \\ &+ \left\{ b_k(\mathbf{x}) + \sum_{j=1}^3 b_{kj}(\mathbf{x})(x_j - y_j^i) \right\} [\phi_a(\mathbf{x} - \mathbf{y}^i)]_{,mn} \Delta \mathbf{y}^i, \quad k = 1, 2, 3, \end{aligned}$$

with $i = 1, 2, \dots, NP$ and $m, n = 1, 2, 3$.

3. Presenting the shape functions: departure from the conventional type

The aim of this section is to present the shape functions that follow from the proposed reproducing equation, and for this purpose we consider two-dimensional shape functions.

In two dimensions, Equation (8) yields three different types of shape functions $\psi_i^0(\mathbf{x})$, $\psi_i^1(\mathbf{x})$ and $\psi_i^2(\mathbf{x})$:

$$\begin{aligned} \psi_i^0(\mathbf{x}) &= \left[b_0(\mathbf{x}) + \sum_{j=1}^2 b_j(\mathbf{x})(x_j - y_j^i) \right] \phi_a(\mathbf{x} - \mathbf{y}^i) \Delta \mathbf{y}^i, \\ \psi_i^k(\mathbf{x}) &= \left[b_k(\mathbf{x}) + \sum_{j=1}^2 b_{kj}(\mathbf{x})(x_j - y_j^i) \right] \phi_a(\mathbf{x} - \mathbf{y}^i) \Delta \mathbf{y}^i, \quad k = 1, 2, \end{aligned}$$

with $i = 1, 2, \dots, NP$. We emphasize that the conventional RKPM has only one shape function $\psi_i(\mathbf{x})$, regardless of the dimension of the problem, whereas the present method gives rise to k additional shape functions, $\psi_i^k(\mathbf{x})$, for k -dimensional Euclidean space.

Figure 1 shows the shape functions for the conventional RKPM, and Figures 2 and 3 depict the shape functions corresponding to GRKPM. In these figures, the region $[0, 5]^2$ contains 11×11 uniformly distributed particles. The dilation parameter is chosen to be twice the particle spacing in each direction. For illustration, Figures 1–3 display the shape functions associated with certain particles. Specifically selected are the corners located at $(0, 0)$, $(5, 0)$, $(5, 5)$, and $(0, 5)$; the mid-edge points $(2.5, 0)$, $(5, 2.5)$, $(2.5, 5)$, and $(0, 2.5)$; and the center $(2.5, 2.5)$. From Figures 1 and 2, the $\psi_i^0(\mathbf{x})$ from GRKPM are, modulo amplitude, the same as the $\psi_i(\mathbf{x})$ from RKPM. Comparing within Figure 3 reveals that the $\psi_i^2(\mathbf{x})$ are simply the $\psi_i^1(\mathbf{x})$ rotated 90° counterclockwise about the region's center. We point out that $\psi_i^1(\mathbf{x})$ and $\psi_i^2(\mathbf{x})$ are the shape functions associated with the first derivative of the function in the x_1 and x_2 -direction.

4. Applying essential boundary conditions

In the meshfree methods (RKPM/EFM), enforcing EBCs has been a controversial issue among investigators. The basic shortcoming of the methods is that the shape functions do not possess the Kronecker delta property. For this reason, enforcing the EBCs is not as convenient as in FEM.

4.1. Statement of the problem. Consider a three-dimensional domain Ω with the boundary Γ and the associated BVP

$$Lu(\mathbf{x}) = f(\mathbf{x}), \quad \mathbf{x} \in \Omega, \quad (9)$$

in which L is a linear differential operator. Natural boundary conditions may have arbitrary form, whereas EBCs may prescribe the field quantity and/or its first derivatives

$$u_{,k}(\mathbf{x}) = g_k(\mathbf{x}), \quad \mathbf{x} \in \Gamma_{\text{eb}}^k, \quad k = 0, 1, 2, 3, \quad (10)$$

where Γ_{eb}^0 and Γ_{eb}^k are the set of all points \mathbf{x} at which $u(\mathbf{x})$ and $u_{,k}(\mathbf{x})$ are prescribed. Thus the essential boundary is

$$\Gamma_{\text{eb}} = \bigcup_{k=0}^3 \Gamma_{\text{eb}}^k.$$

It is interesting to note that $\Gamma_{\text{eb}}^i \cap \Gamma_{\text{eb}}^j$ may not be empty for $i \neq j$. Suppose S is the space of all $H_2^{(2)}(\Omega)$ functions that satisfy the boundary conditions (10), and define V to be the space of all $H_2^{(2)}(\Omega)$ functions that satisfy the homogeneous EBCs. The spaces S and V may be expressed as

$$S \equiv \{u \mid u \in H_2^{(2)}(\Omega), u_{,k}(\mathbf{x}) = g_k(\mathbf{x}) \text{ on } \Gamma_{\text{eb}}^k, \quad k = 0, 1, 2, 3\}, \quad (11a)$$

$$V \equiv \{w \mid w \in H_2^{(2)}(\Omega), w_{,k}(\mathbf{x}) = 0 \text{ on } \Gamma_{\text{eb}}^k, \quad k = 0, 1, 2, 3\}, \quad (11b)$$

where $H_2^{(2)}(\Omega)$ is a Sobolev space. The governing Equation (9) is cast into the weak form

$$\int_{\Omega} w(\mathbf{x})[Lu(\mathbf{x}) - f(\mathbf{x})]^2 d\Omega = 0. \quad (12)$$

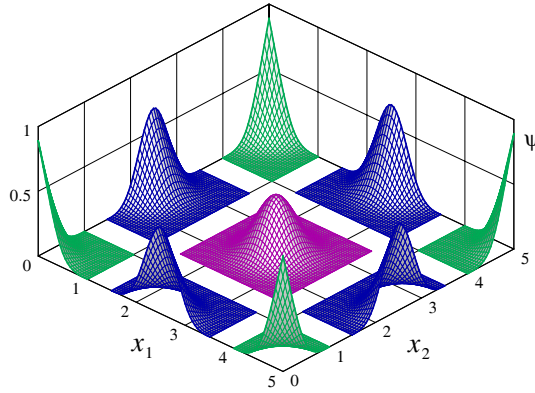


Figure 1. Conventional RKPM shape functions plotted at the corners, mid-edges, and center of the 11×11 uniformly distributed particles with dilation parameter $a = 2\Delta y$.

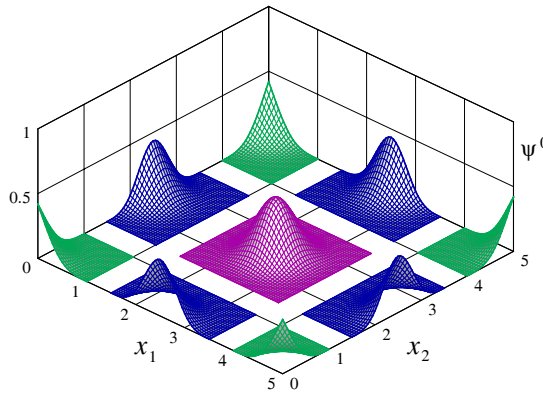


Figure 2. The first type of GRKPM shape functions plotted at the corners, mid-edges, and center of the 11×11 uniformly distributed particles with dilation parameter $a = 2\Delta y$.

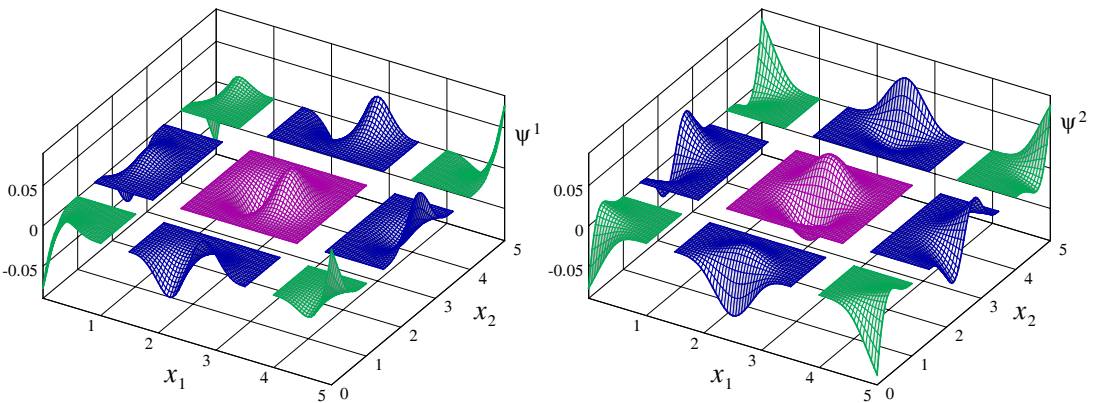


Figure 3. The second and third types of GRKPM shape functions plotted at the corners, mid-edges, and center of the 11×11 uniformly distributed particles with dilation parameter $a = 2\Delta y$.

Employing the shape functions developed in Section 2.3, $u^R(\mathbf{x})$ and $w^R(\mathbf{x})$ may be written as

$$u^R(\mathbf{x}) = \boldsymbol{\psi}(\mathbf{x})\mathbf{d}, \quad (13a)$$

$$w^R(\mathbf{x}) = \boldsymbol{\psi}(\mathbf{x})\mathbf{c}, \quad (13b)$$

with

$$\boldsymbol{\psi}(\mathbf{x}) = [\boldsymbol{\psi}_1(\mathbf{x}) \ \boldsymbol{\psi}_2(\mathbf{x}) \ \cdots \ \boldsymbol{\psi}_{\text{NP}}(\mathbf{x})], \quad (14a)$$

$$\boldsymbol{\psi}_i(\mathbf{x}) = [\psi_i^0(\mathbf{x}) \ \psi_i^1(\mathbf{x}) \ \psi_i^2(\mathbf{x}) \ \psi_i^3(\mathbf{x})], \quad (14b)$$

where $\psi_i^k(\mathbf{x})$, $k = 0, 1, 2, 3$ is given by Equation (8). The vector \mathbf{d} contains the unknowns associated with the degrees of freedom (DOF) u and $u_{,k}$, $k = 1, 2, 3$. We prefer to represent \mathbf{d} as

$$\mathbf{d} = [d_1^T \ d_2^T \ \cdots \ d_{\text{NP}}^T], \quad (15a)$$

$$d_i^T = [d_i^0 \ d_i^1 \ d_i^2 \ d_i^3]. \quad (15b)$$

The unknown vector \mathbf{c} pertains to the test function $w^R(\mathbf{x})$, which we arrange to have the same structure as \mathbf{d} . In view of Equations (13)–(15), Equation (12) may be written as

$$\mathbf{c}^T \mathbf{r} = 0, \quad (16)$$

where

$$\mathbf{r} = \mathbf{K}\mathbf{d} - \mathbf{f}, \quad \mathbf{K} = \int_{\Omega} \boldsymbol{\psi}^T(\mathbf{x})L\boldsymbol{\psi}(\mathbf{x})d\Omega, \quad \mathbf{f} = \int_{\Omega} \boldsymbol{\psi}^T(\mathbf{x})f(\mathbf{x})d\Omega.$$

The matrix \mathbf{K} depends on the operator L . In the next section, we show that the set problem (16) can be rigorously solved for \mathbf{d} by extending the corrected collocation method.

4.2. Extending the corrected collocation method to GRKPM. In collocation methods, the EBCs are enforced exactly at the boundary particles. A number of collocation methods have been developed. The traditional collocation methods, including direct [Lu et al. 1994] and modified [Zhu and Atluri 1998], lead to some inconsistencies when applied to the conventional RKPM [Wagner and Liu 2000]. These inconsistencies exist because the conventional RKPM's shape functions do not possess the Kronecker delta property. Wagner and Liu [2000] give a remedy. Their work is based on the transformation technique [Chen et al. 1996] and is limited to enforcing the EBCs for the function itself. Moreover, the conventional RKPM deals with only one type of shape function. Therefore, in the present situation, where the EBCs involve the function and/or its first derivatives and there are four types of shape functions, the collocation given in [Wagner and Liu 2000] is not applicable and must be modified appropriately.

The starting point is to partition each of the vectors \mathbf{d} , \mathbf{c} , and \mathbf{r} into two subvectors

$$\mathbf{r} = \begin{bmatrix} \mathbf{r}_{\text{eb}} \\ \mathbf{r}_{\sim\text{eb}} \end{bmatrix}, \quad \mathbf{c} = \begin{bmatrix} \mathbf{c}_{\text{eb}} \\ \mathbf{c}_{\sim\text{eb}} \end{bmatrix}, \quad \mathbf{d} = \begin{bmatrix} \mathbf{d}_{\text{eb}} \\ \mathbf{d}_{\sim\text{eb}} \end{bmatrix}. \quad (17)$$

The subscript eb labels the n_{eb} parameters that pertain to the EBCs of Equation (10), whereas $\sim\text{eb}$ labels the remaining $n_{\sim\text{eb}}$ parameters. (Hence $n_{\text{eb}} + n_{\sim\text{eb}}$ counts the total DOF of the system.) Note that each

particle is allowed to have four DOF in u and u_k , $k = 1, 2, 3$. Once the shape function $\boldsymbol{\psi}(\mathbf{x})$ in Equation (14a) and its first derivatives are evaluated for the i th particle \mathbf{x}^i , we may define the matrix

$$\hat{\boldsymbol{\psi}}^T(\mathbf{x}^i) = [\boldsymbol{\psi}^T(\mathbf{x}^i) \ \boldsymbol{\psi}_{,1}^T(\mathbf{x}^i) \ \boldsymbol{\psi}_{,2}^T(\mathbf{x}^i) \ \boldsymbol{\psi}_{,3}^T(\mathbf{x}^i)].$$

The square matrix containing the shape functions and their derivatives for a system with NP particles may be written as

$$\hat{\boldsymbol{\Psi}}^T = [\hat{\boldsymbol{\psi}}^T(\mathbf{x}^1) \ \hat{\boldsymbol{\psi}}^T(\mathbf{x}^2) \ \dots \ \hat{\boldsymbol{\psi}}^T(\mathbf{x}^{\text{NP}})]. \quad (18)$$

Defining

$$\hat{\mathbf{u}}^T(\mathbf{x}^i) = [u(\mathbf{x}^i) \ u_{,1}(\mathbf{x}^i) \ u_{,2}(\mathbf{x}^i) \ u_{,3}(\mathbf{x}^i)],$$

we replace Equation (13a) by

$$\hat{\mathbf{u}}(\mathbf{x}^i) = \hat{\boldsymbol{\psi}}(\mathbf{x}^i)\mathbf{d},$$

and, with the aid of Equation (18), we have

$$\hat{\mathbf{U}} = \hat{\boldsymbol{\Psi}}\mathbf{d}, \quad (19)$$

where

$$\hat{\mathbf{U}}^T = [\hat{\mathbf{u}}^T(\mathbf{x}^1) \ \hat{\mathbf{u}}^T(\mathbf{x}^2) \ \dots \ \hat{\mathbf{u}}^T(\mathbf{x}^{\text{NP}})].$$

Next, we define the vector

$$\hat{\mathbf{W}}^T = [\hat{\mathbf{w}}^T(\mathbf{x}^1) \ \hat{\mathbf{w}}^T(\mathbf{x}^2) \ \dots \ \hat{\mathbf{w}}^T(\mathbf{x}^{\text{NP}})],$$

where

$$\hat{\mathbf{w}}^T(\mathbf{x}^i) = [w(\mathbf{x}^i) \ w_{,1}(\mathbf{x}^i) \ w_{,2}(\mathbf{x}^i) \ w_{,3}(\mathbf{x}^i)],$$

so that, from Equation (18), we have

$$\hat{\mathbf{W}} = \hat{\boldsymbol{\Psi}}\mathbf{c}. \quad (20)$$

Repeating for the vectors $\hat{\mathbf{W}}$ and \mathbf{c} the partition scheme in Equation (17), Equation (20) takes the form

$$\begin{bmatrix} \hat{\mathbf{W}}_{\text{eb}} \\ \hat{\mathbf{W}}_{\sim\text{eb}} \end{bmatrix} = \begin{bmatrix} \hat{\mathbf{E}} & \hat{\mathbf{F}} \\ \hat{\mathbf{G}} & \hat{\mathbf{H}} \end{bmatrix} \begin{bmatrix} \mathbf{c}_{\text{eb}} \\ \mathbf{c}_{\sim\text{eb}} \end{bmatrix}. \quad (21)$$

This, in conjunction with Equation (11b), implies that $\hat{\mathbf{W}}_{\text{eb}} = \mathbf{0}$ and $\hat{\mathbf{W}}_{\sim\text{eb}}$ is arbitrary, hence

$$\begin{bmatrix} \hat{\mathbf{E}} & \hat{\mathbf{F}} \\ \hat{\mathbf{G}} & \hat{\mathbf{H}} \end{bmatrix} \begin{bmatrix} \mathbf{c}_{\text{eb}} \\ \mathbf{c}_{\sim\text{eb}} \end{bmatrix} = \mathbf{0},$$

and $\mathbf{c}_{\sim\text{eb}}$ is arbitrary.

Let

$$\mathbf{T} = \begin{bmatrix} \hat{\mathbf{E}} & \hat{\mathbf{F}} \\ \mathbf{0} & \mathbf{I} \end{bmatrix}, \quad \text{and} \quad \bar{\mathbf{c}} = \mathbf{T}\mathbf{c},$$

then

$$\bar{\mathbf{c}}_{\text{eb}} = \mathbf{0}, \quad (22a)$$

$$\bar{\mathbf{c}}_{\sim\text{eb}} = \mathbf{c}_{\sim\text{eb}} = \text{Arbitrary}. \quad (22b)$$

Likewise, letting $\bar{\mathbf{d}} = \mathbf{T}\mathbf{d}$, then, in view of Equation (19),

$$\bar{\mathbf{d}}_{\text{eb}} = \hat{\mathbf{U}}_{\text{eb}}, \quad \bar{\mathbf{d}}_{\sim\text{eb}} = \mathbf{d}_{\sim\text{eb}}, \quad (23)$$

which relates the elements of $\bar{\mathbf{d}}_{\text{eb}}$ to the prescribed function $g_k(\mathbf{x})$, as defined in Equation (10). Following the procedure given by Wagner and Liu [2000],

$$\begin{bmatrix} \bar{\mathbf{c}}_{\text{eb}}^T & \bar{\mathbf{c}}_{\sim\text{eb}}^T \end{bmatrix} \left(\begin{bmatrix} \bar{\mathbf{K}}_{\text{eb,eb}} & \bar{\mathbf{K}}_{\text{eb,}\sim\text{eb}} \\ \bar{\mathbf{K}}_{\sim\text{eb,eb}} & \bar{\mathbf{K}}_{\sim\text{eb,}\sim\text{eb}} \end{bmatrix} \begin{bmatrix} \bar{\mathbf{d}}_{\text{eb}} \\ \bar{\mathbf{d}}_{\sim\text{eb}} \end{bmatrix} - \begin{bmatrix} \bar{\mathbf{f}}_{\text{eb}} \\ \bar{\mathbf{f}}_{\sim\text{eb}} \end{bmatrix} \right) = 0,$$

where

$$\bar{\mathbf{K}} = (\mathbf{T}^{-1})^T \mathbf{K} \mathbf{T}^{-1}, \quad \bar{\mathbf{f}} = (\mathbf{T}^{-1})^T \mathbf{f},$$

and, using Equation (22) and Equation (23), we have

$$\bar{\mathbf{K}}_{\sim\text{eb,}\sim\text{eb}} \mathbf{d}_{\sim\text{eb}} = \bar{\mathbf{f}}_{\sim\text{eb}} - \bar{\mathbf{K}}_{\sim\text{eb,eb}} \hat{\mathbf{U}}_{\text{eb}}.$$

This equation can be readily solved for $\mathbf{d}_{\sim\text{eb}}$.

5. Kirchhoff plate

Consider a symmetric laminated composite plate on an elastic foundation of varying stiffness $k_f(x_1, x_2)$, as shown in Figure 4. The boundary conditions and the transverse applied loading $q(x_1, x_2)$ are arbitrary. The plate is also subjected to edge forces N_{ij} , $i, j = 1, 2$. According to the classical plate theory known as Kirchhoff theory, the governing partial differential equation associated with the deflection u_3 becomes [Reddy 1984]

$$(-N_{11}u_{3,1} + N_{12}u_{3,2})_{,1} + (-N_{22}u_{3,2} + N_{12}u_{3,1})_{,2} + M_{11,11} + M_{22,22} + 2M_{12,12} + k_f u_3 = q, \quad (24)$$

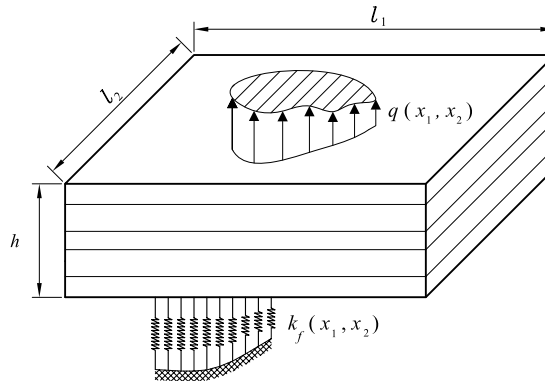


Figure 4. Schematic of a rectangular laminated composite plate with arbitrary loading and boundary conditions.

and the admissible boundary conditions for the present experiments consist of

$$\begin{aligned} \text{on } x_1 = 0, l_1 : & \begin{cases} \text{either } -N_{11}u_{3,1} + N_{12}u_{3,2} + M_{11,1} + 2M_{12,2} = 0 & \text{or } u_3 \text{ specified,} \\ \text{either } M_{11} = 0 & \text{or } u_{3,1} \text{ specified,} \end{cases} \\ \text{on } x_2 = 0, l_2 : & \begin{cases} \text{either } -N_{22}u_{3,2} + N_{12}u_{3,1} + M_{22,2} + 2M_{12,1} = 0 & \text{or } u_3 \text{ specified,} \\ \text{either } M_{22} = 0 & \text{or } u_{3,2} \text{ specified,} \end{cases} \end{aligned} \quad (25)$$

at the corners: either $M_{12} = 0$ or u_3 specified.

In relations (24) and (25),

$$\begin{bmatrix} M_{11} \\ M_{22} \\ M_{12} \end{bmatrix} = \begin{bmatrix} D_{11} & D_{12} & 0 \\ D_{12} & D_{22} & 0 \\ 0 & 0 & D_{66} \end{bmatrix} \begin{bmatrix} u_{3,11} \\ u_{3,22} \\ 2u_{3,12} \end{bmatrix}, \quad (26)$$

where the D_{ij} are called the bending stiffnesses; see [Reddy 1997] for details. For a single isotropic layer with Young's modulus E and Poisson ratio ν , the D_{ij} become

$$D_{11} = D_{22} = D, \quad D_{12} = \nu D, \quad D_{66} = \frac{1-\nu}{2} D, \quad (27)$$

in which $D = Eh^3/(12 - 12\nu^2)$ is called the flexural rigidity of the plate.

The discretized weak form of Equation (24), employing the shape functions for two-dimensional space, $\boldsymbol{\psi}(x_1, x_2)$, yields

$$\begin{aligned} \mathbf{c}^T \mathbf{r} &= 0, \\ \mathbf{r} &= \mathbf{K} \mathbf{d} - \mathbf{f}, \\ \mathbf{K} &= \int_0^{l_2} \int_0^{l_1} dx_1 dx_2 \left[N_{11} \boldsymbol{\psi}_{,1}^T \boldsymbol{\psi}_{,1} + N_{22} \boldsymbol{\psi}_{,2}^T \boldsymbol{\psi}_{,2} + N_{12} (\boldsymbol{\psi}_{,1}^T \boldsymbol{\psi}_{,2} + \boldsymbol{\psi}_{,2}^T \boldsymbol{\psi}_{,1}) \right. \\ &\quad \left. + D_{11} \boldsymbol{\psi}_{,11}^T \boldsymbol{\psi}_{,11} + D_{22} \boldsymbol{\psi}_{,22}^T \boldsymbol{\psi}_{,22} + 4D_{66} \boldsymbol{\psi}_{,12}^T \boldsymbol{\psi}_{,12} \right. \\ &\quad \left. + D_{12} (\boldsymbol{\psi}_{,22}^T \boldsymbol{\psi}_{,11} + \boldsymbol{\psi}_{,11}^T \boldsymbol{\psi}_{,22}) + k_f \boldsymbol{\psi}^T \boldsymbol{\psi} \right], \\ \mathbf{f} &= \int_0^{l_2} \int_0^{l_1} q \boldsymbol{\psi}^T dx_1 dx_2. \end{aligned} \quad (28)$$

For studying the stability of the plate, we put $\mathbf{f} = \mathbf{0}$. This and Equation (28) give

$$\mathbf{c}^T (\mathbf{K}^L - \lambda \mathbf{K}^G) \mathbf{d} = 0, \quad (29)$$

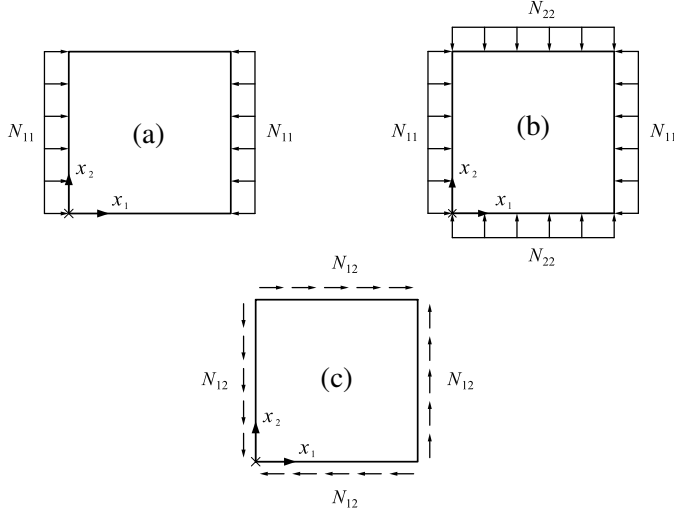


Figure 5. Midplane of an isotropic plate subjected to (a) uniaxial compression, (b) bi-axial compression, and (c) uniform shear.

where

$$\begin{aligned}
 \mathbf{K}^L &= \int_0^{l_2} \int_0^{l_1} dx_1 dx_2 \left[D_{11} \boldsymbol{\psi}_{,11}^T \boldsymbol{\psi}_{,11} + D_{22} \boldsymbol{\psi}_{,22}^T \boldsymbol{\psi}_{,22} + 4D_{66} \boldsymbol{\psi}_{,12}^T \boldsymbol{\psi}_{,12} \right. \\
 &\quad \left. + D_{12} (\boldsymbol{\psi}_{,22}^T \boldsymbol{\psi}_{,11} + \boldsymbol{\psi}_{,11}^T \boldsymbol{\psi}_{,22}) + k_f \boldsymbol{\psi}^T \boldsymbol{\psi} \right], \\
 \mathbf{K}^G &= \int_0^{l_2} \int_0^{l_1} dx_1 dx_2 \left[\hat{N}_{11} \boldsymbol{\psi}_{,1}^T \boldsymbol{\psi}_{,1} + \hat{N}_{22} \boldsymbol{\psi}_{,2}^T \boldsymbol{\psi}_{,2} + \hat{N}_{12} (\boldsymbol{\psi}_{,1}^T \boldsymbol{\psi}_{,2} + \boldsymbol{\psi}_{,2}^T \boldsymbol{\psi}_{,1}) \right], \\
 \lambda &= -\frac{N_{11}}{\hat{N}_{11}} = -\frac{N_{22}}{\hat{N}_{22}} = -\frac{N_{12}}{\hat{N}_{12}}.
 \end{aligned} \tag{30}$$

Equation (29) is an eigenvalue problem, in which λ is the eigenvalue corresponding to the critical load and \mathbf{d} is the eigenvector associated with the DOF. The eigenvector is normalized to have Euclidean length one. Therefore, the displacement obtained from Equation (13a) is dimensionless.

Standard Gaussian quadratures carry out the numerical integrations in Equations (28) and (30). For this, a background mesh is needed, and we set the nodes of the background mesh to coincide with the meshless particles and compute a 4×4 quadrature in each cell.

6. Numerical experiments

In this section, we demonstrate the applicability and efficacy of the proposed method in treating various boundary conditions encountered in plate problems. We compare the accuracy of the results with analytical solutions, whenever they are available. We investigate the method's advantages over conventional meshfree methods by considering several examples.

6.1. GRKPM versus RKPM. Consider a clamped square plate with elastic modulus and Poisson ratio of $E = 2 \times 10^9 \text{ N/m}^2$ and $\nu = 0.3$. For each of the loading conditions in Figure 5, we solve for the critical load and the corresponding mode shape.

The expression for the critical load is

$$N_{ij} = \lambda \frac{\pi^2 D}{l^2}, \quad i, j = 1, 2,$$

in which the analytical values for λ [Timoshenko and Gere 1961] are

$$\lambda_{\text{Anal.}} = \begin{cases} 10.07, & \text{Uniform uniaxial compression,} \\ 5.30, & \text{Uniform biaxial compression,} \\ 14.71, & \text{Uniform shear.} \end{cases} \quad (31)$$

For numerical calculations, we set the plate dimensions to $l = 5 \text{ m}$ and $h = 0.05 \text{ m}$, distribute the particles distributed uniformly in the x_1 and x_2 -directions, and employ the linear correction function. We set the dilation parameter in the x_1 and x_2 -directions to 1.8 times the corresponding interparticle distance Δy_i .

Each loading condition in Figure 5 leads to an eigenvalue problem, with analytical solutions given in Equation (31). Numerically, we solve each by RKPM combined with the penalty method, and also by our GRKPM. For RKPM, Table 1 displays the required CPU time and the percent error for selected numbers of particles; Table 2 does the same for GRKPM.

The GRKPM gives fair accuracy in all cases, even for relatively small numbers of particles. In the very worst case — in shear loading with a 5×5 distribution of particles — the error is only 5.8%. In comparison, the best result (in biaxial loading) for conventional RKPM has 22.5% error, and that was for a considerably larger 16×16 number of particles. In that case, the GRKPM already gives an error of 0.0% (to two-digit accuracy) with the smallest 5×5 number of particles. The GRKPM does cost more in CPU time for a fixed number of particles, but, because it achieves better accuracy using smaller number of particles, the GRKPM significantly outperforms RKPM at fixed CPU time.

We have computed the critical mode shapes using our method with an 8×8 distribution of particles; these are shown in Figure 6. Note that the symmetric loading conditions shown in Figure 5a and b allow us to consider only one-quarter of the plate. For the unsymmetric loading conditions of Figure 5c, the entire plate must be modeled.

Particles		11×11		13×13		14×14		16×16	
Loading	$\lambda_{\text{Anal.}}$	Time (s)	Error (%)	Time (s)	Error (%)	Time (s)	Error (%)	Time (s)	Error (%)
Figure 5a	10.07	2.3	34.5	3.5	28.8	4.5	26.7	7.6	23.4
Figure 5b	5.30	2.3	33.0	3.6	27.5	4.5	25.7	7.8	22.5
Figure 5c	14.71	2.6	39.0	3.8	31.3	4.8	28.7	7.8	24.7

Table 1. CPU time and percent error of the buckling parameters using RKPM, with $\alpha = 1.8\Delta y$.

Particles		5×5		6×6		7×7		8×8	
Loading	$\lambda_{\text{Anal.}}$	Time (s)	Error (%)	Time (s)	Error (%)	Time (s)	Error (%)	Time (s)	Error (%)
Figure 5a	10.07	2.4	0.2	3.4	0.1	4.8	0.1	7.2	0.0
Figure 5b	5.30	2.4	0.0	3.4	0.0	4.9	0.0	7.3	0.0
Figure 5c	14.71	2.4	5.8	3.3	1.6	4.8	1.3	7.1	1.1

Table 2. CPU time and percent error of the buckling parameters using GRKPM, with $a = 1.8\Delta y$.

6.2. GRKPM and effects of the dilation parameter. Zhao et al.[2003; 2004] and Liew et al. 2005 have investigated how the dilation parameter and particle distribution influence the convergence of meshless approaches such as RKPM; these studies have proved useful. This section performs such studies for GRKPM. To this end, we consider the clamped square plate defined in the previous section. The problem is solved with uniform distributions of particles and various values for the ratio of the dilation parameter to the interparticle distance, $a_i/\Delta y_i = 1.75, 2.00, 2.25, 2.5$. For uniaxial and biaxial compression, only one quarter of the plate is modeled, due to symmetry, and the region of the plate is $[0, 2.5]^2$. The number of particles along each edge varies from 5×5 to 9×9 . Figure 7 shows how the buckling factor λ varies with the number of particles along each edge for uniaxial and biaxial cases. This figure show monotonic convergence and remarkably accurate results for all the dilation parameters. The most accurate outcomes obtain when $a_i/\Delta y_i = 1.75$. For larger dilation parameters, the results are less accurate, but the accuracy quickly approaches that of smaller parameters as the number of particles increases.

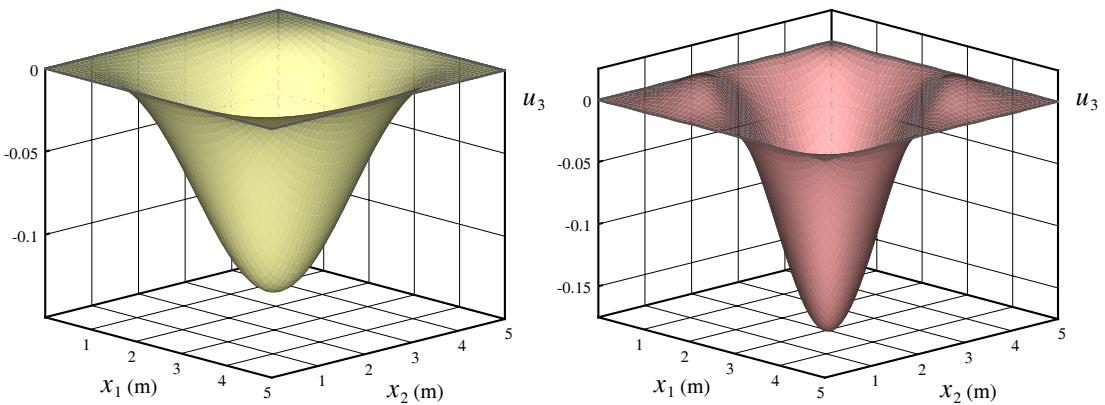


Figure 6. Critical buckling mode shapes of the isotropic square plate of Figure 5a, b, and, at right, from the uniform shear of the clamped square isotropic plate. At left, the plate is under uniaxial/biaxial compression; at right it is under uniform shear. See Figure 5.

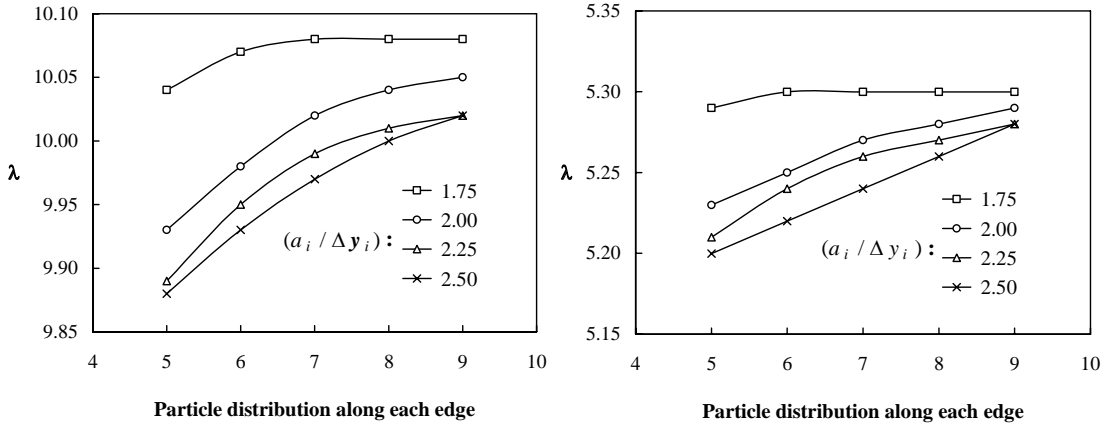


Figure 7. Convergence of the buckling parameter λ with increasing number of particles along each edge and for various dilation parameters. At left, the clamped square plate is under uniaxial compression; at right, it is under biaxial compression. See Section 6.1.

For the uniform shear test, we model the entire plate, and the region of analysis is $[0, 5]^2$. We consider various uniform distributions of particles ranging from 6×6 to 10×10 . (The number of particles varies from 36 to 100.) Figure 8 displays how the buckling factor λ varies with the number of particles along each edge. The results converge monotonically and, for any distribution of particles, are always closest when $a_i / \Delta y_i = 1.75$. Because we reached the same conclusion before in uniform uniaxial and biaxial compression tests, we adopt the value $a_i / \Delta y_i = 1.75$ for further experiments.

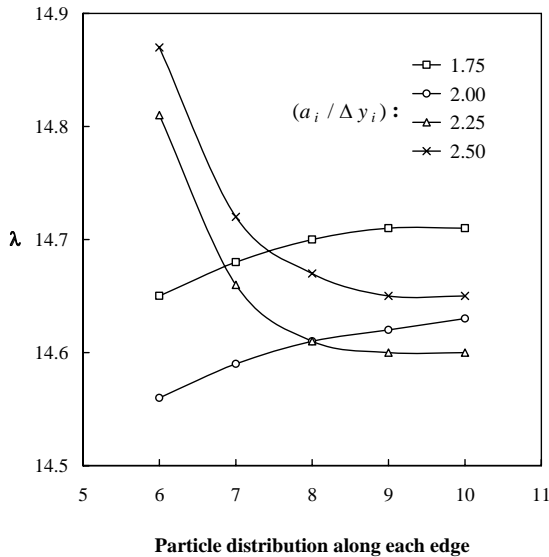


Figure 8. Convergence of the buckling parameter λ with increasing number of particles along each edge and for various dilation parameters. The clamped square plate is under uniform shear. See Section 6.1.

6.3. GRKPM versus EFGM. Consider a thin rectangular plate of thickness h and dimensions l_1 and l_2 in x_1 and x_2 . To compare the performance of EFGM and GRKPM, we compute the critical buckling load for various aspect ratios l_1/l_2 and different types of boundary conditions by both methods. The edge load is applied in the x_1 -direction, as shown in Figure 5a. In the numerical calculations, we use $l_2 = 10$ m and $h = 0.06$ m and assume the plate to be isotropic with $E = 2.45 \times 10^6$ N/m² and $\nu = 0.23$. The buckling load N and the buckling factor λ are related as

$$N = \lambda \frac{\pi^2 D}{l_2^2}.$$

Table 3 tabulates the analytical [Timoshenko and Gere 1961] and computed values of λ for simply supported boundary conditions along all the edges and for different aspect ratios l_1/l_2 . The numerical calculations used a 13×13 uniform distribution of particles. The results of EFGM in conjunction with the penalty method are cited from [Liu 2003]. There, Liu [2003] notes that the optimal dilation parameter is somewhere between 3.5 to 3.9 times the interparticle distance. Accordingly, for each l_1/l_2 , the dilation parameter is tuned within this rather tight range [Liu 2003]. Moreover, this particular EFGM uses the second-order base function instead of the first. In contrast, the GRKPM here employs the first-order base function. Moreover, for each l_1/l_2 , we examine two rather different dilation parameters, $a_i = 1.72\Delta y_i$ and $a_i = 3.5\Delta y_i$. Even though these dilation parameters differ by more than a factor of two, the results in either case are much better than those given by the EFGM with restricted dilation parameters. We conclude that the GRKPM is somewhat indifferent to the dilation parameter.

Method	Analytical	EFGM	GRKPM	
$a_i/\Delta y_i$	—	3.5–3.9	1.72	3.5
l_1/l_2	λ	Percent error		
0.20	27.00	0.33	0.15	0.15
0.30	13.20	0.15	0.00	0.00
0.40	8.41	0.12	0.00	0.00
0.50	6.25	0.00	0.00	−0.16
0.60	5.14	−0.19	0.00	0.00
0.70	4.53	0.00	0.00	0.00
0.80	4.20	0.00	0.00	0.00
0.90	4.04	0.00	0.00	0.00
1.00	4.00	1.00	0.00	0.00
1.10	4.04	0.25	0.00	0.00
1.20	4.13	0.00	0.00	0.00
1.30	4.28	0.00	0.00	0.00
1.40	4.47	0.22	0.00	−0.45

Table 3. Buckling factor for the simply supported rectangular plate.

Method	Analytical	EFGM	GRKPM	
$a_i/\Delta y_i$	—	3.5–3.9	1.72	3.5
I_1/I_2	λ	Percent error		
0.4	9.44	0.42	0.00	0.00
0.5	7.69	0.39	0.00	0.00
0.6	7.05	0.85	0.00	0.00
0.7	7.00	0.71	−0.14	0.00
0.8	7.29	1.23	0.14	0.14
0.9	7.83	1.66	0.26	0.26
1.0	7.69	1.04	0.00	0.00

Table 4. Buckling factor for the rectangular plate with simply supported, and clamped edges.

Table 4 displays the analytical [Timoshenko and Gere 1961] and computed values of λ when the edges $x_1 = 0, l_1$ are simply supported and the edges $x_2 = 0, l_2$ are fixed. All the other conditions and parameters are kept from the previous case. Again, for a given particle distribution, GRKPM allows more flexibility in choosing the dilation parameter and yields more accurate results. As before, EFGM uses the second-order base function, while the GRKPM uses first-order base function.

6.4. GRKPM and various types of boundary conditions. Figure 9 shows a schematic of a cross-ply laminate (90/0/90). The mark \times locates the origin of the Cartesian coordinate system. The edges $x_2 = 0, l$ are assumed to be simply supported and under a uniform compressive load along the x_2 -direction. For the other two edges, $x_1 = 0, l$, we consider various combinations of free, simply supported, and clamped boundary conditions, denoted respectively by F, S, and C. We put $l = 5$ m and the thickness of each lamina to 0.05 m. We assume that each lamina is made of carbon-epoxy with the material properties $E_1 = 40E_2$, $G_{12} = 0.6E_2$ and $\nu_{12} = 0.25$.

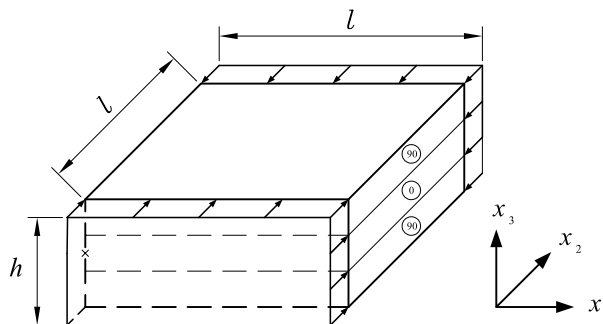


Figure 9. Square cross-ply laminate (90/0/90) subjected to uniform compressive load along the x_2 axis.

BC	Levy		GRKPM				
	λ	Particles	λ	% Err.	Particles	λ	% Err.
FF	31.76	5×5	31.41	-1.10	9×9	31.66	-0.33
FS	32.34	9×5	31.85	-1.49	17×9	32.22	-0.37
FC	32.81	9×5	32.18	-1.92	17×9	32.65	-0.48
SS	36.16	5×5	35.97	-0.52	9×9	36.12	-0.11
SC	39.43	9×5	39.36	-0.17	17×9	39.41	-0.05
CC	45.06	5×5	44.78	-0.63	9×9	45.02	-0.10

Table 5. Buckling factor for the cross-ply (90/0/90) square plate with mixed boundary conditions.

For this problem, the buckling load N and the buckling factor λ are related as

$$N = \lambda \frac{l^2}{E_2 h^3}. \quad (32)$$

The Levy method [Reddy 1997] is used to calculate the analytical values of λ . In our GRKPM, we find λ using a uniform distribution of particles and a dilation parameter of 1.75 times the interparticle distance. For SS, CC, and FF boundary conditions, we model only one quarter of the plate, whereas, for FS, FC, and SC conditions, we model half the plate. Table 5 compares the results with the analytical solutions. The BVPs associated with FF, SS and CC boundary conditions are solved for 5×5 and 9×9 particles, whereas, for the cases FS, FC and SC, we use 9×5 and 17×9 particles. Table 5 shows that the GRKPM yields satisfactory results even with the smallest number of particles. The maximum error obtains with the FC boundary conditions; the error is -1.92% for 9×5 particles and -0.48% for 17×9 particles. The SC boundary conditions, on the other hand, minimize the error; it is -0.17% for 9×5 and -0.05% for 17×9 particles. Table 5 shows clearly that the results improve as the number of particles increases.

6.5. Symmetric laminated composite plate under the most general conditions via GRKPM. To implement the proposed approach, we have developed a powerful program we call ALCP-GRKPM (analysis of laminated composite plates via GRKPM) for analyzing symmetric laminated composite plates with arbitrary loading and boundary conditions. For example, consider the laminated composite $(70/-20)_S$ shown in Figure 10, in which the thicknesses of the layers are $(0.02 \text{ m}/0.03 \text{ m})_S$. Each lamina is made of carbon-epoxy (AS4/3501-6) with $E_1 = 148 \text{ GPa}$, $E_2 = 10.5 \text{ GPa}$, $G_{12} = G_{13} = 5.61 \text{ GPa}$, $G_{23} = 3.17 \text{ GPa}$, $\nu_{12} = \nu_{13} = 0.3$ and $\nu_{23} = 0.59$. The edge $x_2 = 0$ is free and the remaining edges are clamped. A roller type support is placed in the middle of the plate, and part of the plate is placed on elastic foundation. We solve this set problem for two different cases: (1) uniform spring constant and distributed load; and (2) variable spring constant and distributed load. For both cases, a concentrated load of $P = 50 \text{ kN}$ is applied at the location marked \odot in Figure 10. In this computation, we intend to find the location and value of the maximum deflection. We use 9×5 , 17×9 , 33×17 , and 65×33 uniformly distributed particles. We set the dilation parameter equal to 1.75 times the interparticle distance.

Case 1: Uniform spring constant and uniformly distributed load. In this case the spring constant and distributed load are $k_f = 10^5 \text{ kN/m}^3$ and $q = 80 \text{ kN/m}^2$. For reference, we analyze the problem by

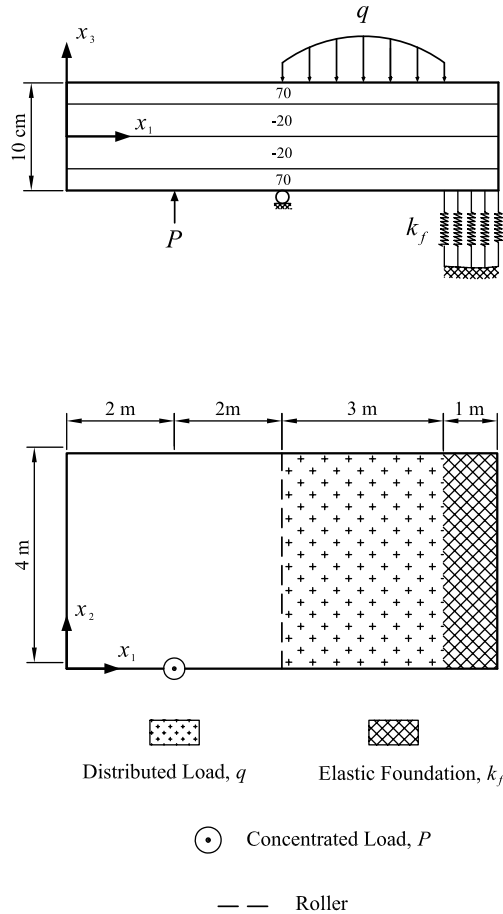


Figure 10. An example of a rectangular symmetric laminate $(70/-20)_s$ under a set of complex loadings and boundary conditions.

Method	Particles	$(u_3)_{\max}$ (cm)	x_1 (m)	x_2 (m)
GRKPM	9×5	-2.002	5.6250	0.000
	17×9	-2.003	5.6250	0.000
	33×17	-2.005	5.6250	0.000
	65×33	-2.006	5.6250	0.000
ANSYS	65×33	-2.072	5.6250	0.000

Table 6. Location and value of the maximum deflection for the plate shown in Figure 10 with a uniform elastic constant and a uniformly distributed load.

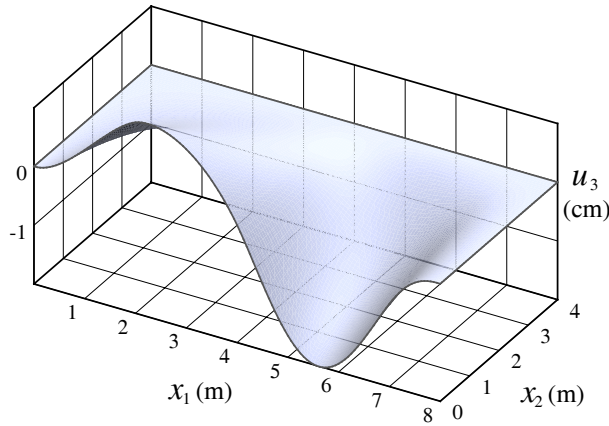


Figure 11. ALCP-GRKPM result for the deflection corresponding to the example shown in Figure 10 with uniform elastic constant and a uniformly distributed load.

ANSYS using 65×33 uniformly spaced nodes. In employing ANSYS, we use the 8-node ‘Shell 99’ element. Appendix A gives its interpolation functions, assumptions, and restrictions. At each node, the element has three displacement and three rotational DOF. Because of this, the DOF per node in ANSYS is twice the DOF per particle GRKPM. Table 6 shows the maximum deflection of the plate and where it occurs. GRKPM with 45 particles already gives a satisfactory result, and making more particles only affects the third decimal digit in the maximum deflection. The small discrepancy between the results of ANSYS and GRKPM for the maximum deflection arises because ANSYS applies the first-order shear deformation laminated plate theory (FSDT) [Reddy 1997] which considers shear deflections, whereas we use the classical plate theory which disregards these deflections. To suppress the shear deflections in FSDT, the lateral shear moduli G_{13} and G_{23} should be assigned significantly larger than G_{12} . Ansys [1997] recommends taking $G_{13} = G_{23} = 1000G_{12}$. By doing so, the computed maximum deflection equals 2.006, which agrees with the GRKPM result to within three decimal places. The deflection, $u_3(x_1, x_2)$, is computed by GRKPM with 65×33 particles, and its variation is shown in Figure 11.

Case 2: Variable spring constant and variably distributed load. The program ALCP-GRKPM can accept $q(x_1)$ and $k_f(x_1, x_2)$ as functions. For example, consider the plate shown in Figure 10 with the spring constant and distributed load assigned to vary as

$$k_f = \frac{10^6}{x_1 + x_2} \text{ kN/m}^3, \quad q = 55(x_1 - 4)(x_1 - 7) \text{ kN/m}^2.$$

Table 7 gives the corresponding results for 9×5 , 17×9 , 33×17 and 65×33 uniformly distributed particles. As in the previous example, increasing the number of particles only affects the third decimal digit in the maximum displacement.

7. Conclusions

We have demonstrated that our method is robust by considering plate boundary value problems. The results demonstrate that the method succeeds in treating different kinds of EBCs including those with

Method	Particles	$(u_3)_{\max}$ (cm)	x_1 (m)	x_2 (m)
GRKPM	9×5	-2.363	5.5625	0.000
	17×9	-2.366	5.6250	0.000
	33×17	-2.368	5.6250	0.000
	65×33	-2.370	5.6250	0.000

Table 7. Location and value of the maximum deflection for the plate shown in Figure 10 for variable elastic constant and a variably distributed load.

derivatives of the field function. The examples compute buckling load and analyze deflection under various types of loading and support, including elastic foundation with variable stiffness as explored in Section 6.5.

In the example of Section 6.1, comparing the performance of GRKPM and conventional RKPM reveals that using GRKPM with much smaller numbers of particles leads to results of excellent accuracy. In Section 6.2, from studying how the number of particles and the dilation parameter affect the performance of GRKPM, we conclude the GRKPM converges well as the number of particles increases. In Section 6.3, we conclude that for GRKPM the base function of order one suffices for obtaining better accuracy than from EFGM with the second-order base function. Moreover, for the cross-ply laminate with various types of EBCs considered in Section 6.4, the GRKPM solution converges rapidly with growing number of particles.

The presently formulated GRKPM achieves high performance because it expands the degrees of freedoms to include slopes and because it enforces EBCs by generalizing the corrected collocation method. Hence, the advantages become more pronounced for plates clamped at the boundaries. Given its so-far excellent features, GRKPM may hold promise for other problems of engineering science.

Appendix A

‘Shell 99’ is an 8-node quadrilateral element in 3-dimensions with rotational DOF and shear deflection [Ansys 1997]. It is suitable for laminate composites and can accept up to 100 different layers. This element is discussed by Yunus et al. [1989]. A planner view of this element is given in Figure 12.

Let define the shape functions for each node as

$$\begin{aligned}
 \psi_1 &= \frac{(1-s)(1-t)(-s-t-1)}{4}, & \psi_2 &= \frac{(1+s)(1-t)(s-t-1)}{4}, \\
 \psi_3 &= \frac{(1+s)(1+t)(s+t-1)}{4}, & \psi_4 &= \frac{(1-s)(1+t)(-s+t-1)}{4}, \\
 \psi_5 &= \frac{(1-s^2)(1-t)}{2}, & \psi_6 &= \frac{(1+s)(1-t^2)}{2}, \\
 \psi_7 &= \frac{(1-s^2)(1+t)}{2}, & \psi_8 &= \frac{(1-s)(1-t^2)}{2}.
 \end{aligned}$$

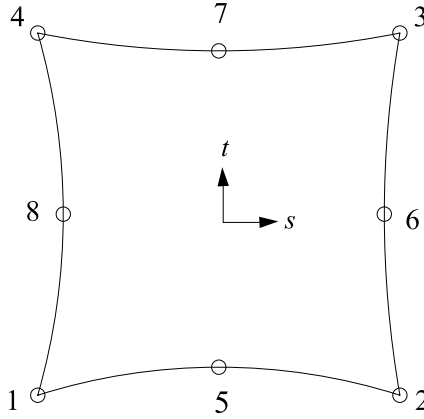


Figure 12. A planner view of the ‘Shell 99’ element used by ANSYS.

Subsequently, the interpolation functions are

$$\begin{bmatrix} u_1 \\ u_2 \\ u_3 \end{bmatrix} = \sum_{i=1}^8 \psi_i \begin{bmatrix} u_1^i \\ u_2^i \\ u_3^i \end{bmatrix} + \sum_{i=1}^8 \psi_i \frac{rt_i}{2} \begin{bmatrix} \hat{a}_1^i & \hat{b}_1^i \\ \hat{a}_2^i & \hat{b}_2^i \\ \hat{a}_3^i & \hat{b}_3^i \end{bmatrix} \begin{bmatrix} \theta_1^i \\ \theta_2^i \end{bmatrix}, \tag{A.1}$$

where u_1^i , u_2^i , and u_3^i are motions of node i , r is the coordinate along the thickness, and t_i is the thickness at node i . \hat{a} is the unit vector in the s direction and \hat{b} is the unit vector in the plane of element and normal to \hat{a} . θ_1^i and θ_2^i are the rotations of node i about vector \hat{a} and \hat{b} , respectively. An interesting observation is made by comparing the interpolation functions (A.1) with those of GRKPM given by Equation (7). The latter gives four different types of shape functions for the displacements and rotations of each node, whereas Equation (A.1) gives only one.

There are some assumptions and restrictions for this element:

- Normals to the center plane are assumed to remain straight after deformation, but not necessarily normal to the center plane.
- Each pair of integration points in the r direction is assumed to have the same material orientation.
- There is no significant stiffness associated with rotation about the element r axis. However, a nominal value of stiffness is present to prevent free rotation at the node.

Acknowledgement

This work was in part supported by the center of excellence in structures and earthquake engineering at Sharif University of Technology.

References

[Ansys 1997] Ansys, “ANSYS 5.4 Documentation”, Technical report, ANSYS Incorporated, 1997.
 [Atluri et al. 1999] S. N. Atluri, J. Y. Cho, and H.-G. Kim, “Analysis of thin beams, using the meshless local Petrov–Galerkin method, with generalized moving least squares interpolations”, *Comput. Mech.* **24**:5 (1999), 334–347.

- [Belytschko et al. 1994a] T. Belytschko, L. Gu, and Y. Y. Lu, “Fracture and crack growth by element free Galerkin methods”, *Model. Simul. Mater. Sc.* **2**:3A (1994), 519–534.
- [Belytschko et al. 1994b] T. Belytschko, Y. Y. Lu, and L. Gu, “Element-free Galerkin methods”, *Int. J. Numer. Meth. Eng.* **37**:2 (1994), 229–256.
- [Chen et al. 1996] J. S. Chen, C. Pan, C. T. Wu, and W. K. Liu, “Reproducing kernel particle methods for large deformation analysis of non-linear structures”, *Comput. Method. Appl. M.* **139**:1-4 (1996), 195–227.
- [Donning and Liu 1998] B. M. Donning and W. K. Liu, “Meshless methods for shear-deformable beams and plates”, *Comput. Method. Appl. M.* **152**:1-2 (1998), 47–71.
- [Hashemian 2000] A. Hashemian, “A study of Columns’ buckling loads and modes by meshfree methods”, Master’s Thesis, Sharif University of Technology, Tehran, 2000.
- [Krongauz and Belytschko 1996] Y. Krongauz and T. Belytschko, “Enforcement of essential boundary conditions in meshless approximations using finite elements”, *Comput. Method. Appl. M.* **131**:1-2 (1996), 133–145.
- [Lam et al. 2006] K. Y. Lam, H. Li, Y. K. Yew, and T. Y. Ng, “Development of the meshless Hermite-Cloud method for structural mechanics applications”, *Int. J. Mech. Sci.* **48**:4 (2006), 440–450.
- [Lancaster and Salkauskas 1981] P. Lancaster and K. Salkauskas, “Surfaces generated by moving least squares methods”, *Math. Comput.* **37**:155 (1981), 141–158.
- [Li and Liu 2002] S. Li and W. K. Liu, “Meshfree and particle methods and their applications”, *Appl. Mech. Rev. (Trans. ASME)* **55**:1 (2002), 1–34.
- [Li et al. 2003] H. Li, T. Y. Ng, J. Q. Cheng, and K. Y. Lam, “Hermite-Cloud: a novel true meshless method”, *Comput. Mech.* **33**:1 (2003), 30–41.
- [Li et al. 2004] S. Li, H. Lu, W. Han, W. K. Liu, and D. C. Simkins, “Reproducing kernel element method, II: globally conforming I^m/C^n hierarchies”, *Comput. Method. Appl. M.* **193**:12-14 (2004), 953–987.
- [Liew et al. 2005] K. M. Liew, T. Y. Ng, and X. Zhao, “Free vibration analysis of conical shells via the element-free kp-Ritz method”, *J. Sound Vib.* **281**:3-5 (2005), 627–645.
- [Liu 2003] G. R. Liu, *Mesh free methods: moving beyond the finite element method*, CRC Press, Boca Raton, FL, 2003.
- [Liu et al. 1995] W. K. Liu, S. Jun, and Y. F. Zhang, “Reproducing kernel particle methods”, *Int. J. Numer. Meth. Fl.* **20**:8-9 (1995), 1081–1106.
- [Liu et al. 1996a] W. K. Liu, Y. J. Chen, R. A. Uras, and C. T. Chang, “Generalized multiple scale reproducing kernel particle methods”, *Comput. Method. Appl. M.* **139**:1-4 (1996), 91–157.
- [Liu et al. 1996b] W. K. Liu, S. Jun, J. S. Chen, T. Belytschko, C. Pan, R. A. Uras, and C. T. Chang, “Overview and applications of the reproducing kernel particle methods”, *Arch. Comput. Method E* **3** (1996), 3–80.
- [Liu et al. 1997] W. K. Liu, R. A. Uras, and Y. Chen, “Enrichment of the finite element method with reproducing kernel particle method”, *J. Appl. Mech. (Trans. ASME)* **64** (1997), 861–870.
- [Liu et al. 2004] W. K. Liu, W. Han, H. Lu, S. Li, and J. Cao, “Reproducing kernel element method, I: theoretical formulation”, *Comput. Method. Appl. M.* **193**:12-14 (2004), 933–951.
- [Lu et al. 1994] Y. Y. Lu, T. Belytschko, and L. Gu, “A new implementation of the element free Galerkin method”, *Comput. Method. Appl. M.* **113**:3-4 (1994), 397–414.
- [Lucy 1977] L. B. Lucy, “A numerical approach to the testing of the fission hypothesis”, *The Astro. J.* **82** (1977), 1013–1024.
- [Reddy 1984] J. N. Reddy, *Energy and variational methods in applied mechanics: with an introduction to the finite element method*, John Wiley & Sons, New York, 1984.
- [Reddy 1997] J. N. Reddy, *Mechanics of laminated composite plates: theory and analysis*, CRC Press, Boca Raton, FL, 1997.
- [Tiago and Leitão 2004] C. Tiago and V. M. A. Leitão, “Further developments on GMLS: plates on elastic foundation”, pp. 1378–1383 in *Proceedings of the 2004 international conference on computational and experimental engineering and science* (Madeira, Portugal), edited by A. Tadeu and S. N. Atluri, Tech Science Press, 2004, Available at http://www.civil.ist.utl.pt/~ctf/docs/04b_madeira.pdf.
- [Timoshenko and Gere 1961] S. P. Timoshenko and J. M. Gere, *Theory of elastic stability*, 2nd ed., McGraw-Hill, New York, 1961.

- [Wagner and Liu 2000] G. J. Wagner and W. K. Liu, "Application of essential boundary conditions in mesh-free methods: a corrected collocation method", *Int. J. Numer. Meth. Eng.* **47**:8 (2000), 1367–1379.
- [Yunus et al. 1989] S. M. Yunus, P. C. Kohnke, and S. Saigal, "An efficient through-thickness integration scheme in an unlimited layer doubly curved isoparametric composite shell element", *Int. J. Numer. Meth. Eng.* **28**:12 (1989), 2777–2793.
- [Zhao et al. 2003] X. Zhao, K. M. Liew, and T. Y. Ng, "Vibration analysis of laminated composite cylindrical panels via a meshfree approach", *Int. J. Solids Struct.* **40**:1 (2003), 161–180.
- [Zhao et al. 2004] X. Zhao, T. Y. Ng, and K. M. Liew, "Free vibration of two-side simply-supported laminated cylindrical panels via the mesh-free kp-Ritz method", *Int. J. Mech. Sci.* **46**:1 (2004), 123–142.
- [Zhu and Atluri 1998] T. Zhu and S. N. Atluri, "A modified collocation method and a penalty formulation for enforcing the essential boundary conditions in the element free Galerkin method", *Comput. Mech.* **21**:3 (1998), 211–222.

Received 16 Oct 2006. Accepted 31 May 2007.

ALIREZA HASHEMIAN: al.hash@gmail.com

Center of Excellence in Structures and Earthquake Engineering, Department of Civil Engineering, Sharif University of Technology, P.O. Box 11365-9311, Tehran, Iran

HOSSEIN M. SHODJA: shodja@sharif.edu

Center of Excellence in Structures and Earthquake Engineering, Department of Civil Engineering, Sharif University of Technology, P.O. Box 11365-9311, Tehran, Iran

ON THE ELASTIC MODULI AND COMPLIANCES OF TRANSVERSELY ISOTROPIC AND ORTHOTROPIC MATERIALS

VLADO A. LUBARDA AND MICHELLE C. CHEN

The relationships between the elastic moduli and compliances of transversely isotropic and orthotropic materials, which correspond to different appealing sets of linearly independent fourth-order base tensors used to cast the elastic moduli and compliances tensors, are derived by performing explicit inversions of the involved fourth-order tensors. The deduced sets of elastic constants are related to each other and to common engineering constants expressed in the Voigt notation with respect to the coordinate axes aligned along the directions orthogonal to the planes of material symmetry. The results are applied to a transversely isotropic monocrystalline zinc and an orthotropic human femoral bone.

1. Introduction

There has been a significant amount of research devoted to tensorial representation of elastic constants of anisotropic materials, which are the components of the fourth-order tensors in three-dimensional geometrical space, or the second-order tensors in six-dimensional stress or strain space. This was particularly important for the spectral decompositions of the fourth-order stiffness and compliance tensors and the determination of the corresponding eigenvalues and eigentensors for materials with different types of elastic anisotropy. The spectral decomposition, for example, allows an additive decomposition of the elastic strain energy into a sum of six or fewer uncoupled energy modes, which are given by trace products of the corresponding pairs of stress and strain eigentensors. The representative references include [Rychlewski 1984; Walpole 1984; Theocaris and Philippidis 1989; Mehrabadi and Cowin 1990; Sutcliffe 1992; Theocaris and Sokolis 2000]. A study of the fourth-order tensors of elastic constants, and their equivalent matrix representations, is also important in the analysis of the invariants of the fourth-order tensors and identification of the invariant combinations of anisotropic elastic constants [Srinivasan and Nigam 1969; Betten 1987; Zheng 1994; Ting 1987; 2000; Ting and He 2006]. Furthermore, a study of the representation of the fourth-order tensors with respect to different bases can facilitate tensor operations and the analytical determination of the inverse tensors [Kunin 1981; 1983; Walpole 1984; Lubarda and Krajcinovic 1994; Nadeau and Ferrari 1998; Gangi 2000].

The objective of the present paper is to derive the relationships between the elastic moduli and compliances of transversely isotropic and orthotropic materials, which correspond to different appealing sets of linearly independent fourth-order base tensors used to cast the elastic stiffness and compliance tensors. In the case of transversely isotropic materials we begin the analysis with a stress-strain relationship which follows from the representation theorem for transversely isotropic tensor functions of a symmetric second-order tensor and a unit vector. This leads to the representation of the stiffness tensor in terms of

Keywords: algebra of tensors, elastic constants, human femur, orthotropic materials, transverse isotropy, zinc.
Research support from the Montenegrin Academy of Sciences and Arts is kindly acknowledged.

6 linearly independent tensors (\mathbf{I}_r) forming a basis of an algebra of fourth-order tensors that are made of the Kronecker delta and the unit vector. The corresponding elastic moduli are denoted by c_r . Since the multiplication table for \mathbf{I}_r tensors is dense with nonzero tensors, and thus operationally less practical, we introduce a set of new base tensors (\mathbf{J}_r) following the procedure developed by Kunin [1981] and Walpole [1984]. The corresponding elastic moduli, denoted by \bar{c}_r , are related to the original moduli c_r . We then derive the explicit expressions for the elastic compliances tensor with respect to both bases, and the relationships between the corresponding parameters s_r and \bar{s}_r and the original moduli c_r and \bar{c}_r . The two sets of elastic constants are also expressed in terms of the engineering constants, defined with respect to the coordinate system in which one of the axes is parallel to the axis of material symmetry.

Extending the analysis to orthotropic materials, three different representations of the elastic moduli tensor are constructed by using three different sets of 12 linearly independent fourth-order base tensors. This is achieved on the basis of the representation theorems for orthotropic tensor functions of a symmetric second-order tensor and the structural tensors associated with the principal axes of orthotropy [Spencer 1982; Boehler 1987]. The three sets of different elastic moduli, denoted by c_r , \bar{c}_{rs} and \hat{c}_{rs} (nine of which are independent in each case) are related to each other. The tensor of elastic compliances is then deduced by explicit inversion of the stiffness tensor expressed with respect to all three sets of base tensors. The corresponding compliances, denoted by s_r , \bar{s}_{rs} , and \hat{s}_{rs} , are related to each other and to the moduli c_r , \bar{c}_{rs} , and \hat{c}_{rs} . The three sets of elastic constants are then expressed in terms of engineering constants, appearing in the Voigt notation as the entries of 6×6 matrices [Voigt 1928], which do not constitute the components of the second-order tensor [Hearmon 1961; Nye 1964; Cowin and Mehrabadi 1995] and which are thus not amenable to easy tensor manipulations. The results are applied to calculate the different sets of elastic constants for a transversely isotropic monocrystalline zinc and an orthotropic human femur.

2. Elastic moduli of transversely isotropic materials

The stress-strain relationship for a linearly elastic transversely isotropic material, based on the representation theorems for transversely isotropic tensor function of a strain tensor and a unit vector [Spencer 1982], can be written as

$$\sigma_{ij} = \lambda \epsilon_{kk} \delta_{ij} + 2\mu \epsilon_{ij} + \alpha (n_k n_l \epsilon_{kl} \delta_{ij} + n_i n_j \epsilon_{kk}) + 2(\mu_0 - \mu)(n_i n_k \epsilon_{kj} + n_j n_k \epsilon_{ki}) + \beta n_i n_j n_k n_l \epsilon_{kl}. \quad (1)$$

The rectangular components of the unit vector parallel to the axis of transverse isotropy are n_i . The elastic shear modulus within the plane of isotropy is μ , the other Lamé constant is λ , and the out-of-plane elastic shear modulus is μ_0 . The remaining two moduli reflecting different elastic properties in the plane of isotropy and perpendicular to it are denoted by α and β .

The elastic stiffness tensor Λ corresponding to Equation (1), and defined such that $\sigma_{ij} = \Lambda_{ijkl} \epsilon_{kl}$, is

$$\Lambda = \sum_{r=1}^6 c_r \mathbf{I}_r, \quad (2)$$

where the fourth-order base tensors \mathbf{I}_r are defined by

$$\begin{aligned}\mathbf{I}_1 &= \frac{1}{2} \boldsymbol{\delta} \circ \boldsymbol{\delta}, & \mathbf{I}_2 &= \boldsymbol{\delta} \boldsymbol{\delta}, & \mathbf{I}_3 &= \mathbf{p} \boldsymbol{\delta}, & \mathbf{I}_4 &= \boldsymbol{\delta} \mathbf{p}, \\ \mathbf{I}_5 &= \frac{1}{2} \mathbf{p} \circ \boldsymbol{\delta}, & \mathbf{I}_6 &= \mathbf{p} \mathbf{p}.\end{aligned}\quad (3)$$

The second order tensor \mathbf{p} has the components $p_{ij} = n_i n_j$. The tensor products between the second-order tensors \mathbf{p} and $\boldsymbol{\delta}$ are such that

$$(\mathbf{p} \boldsymbol{\delta})_{ijkl} = p_{ij} \delta_{kl}, \quad (\mathbf{p} \circ \boldsymbol{\delta})_{ijkl} = \frac{1}{2} (p_{ik} \delta_{jl} + p_{il} \delta_{jk} + p_{jl} \delta_{ik} + p_{jk} \delta_{il}). \quad (4)$$

In the component form, the fourth-order tensors \mathbf{I}_r are

$$\begin{aligned}I_{ijkl}^{(1)} &= \frac{1}{2} (\delta_{ik} \delta_{jl} + \delta_{il} \delta_{jk}), & I_{ijkl}^{(2)} &= \delta_{ij} \delta_{kl}, \\ I_{ijkl}^{(3)} &= n_i n_j \delta_{kl}, & I_{ijkl}^{(4)} &= \delta_{ij} n_k n_l, \\ I_{ijkl}^{(5)} &= \frac{1}{2} (\delta_{ik} n_j n_l + \delta_{il} n_j n_k + \delta_{jl} n_i n_k + \delta_{jk} n_i n_l), & I_{ijkl}^{(6)} &= n_i n_j n_k n_l.\end{aligned}\quad (5)$$

The material parameters (elastic moduli), appearing in Equation (2), are

$$c_1 = 2\mu, \quad c_2 = \lambda, \quad c_3 = c_4 = \alpha, \quad c_5 = 2(\mu_0 - \mu), \quad c_6 = \beta. \quad (6)$$

The set of linearly independent tensors \mathbf{I}_r forms a basis of an algebra (of order 6) of the fourth-rank tensors made up of the Kronecker delta and the unit vector, symmetric with respect to first and second pair of indices, but not necessarily with respect to permutation of pairs. All such fourth-rank tensors can be represented as a linear combination of the base tensors.

Since the multiplication table of the tensors \mathbf{I}_r is dense with nonzero tensors (see the upper left corner of Table 9 in the Appendix), and thus less convenient for tensor operations and the determination of the inverse tensors, we recast the elastic stiffness tensor (2) in terms of an alternative set of base tensors \mathbf{J}_r , which is characterized by a simple multiplication table, in which each product is equal to either zero tensor or to one of the tensors from the basis. Thus,

$$\boldsymbol{\Lambda} = \sum_{r=1}^6 \bar{c}_r \mathbf{J}_r, \quad (7)$$

where the modified elastic moduli are

$$\begin{aligned}\bar{c}_1 &= c_1 + c_2 + 2c_3 + 2c_5 + c_6 = \lambda + 4\mu_0 - 2\mu + 2\alpha + \beta, \\ \bar{c}_2 &= c_1 + 2c_2 = 2(\lambda + \mu), \\ \bar{c}_3 &= \bar{c}_4 = \sqrt{2} (c_2 + c_3) = \sqrt{2} (\lambda + \alpha), \\ \bar{c}_5 &= c_1 = 2\mu, \quad \bar{c}_6 = c_1 + c_5 = 2\mu_0,\end{aligned}\quad (8)$$

with the inverse relationships

$$\begin{aligned} c_1 &= \bar{c}_5, & c_2 &= \frac{1}{2}(\bar{c}_2 - \bar{c}_5), & c_5 &= \bar{c}_6 - \bar{c}_5, \\ c_3 &= c_4 = \frac{1}{\sqrt{2}}\bar{c}_3 - \frac{1}{2}(\bar{c}_2 - \bar{c}_5), \\ c_6 &= \bar{c}_1 + \frac{1}{2}\bar{c}_2 - \sqrt{2}\bar{c}_3 + \frac{1}{2}\bar{c}_5 - 2\bar{c}_6. \end{aligned} \quad (9)$$

The base tensors \mathbf{J}_r are defined by Walpole [1984],¹

$$\begin{aligned} \mathbf{J}_1 &= \mathbf{p} \mathbf{p}, & \mathbf{J}_2 &= \frac{1}{2} \mathbf{q} \mathbf{q}, \\ \mathbf{J}_3 &= \frac{1}{\sqrt{2}} \mathbf{p} \mathbf{q}, & \mathbf{J}_4 &= \frac{1}{\sqrt{2}} \mathbf{q} \mathbf{p}, \\ \mathbf{J}_5 &= \frac{1}{2} (\mathbf{q} \circ \mathbf{q} - \mathbf{q} \mathbf{q}), & \mathbf{J}_6 &= \mathbf{p} \circ \mathbf{q}. \end{aligned} \quad (10)$$

The second order tensor \mathbf{q} is introduced such that

$$q_{ij} = \delta_{ij} - p_{ij}, \quad p_{ij} = n_i n_j. \quad (11)$$

When applied to an arbitrary vector v_j , the tensors \mathbf{p} and \mathbf{q} decompose that vector into its components parallel to n_i , $p_{ij}v_j = (v_j n_j)n_i$, and orthogonal to it, $q_{ij}n_j = v_i - p_{ij}v_j$. It readily follows that

$$\begin{aligned} p_{ik}p_{kj} &= p_{ij}, & p_{ij}p_{ij} &= 1, & p_{ii} &= 1, \\ q_{ik}q_{kj} &= q_{ij}, & q_{ij}q_{ij} &= 2, & q_{ii} &= 2, \\ p_{ik}q_{kj} &= 0, & q_{ik}p_{kj} &= 0. \end{aligned} \quad (12)$$

The two types of tensor products between the involved second-order tensors are defined by the type Equation (4), that is,

$$(\mathbf{p} \mathbf{q})_{ijkl} = p_{ij}q_{kl}, \quad (\mathbf{p} \circ \mathbf{q})_{ijkl} = \frac{1}{2}(p_{ik}q_{jl} + p_{il}q_{jk} + p_{jl}q_{ik} + p_{jk}q_{il}). \quad (13)$$

It can be easily verified that

$$\mathbf{p} \circ \mathbf{q} = \mathbf{q} \circ \mathbf{p}, \quad \mathbf{p} \circ \mathbf{p} = 2 \mathbf{p} \mathbf{p}. \quad (14)$$

The trace products of the tensors $\mathbf{J}_r : \mathbf{J}_s$ of the type $J_{ijmn}^{(r)} J_{mnlk}^{(s)}$ can be readily evaluated by using Equation (12), with the results listed in Table 1. The symbol $\overset{r}{\cdot}$ indicates that the products are in the order: *a tensor from the left column* traced with *a tensor from the top row*.

2.1. Elastic compliances of transversely isotropic materials. To derive the elastic compliances tensor, it is more convenient to invert the elastic stiffness tensor Λ in its representation (7) than (2). Thus, by writing

$$\Lambda^{-1} = \sum_{r=1}^6 \bar{s}_r \mathbf{J}_r, \quad (15)$$

and by using Table 1 to expand the trace products appearing in

$$\Lambda : \Lambda^{-1} = \Lambda^{-1} : \Lambda = \mathbf{I}_1, \quad (16)$$

¹An alternative set of base tensors was used by Kunin[1981; 1983] and Lubarda and Krajcinovic [1994].

\vec{r}	\mathbf{J}_1	\mathbf{J}_2	\mathbf{J}_3	\mathbf{J}_4	\mathbf{J}_5	\mathbf{J}_6
\mathbf{J}_1	\mathbf{J}_1	0	\mathbf{J}_3	0	0	0
\mathbf{J}_2	0	\mathbf{J}_2	0	\mathbf{J}_4	0	0
\mathbf{J}_3	0	\mathbf{J}_3	0	\mathbf{J}_1	0	0
\mathbf{J}_4	\mathbf{J}_4	0	\mathbf{J}_2	0	0	0
\mathbf{J}_5	0	0	0	0	\mathbf{J}_5	0
\mathbf{J}_6	0	0	0	0	0	\mathbf{J}_6

Table 1. Table of products $\mathbf{J}_r : \mathbf{J}_s$.

there follows

$$\bar{s}_1 = \bar{c}_2/\bar{c}, \quad \bar{s}_2 = \bar{c}_1/\bar{c}, \quad \bar{s}_3 = \bar{s}_4 = -\bar{c}_3/\bar{c}, \quad \bar{s}_5 = 1/\bar{c}_5, \quad \bar{s}_6 = 1/\bar{c}_6, \quad (17)$$

where

$$\bar{c} = \bar{c}_1\bar{c}_2 - \bar{c}_3^2. \quad (18)$$

Note that the fourth-order identity tensor \mathbf{I}_1 can be expressed in terms of the base tensors \mathbf{J}_r as

$$\mathbf{I}_1 = \mathbf{J}_1 + \mathbf{J}_2 + \mathbf{J}_5 + \mathbf{J}_6,$$

which was used in Equation (16).

The elastic compliances tensor can be expressed in the original basis \mathbf{I}_r by using the connections between the two bases, which are

$$\begin{aligned} \mathbf{I}_1 &= \frac{1}{2} \boldsymbol{\delta} \circ \boldsymbol{\delta} = \mathbf{p} \mathbf{p} + \mathbf{p} \circ \mathbf{q} + \frac{1}{2} \mathbf{q} \circ \mathbf{q} = \mathbf{J}_1 + \mathbf{J}_2 + \mathbf{J}_5 + \mathbf{J}_6, \\ \mathbf{I}_2 &= \boldsymbol{\delta} \boldsymbol{\delta} = (\mathbf{p} + \mathbf{q})(\mathbf{p} + \mathbf{q}) = \mathbf{J}_1 + 2\mathbf{J}_2 + \sqrt{2}(\mathbf{J}_3 + \mathbf{J}_4), \\ \mathbf{I}_3 &= \mathbf{p} \boldsymbol{\delta} = \mathbf{p} \mathbf{p} + \mathbf{p} \mathbf{q} = \mathbf{J}_1 + \sqrt{2} \mathbf{J}_3, & \mathbf{I}_4 &= \boldsymbol{\delta} \mathbf{p} = \mathbf{p} \mathbf{p} + \mathbf{q} \mathbf{p} = \mathbf{J}_1 + \sqrt{2} \mathbf{J}_4, \\ \mathbf{I}_5 &= \mathbf{p} \circ \boldsymbol{\delta} = 2\mathbf{p} \mathbf{p} + \mathbf{p} \circ \mathbf{q} = 2\mathbf{J}_1 + \mathbf{J}_6, & \mathbf{I}_6 &= \mathbf{p} \mathbf{p} = \mathbf{J}_1. \end{aligned} \quad (19)$$

Their inverse relationships are

$$\begin{aligned} \mathbf{J}_1 &= \mathbf{I}_6, & \mathbf{J}_2 &= \frac{1}{2} (\mathbf{I}_2 - \mathbf{I}_3 - \mathbf{I}_4 + \mathbf{I}_6), \\ \mathbf{J}_3 &= \frac{1}{\sqrt{2}} (\mathbf{I}_3 - \mathbf{I}_6), & \mathbf{J}_4 &= \frac{1}{\sqrt{2}} (\mathbf{I}_4 - \mathbf{I}_6), \\ \mathbf{J}_5 &= \frac{1}{2} (2\mathbf{I}_1 - \mathbf{I}_2 + \mathbf{I}_3 + \mathbf{I}_4 - 2\mathbf{I}_5 + \mathbf{I}_6), & \mathbf{J}_6 &= \mathbf{I}_5 - 2\mathbf{I}_6. \end{aligned} \quad (20)$$

The elastic compliance tensor is expressed in terms of the base tensors \mathbf{I}_r by substituting (20) into (15). The result is

$$\boldsymbol{\Lambda}^{-1} = \sum_{r=1}^6 s_r \mathbf{I}_r, \quad (21)$$

with the corresponding compliances

$$\begin{aligned}
 s_1 &= \bar{s}_5, & s_2 &= \frac{1}{2}(\bar{s}_2 - \bar{s}_5), \\
 s_3 = s_4 &= \frac{1}{\sqrt{2}}\bar{s}_3 - \frac{1}{2}(\bar{s}_2 - \bar{s}_5), & s_5 &= \bar{s}_6 - \bar{s}_5, \\
 s_6 &= \bar{s}_1 + \frac{1}{2}\bar{s}_2 - \sqrt{2}\bar{s}_3 + \frac{1}{2}\bar{s}_5 - 2\bar{s}_6.
 \end{aligned} \tag{22}$$

The same type of relationships hold between the moduli \bar{c}_r and c_r appearing in Equation (2) and (7). The inverse expressions to (22) are

$$\begin{aligned}
 \bar{s}_1 &= s_1 + s_2 + 2s_3 + 2s_5 + s_6, & \bar{s}_2 &= s_1 + 2s_2, \\
 \bar{s}_3 = \bar{s}_4 &= \sqrt{2}(s_2 + s_3), & \bar{s}_5 &= s_1, \\
 \bar{s}_6 &= s_1 + s_5.
 \end{aligned} \tag{23}$$

2.2. Relationships to engineering constants in Voigt notation. The parameters c_r are related to commonly used engineering moduli C_{ij} (in Voigt notation, with the axis of isotropy along the x_3 direction) by

$$\begin{aligned}
 c_1 &= C_{11} - C_{12} = 2C_{66}, & c_2 &= C_{12}, & c_3 = c_4 &= C_{13} - C_{12}, \\
 c_5 &= 2(C_{55} - C_{66}), & c_6 &= C_{11} + C_{33} - 2C_{13} - 4C_{55},
 \end{aligned} \tag{24}$$

which is in accord with [Boehler 1987]. The (symmetric) elastic moduli C_{ij} are defined such that

$$\begin{bmatrix} \sigma_{11} \\ \sigma_{22} \\ \sigma_{33} \\ \sigma_{23} \\ \sigma_{31} \\ \sigma_{12} \end{bmatrix} = \begin{bmatrix} C_{11} & C_{12} & C_{13} & 0 & 0 & 0 \\ C_{21} & C_{22} & C_{23} & 0 & 0 & 0 \\ C_{31} & C_{32} & C_{33} & 0 & 0 & 0 \\ 0 & 0 & 0 & C_{44} & 0 & 0 \\ 0 & 0 & 0 & 0 & C_{55} & 0 \\ 0 & 0 & 0 & 0 & 0 & C_{66} \end{bmatrix} \cdot \begin{bmatrix} \epsilon_{11} \\ \epsilon_{22} \\ \epsilon_{33} \\ 2\epsilon_{23} \\ 2\epsilon_{31} \\ 2\epsilon_{12} \end{bmatrix}, \tag{25}$$

where for transversely isotropic materials: $C_{11} = C_{22}$, $C_{23} = C_{31}$, $C_{44} = C_{55}$, and $C_{66} = (C_{11} - C_{12})/2$. The relationships between \bar{c}_r and C_{ij} are deduced from Equation (8) and (24). They are

$$\bar{c}_1 = C_{33}, \quad \bar{c}_2 = C_{11} + C_{12}, \quad \bar{c}_3 = \bar{c}_4 = \sqrt{2}C_{13}, \tag{26}$$

$$\bar{c}_5 = 2C_{66}, \quad \bar{c}_6 = 2C_{55}. \tag{27}$$

The compliance constants s_i are related to the engineering compliances S_{ij} by

$$s_1 = S_{11} - S_{12} = S_{66}/2, \quad s_2 = S_{12}, \quad s_3 = s_4 = S_{13} - S_{12}, \tag{28}$$

$$s_5 = (S_{55} - S_{66})/2, \quad s_6 = S_{11} + S_{33} - 2S_{13} - S_{55}. \tag{29}$$

The compliances S_{ij} are also defined with respect to the coordinate system in which the axis of isotropy is along the x_3 direction, so that, in Voigt notation,

$$\begin{bmatrix} \epsilon_{11} \\ \epsilon_{22} \\ \epsilon_{33} \\ 2\epsilon_{23} \\ 2\epsilon_{31} \\ 2\epsilon_{12} \end{bmatrix} = \begin{bmatrix} S_{11} & S_{12} & S_{13} & 0 & 0 & 0 \\ S_{21} & S_{22} & S_{23} & 0 & 0 & 0 \\ S_{31} & S_{32} & S_{33} & 0 & 0 & 0 \\ 0 & 0 & 0 & S_{44} & 0 & 0 \\ 0 & 0 & 0 & 0 & S_{55} & 0 \\ 0 & 0 & 0 & 0 & 0 & S_{66} \end{bmatrix} \cdot \begin{bmatrix} \sigma_{11} \\ \sigma_{22} \\ \sigma_{33} \\ \sigma_{23} \\ \sigma_{31} \\ \sigma_{12} \end{bmatrix}, \quad (30)$$

where $S_{11} = S_{22}$, $S_{23} = S_{31}$, $S_{44} = S_{55}$, and $S_{66} = 2(S_{11} - S_{12})$. The well known connections between S_{ij} and C_{ij} are

$$\begin{aligned} S_{11} &= \frac{C_{11} - C_{13}^2/C_{33}}{C_{11} - C_{12}} S, & S_{12} &= -\frac{C_{12} - C_{13}^2/C_{33}}{C_{11} - C_{12}} S, \\ S_{13} &= -\frac{C_{13}}{C_{33}} S, & S_{33} &= \frac{C_{11} + C_{12}}{C_{33}} S, \\ S_{44} &= \frac{1}{C_{44}}, & S_{66} &= \frac{1}{C_{66}}, \\ S &= \frac{1}{C_{11} + C_{12} - 2C_{13}^2/C_{33}}. \end{aligned} \quad (31)$$

The inverse relationships are obtained by reversing the role of C 's and S 's in Equation (31). The relationships between \bar{s}_r and S_{ij} are obtained by substituting (28) into (23), with the result

$$\bar{s}_1 = S_{33}, \quad \bar{s}_2 = S_{11} + S_{12}, \quad \bar{s}_3 = \bar{s}_4 = \sqrt{2}S_{13}, \quad (32)$$

$$\bar{s}_5 = \frac{1}{2} S_{66}, \quad \bar{s}_6 = \frac{1}{2} S_{55}. \quad (33)$$

Let E and E_0 be the Young's moduli in the plane of isotropy and in the direction perpendicular to it; ν is the Poisson ratio characterizing transverse contraction in the plane of isotropy due to applied tension in the orthogonal direction within the plane of isotropy; ν_0 is the same due to applied tension perpendicular to the plane of isotropy; μ is the shear modulus in the plane of isotropy, and μ_0 in any plane perpendicular to the plane of isotropy (see [Lekhnitskii 1981]). Then, the elastic compliances S_{ij} in Equation (30) are

$$\begin{aligned} S_{11} = S_{22} &= \frac{1}{E}, & S_{33} &= \frac{1}{E_0}, & S_{12} &= -\frac{\nu}{E}, \\ S_{23} = S_{31} &= -\frac{\nu_0}{E_0}, & S_{44} = S_{55} &= \frac{1}{\mu_0}, & S_{66} &= 2(S_{11} - S_{12}) = \frac{1}{\mu} = \frac{2(1 + \nu)}{E}. \end{aligned} \quad (34)$$

The matrices $[S_{ij}]$ and $[C_{ij}]$ are inverse to each other, although their components are not the components of the second-order tensors [Hearmon 1961; Nye 1964]. The substitution of (34) into (28) gives

$$s_1 = \frac{1+\nu}{E} = \frac{1}{2\mu}, \quad s_2 = -\frac{\nu}{E}, \quad s_3 = s_4 = \frac{\nu}{E} - \frac{\nu_0}{E_0}, \quad (35)$$

$$s_5 = \frac{1}{\mu_0} - \frac{1}{\mu}, \quad s_6 = \frac{1}{E} + \frac{1+2\nu_0}{E_0} - \frac{1}{\mu_0}. \quad (36)$$

The inverse relations are

$$E = \frac{1}{s_1 + s_2}, \quad \nu = -Es_2, \quad \mu = \frac{1}{2s_1}, \quad (37)$$

$$E_0 = \frac{1}{s_1 + s_2 + 2s_3 + s_5 + s_6}, \quad \nu_0 = -E_0(s_2 + s_3), \quad \mu_0 = \frac{1}{2s_1 + s_5}.$$

These expressions reveal the relationships between the original moduli appearing in Equation (6) and the engineering moduli. For example, the Young's modulus in the plane of isotropy is

$$E = 4 \left[\frac{\lambda + 4\mu_0 - 2\mu + 2\alpha + \beta}{(\lambda + \mu)(\lambda + 4\mu_0 - 2\mu + 2\alpha + \beta) - (\lambda + \alpha)^2} + \frac{1}{\mu} \right]^{-1}. \quad (38)$$

If $\alpha = \beta = 0$ and $\mu_0 = \mu$ this reduces to the isotropic elasticity result $E = \mu(3\lambda + 2\mu)/(\lambda + \mu)$.

2.3. Elastic constants of a monocrystalline zinc. The elastic moduli C_{ij} of a transversely isotropic monocrystalline zinc, in units of GPa and with x_3 axis as the axis of isotropy, are [Landolt-Börnstein 1979]

$$\begin{bmatrix} C_{11} & C_{12} & C_{13} \\ C_{21} & C_{22} & C_{23} \\ C_{31} & C_{32} & C_{33} \end{bmatrix} = \begin{bmatrix} 160.28 & 29.04 & 47.84 \\ 29.04 & 160.28 & 47.84 \\ 47.84 & 47.84 & 60.28 \end{bmatrix}, \quad \begin{bmatrix} C_{44} \\ C_{55} \\ C_{66} \end{bmatrix} = \begin{bmatrix} 39.53 \\ 39.53 \\ 65.62 \end{bmatrix}.$$

The moduli c_i and \bar{c}_i follow from Equation (24) and Equation (26) and are listed in Table 2. The moduli $\mu, \lambda, \mu_0, \alpha,$ and β , calculated from Equation (6), are listed in Table 3. The elastic compliances S_{ij} (in units of TPa^{-1}), corresponding to elastic moduli C_{ij} given above, are

$$\begin{bmatrix} S_{11} & S_{12} & S_{13} \\ S_{21} & S_{22} & S_{23} \\ S_{31} & S_{32} & S_{33} \end{bmatrix} = \begin{bmatrix} 8.22 & 0.6 & -7 \\ 0.6 & 8.22 & -7 \\ -7 & -7 & 27.7 \end{bmatrix}, \quad \begin{bmatrix} S_{44} \\ S_{55} \\ S_{66} \end{bmatrix} = \begin{bmatrix} 25.3 \\ 25.3 \\ 15.24 \end{bmatrix}.$$

c_1	c_2	$c_3 = c_4$	c_5	c_6
131.24	29.04	18.80	-52.18	-33.24
\bar{c}_1	\bar{c}_2	$\bar{c}_3 = \bar{c}_4$	\bar{c}_5	\bar{c}_6
60.28	189.32	67.66	131.24	79.06

Table 2. Elastic moduli c_i and \bar{c}_i (in units of GPa).

$\mu = c_1/2$	$\lambda = c_2$	$\alpha = c_3$	$\mu_0 = \mu + c_5/2$	$\beta = c_6$
65.62	29.04	18.80	39.53	-33.24

Table 3. Table of elastic moduli μ , λ , μ_0 , α , and β (in units of GPa).

s_1	s_2	$s_3 = s_4$	s_5	s_6
7.62	0.6	-7.6	5.03	24.62
\bar{s}_1	\bar{s}_2	$\bar{s}_3 = \bar{s}_4$	\bar{s}_5	\bar{s}_6
27.7	8.82	-9.9	7.62	12.65

Table 4. Elastic compliances s_i and \bar{s}_i (in units of TPa^{-1}).

The compliance coefficients s_i and \bar{s}_i are readily calculated from Equation (28) and Equation (32), and are listed in Table 4. Finally, the elastic constants E , E_0 , μ , μ_0 , ν , and ν_0 are determined from Equation (37), and are given in Table 5. Since $s_2 = 0.6 > 0$ and $\nu = -s_2 E$, the Poisson ratio in the (basal) plane of isotropy is negative ($\nu = -0.073$). This was first noted by Lubarda and Meyers [1999], who also determined the range of the directions associated with negative values of the Poisson ratio.

3. Elastic moduli of orthotropic materials

Consider an orthotropic elastic material whose principal axes of orthotropy are along the directions \mathbf{a} , \mathbf{b} , and \mathbf{c} , arbitrarily oriented with respect to the reference coordinate system. From the representation theorems for orthotropic tensor functions [Spencer 1982], it follows that the components of the stress tensor σ_{ij} can be expressed in terms of the strain components ϵ_{ij} , and the vector components a_i and b_i , as

$$\begin{aligned} \sigma_{ij}^e = & (\lambda \epsilon_{kk} + \alpha_1 \epsilon_a + \alpha_2 \epsilon_b) \delta_{ij} + 2\mu \epsilon_{ij} \\ & + (\alpha_1 \epsilon_{kk} + \beta_1 \epsilon_a + \beta_3 \epsilon_b) a_i a_j + (\alpha_2 \epsilon_{kk} + \beta_3 \epsilon_a + \beta_2 \epsilon_b) b_i b_j \\ & + 2\mu_1 (a_i a_k \epsilon_{kj} + a_j a_k \epsilon_{ki}) + 2\mu_2 (b_i b_k \epsilon_{kj} + b_j b_k \epsilon_{ki}). \end{aligned} \quad (39)$$

The longitudinal strains in the directions of two of the principal axes of orthotropy are $\epsilon_a = a_k a_l \epsilon_{kl}$ and $\epsilon_b = b_k b_l \epsilon_{kl}$. The nine elastic moduli are λ , μ , μ_1 , μ_2 , α_1 , α_2 , and β_1 , β_2 , β_3 . The elastic stiffness tensor

E	E_0	μ	μ_0	ν	ν_0
121.66	44.11	65.62	49.34	-0.073	0.309

Table 5. Elastic moduli E , E_0 , μ , μ_0 (in units of GPa) and Poisson's ratios ν and ν_0 .

corresponding to Equation (39) is

$$\mathbf{\Lambda} = \sum_{r=1}^{12} c_r \mathbf{I}_r, \quad (40)$$

where the material parameters c_r are

$$\begin{aligned} c_1 = 2\mu, \quad c_2 = \lambda, \quad c_3 = c_4 = \alpha_1, \quad c_5 = c_6 = \alpha_2, \\ c_7 = 2\mu_1, \quad c_8 = 2\mu_2, \quad c_9 = \beta_1, \quad c_{10} = \beta_2, \quad c_{11} = c_{12} = \beta_3. \end{aligned} \quad (41)$$

The fourth-order tensors \mathbf{I}_r are defined by

$$\begin{aligned} \mathbf{I}_1 &= \frac{1}{2} \boldsymbol{\delta} \circ \boldsymbol{\delta}, & \mathbf{I}_2 &= \boldsymbol{\delta} \boldsymbol{\delta}, \\ \mathbf{I}_3 &= \mathbf{A} \boldsymbol{\delta}, & \mathbf{I}_4 &= \boldsymbol{\delta} \mathbf{A}, \\ \mathbf{I}_5 &= \mathbf{B} \boldsymbol{\delta}, & \mathbf{I}_6 &= \boldsymbol{\delta} \mathbf{B}, \\ \mathbf{I}_7 &= \mathbf{A} \circ \boldsymbol{\delta}, & \mathbf{I}_8 &= \mathbf{B} \circ \boldsymbol{\delta}, \\ \mathbf{I}_9 &= \mathbf{A} \mathbf{A}, & \mathbf{I}_{10} &= \mathbf{B} \mathbf{B}, \\ \mathbf{I}_{11} &= \mathbf{A} \mathbf{B}, & \mathbf{I}_{12} &= \mathbf{B} \mathbf{A}. \end{aligned} \quad (42)$$

In these expressions the (idempotent) tensors \mathbf{A} , \mathbf{B} , and \mathbf{C} have the components

$$A_{ij} = a_i a_j, \quad B_{ij} = b_i b_j, \quad C_{ij} = c_i c_j, \quad (43)$$

which are related by the identity $A_{ij} + B_{ij} + C_{ij} = \delta_{ij}$. Two types of tensor products are defined by the formulas of the following type:

$$\begin{aligned} (\mathbf{A} \mathbf{B})_{ijkl} &= A_{ij} B_{kl}, \\ (\mathbf{A} \circ \mathbf{B})_{ijkl} &= \frac{1}{2} (A_{ik} B_{jl} + A_{il} B_{jk} + A_{jl} B_{ik} + A_{jk} B_{il}). \end{aligned} \quad (44)$$

It can be easily verified that

$$\mathbf{A} \circ \mathbf{B} = \mathbf{B} \circ \mathbf{A}, \quad \mathbf{A} \circ \mathbf{A} = 2\mathbf{A} \mathbf{A}. \quad (45)$$

The symmetric tensors such as $\mathbf{A} \mathbf{A}$, and $\mathbf{A} \circ \mathbf{B}$ are also idempotent.

The multiplication table for tensors \mathbf{I}_r (Table 9 of the Appendix) is dense with nonzero entries, although these are simple multiples of one of the \mathbf{I}_r tensors, except for

$$\mathbf{I}_7 : \mathbf{I}_7 = \mathbf{I}_7 + 2\mathbf{I}_9, \quad \mathbf{I}_8 : \mathbf{I}_8 = \mathbf{I}_8 + 2\mathbf{I}_{10}, \quad (46)$$

and

$$\mathbf{I}_7 : \mathbf{I}_8 = \mathbf{I}_8 : \mathbf{I}_7 = \mathbf{A} \circ \mathbf{B}. \quad (47)$$

The latter can be expressed as a linear combination of \mathbf{I}_r tensors, given by the tensor \mathbf{E}_{66} introduced in the sequel.

The elastic stiffness Equation (40) can be recast in terms of a more convenient set of base tensors \mathbf{E}_{rs} , such that

$$\mathbf{\Lambda} = \sum_{r,s=1}^3 \bar{c}_{rs} \mathbf{E}_{rs} + \bar{c}_{44} \mathbf{E}_{44} + \bar{c}_{55} \mathbf{E}_{55} + \bar{c}_{66} \mathbf{E}_{66}. \quad (48)$$

The corresponding moduli are

$$\begin{aligned}
\bar{c}_{11} &= c_1 + c_2 + 2c_3 + 2c_7 + c_9 = \lambda + 2\mu + 4\mu_1 + 2\alpha_1 + \beta_1, \\
\bar{c}_{22} &= c_1 + c_2 + 2c_5 + 2c_8 + c_{10} = \lambda + 2\mu + 4\mu_2 + 2\alpha_2 + \beta_2, \\
\bar{c}_{33} &= c_1 + c_2 = \lambda + 2\mu, \\
\bar{c}_{12} &= \bar{c}_{21} = c_2 + c_3 + c_5 + c_{11} = \lambda + \alpha_1 + \alpha_2 + \beta_3, \\
\bar{c}_{23} &= \bar{c}_{32} = c_2 + c_5 = \lambda + \alpha_2, \\
\bar{c}_{31} &= \bar{c}_{13} = c_2 + c_3 = \lambda + \alpha_1, \\
\bar{c}_{44} &= c_1 + c_8 = 2(\mu + \mu_2), \\
\bar{c}_{55} &= c_1 + c_7 = 2(\mu + \mu_1), \\
\bar{c}_{66} &= c_1 + c_7 + c_8 = 2(\mu + \mu_1 + \mu_2).
\end{aligned} \tag{49}$$

The base \mathbf{E}_{rs} are defined by

$$\begin{aligned}
\mathbf{E}_{11} &= \mathbf{A} \mathbf{A}, & \mathbf{E}_{12} &= \mathbf{A} \mathbf{B}, & \mathbf{E}_{13} &= \mathbf{A} \mathbf{C}, \\
\mathbf{E}_{21} &= \mathbf{B} \mathbf{A}, & \mathbf{E}_{22} &= \mathbf{B} \mathbf{B}, & \mathbf{E}_{23} &= \mathbf{B} \mathbf{C}, \\
\mathbf{E}_{31} &= \mathbf{C} \mathbf{A}, & \mathbf{E}_{32} &= \mathbf{C} \mathbf{B}, & \mathbf{E}_{33} &= \mathbf{C} \mathbf{C},
\end{aligned} \tag{50}$$

and

$$\mathbf{E}_{44} = \mathbf{B} \circ \mathbf{C}, \quad \mathbf{E}_{55} = \mathbf{C} \circ \mathbf{A} \quad \mathbf{E}_{66} = \mathbf{A} \circ \mathbf{B}. \tag{51}$$

The ordering of the last three tensors is made to facilitate the later comparison with the classical moduli given in the Voigt notation.

The trace products of the tensors \mathbf{E}_{rs} are specified by the following rules [Walpole 1984]

$$\begin{aligned}
\mathbf{E}_{pq} : \mathbf{E}_{qr} &= \mathbf{E}_{pr}, & (\text{no sum on } q), \\
\mathbf{E}_{pq} : \mathbf{E}_{rs} &= \mathbf{0}, & (q \neq r).
\end{aligned} \tag{52}$$

Furthermore, a zero trace product is obtained when any one of \mathbf{E}_{44} , \mathbf{E}_{55} , and \mathbf{E}_{66} is traced with the other two or any one of \mathbf{E}_{rs} (see Table 10 of the Appendix).

An alternative representation of the elastic stiffness tensor is obtained from the representation theorem for orthotropic tensor functions, if the stress tensor $\boldsymbol{\sigma}$ is expressed in terms of the strain tensor $\boldsymbol{\epsilon}$ and the structural tensors \mathbf{A} , \mathbf{B} , and \mathbf{C} [Boehler 1987]. This is

$$\boldsymbol{\sigma} = \hat{c}_1 \mathbf{A} + \hat{c}_2 \mathbf{B} + \hat{c}_3 \mathbf{C} + \hat{c}_4 (\mathbf{A} \cdot \boldsymbol{\epsilon} + \boldsymbol{\epsilon} \cdot \mathbf{A}) + \hat{c}_5 (\mathbf{B} \cdot \boldsymbol{\epsilon} + \boldsymbol{\epsilon} \cdot \mathbf{B}) + \hat{c}_6 (\mathbf{C} \cdot \boldsymbol{\epsilon} + \boldsymbol{\epsilon} \cdot \mathbf{C}). \tag{53}$$

To preserve the linear dependence on strain, the functions \hat{c}_r are

$$\hat{c}_r = \hat{c}_{r1} \mathbf{A} : \boldsymbol{\epsilon} + \hat{c}_{r2} \mathbf{B} : \boldsymbol{\epsilon} + \hat{c}_{r3} \mathbf{C} : \boldsymbol{\epsilon}, \quad r = 1, 2, 3, \tag{54}$$

where the parameters \hat{c}_{rs} , $\hat{c}_4 = \hat{c}_{44}$, $\hat{c}_5 = \hat{c}_{55}$, and $\hat{c}_6 = \hat{c}_{66}$ are the material constants. The dot (\cdot) denotes the inner tensor product, and $:$ is used for the trace product. The elastic stiffness tensor associated with

Equation (53) and (54) is

$$\mathbf{\Lambda} = \sum_{r,s=1}^3 \hat{c}_{rs} \mathbf{E}_{rs} + \hat{c}_{44} \mathbf{A} \circ \boldsymbol{\delta} + \hat{c}_{55} \mathbf{B} \circ \boldsymbol{\delta} + \hat{c}_{66} \mathbf{C} \circ \boldsymbol{\delta}. \quad (55)$$

3.1. Elastic compliances of orthotropic materials. If the elastic moduli tensor Equation (48) is symbolically written, with respect to the basis of \mathbf{E}_{rs} tensors, as

$$\mathbf{\Lambda} = \left\{ \begin{bmatrix} \bar{c}_{11} & \bar{c}_{12} & \bar{c}_{13} \\ \bar{c}_{21} & \bar{c}_{22} & \bar{c}_{23} \\ \bar{c}_{31} & \bar{c}_{32} & \bar{c}_{33} \end{bmatrix}, \bar{c}_{44}, \bar{c}_{55}, \bar{c}_{66} \right\}, \quad (56)$$

then its inverse, the elastic compliances tensor, can be symbolically written as [Walpole 1984]

$$\mathbf{\Lambda}^{-1} = \left\{ \begin{bmatrix} \bar{c}_{11} & \bar{c}_{12} & \bar{c}_{13} \\ \bar{c}_{21} & \bar{c}_{22} & \bar{c}_{23} \\ \bar{c}_{31} & \bar{c}_{32} & \bar{c}_{33} \end{bmatrix}^{-1}, \bar{c}_{44}^{-1}, \bar{c}_{55}^{-1}, \bar{c}_{66}^{-1} \right\}. \quad (57)$$

Thus,

$$\mathbf{\Lambda}^{-1} = \sum_{r,s=1}^3 \bar{s}_{rs} \mathbf{E}_{rs} + \bar{s}_{44} \mathbf{E}_{44} + \bar{s}_{55} \mathbf{E}_{55} + \bar{s}_{66} \mathbf{E}_{66}, \quad (58)$$

where

$$\begin{aligned} \bar{s}_{11} &= (\bar{c}_{22}\bar{c}_{33} - \bar{c}_{23}^2)/\bar{c}, & \bar{s}_{12} &= \bar{s}_{21} = (\bar{c}_{31}\bar{c}_{23} - \bar{c}_{12}\bar{c}_{33})/\bar{c}, & \bar{s}_{22} &= (\bar{c}_{11}\bar{c}_{33} - \bar{c}_{31}^2)/\bar{c}, \\ \bar{s}_{23} &= \bar{s}_{32} = (\bar{c}_{12}\bar{c}_{31} - \bar{c}_{11}\bar{c}_{23})/\bar{c}, & \bar{s}_{31} &= \bar{s}_{13} = (\bar{c}_{12}\bar{c}_{23} - \bar{c}_{31}\bar{c}_{22})/\bar{c}, & \bar{s}_{33} &= (\bar{c}_{11}\bar{c}_{22} - \bar{c}_{12}^2)/\bar{c}, \\ \bar{s}_{44} &= 1/\bar{c}_{44}, & \bar{s}_{55} &= 1/\bar{c}_{55}, & \bar{s}_{66} &= 1/\bar{c}_{66}, \end{aligned} \quad (59)$$

and

$$\bar{c} = \bar{c}_{11}\bar{c}_{22}\bar{c}_{33} + 2\bar{c}_{12}\bar{c}_{23}\bar{c}_{31} - \bar{c}_{11}\bar{c}_{23}^2 - \bar{c}_{22}\bar{c}_{31}^2 - \bar{c}_{33}\bar{c}_{12}^2. \quad (60)$$

The results for transversely isotropic materials can be recovered from the above results by taking $\bar{c}_{22} = \bar{c}_{11}$, $\bar{c}_{23} = \bar{c}_{31}$, and $\bar{c}_{55} = \bar{c}_{44} = \bar{c}_{11} - \bar{c}_{12}$.

The compliances tensor can also be derived by the inversion of the elastic moduli tensor expressed with respect to the set of base tensors used in Equation (55). This gives

$$\mathbf{\Lambda}^{-1} = \sum_{r,s=1}^3 \hat{s}_{rs} \mathbf{E}_{rs} + \hat{s}_{44} \mathbf{A} \circ \boldsymbol{\delta} + \hat{s}_{55} \mathbf{B} \circ \boldsymbol{\delta} + \hat{s}_{66} \mathbf{C} \circ \boldsymbol{\delta}, \quad (61)$$

with the corresponding compliances

$$\begin{aligned} \hat{s}_{11} &= \bar{s}_{11} - \bar{s}_{66} + \bar{s}_{44} - \bar{s}_{55}, & \hat{s}_{22} &= \bar{s}_{22} - \bar{s}_{44} + \bar{s}_{55} - \bar{s}_{66}, & \hat{s}_{33} &= \bar{s}_{33} - \bar{s}_{44} + \bar{s}_{66} - \bar{s}_{55}, \\ \hat{s}_{12} &= \bar{s}_{12}, & \hat{s}_{23} &= \bar{s}_{23}, & \hat{s}_{31} &= \bar{s}_{31}, \\ \hat{s}_{44} &= \frac{1}{2}(\bar{s}_{55} + \bar{s}_{66} - \bar{s}_{44}), & \hat{s}_{55} &= \frac{1}{2}(\bar{s}_{44} + \bar{s}_{66} - \bar{s}_{55}), & \hat{s}_{66} &= \frac{1}{2}(\bar{s}_{44} + \bar{s}_{55} - \bar{s}_{66}). \end{aligned} \quad (62)$$

3.2. Relationships to engineering constants in Voigt notation. The elastic moduli c_r are related to commonly used engineering moduli C_{ij} , appearing in Equation (25), by

$$\begin{aligned} c_1 &= 2(C_{44} + C_{55} - C_{66}), & c_2 &= C_{33} - c_1, & c_3 &= c_4 = C_{31} - c_2, \\ c_5 &= c_6 = C_{23} - c_2, & c_7 &= 2(C_{66} - C_{44}), & c_8 &= 2(C_{66} - C_{55}), \\ c_9 &= C_{11} + C_{33} - 2C_{31} - 4C_{55}, & c_{10} &= C_{22} + C_{33} - 2C_{23} - 4C_{44}, & c_{11} &= c_{12} = c_2 + C_{12} - C_{23} - C_{31}. \end{aligned} \quad (63)$$

The relationships between \bar{c}_{ij} and C_{ij} are

$$\begin{aligned} \bar{c}_{11} &= C_{11}, & \bar{c}_{22} &= C_{22}, & \bar{c}_{33} &= C_{33}, \\ \bar{c}_{12} &= C_{12}, & \bar{c}_{23} &= C_{23}, & \bar{c}_{31} &= C_{31}, \\ \bar{c}_{44} &= 2C_{44}, & \bar{c}_{55} &= 2C_{55}, & \bar{c}_{66} &= 2C_{66}. \end{aligned} \quad (64)$$

To derive the relationship between the moduli \hat{c}_{ij} appearing the stiffness representation Equation (55) and the moduli \bar{c}_{ij} or C_{ij} , we first note that

$$\mathbf{C} \circ \boldsymbol{\delta} = (\boldsymbol{\delta} - \mathbf{A} - \mathbf{B}) \circ \boldsymbol{\delta} = 2\mathbf{I}_1 - \mathbf{I}_7 - \mathbf{I}_8. \quad (65)$$

It then readily follows that

$$\begin{aligned} \hat{c}_{11} &= \bar{c}_{11} - \bar{c}_{66} + \bar{c}_{44} - \bar{c}_{55}, & \hat{c}_{12} &= \bar{c}_{12}, & \hat{c}_{23} &= \bar{c}_{23}, \\ \hat{c}_{22} &= \bar{c}_{22} - \bar{c}_{44} + \bar{c}_{55} - \bar{c}_{66}, & \hat{c}_{44} &= \frac{1}{2}(\bar{c}_{55} + \bar{c}_{66} - \bar{c}_{44}), & \hat{c}_{55} &= \frac{1}{2}(\bar{c}_{44} + \bar{c}_{66} - \bar{c}_{55}), \\ \hat{c}_{33} &= \bar{c}_{33} - \bar{c}_{44} + \bar{c}_{66} - \bar{c}_{55}, & \hat{c}_{31} &= \bar{c}_{31}, & \hat{c}_{66} &= \frac{1}{2}(\bar{c}_{44} + \bar{c}_{55} - \bar{c}_{66}), \end{aligned} \quad (66)$$

in agreement with the corresponding expressions derived by other means in [Boehler 1987].

The compliance coefficients \bar{s}_{ij} are related to the usual engineering constants of orthotropic materials (defined with respect to its principal axes of orthotropy \mathbf{a} , \mathbf{b} , and \mathbf{c}) by

$$\begin{aligned} \bar{s}_{11} &= \frac{1}{E_a}, & \bar{s}_{12} &= -\frac{\nu_{ab}}{E_a}, & \bar{s}_{13} &= -\frac{\nu_{ac}}{E_a}, \\ \bar{s}_{22} &= \frac{1}{E_b}, & \bar{s}_{23} &= -\frac{\nu_{bc}}{E_b}, & \bar{s}_{33} &= \frac{1}{E_c}, \\ \bar{s}_{44} &= \frac{1}{2G_{bc}}, & \bar{s}_{55} &= \frac{1}{2G_{ac}}, & \bar{s}_{66} &= \frac{1}{2G_{ab}}. \end{aligned} \quad (67)$$

The compliances \bar{s}_{ij} are actually equal to S_{ij} , except for the shear compliances which are related by the coefficient of 2 (that is, $S_{44} = 2\bar{s}_{44}$, $S_{55} = 2\bar{s}_{55}$, and $S_{66} = 2\bar{s}_{66}$).

To express the elastic compliances tensor in terms of the original base tensors, we first express the tensors \mathbf{I}_r in terms of the tensors \mathbf{E}_{rs} . The connections are

$$\begin{aligned}
 \mathbf{I}_1 &= \mathbf{E}_{11} + \mathbf{E}_{22} + \mathbf{E}_{33} + \mathbf{E}_{44} + \mathbf{E}_{55} + \mathbf{E}_{66}, \\
 \mathbf{I}_2 &= \mathbf{E}_{11} + \mathbf{E}_{12} + \mathbf{E}_{13} + \mathbf{E}_{21} + \mathbf{E}_{22} + \mathbf{E}_{23} + \mathbf{E}_{31} + \mathbf{E}_{32} + \mathbf{E}_{33}, \\
 \mathbf{I}_3 &= \mathbf{E}_{11} + \mathbf{E}_{12} + \mathbf{E}_{13}, \quad \mathbf{I}_4 = \mathbf{E}_{11} + \mathbf{E}_{21} + \mathbf{E}_{31}, \\
 \mathbf{I}_5 &= \mathbf{E}_{21} + \mathbf{E}_{22} + \mathbf{E}_{23}, \quad \mathbf{I}_6 = \mathbf{E}_{12} + \mathbf{E}_{22} + \mathbf{E}_{32}, \\
 \mathbf{I}_7 &= 2\mathbf{E}_{11} + \mathbf{E}_{55} + \mathbf{E}_{66}, \quad \mathbf{I}_8 = 2\mathbf{E}_{22} + \mathbf{E}_{44} + \mathbf{E}_{66}, \\
 \mathbf{I}_9 &= \mathbf{E}_{11}, \quad \mathbf{I}_{10} = \mathbf{E}_{22}, \quad \mathbf{I}_{11} = \mathbf{E}_{12}, \quad \mathbf{I}_{12} = \mathbf{E}_{21},
 \end{aligned} \tag{68}$$

with the inverse expressions

$$\begin{aligned}
 \mathbf{E}_{11} &= \mathbf{I}_9, \quad \mathbf{E}_{12} = \mathbf{I}_{11}, \quad \mathbf{E}_{13} = \mathbf{I}_3 - \mathbf{I}_9 - \mathbf{I}_{11}, \\
 \mathbf{E}_{21} &= \mathbf{I}_{12}, \quad \mathbf{E}_{22} = \mathbf{I}_{10}, \quad \mathbf{E}_{23} = \mathbf{I}_5 - \mathbf{I}_{10} - \mathbf{I}_{12}, \\
 \mathbf{E}_{31} &= \mathbf{I}_4 - \mathbf{I}_9 - \mathbf{I}_{12}, \quad \mathbf{E}_{32} = \mathbf{I}_6 - \mathbf{I}_{10} - \mathbf{I}_{11}, \\
 \mathbf{E}_{33} &= \mathbf{I}_2 - \mathbf{I}_3 - \mathbf{I}_4 - \mathbf{I}_5 - \mathbf{I}_6 + \mathbf{I}_9 + \mathbf{I}_{10} + \mathbf{I}_{11} + \mathbf{I}_{12}, \\
 \mathbf{E}_{44} &= \mathbf{I}_1 - \mathbf{I}_2 + \mathbf{I}_3 + \mathbf{I}_4 + \mathbf{I}_5 + \mathbf{I}_6 - \mathbf{I}_7 - 2\mathbf{I}_{10} - \mathbf{I}_{11} - \mathbf{I}_{12}, \\
 \mathbf{E}_{55} &= \mathbf{I}_1 - \mathbf{I}_2 + \mathbf{I}_3 + \mathbf{I}_4 + \mathbf{I}_5 + \mathbf{I}_6 - \mathbf{I}_8 - 2\mathbf{I}_9 - \mathbf{I}_{11} - \mathbf{I}_{12}, \\
 \mathbf{E}_{66} &= -\mathbf{I}_1 + \mathbf{I}_2 - \mathbf{I}_3 - \mathbf{I}_4 - \mathbf{I}_5 - \mathbf{I}_6 + \mathbf{I}_7 + \mathbf{I}_8 + \mathbf{I}_{11} + \mathbf{I}_{12}.
 \end{aligned} \tag{69}$$

The substitution of Equation (69) into (58) then gives

$$\mathbf{\Lambda}^{-1} = \sum_{r=1}^{12} s_r \mathbf{I}_r. \tag{70}$$

The corresponding elastic compliances are

$$\begin{aligned}
 s_1 &= \bar{s}_{55} + \bar{s}_{66} - \bar{s}_{44}, & s_2 &= \bar{s}_{33} + \bar{s}_{44} - \bar{s}_{55} - \bar{s}_{66}, \\
 s_3 &= s_4 = \bar{s}_{13} - \bar{s}_{33} - \bar{s}_{44} + \bar{s}_{55} + \bar{s}_{66}, & s_5 &= s_6 = \bar{s}_{23} - \bar{s}_{33} - \bar{s}_{44} + \bar{s}_{55} + \bar{s}_{66}, \\
 s_7 &= \bar{s}_{44} - \bar{s}_{55}, & s_8 &= \bar{s}_{44} - \bar{s}_{66}, \\
 s_9 &= \bar{s}_{11} - 2\bar{s}_{31} + \bar{s}_{33} - 2\bar{s}_{66}, & s_{10} &= \bar{s}_{22} - 2\bar{s}_{23} + \bar{s}_{33} - 2\bar{s}_{55}, \\
 s_{11} &= s_{12} = \bar{s}_{21} - \bar{s}_{23} - \bar{s}_{31} + \bar{s}_{33} + \bar{s}_{44} - \bar{s}_{55} - \bar{s}_{66}.
 \end{aligned} \tag{71}$$

Since \bar{s}_{rs} are specified in terms of \bar{c}_{rs} by Equation (59), and \bar{c}_{rs} in terms of c_r by Equation (49), the compliances s_r in Equation (71) are all expressed in terms of the elastic moduli c_r .

The relationships Equation (71) reveal the connections between the original moduli appearing in Equation (41) and the engineering moduli. The resulting expressions in an explicit form are lengthy, but their numerical evaluations are simple. For example, the Young's modulus in the direction of principal orthotropy \mathbf{a} is

$$E_a = \frac{1}{s_{11}} = \frac{\bar{c}}{\bar{c}_{22}\bar{c}_{33} - \bar{c}_{23}^2}, \tag{72}$$

c_1	c_2	$c_3=c_4$	$c_5=c_6$	c_7	c_8	c_9	c_{10}	$c_{11}=c_{12}$
14.64	12.96	-2.86	-2.26	-3.42	-2.18	2.96	1.48	2.14

Table 6. Elastic moduli c_i (in units of GPa).

where \bar{c}_{ij} are given by Equation (49) and \bar{c} by (60). In the case of transverse isotropy, with the axis of isotropy parallel to \mathbf{c} ($\bar{c}_{22} = \bar{c}_{11}$, $\bar{c}_{23} = \bar{c}_{31}$, and $\bar{c}_{55} = \bar{c}_{44} = \bar{c}_{11} - \bar{c}_{12}$), this reduces to Equation (72), while in the isotropic case ($\alpha_1 = \alpha_2 = \beta_1 = \beta_2 = \beta_3 = 0$ and $\mu_1 = \mu_2 = \mu$), we recover the result $E = \mu(3\lambda + 2\mu)/(\lambda + \mu)$.

3.3. Elastic constants of a human femur. Elastic moduli C_{ij} of a human femoral bone, determined by ultrasound measurement technique, were reported in Ashman and Buskirk (1987) as

$$\begin{bmatrix} C_{11} & C_{12} & C_{13} \\ C_{21} & C_{22} & C_{23} \\ C_{31} & C_{32} & C_{33} \end{bmatrix} = \begin{bmatrix} 18 & 9.98 & 10.1 \\ 9.98 & 20.2 & 10.7 \\ 10.1 & 10.7 & 27.6 \end{bmatrix}, \quad \begin{bmatrix} C_{44} \\ C_{55} \\ C_{66} \end{bmatrix} = \begin{bmatrix} 6.23 \\ 5.61 \\ 4.52 \end{bmatrix} \quad (\text{GPa}).$$

The corresponding moduli \bar{c}_{ij} and \hat{c}_{ij} follow from (64) and (66). In units of GPa, they are

$$\begin{bmatrix} \bar{c}_{11} & \bar{c}_{12} & \bar{c}_{13} \\ \bar{c}_{21} & \bar{c}_{22} & \bar{c}_{23} \\ \bar{c}_{31} & \bar{c}_{32} & \bar{c}_{33} \end{bmatrix} = \begin{bmatrix} 18 & 9.98 & 10.1 \\ 9.98 & 20.2 & 10.7 \\ 10.1 & 10.7 & 27.6 \end{bmatrix}, \quad \begin{bmatrix} \bar{c}_{44} \\ \bar{c}_{55} \\ \bar{c}_{66} \end{bmatrix} = \begin{bmatrix} 12.46 \\ 11.22 \\ 9.04 \end{bmatrix},$$

$$\begin{bmatrix} \hat{c}_{11} & \hat{c}_{12} & \hat{c}_{13} \\ \hat{c}_{21} & \hat{c}_{22} & \hat{c}_{23} \\ \hat{c}_{31} & \hat{c}_{32} & \hat{c}_{33} \end{bmatrix} = \begin{bmatrix} 10.2 & 9.98 & 10.1 \\ 9.98 & 9.92 & 10.7 \\ 10.1 & 10.7 & 12.96 \end{bmatrix}, \quad \begin{bmatrix} \hat{c}_{44} \\ \hat{c}_{55} \\ \hat{c}_{66} \end{bmatrix} = \begin{bmatrix} 3.9 \\ 5.14 \\ 7.32 \end{bmatrix}.$$

The moduli c_i , calculated from Equation (63), are listed in Table 6.

The elastic compliances S_{ij} (in units of TPa⁻¹), corresponding to elastic moduli C_{ij} given above, are

$$\begin{bmatrix} S_{11} & S_{12} & S_{13} \\ S_{21} & S_{22} & S_{23} \\ S_{31} & S_{32} & S_{33} \end{bmatrix} = \begin{bmatrix} 83.24 & -31.45 & -18.27 \\ -31.45 & 74.18 & -17.25 \\ -18.27 & -17.25 & 49.60 \end{bmatrix}, \quad \begin{bmatrix} S_{44} \\ S_{55} \\ S_{66} \end{bmatrix} = \begin{bmatrix} 160.52 \\ 178.26 \\ 221.24 \end{bmatrix}.$$

The compliances \bar{s}_{ij} and \hat{s}_{ij} follow from (59) and (62). In units of TPa⁻¹, they are

$$\begin{bmatrix} \bar{s}_{11} & \bar{s}_{12} & \bar{s}_{13} \\ \bar{s}_{21} & \bar{s}_{22} & \bar{s}_{23} \\ \bar{s}_{31} & \bar{s}_{32} & \bar{s}_{33} \end{bmatrix} = \begin{bmatrix} 83.24 & -31.45 & -18.27 \\ -31.45 & 74.18 & -17.25 \\ -18.27 & -17.25 & 49.60 \end{bmatrix}, \quad \begin{bmatrix} \bar{s}_{44} \\ \bar{s}_{55} \\ \bar{s}_{66} \end{bmatrix} = \begin{bmatrix} 80.26 \\ 89.13 \\ 110.62 \end{bmatrix},$$

$$\begin{bmatrix} \hat{s}_{11} & \hat{s}_{12} & \hat{s}_{13} \\ \hat{s}_{21} & \hat{s}_{22} & \hat{s}_{23} \\ \hat{s}_{31} & \hat{s}_{32} & \hat{s}_{33} \end{bmatrix} = \begin{bmatrix} -36.24 & -31.45 & -18.27 \\ -31.45 & -27.57 & -17.25 \\ -18.27 & -17.25 & -9.16 \end{bmatrix}, \quad \begin{bmatrix} \hat{s}_{44} \\ \hat{s}_{55} \\ \hat{s}_{66} \end{bmatrix} = \begin{bmatrix} 59.74 \\ 50.87 \\ 29.38 \end{bmatrix}.$$

The above results show that for human femur S_{ij} and \bar{s}_{ij} are negative for $i \neq j$, while \hat{s}_{ij} are negative for all $i, j = 1, 2, 3$. The compliance coefficients s_i , calculated from Equation (71), are listed in Table 7. The longitudinal and shear moduli and the Poisson ratios, with respect to the principal axes of

s_1	s_2	$s_3=s_4$	$s_5=s_6$	s_7	s_8	s_9	s_{10}	$s_{11}=s_{12}$
119.49	-69.88	51.61	52.63	-8.87	-30.36	-51.85	-19.97	-65.81

Table 7. Elastic compliances s_i (in units of TPa^{-1}).

E_a	E_b	E_c	G_{ab}	G_{bc}	G_{ac}	ν_{ab}	ν_{bc}	ν_{ac}
12.01	13.48	20.16	4.52	6.23	5.61	0.378	0.233	0.219

Table 8. Longitudinal and shear moduli (in units of GPa) and the Poisson ratios.

orthotropy, follow from Equation (67) and are given in Table 8. The remaining three Poisson's ratios are determined from the well known connections $\nu_{ba} = \nu_{ab}E_b/E_a = 0.424$, $\nu_{cb} = \nu_{bc}E_c/E_b = 0.348$, and $\nu_{ca} = \nu_{ac}E_c/E_a = 0.368$.

4. Conclusion

In this paper we have derived the relationships between the elastic moduli and compliances of transversely isotropic materials, which correspond to two different sets of linearly independent fourth-order base tensors used to cast the tensorial representation of the elastic moduli and compliances tensors. The two sets of elastic constants are related to engineering constants defined with respect to the coordinate system in which one of the axes is parallel to the axis of material symmetry. Extending the analysis to orthotropic materials, three different representations of the elastic moduli tensor are constructed by choosing three appealing sets of twelve linearly independent fourth-order base tensors. This was accomplished on the basis of the representation theorems for orthotropic tensor functions of a symmetric second-order tensor and the structural tensors associated with the principal axes of orthotropy. The three sets of the corresponding elastic moduli are related to each other. The compliances tensor is deduced by an explicit inversion of the stiffness tensor for all considered sets of the base tensors. The different compliances are related to each other, and to classical engineering constants expressed in the Voigt notation. The formulas are applied to calculate the elastic constants for a transversely isotropic monocrystalline zinc and an orthotropic human femoral bone. Apart from the analytical point of view, the derived results may be of interest for the analysis of anisotropic elastic and inelastic material response (with an elastic component of strain or stress) in the mechanics of fiber reinforced composite materials [Hyer 1998; Vasiliev and Morozov 2001], creep mechanics [Drozdov 1998; Betten 2002], damage-elastoplasticity [Lubarda 1994], mechanics of brittle materials weakened by anisotropic crack distributions [Krajcinovic 1996; Voyiadjis and Kattan 1999], and biological materials (membranes or tissues) with embedded filament networks [Evans and Skalak 1980; Fung 1990; Humphrey 2002; Lubarda and Hoger 2002; Asaro and Lubarda 2006].

$\vec{\Gamma}$	\mathbf{I}_1	\mathbf{I}_2	\mathbf{I}_3	\mathbf{I}_4	\mathbf{I}_5	\mathbf{I}_6	\mathbf{I}_7	\mathbf{I}_8	\mathbf{I}_9	\mathbf{I}_{10}	\mathbf{I}_{11}	\mathbf{I}_{12}
\mathbf{I}_1	\mathbf{I}_1	\mathbf{I}_2	\mathbf{I}_3	\mathbf{I}_4	\mathbf{I}_5	\mathbf{I}_6	\mathbf{I}_7	\mathbf{I}_8	\mathbf{I}_9	\mathbf{I}_{10}	\mathbf{I}_{11}	\mathbf{I}_{12}
\mathbf{I}_2	\mathbf{I}_2	$3\mathbf{I}_2$	\mathbf{I}_2	$3\mathbf{I}_4$	\mathbf{I}_2	$3\mathbf{I}_6$	$2\mathbf{I}_4$	$2\mathbf{I}_6$	\mathbf{I}_4	\mathbf{I}_6	\mathbf{I}_6	\mathbf{I}_4
\mathbf{I}_3	\mathbf{I}_3	$3\mathbf{I}_3$	\mathbf{I}_3	$3\mathbf{I}_9$	\mathbf{I}_3	$3\mathbf{I}_{11}$	$2\mathbf{I}_9$	$2\mathbf{I}_{11}$	\mathbf{I}_9	\mathbf{I}_{11}	\mathbf{I}_{11}	\mathbf{I}_9
\mathbf{I}_4	\mathbf{I}_4	\mathbf{I}_2	\mathbf{I}_2	\mathbf{I}_4	0	\mathbf{I}_6	$2\mathbf{I}_4$	0	\mathbf{I}_4	0	\mathbf{I}_6	0
\mathbf{I}_5	\mathbf{I}_5	$3\mathbf{I}_5$	\mathbf{I}_5	$3\mathbf{I}_{12}$	\mathbf{I}_5	$3\mathbf{I}_{10}$	$2\mathbf{I}_{12}$	$2\mathbf{I}_{10}$	\mathbf{I}_{12}	\mathbf{I}_{10}	\mathbf{I}_{10}	\mathbf{I}_{12}
\mathbf{I}_6	\mathbf{I}_6	\mathbf{I}_2	0	\mathbf{I}_4	\mathbf{I}_2	\mathbf{I}_6	0	$2\mathbf{I}_6$	0	\mathbf{I}_6	0	\mathbf{I}_4
\mathbf{I}_7	\mathbf{I}_7	$2\mathbf{I}_3$	$2\mathbf{I}_3$	$2\mathbf{I}_9$	0	$2\mathbf{I}_{11}$	$\mathbf{I}_7 + 2\mathbf{I}_9$	$\mathbf{A} \circ \mathbf{B}$	$2\mathbf{I}_9$	0	$2\mathbf{I}_{11}$	0
\mathbf{I}_8	\mathbf{I}_8	$2\mathbf{I}_5$	0	$2\mathbf{I}_{12}$	$2\mathbf{I}_5$	$2\mathbf{I}_{10}$	$\mathbf{A} \circ \mathbf{B}$	$\mathbf{I}_8 + 2\mathbf{I}_{10}$	0	$2\mathbf{I}_{10}$	0	$2\mathbf{I}_{12}$
\mathbf{I}_9	\mathbf{I}_9	\mathbf{I}_3	\mathbf{I}_3	\mathbf{I}_9	0	\mathbf{I}_{11}	$2\mathbf{I}_9$	0	\mathbf{I}_9	0	\mathbf{I}_{11}	0
\mathbf{I}_{10}	\mathbf{I}_{10}	\mathbf{I}_5	0	\mathbf{I}_{12}	\mathbf{I}_5	\mathbf{I}_{10}	0	$2\mathbf{I}_{10}$	0	\mathbf{I}_{10}	0	\mathbf{I}_{12}
\mathbf{I}_{11}	\mathbf{I}_{11}	\mathbf{I}_3	0	\mathbf{I}_9	\mathbf{I}_3	\mathbf{I}_{11}	0	$2\mathbf{I}_{11}$	0	\mathbf{I}_{11}	0	\mathbf{I}_9
\mathbf{I}_{12}	\mathbf{I}_{12}	\mathbf{I}_5	\mathbf{I}_5	\mathbf{I}_{12}	0	\mathbf{I}_{10}	$2\mathbf{I}_{12}$	0	\mathbf{I}_{12}	0	\mathbf{I}_{10}	0

Table 9. Table of products $\mathbf{I}_r : \mathbf{I}_s$.

$\vec{\Gamma}$	\mathbf{E}_{11}	\mathbf{E}_{12}	\mathbf{E}_{13}	\mathbf{E}_{21}	\mathbf{E}_{22}	\mathbf{E}_{23}	\mathbf{E}_{31}	\mathbf{E}_{32}	\mathbf{E}_{33}	\mathbf{E}_{44}	\mathbf{E}_{55}	\mathbf{E}_{66}
\mathbf{E}_{11}	\mathbf{E}_{11}	\mathbf{E}_{12}	\mathbf{E}_{13}	0	0	0	0	0	0	0	0	0
\mathbf{E}_{12}	0	0	0	\mathbf{E}_{11}	\mathbf{E}_{12}	\mathbf{E}_{13}	0	0	0	0	0	0
\mathbf{E}_{13}	0	0	0	0	0	0	\mathbf{E}_{11}	\mathbf{E}_{12}	\mathbf{E}_{13}	0	0	0
\mathbf{E}_{21}	\mathbf{E}_{21}	\mathbf{E}_{22}	\mathbf{E}_{23}	0	0	0	0	0	0	0	0	0
\mathbf{E}_{22}	0	0	0	\mathbf{E}_{21}	\mathbf{E}_{22}	\mathbf{E}_{23}	0	0	0	0	0	0
\mathbf{E}_{23}	0	0	0	0	0	0	\mathbf{E}_{21}	\mathbf{E}_{22}	\mathbf{E}_{23}	0	0	0
\mathbf{E}_{31}	\mathbf{E}_{31}	\mathbf{E}_{32}	\mathbf{E}_{33}	0	0	0	0	0	0	0	0	0
\mathbf{E}_{32}	0	0	0	\mathbf{E}_{31}	\mathbf{E}_{32}	\mathbf{E}_{33}	0	0	0	0	0	0
\mathbf{E}_{33}	0	0	0	0	0	0	\mathbf{E}_{31}	\mathbf{E}_{32}	\mathbf{E}_{33}	0	0	0
\mathbf{E}_{44}	0	0	0	0	0	0	0	0	0	\mathbf{E}_{44}	0	0
\mathbf{E}_{55}	0	0	0	0	0	0	0	0	0	0	\mathbf{E}_{55}	0
\mathbf{E}_{66}	0	0	0	0	0	0	0	0	0	0	0	\mathbf{E}_{66}

Table 10. Table of products $\mathbf{E}_{rs} : \mathbf{E}_{pq}$.

Appendix: Multiplication tables for tensors \mathbf{I}_r and \mathbf{E}_{rs}

The trace products $\mathbf{I}_r : \mathbf{I}_s$ are listed in Table 9. The tensors \mathbf{I}_r are defined in Equation (42). The symbol $\overline{}$ indicates that the products are in the order: *a tensor from the left column traced with a tensor from the top row*. The products $\mathbf{E}_{rs} : \mathbf{E}_{pq}$, where the tensors \mathbf{E}_{rs} are defined in Equation (50) and (51), are listed in Table 10.

References

- [Asaro and Lubarda 2006] R. J. Asaro and V. A. Lubarda, *Mechanics of solids and materials*, Cambridge University Press, Cambridge, 2006.
- [Betten 1987] J. Betten, “Invariants of fourth-order tensors”, pp. 203–226 in *Applications of tensor functions in solid mechanics*, edited by J. P. Boehler, CISM Courses and Lectures **292**, Springer-Verlag, Wien, 1987.
- [Betten 2002] J. Betten, *Creep mechanics*, Springer-Verlag, Berlin, 2002.
- [Boehler 1987] J. P. Boehler, “Representations for isotropic and anisotropic non-polynomial tensor functions”, pp. 31–53 in *Applications of tensor functions in solid mechanics*, edited by J. P. Boehler, CISM Courses and Lectures **292**, Springer, Wien, 1987.
- [Cowin and Mehrabadi 1995] S. C. Cowin and M. M. Mehrabadi, “Anisotropic symmetries in linear elasticity”, *Appl. Mech. Rev.* **48** (1995), 247–285.
- [Drozdov 1998] A. D. Drozdov, *Mechanics of Viscoelastic Solids*, John Wiley & Sons, New York, 1998.
- [Evans and Skalak 1980] E. A. Evans and R. Skalak, *Mechanics and thermodynamics of biomembranes*, CRC Press, Boca Raton, Florida, 1980.
- [Fung 1990] Y.-C. Fung, *Biomechanics: motion, flow, stress, and growth*, Springer-Verlag, New York, 1990.
- [Gangi 2000] A. F. Gangi, “Fourth-order elastic-moduli tensors by inspection”, pp. 1–10 in *Fractures, converted waves and case studies—proceedings of the ninth international workshop on seismic anisotropy*, Tulsa, OK, 2000.
- [Hearmon 1961] R. F. E. Hearmon, *An introduction to applied anisotropic elasticity*, Clarendon Press, Oxford, 1961.
- [Humphrey 2002] J. D. Humphrey, *Cardiovascular solid mechanics: cells, tissues, and organs*, Springer-Verlag, New York, 2002.
- [Hyer 1998] M. W. Hyer, *Stress analysis of fiber-reinforced composite materials*, McGraw-Hill, Boston, 1998.
- [Krajcinovic 1996] D. Krajcinovic, *Damage mechanics*, Elsevier, New York, 1996.
- [Kunin 1981] I. A. Kunin, “An algebra of tensor operations and its applications to elasticity”, *Int. J. Engng. Sci.* **19** (1981), 1551–1561.
- [Kunin 1983] I. A. Kunin, *Elastic media with microstructure, part II*, Springer-Verlag, Berlin, 1983.
- [Landolt-Börnstein 1979] Landolt-Börnstein, *Numerical data and functional relationships in science and technology*, vol. 11, edited by K.-H. Hellwege and A. M. Hellwege, Group III, Springer-Verlag, Berlin, 1979.
- [Lekhnitskii 1981] S. G. Lekhnitskii, *Theory of elasticity of an anisotropic elastic body*, Mir Publishers, Moscow, 1981.
- [Lubarda 1994] V. A. Lubarda, “An analysis of large-strain damage elastoplasticity”, *Int. J. Solids Struct.* **31** (1994), 2951–2964.
- [Lubarda and Hoger 2002] V. A. Lubarda and A. Hoger, “On the mechanics of solids with a growing mass”, *Int. J. Solids Struct.* **39** (2002), 4627–4664.
- [Lubarda and Krajcinovic 1994] V. A. Lubarda and D. Krajcinovic, “Tensorial representation of the effective elastic properties of the damaged material”, *Int. J. Damage Mech.* **3** (1994), 38–56.
- [Lubarda and Meyers 1999] V. A. Lubarda and M. A. Meyers, “On the negative Poisson ratio in monocrystalline zinc”, *Scripta Mater.* **40** (1999), 975–977.
- [Mehrabadi and Cowin 1990] M. M. Mehrabadi and S. C. Cowin, “Eigentensors of linear anisotropic elastic materials”, *Q. Jl. Mech. Appl. Math.* **43** (1990), 15–41.

- [Nadeau and Ferrari 1998] J. C. Nadeau and M. Ferrari, “Invariant tensor-to-matrix mappings for evaluation of tensorial expressions”, *J. Elasticity* **52** (1998), 43–61.
- [Nye 1964] J. F. Nye, *Physical properties of crystals: their representation by tensors and matrices*, Clarendon Press, Oxford, 1964.
- [Rychlewski 1984] J. Rychlewski, “On Hooke’s law”, *J. Appl. Mech. Math.* **48** (1984), 303–314.
- [Spencer 1982] A. J. M. Spencer, “The formulation of constitutive equation for anisotropic solids”, pp. 2–26 in *Mechanical behavior of anisotropic solids*, edited by J. P. Boehler, Martinus Nijhoff Publishers, The Hague, 1982.
- [Srinivasan and Nigam 1969] T. P. Srinivasan and S. D. Nigam, “Invariant elastic constants for crystals”, *J. Math. Mech.* **19** (1969), 411–420.
- [Sutcliffe 1992] S. Sutcliffe, “Spectral decomposition of the elasticity tensor”, *J. Appl. Mech.* **59** (1992), 762–773.
- [Theocaris and Philippidis 1989] P. S. Theocaris and T. P. Philippidis, “Elastic eigenstates of a medium with transverse isotropy”, *Arch. Mech.* **41** (1989), 717–724.
- [Theocaris and Sokolis 2000] P. S. Theocaris and D. P. Sokolis, “Spectral decomposition of the compliance fourth-rank tensor for orthotropic materials”, *Arch. Appl. Mech.* **70** (2000), 289–306.
- [Ting 1987] T. C. T. Ting, “Invariants of anisotropic elastic constants”, *Q. Jl. Mech. Appl. Math.* **40** (1987), 431–448.
- [Ting 2000] T. C. T. Ting, “Anisotropic elastic constants that are structurally invariant”, *Q. Jl. Mech. Appl. Math.* **53** (2000), 511–523.
- [Ting and He 2006] T. C. T. Ting and Q.-C. He, “Decomposition of elasticity tensors and tensors that are structurally invariant in three dimensions”, *Q. Jl. Mech. Appl. Math.* **59** (2006), 323–341.
- [Vasiliev and Morozov 2001] V. V. Vasiliev and E. V. Morozov, *Mechanics and analysis of composite materials*, Elsevier, Amsterdam, 2001.
- [Voigt 1928] W. Voigt, *Lehrbuch der Kristallphysik*, Johnson Reprint Corporation, New York, 1928. (1966 reprint).
- [Voyiadjis and Kattan 1999] G. Z. Voyiadjis and P. I. Kattan, *Advances in damage mechanics: metals and metal matrix composites*, Elsevier, New York, 1999.
- [Walpole 1984] L. J. Walpole, “Fourth-rank tensors of the thirty-two crystal classes: multiplication tables”, *Proc. Royal Soc. London A* **391** (1984), 149–179.
- [Zheng 1994] Q.-S. Zheng, “Theory of representations for tensor functions—a unified invariant approach to constitutive equations”, *Appl. Mech. Rev.* **47** (1994), 545–587.

Received 19 Mar 2007. Revised 8 Jun 2007. Accepted 11 Jun 2007.

VLADO A. LUBARDA: vlubarda@ucsd.edu

Department of Mechanical and Aerospace Engineering, University of California, San Diego, 9500 Gilman Drive, La Jolla, CA 92093-0411, United States

MICHELLE C. CHEN: mcchen@ucsd.edu

Department of Structural Engineering, University of California, San Diego, 9500 Gilman Drive, La Jolla, CA 92093-0085, United States

EXPERIMENTAL INVESTIGATIONS OF SPONTANEOUS BIMATERIAL INTERFACIAL FRACTURES

KAIWEN XIA, CARL-ERNST ROUSSEAU AND ARES ROSAKIS

Following our innovative experimental spontaneous fracture models for frictional fractures (compression and shear) and mixed-mode fractures (tension and shear) in identical materials, we designed a laboratory model to investigate the effects of material contrast on mixed-mode spontaneous fracture along a bimaterial interface. A series of interesting phenomena are observed, including asymmetry of crack propagation, with different speeds and levels of fracture parameters. Crack tips fracture parameters are observed to depend on crack speeds, on far-field loading, and on far-field mode-mixity. A strong dependence is also identified between mode-mixity and crack length. Most importantly, the fracture parameters are found to exhibit a strong dependence upon crack length and only a weak dependence on crack speed as is commonly thought. These observations are discussed in details in relation to material contrast. It is expected that these observations will have a profound influence on engineering practice involving the application of materials and structures with bimaterial interfaces.

Introduction

Interfacial fracture has long been identified as one of the primary causes of failure in layered materials and adhesive joints, and has therefore received much scrutiny [Hutchinson and Suo 1992]. Interfacial fracture spans length scales from submicrons in multiphase nanomaterials to thousands of kilometers in geological faults. Among various scenarios, two situations can be commonly recognized under dominant tensile loading conditions [Kitey and Tippur 2005]. First, when an interface is stronger than the weaker constituent material, cracks tend to kink into the weak material and grow nearly parallel to the interface [Hutchinson et al. 1987]. Thus, failure is controlled by the properties of the weak material constituent. The second scenario appears when the interface is the weakest component in the bimaterial system, and crack initiation and propagation occurs along the interface. In the latter case, which will be elaborated upon in this paper, the weakness pertinent to such multimaterial systems arises from the inherent disadvantage present at interfaces that can be no stronger than the weaker of the two adjacent materials. The physical nature of such composites is further complicated by a discrepancy in elastic properties that gives rise to inbuilt mode-mixity in stress states.

Although the resulting cracks can initiate and propagate in either the quasistatic or the dynamic regime, the latter is more catastrophic and is also more difficult to evaluate experimentally and theoretically. Consequently, direct measurements of dynamic stress states for bimaterial cracks were initiated only a decade ago, utilizing optical methods combined with high speed photography. Pioneering experimental

Keywords: spontaneous dynamic fracture, bimaterial interfacial fracture, stress intensity factor, photoelasticity.
This work is partially supported by the University of Toronto through the start-up funding received by KX.

investigation in dynamic bimaterial fracture includes the works of Tippur and Rosakis [1991], Lambros and Rosakis [1995], and Singh and Shukla [1995].

Modeling of dynamic interfacial fracture, however, started earlier, dating back to the 1967 work by Goldshte [1967]. This work predicted the possibility of attaining wave speeds in excess of the lower of the two Rayleigh wave speeds of the material constituents. This was subsequently confirmed by Lambros and Rosakis [1995], by means of optical measurements. Several new experiments have since been conducted to further reinforce these findings.

Analytical developments have also emerged to assist in the interpretation of these experimental developments. Yang et al. [1991] have formulated expressions that describe the crack tip field for steadily growing interfacial cracks between two different isotropic materials. Through their work, the velocity dependence of the universal bimaterial oscillatory index was for the first time ascertained. Further, Deng [1993] performed a steady-state asymptotic analysis for interfacial cracks that resulted in the establishment of higher-order terms associated with the bimaterial crack tip stress field. Similar results for nonsteady-state crack growth soon followed. Indeed, Liu et al. [1993] uncovered the requisite analytical expressions along with the associated higher-order terms. The work was also accompanied by experimental investigation.

Although the historical context of this problem has focused on material decohesion, the associated concepts are applicable also to the modeling of earthquakes [Andrews and Ben-Zion 1997; Cochard and Rice 2000] and to the spontaneous rupture of unbonded but otherwise joined materials in relatively firm contact. The latter case, also called laboratory earthquakes, is intended to understand earthquakes resulting from disturbances to natural faults and was explored by Xia et al. [2005b]. Recently, the idea of spontaneous fracture experiments was extended to the study of coherent interfacial fractures between identical and dissimilar materials under far-field mixed-mode loading [Rosakis et al. 2006]. As will be discussed later, there are several advantages to using spontaneous experimental fracture setups over traditional interfacial experimental designs inherited from standard static fracture experiments such as three-point bent, compact tension, and wedge driving cracks. Another reason to investigate spontaneous fractures is that spontaneous fracture is the main dynamic crack failure mode in engineering materials and engineering structures. The present work expands upon the interfacial fracture under mixed-mode far-field loading [Rosakis et al. 2006] to establish a comprehensive and more complete understanding of dynamic interfacial failure in bimaterial systems.

Experimental design of spontaneous interfacial fracture

The bimaterial system consists of two adjoining birefringent materials, Homalite-100 and polycarbonate (9.5 mm in thickness), that exhibit different elastic and constitutive properties as shown in Table 1. The wave speeds listed in the table are measured using a 10 MHz ultrasonic sensor, while the remaining properties are obtained from the literature [Dally and Riley 1991]. The two equally sized plates are joined to form a complete square specimen with each side measuring 150 mm. Before bonding the two halves of the specimen, a small groove, 0.15 mm in depth, is machined on the interface of one of the two half plates through its thickness. A thin metal wire of diameter 0.1 mm is then placed in the groove and the plates are bonded using an adhesive with elastic properties similar to those of Homalite-100. However, the adhesive possesses a much lower fracture toughness than either of the base materials, which constrains

Material Property	Homalite-100	Polycarbonate
Young's Modulus E (MPa)	3860	2480
Poisson's Ratio ν	0.35	0.38
Stress fringe value f_σ (kN/m)	23.6	7.0
P Wave Speed C_P (km/s)	2.104	1.724
S Wave Speed C_S (km/s)	1.200	0.960
Density ρ (kg/m ³)	1230	1192

Table 1. Summary of optical and dynamic mechanical properties of photoelastic materials.

any possible propagating rupture to the interfacial corridor. An average interface thickness of 0.1 mm is achieved. The static mode-I fracture toughness of the bonding is $0.46 \text{ MPa}\cdot\text{m}^{1/2}$ [Rosakis et al. 2006].

Figure 1 describes the configuration used in this study. The explosion box, which constitutes the most critical aspect of this experiment, provides the electric energy to transform the metal wire into a high pressure, high temperature plasma within $10 \mu\text{s}$. The expansion of the plasma results in a controlled isotropic line loading pulse across the sample thickness [Xia et al. 2005a]. Upon ignition, the exploding wire creates a small incipient crack that propagates along the interface only because the toughness of the adhesive is lower than that of either of the constituents of the bimaterial system. If the far-field loading is large enough, this initial small crack is unstable and propagates dynamically.

The interface is inclined at an angle α to the horizontal direction. Therefore, the nature of the far-field loading provided through the uniaxial tension in the vertical direction is mixed-mode with respect to the fracture path (bonding line). Upon sending the ultra high electric voltage (several kilovolts) to the exploding wire, the explosion box simultaneously provides a low voltage level triggering signal to the high speed camera. The camera system (Cordin 220) is able to capture the images at a framing rate of 100 million frames per second with exposure times as low as 10 nanoseconds. In this specific study, the high speed camera is operated at a much slower speed, around 0.2–0.4 million frames per second. A uniquely designed tensile fixture is used to maintain a static far-field load in the vertical direction, which applies the load to the sample through two compressed springs by a hydraulic press. The sample is attached on two sides, top and bottom, to two steel plates, which are fixed to the loading fixture to apply different levels of tensile loading.

The spontaneous fracture setup has several advantages over traditional dynamic fracture experimental techniques. First, the flawless sample is loaded statically before the dynamic initiation and propagation of the fracture. This results in increased accuracy of the foreknowledge of the stress field. This is especially important for exacting stress intensity factors with the full-field optical diagnostics (photoelasticity in this study). Second, the load is time independent throughout the duration of the crack propagation. Thus, theoretically, the dynamic stress intensity factor is related to the equivalent static stress intensity factor through a universal function of crack speed [Yang et al. 1991; Freund 1990]. Third, the sudden initiation of the small incipient crack in the center of the specimen enables treatment of the problem, dynamically, as that of a finite crack extending in an infinite domain before the waves get reflected from the boundaries of the sample. This technique circumvents edge effects that are generally unavoidable in other designs

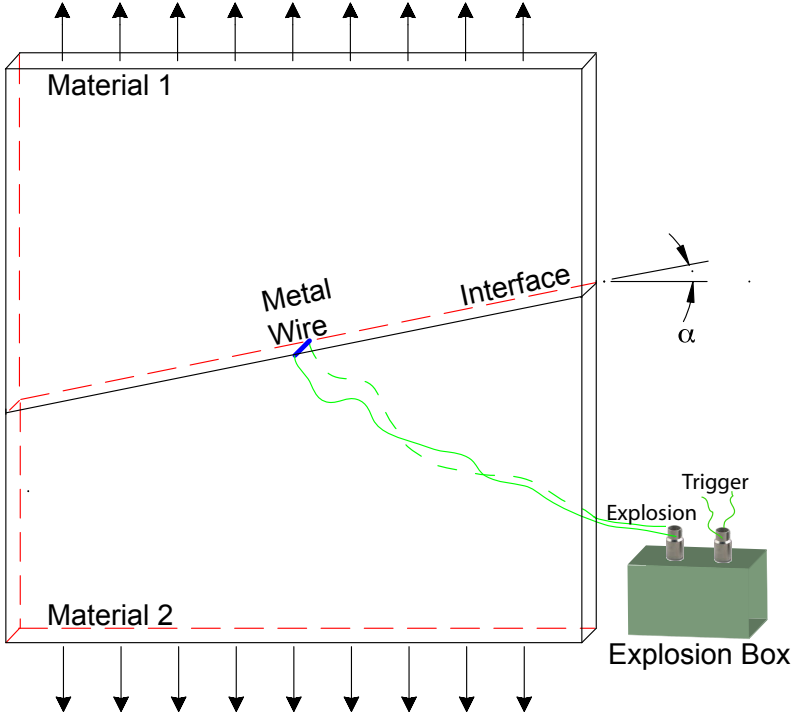


Figure 1. Specimen geometry of spontaneous fracture along bimaterial interface with the triggering mechanism.

of dynamic fracture experiments. Thus, existing exact analytical solutions may be used with confidence. Finally, the methodology used for initiating the crack provides an easy and reliable way to synchronize the diagnostic system (optical method combined with high speed photography) with the fracture process [Xia et al. 2004].

Extraction of stress intensity factor

A. Crack tip stress field at a bimaterial interface. Consider a crack propagating spontaneously and nonuniformly along a line defining the interface of two homogeneous, isotropic, and linearly elastic solids, at speeds bounded by the lowest Rayleigh wave speed pertaining to either material. The state of stress describing the ambient conditions surrounding such a two dimensional crack has been established by Liu et al. [1993], via asymptotic higher-order analysis. Relations necessary to the immediate and complete understanding of this experimental effort are reproduced below. Thus, individual stress components are given by:

$$\begin{aligned}
 \sigma_{11}^{(m)} &= \mu \Re \{ (1 + 2\alpha_l^2 - \alpha_s^2) F_m''(z_l; t) + 2\alpha_s G_m''(z_s; t) \}, \\
 \sigma_{22}^{(m)} &= -\mu \Re \{ (1 + \alpha_s^2) F_m''(z_l; t) + 2\alpha_s G_m''(z_s; t) \}, \\
 \sigma_{12}^{(m)} &= -\mu \Im \{ 2\alpha_l F_m''(z_l; t) + (1 + \alpha_s^2) G_m''(z_s; t) \}.
 \end{aligned}
 \tag{1}$$

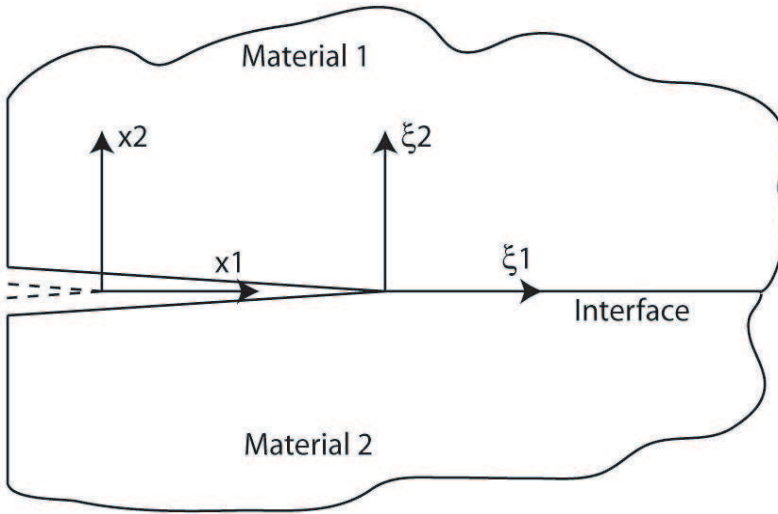


Figure 2. Schematic of dynamic growth of a crack along a bimaterial interface.

Each prime symbol denotes a derivative of the corresponding complex arguments, and \Re and \Im are the real and imaginary parts of the complex argument. The variable μ is the shear modulus of material 1 (see Figure 2).

Designating the longitudinal and shear wave speeds of the material by c_l and c_s , respectively, and the instantaneous crack speed by v , one can define the angle of inclination, α , as follows:

$$\alpha_{l,s}^2(t) = 1 - \frac{v^2(t)}{c_{l,s}^2}. \tag{2}$$

Further, a modified coordinate system is introduced such that $z_{l,s} = \eta_1 + i\alpha_{l,s}\eta_2$, where $\eta_i = (\xi_i/\varepsilon')$ and $i \in \{1, 2\}$, with ε' is a small arbitrary positive number. The complex functions $F(z_l; t)$ and $G(z_s; t)$ are defined as follows:

$$F_m(z_l; t) = -\frac{[(1 + \alpha_s^2) - 2\eta\alpha_s]e^{\pi\varepsilon}}{\mu D(v) \cosh(\varepsilon\pi)} z_l^{3/2+i\varepsilon} A_m(z_l; t) + \frac{[(1 + \alpha_s^2) + 2\eta\alpha_s]e^{-\pi\varepsilon}}{\mu D(v) \cosh(\varepsilon\pi)} z_l^{3/2-i\varepsilon} \bar{A}_m(z_l; t) - \frac{1}{\mu D(v)} \left\{ \left(\frac{1 + \alpha_s^2}{1 + \omega_l} - \frac{2\alpha_s}{1 + \omega_s} \right) B_m(z_l; t) - \left(\frac{1 + \alpha_s^2}{1 + \omega_l} + \frac{2\alpha_s}{1 + \omega_s} \right) \bar{B}_m(z_l; t) \right\} z_l^2, \tag{3}$$

and

$$G_m(z_s; t) = \frac{[2\alpha_l - \eta(1 + \alpha_s^2)]e^{\pi\varepsilon}}{\mu D(v) \cosh(\varepsilon\pi)} z_s^{3/2+i\varepsilon} A_m(z_s; t) + \frac{[2\alpha_l + \eta(1 + \alpha_s^2)]e^{-\pi\varepsilon}}{\mu D(v) \cosh(\varepsilon\pi)} z_s^{3/2-i\varepsilon} \bar{A}_m(z_s; t) + \frac{1}{\mu D(v)} \left\{ \left(\frac{2\alpha_l}{1 + \omega_l} - \frac{1 + \alpha_s^2}{1 + \omega_s} \right) B_m(z_s; t) - \left(\frac{2\alpha_l}{1 + \omega_l} + \frac{1 + \alpha_s^2}{1 + \omega_s} \right) \bar{B}_m(z_l; t) \right\} z_s^2. \tag{4}$$

In the above equations, several new variables are introduced. However, they are all universal to the field of linear elastic fracture mechanics and their complete definition can be found in [Liu et al. 1993]

and in [Freund 1990]. $A_m(z, t)$ and $B_m(z, t)$ are entire function to be expanded into Taylor series, such that:

$$\begin{aligned}
 A_m(z, t) &= \sum_{n=0}^{\infty} A_m^{(n)}(t) z^n, \\
 B_m(z, t) &= \sum_{n=0}^{\infty} B_m^{(n)}(t) z^n.
 \end{aligned}
 \tag{5}$$

In the present work, only the terms for which $m = 0$ are used in the expansions. In this case, the dynamic stress intensity factor is readily derived from the complex expression:

$$A_0^{(0)}(t) = -\frac{1}{2\sqrt{2\pi}} \frac{K^d(t)}{(3/2 + i\varepsilon)(1/2 + i\varepsilon)}.
 \tag{6}$$

Evaluation of the energy release rate follows directly from the stress intensity factor:

$$G = \frac{K_1^2 + K_2^2}{[4 \cosh(\varepsilon\pi)]^2} \left[\left\{ \frac{\alpha_l(1 - \alpha_s^2)}{\mu D(v)} \right\}_1 + \left\{ \frac{\alpha_l(1 - \alpha_s^2)}{\mu D(v)} \right\}_2 \right],
 \tag{7}$$

where K_1 and K_2 are the real and imaginary arguments, respectively, of the complex bimaterial stress intensity factor. Finally, the mode-mixity inherent to all bimaterial systems is derived from the arctangent of the ratio of the imaginary to the real arguments of the stress intensity factor, or:

$$\psi = \tan^{-1} \left(\frac{K_2}{K_1} \right).
 \tag{8}$$

B. Extraction of fracture parameters. The fundamental relation pertaining to photoelasticity is represented by the stress-optic law:

$$\frac{Nf_\sigma}{2h} = \tau_{\max},
 \tag{9}$$

where N is the observed fringe order number, f_σ is the fringe constant of the photoelastic material, and h is the material thickness. The relation between these various parameters results in a visual representation of the contours of constant maximum shear stress in the material. Substitution of the dynamic bimaterial stress field equations into the above expression relates the isochromatic fringe patterns surrounding the advancing crack tip to dynamic stress intensity factor, crack tip speed, and other nonsingular higher-order terms, through:

$$\begin{aligned}
 \left(\frac{Nf_\sigma}{2h} \right)^2 &= \mu^2 \left\{ [(1 + \alpha_l^2)\Re F_0''(z_l; t) + 2\alpha_s\Re G_0''(z_s; t)]^2 \right. \\
 &\quad \left. + [2\alpha_l\Im F_0''(z_l; t) + (1 + \alpha_s^2)\Im G_0''(z_s; t)]^2 \right\}.
 \end{aligned}
 \tag{10}$$

In the present work inference of the dynamic stress intensity factor is conducted through an over deterministic method in which up to six higher-order terms are used. The unknown coefficients A_m and B_m appear as nonlinear terms in Equation (10). The solution is obtained by first designating the real and imaginary expressions of the above equation as D and T respectively. Subsequently, for each digitized

fringe data point, the following relation is established:

$$g_k = D_k^2 + T_k^2 - \left(\frac{N_k f_\sigma}{2h} \right)^2 = 0. \quad (11)$$

The set of k nonlinear equations is solved simultaneously using a least-squares analysis based on initial estimates of A_m and B_m . Correction factors are subsequently introduced, and the process is iterated until Equation (11) is satisfied to within an error upper bound of 0.0001. Further comprehensive details of the solution scheme can be found in the original work of Sanford and Dally [1979].

Experimental results and discussions

Experiments featuring spontaneous interfacial fractures between polycarbonate and Homalite-100, which were bonded along their common interface, were conducted. Each specimen possessed a different angle of inclination, α , and was loaded at a different level of uniaxial tension. The results of these experiments revealed that each specimen responded identically to the loading environment. First, the bilaterally propagating spontaneous fracture occurs at two different speeds. Second, shortly following fracture initiation, a constant speed level is established in both directions, with negligible variation. Finally, larger far-field load levels induce faster crack propagation.

A. Asymmetry of crack speeds and the variations of energy release rate. Figure 3 shows three typical isochromatic fringe patterns displayed with accompanying plots that identify crack-tip location and energy release rate histories featuring the different levels of uniaxial tension (7.5 MPa in (a) and (b), and 5.6 MPa in (c)). In Figures 3a and 3c, the inclination angle is 27.5° , while in Figure 3b, the inclination angle is 17.5° . Within each frame, the appearance of each set of fringes associated with each of the moving faults is clearly asymmetric. For instance the fringes coupled with the left moving cracks in the first two figures are larger than those pertaining to the right moving ones. This indicated greater stress levels, and therefore higher values of crack parameters. Also striking is the higher level of distortion pertaining to the right moving cracks in those same frames, a fact generally attributed to crack speeds approaching limiting values of the materials. The inverse is true for the third figure in the sequence.

Other observations can be drawn from these figures. First, the two crack tips propagate essentially at constant speeds with one end faster than the other. If the particle motion is resolved to coincide with the direction of the interface, propagation of the faster side is in the direction of the resolved shear particle motion of the more compliant constituent of the bimaterial system (polycarbonate). For the cases corresponding to Figures 3a and 3b, the lower material is more compliant, resulting in faster propagation to the right. In Figure 3c, the upper material is more compliant, causing the velocity trend to reverse. This asymmetry in speed is attributed to the existence of material contrast across the interface and the coupling between shear and tension resulting from this contrast [Cochard and Rice 2000; Weertman 1980]. For the case of shear fractures in frictionally held interfaces with combined shear and compressive loading, a configuration very different from the one tested here, similar phenomena have been predicted theoretically [Qian and Sun 1998] and have been observed experimentally [Xia et al. 2005b]. The shear induced compression may result in frictional contact of crack surfaces in both static and dynamic interfacial cracks in bimaterials [Sun and Qian 1997; Rosakis et al. 1998]. In the cases discussed here, however, the presence of the tensile load prevents any frictional contact behind the crack tip from interfering with crack

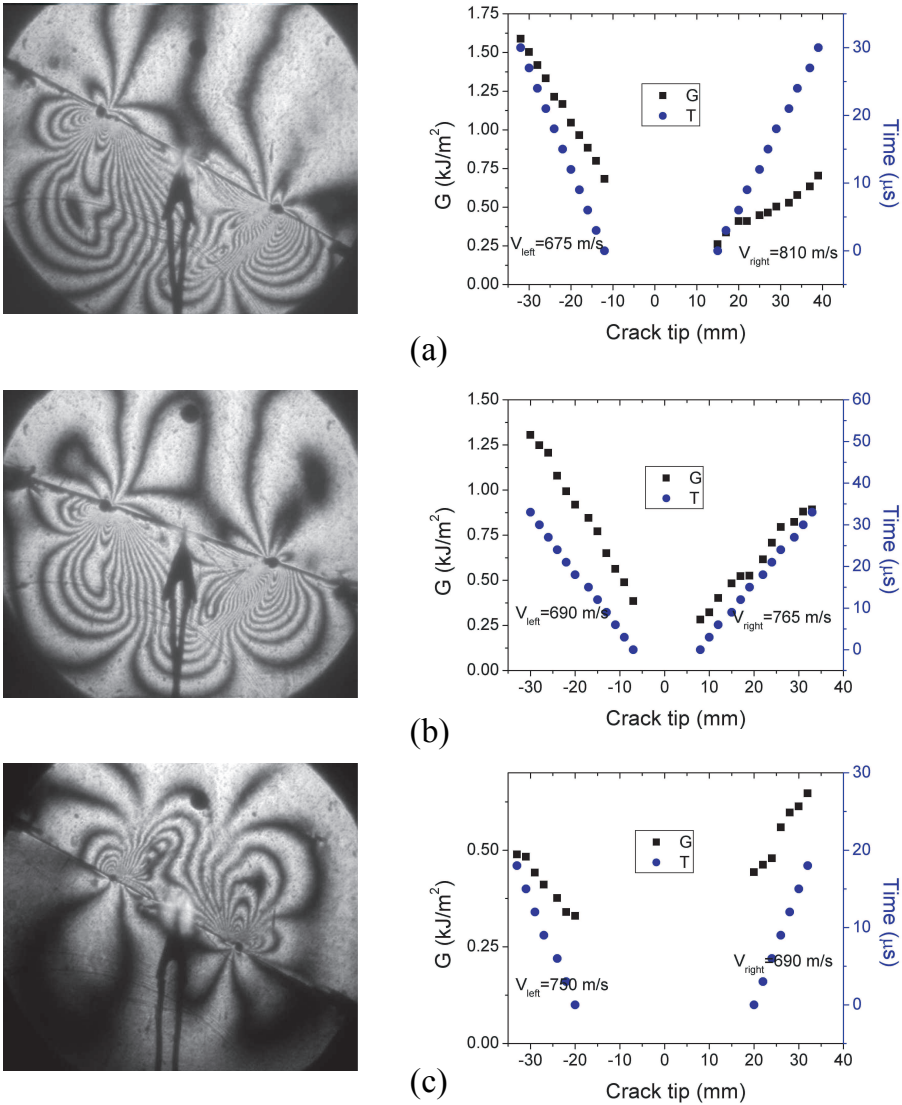


Figure 3. Isochromatic fringe patterns with plots of energy release rate and crack tip time history (The black dot on the top plate of each isochromatic picture is a 6.25 mm diameter length scale). (a) Inclination angle is 27.5°, top is Homalite-100. (b) Inclination angle is 17.5°, top is Homalite-100. (c) Inclination angle is 27.5°, top is polycarbonate.

propagation. Indeed, from the isochromatic fringe patterns shown in Figure 3, no evidence of contact like those observed in stress wave induced dynamic shear crack propagation in bimaterial interfaces [Rosakis et al. 1998] can be identified. The observations here of asymmetric crack propagation further validate the theory of material contrast induced coupling between shear and normal motions.

It is noted that fracture energy, and equivalently energy release rate, increases linearly with the crack length at both crack locations. The fracture parameters are calculated using Equation (7), with stress intensity factors obtained by using the inversion scheme discussed above. A similar phenomenon, directly relating larger fracture parameters to increasing crack length, has also been identified for spontaneous mode I [Xia et al. 2006] and mixed-mode interfacial fracture in identically bonded materials [Rosakis et al. 2006]. As is the case for these earlier results, this increase of fracture energy with crack length is consistent with the observation of constant crack speeds and time independent loading, which implies that the dynamic energy release rate is related to the equivalent static energy release rate through the multiplication of a universal function depending only on the fracture velocity [Yang et al. 1991]. Consequently, for a given speed of spontaneous fracture, the energy release rate is proportional to the square of the equivalent static stress intensity factor. Since the equivalent static stress intensity factor is proportional to the square root of the crack length, the energy release rate is then proportional to the crack length. If, instead, the fracture energy remains constant during the crack propagation, the crack will accelerate to its limiting speed at which the energy release rate tends to zero and most of the released strain energy will be converted into kinetic energy [Freund 1990; Broberg 1999]. This observation of a constant speed crack thus casts doubt on the validity of using the fracture energy concept as a material parameter to describe crack propagation resistance. Crack propagation resistance, or, more precisely, the nominal crack propagation resistance that may involve damage of the crack path, might be more appropriately attributed to loading conditions and geometry [Broberg 2002]. It should also be noted that at the slower propagating end, the energy release rate is always larger than that of the faster end for the same length crack. This can be explained by the decreasing nature of the universal function dependence on the crack speed [Yang et al. 1991; Freund 1990; Broberg 1999].

B. Stress intensity factors and variations of mode-mixity. Figure 4 presents the crack tip history, energy release rate, stress intensity factors (K_1 for mode I and K_2 for mode II), and the mode-mixity ($\psi = \tan^{-1}(K_2/K_1)$) as in Equation (8)) for an experiment featuring 7.5 MPa far-field loading and 27.5° inclination angle. This test was performed under identical conditions as the one shown in Figure 3a.

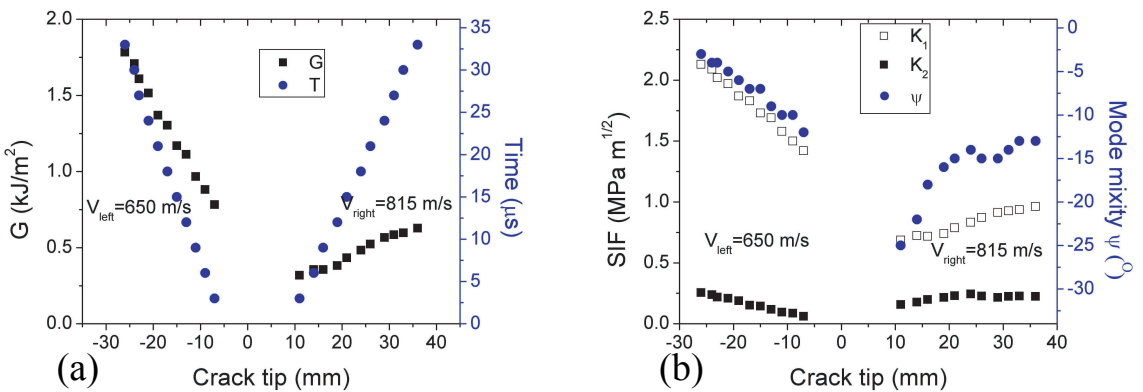


Figure 4. (a) Energy release rate (G), crack tip time history (T) and (b) the evolution of stress intensity factors (K_1 , K_2) and mode-mixity (ψ) for a typical experiment.

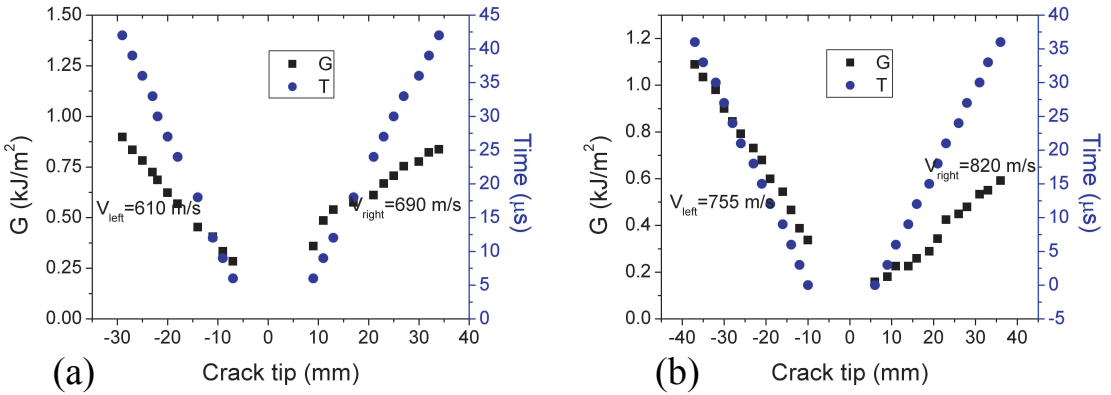


Figure 5. Figure 5. Energy release rate and crack tip time history. (a) Inclin. angle is 25° and far-field load is 6.8 MPa. (b) Inclin. angle is 25° and far-field load is 7.5 MPa.

Note that the crack speeds of the two experiments are very similar (Figure 4a), which demonstrates the repeatability of the experimental design.

As shown in Figure 4b, the mode-mixities of both ends are smaller than the far-field mode-mixity of 27.5° . The mode-mixity of the slower end is smaller than that of the faster end for the same length of propagation. The asymmetry is a result of the mode coupling discussed earlier. The fast crack tip has more mode II component than the slow crack tip. This result is consistent with that reported in the numerical simulation study of mixed-mode interfacial fracture propagation in identical materials [Geubelle and Kubair 2001]. The result is to be expected because the limiting speed of mode II cracks (longitudinal wave speed) is higher than that of mode I cracks (Rayleigh wave speed) [Freund 1990; Broberg 1999]. From a material response point of view, the result demonstrates that the debonding process is facilitated by greater prominence of mode II stress components. In other words, it is easier for a mixed-mode crack to propagate at fast speeds when it has higher levels of mode II components.

C. Dependence of crack speeds on far-field load. Figure 5 presents the crack tip history and energy release rate for two experiments featuring the same inclination angle (25°) and different load levels (7.5 MPa and 6.8 MPa respectively). Again it can be seen clearly that for both tests the energy release rate increases with the crack length. In the case where the load level is higher (Figure 5b), the speed of the left crack is faster than that corresponding to the case where the load level is lower (Figure 5a). The same conclusion holds for the right propagating crack. Detailed analytical study is needed to obtain the dependence of the crack speeds on far-field load. For self-similar mode I cracks, a theoretical relationship was proposed by Broberg [2002].

Conclusions

The experiments conducted herein feature bimaterial systems composed of polycarbonate and Homalite-100, bonded along an interface. Symmetric and central spontaneous initiation of a dual crack through plasma explosion resulted in asymmetric propagation, with the faster side proceeding in the direction of

the resolved shear particle motion of the more compliant constituent. This is the first published set of experiments where two opposing propagating cracks have been set to propagate simultaneously along a bimaterial interface. It is noted that the magnitude of the fracture parameters are always correlated to crack length. Surprisingly also, energy release rate is shown to be more weakly dependent on the crack speed than to the crack length, an observation that will undoubtedly stimulate theoretical discussions on the subject of crack propagation in general, and more specifically on crack propagation in bimaterial systems. It is also observed that higher load results in faster crack propagation.

Acknowledgements

Helpful discussions with Prof. G. Ravichandran from California Institute of Technology, with Prof. A. Shukla from University of Rhode Island, and with Prof. H. Gao from Brown University are acknowledged. The authors appreciate constructive comments from one anonymous reviewer.

References

- [Andrews and Ben-Zion 1997] D. J. Andrews and Y. Ben-Zion, "Wrinkle-like slip pulse on a fault between different materials", *J. Geophys. Res.-Solid Earth* **102**:B1 (1997), 553–571.
- [Broberg 1999] K. B. Broberg, *Cracks and fracture*, Academic Press., San Diego, 1999. 752.
- [Broberg 2002] K. B. Broberg, "Constant velocity crack propagation - dependence on remote load", *Int. J. Solids Struct.* **39**:26 (2002), 6403–6410.
- [Cochard and Rice 2000] A. Cochard and J. R. Rice, "Fault rupture between dissimilar materials: Ill-posedness, regularization, and slip-pulse response", *J. Geophys. Res.-Solid Earth* **105**:B11 (2000), 25891–25907.
- [Dally and Riley 1991] J. W. Dally and W. F. Riley, *Experimental stress analysis*, 3rd ed. ed., McGraw-Hill, Inc., New York, 1991. 639.
- [Deng 1993] X. Deng, "General crack-tip fields for stationary and steadily growing interface cracks in anisotropic bimaterials", *J. Appl. Mech. (Trans. ASME)* **60**:1 (1993), 183–189.
- [Freund 1990] L. B. Freund, *Dynamic fracture mechanics*, Cambridge University Press., Cambridge; New York, 1990. 563.
- [Geubelle and Kubair 2001] P. H. Geubelle and D. V. Kubair, "Intersonic crack propagation in homogeneous media under shear-dominated loading: numerical analysis", *J. Mech. Phys. Solids* **49**:3 (2001), 571–587.
- [Goldshte 1967] R. Goldshte, "On surface waves in joined elastic materials and their relation to crack propagation along junction", *J. Appl. Math. Mech.-Ussr* **31**:3 (1967), 496–502.
- [Hutchinson and Suo 1992] J. W. Hutchinson and Z. Suo, "Mixed-mode cracking in layered materials", *Adv. Appl. Mech.* **29** (1992), 63–191.
- [Hutchinson et al. 1987] J. W. Hutchinson, M. E. Mear, and J. R. Rice, "On crack paths", *J. Appl. Mech. (Trans. ASME)* **54** (1987), 828–832.
- [Kitey and Tippur 2005] R. Kitey and H. V. Tippur, "Dynamic crack growth in particulate bimaterials having discrete and diffuse interfaces: Role of microstructure", *Eng. Fract. Mech.* **72**:18 (2005), 2721–2743.
- [Lambros and Rosakis 1995] J. Lambros and A. J. Rosakis, "Shear dominated transonic interfacial crack-growth in a bimaterial. 1. experimental-observations", *J. Mech. Phys. Solids* **43**:2 (1995), 169–188.
- [Liu et al. 1993] C. Liu, J. Lambros, and A. J. Rosakis, "Highly transient elastodynamic crack-growth in a bimaterial interface - higher-order asymptotic analysis and optical experiments", *J. Mech. Phys. Solids* **41**:12 (1993), 1887–1954.
- [Qian and Sun 1998] W. Qian and C. T. Sun, "A frictional interfacial crack under combined shear and compression", *Compos. Sci. Technol.* **58**:11 (1998), 1753–1761.
- [Rosakis et al. 1998] A. J. Rosakis et al., "Intersonic crack propagation in bimaterial systems", *J. Mech. Phys. Solids* **46**:10 (1998), 1789–1813.

- [Rosakis et al. 2006] A. J. Rosakis, H. Kanamori, and K. Xia, “Laboratory earthquakes”, *Int. J. Fract.* **138**:1–4 (2006), 211–218.
- [Sanford and Dally 1979] R. J. Sanford and J. W. Dally, “General-method for determining mixed-mode stress intensity factors from isochromatic fringe patterns”, *Eng. Fract. Mech.* **11**:4 (1979), 621–633.
- [Singh and Shukla 1995] R. P. Singh and A. Shukla, “Dynamic failure of bimaterial interfaces: A photoelastic investigation”, in *Proc. of SEM Spring Conference*, 1995. Grand Rapids, MI: SEM. Available on CD.
- [Sun and Qian 1997] C. T. Sun and W. Qian, “The use of finite extension strain energy release rates in fracture of interfacial cracks”, *Int. J. Solids Struct.* **34**:20 (1997), 2595–2609.
- [Tippur and Rosakis 1991] H. V. Tippur and A. J. Rosakis, “Quasi-static and dynamic crack-growth along bimaterial interfaces - a note on crack-tip field-measurements using coherent gradient sensing”, *Exp. Mech.* **31**:3 (1991), 243–251.
- [Weertman 1980] J. Weertman, “Unstable slippage across a fault that separates elastic media of different elastic-constants”, *J. Geophys. Res.* **85**:NB3 (1980), 1455–1461.
- [Xia et al. 2004] K. W. Xia, A. J. Rosakis, and H. Kanamori, “Laboratory earthquakes: The sub-Rayleigh-to-supershear rupture transition”, *Science* **303**:5665 (2004), 1859–1861.
- [Xia et al. 2005a] K. Xia, A. J. Rosakis, and H. Kanamori, “Supershear and sub-Rayleigh to supershear transition observed in laboratory earthquake experiments”, *Exp. Tech.* **29**:3 (2005), 63–66.
- [Xia et al. 2005b] K. W. Xia, A. J. Rosakis, H. Kanamori, and J. R. Rice, “Laboratory earthquakes along inhomogeneous faults: Directionality and supershear”, *Science* **308**:5722 (2005), 681–684.
- [Xia et al. 2006] K. Xia, V. B. Chalivendra, and A. J. Rosakis, “Observing ideal ‘self-similar’ crack growth in experiments”, *Eng. Fract. Mech.* **73** (2006), 2748–2755.
- [Yang et al. 1991] W. Yang, Z. Suo, and C. F. Shih, “Mechanics of dynamic debonding”, *P. Roy. Soc. Lond. A Mat.* **433**:1889 (1991), 679–697.

Received 8 Apr 2007. Revised 19 Jul 2007. Accepted 23 Jul 2007.

KAIWEN XIA: kaiwen@ecf.utoronto.ca

Department of Civil Engineering, University of Toronto, 35 St. George Street, Toronto ON M5S 1A4, Canada

CARL-ERNST ROUSSEAU: roussea@egr.uri.edu

222-B Wales Hall, Dept. of Mechanical Engineering, University of Rhode Island, Kingston, RI 02881, United States

ARES ROSAKIS: rosakis@aero.caltech.edu

Graduate Aeronautical Laboratory, California Institute of Technology, Pasadena, CA 91125, United States

A GLOBAL COLLOCATION METHOD FOR TWO-DIMENSIONAL RECTANGULAR DOMAINS

CHRISTOPHER G. PROVATIDIS

This paper proposes the use of a global collocation procedure in conjunction with a previously developed functional set suitable for the numerical solution of Poisson's equation in rectangular domains. We propose to expand the unknown variable in a bivariate series of monomials $x^i y^j$ that exist in Pascal's triangle. We also propose the use of the bivariate Gordon–Coons interpolation, apart from previous intuitive choices of the aforementioned monomials. The theory is sustained by two numerical examples of Dirichlet boundary conditions, in which we find that the approximate solution monotonically converges towards the exact solution.

1. Introduction

The use of collocation methods for the solution of partial differential equations (PDE) has become a subject of intensive interest in the past [Lanczos 1938; Ronto 1971; Russell and Shampine 1972; Finlayson 1972; De Boor and Swartz 1973; Diaz 1977; Houstis 1978; Botha and Pinder 1983]. While most research has focused on the local interpolation of a variable, not many works have appeared concerning the global collocation in two-dimensional problems [Frind and Pinder 1979; Hayes 1980; Van Blerk and Botha 1993]. In contrast, global approximations have been successfully applied in conjunction with the standard Galerkin–Ritz procedure either using the Gordon–Coons bivariate interpolation [Cavendish et al. 1976] or higher order p -methods [Szabó and Babuška 1991].

Moreover, closely related to the abovementioned p -methods [Szabó and Babuška 1991], an alternative Gordon–Coons method has been proposed for the static and dynamic analysis of structures [Provatidis 2006a; 2006b; 2006c; 2006d]. In these works, the standard Galerkin–Ritz procedure was applied, thus leading to stiffness and mass matrices in the form of integrals over the entire domain. This method has been called the *Coons patch macroelement* (CPM) approach [Provatidis 2006a; 2006b; 2006c; 2006d]. Although CPM works perfectly well, and can deal with even Π -shaped domains [Provatidis 2006a; 2006d], one could say that it has the disadvantage of fully populated matrices particularly when Lagrange polynomials (with no compact support) are used.

This paper contributes to overcoming the abovementioned shortcoming and modifies the previous CPM methodology first by preserving the global functional space, and second by moving from the Galerkin–Ritz to a *collocation* procedure in which no integral is needed. Quite recently, as a pilot study, this idea has been successfully applied to one-dimensional eigenvalue problems [Provatidis 2007].

It should be noted that the proposed collocation method could be formulated in terms of the global cardinal shape functions of the CPM approach, which are applicable even to curvilinear domains [Provatidis 2006a; 2006b; 2006d]. However, the aforementioned shape functions are derived through a numerical

Keywords: global collocation, Coons interpolation, Poisson's equation.

procedure in which the original information is lost. It is therefore preferable to work instead in conjunction with the basis functions. It has recently been shown that when the Gordon–Coons interpolation is applied to the reference $\xi\eta$ -square ($0 \leq \xi, \eta \leq 1$), it leads to the functional space, $\xi^i\eta^j$, which consists of the well known monomials of Pascal’s triangle [Provatidis 2006a; 2006b; 2006d]. Obviously, in the case of a rectangular domain, these monomials correspond to the usual $x^i y^j$ monomials that appear in the classical Taylor’s series expansion. It is important to mention here that while an intuitively selected part (that is, relevant indices i, j) of a Taylor’s series expansion may lead to a noninvertible equation matrix [Zienkiewicz 1977, p.151], the Gordon–Coons interpolation [Gordon 1971] always ensures a smooth approximation because it is based on the solid foundations of Computational Geometry [Farin 1990]. It is remarkable that the ideas just described can be extended to three-dimensional domains, that is, to the reference $\xi\eta\zeta$ -cube [Provatidis 2006c].

In brief, this paper utilizes the advantage of the abovementioned complete functional set, and applies a global collocation that achieves solutions to boundary value problems in rectangular domains. In this work, the performance of the proposed method is shown in two examples under the Dirichlet boundary conditions.

2. The proposed global functional set

Let us consider a rectangular domain $\Omega = (ABCD) = [0, a] \times [0, b]$ in \mathbb{R}^2 . The axis origin is chosen to be the corner A , and the Cartesian axes x and y lie on the sides AB and AD , respectively. The sides (AB, CD) and (BC, DA) are divided into p and q segments, respectively, thus leading to $(p + 1)$ nodes along AB or CD , as well as $(q + 1)$ nodes along BC or DA . As a result, the univariate function $u(x, 0)$ along the side AB can be interpolated through a polynomial of p -th degree in x (thus including the set $\{1, x, x^2, \dots, x^p\}$), while the function $u(0, y)$ along the side DA can be interpolated through a polynomial of q -th degree in y (thus including the set $\{1, y, y^2, \dots, y^q\}$).

2.1. Boundary functions. Given the univariate polynomial degrees p and q , one of the most apparent extensions in the two-dimensional approximation is perhaps the use of Coons’ interpolation [Farin 1990], which assumes a linear blending of the aforementioned univariate polynomials. If $u \in C^{2,2}(\Omega_{st})$ where $\Omega_{st} = [0, 1] \times [0, 1]$ is the *standard* reference square, then in terms of normalized coordinates, ξ and η ($0 \leq \xi, \eta \leq 1$), Coons interpolation can be written as:

$$\tilde{u}(\xi, \eta) = (1 - \xi)u(0, \eta) + \xi u(1, \eta) + (1 - \eta)u(\xi, 0) + \eta u(\xi, 1) - \tilde{\tilde{u}}(\xi, \eta), \quad (1)$$

where

$$\tilde{\tilde{u}}(\xi, \eta) = (1 - \xi)(1 - \eta)u(0, 0) + \xi(1 - \eta)u(1, 0) + (1 - \xi)\eta u(0, 1) + \xi\eta u(1, 1).$$

For the rectangular domain, it holds that $x = a\xi$ and $y = b\eta$, and hereafter we replace the normalized coordinates by the Cartesian ones. Therefore, the polynomial set $\{1, x, x^2, \dots, x^p\}$ along AB ($\eta = 0, y = 0$) is projected by the blending function $(1 - y/b)$ towards the y -axis, thus including the monomials involved in the product $\{1, x, x^2, \dots, x^p\}(1 - y/b)$. In an analogous way, the interpolation along DA ($\xi = 0, x = 0$) leads to the terms involved in the product $\{1, y, y^2, \dots, y^q\}(1 - x/a)$. In summary, for the case of nodal points arranged along the boundary of the rectangular domain $ABCD$, the variable $u(x, y)$ is expanded in a series (Equation (3)) comprising the aforementioned $2(p + q)$ monomials that compose a set, here

denoted as S_0 , which constitutes the ‘legs’ of Pascal’s triangle with a surplus (‘thickness’) of two layers of terms. The particular case of this scheme for $p = q$ can be found in standard textbooks such as [Zienkiewicz 1977, p.160].

The above justified choice constitutes a subset of the space $S^p(\Omega_{st}^{(q)})$ of polynomials on the unit reference square, $\Omega_{st}^{(q)}$, which was introduced by Szabó and Babuška in their pioneering works concerning higher-order p -methods [Szabó and Babuška 1991]. The space $S^p(\Omega_{st}^{(q)})$ is spanned by the set of monomials

$$x^i y^j, \quad i, j = 0, 1, \dots, p, \quad i + j = 0, 1, \dots, p,$$

supplemented by the following monomials:

- (a) in the case $p = 1$, the monomial xy ;
- (b) in the case $p \geq 2$, the monomials $x^p y$ and xy^p [Szabó and Babuška 1991, p.97].

In the particular case that $p = q$, it is trivial to verify that the proposed set of equations (Equation (1)) does *not* coincide with that proposed by Szabó and Babuška [1991]. For example, in the case of $p = 4$, the proposed Coons-based functional set misses the term $x^2 y^2$ (it belongs to the third layer parallel to the ‘legs’ of Pascal’s triangle), which can, however, easily be obtained in the sequence by considering one internal node (see Section 2.2).

2.2. Internal functions. In order to get full polynomials, it is necessary to use internal nodes where the PDE will be collocated. One extreme case is to use $(p - 1) \times (q - 1)$ internal nodes, a choice that corresponds to the well known Lagrange type finite element. The corresponding space is denoted by $S^{p,q}(\Omega_{st}^{(q)})$ [Szabó and Babuška 1991, p.97] and it is spanned by the set of all monomials

$$x^i y^j, \quad i = 0, 1, 2, \dots, p, \quad j = 0, 1, 2, \dots, q.$$

Alternatively, the author has recently presented a general systematic and automatic procedure to deal with any number of internal nodes, preferably distributed at equidistant locations, and the number of these nodes may be smaller or even larger than those in the Lagrange type element that occupies the entire domain Ω [Provatidis 2006a]. In more detail, the Gordon–Coons transfinite interpolation is applied so that the boundary (and interboundary) data are blended through higher order functions, thus leading to monomials outside the ‘legs’ of Pascal’s triangle with a surplus of two. For reasons of simplicity, in this paper we proceed in a slightly different but equivalent way. Apart from the monomials mentioned in Section 2.1, we consider up to nine additional monomials as follows. The first subset,

$$S_1 = \{x^2 y^2\}$$

is related to a central node ($x = a/2, y = b/2$); the second set,

$$S_2 = S_1 \cup \{x^3 y^2, x^2 y^3, x^3 y^3\}$$

to a tensor product of 2×2 (four) points, while the third set,

$$S_3 = S_1 \cup S_2 \cup \{x^4 y^2, x^2 y^4, x^4 y^3, x^3 y^4, x^4 y^4\},$$

is related to a tensor product of 3×3 (nine) points in the interior. Finally, as an extreme case, for a certain boundary discretization through p segments per side, the abovementioned space of Lagrange-type

finite elements, $S^{p,q}(\Omega_{st}^{(q)})$, is also considered as a candidate approximation (in the proposed collocation method) of which the performance will be validated.

3. The proposed global collocation procedure

3.1. General. In any collocation method, for a given PDE:

$$D(u) - f(x, y) = 0, \quad \text{in } \Omega = [0, a] \times [0, b], \quad (2)$$

we generally seek an approximate solution to Equation (2) which is a linear combination of the global basis functions $\{\phi_i(x, y)\}$, $i = 1, 2, \dots, n$:

$$\tilde{u}(x, y) = \sum_{j=1}^n \alpha_j \phi_j(x, y). \quad (3)$$

For the sake of simplicity, in this work we deal with the Dirichlet conditions that hold along the entire boundary $\partial\Omega$.

For a given number of uniform boundary subdivisions, that is, p and q towards the x and y axes respectively, the boundary includes $n_b = 2(p + q)$ nodes. In order to achieve a complete numerical solution we also use n_I internal nodes [Provatidis 2006a; 2006b]. Then, we solve for both the n_b unknown fluxes ($\partial u / \partial n$) along $\partial\Omega$ and for the unknown variable u at the n_I internal nodes, a total of $n = n_b + n_I$ unknowns. Therefore, we need to form n linearly independent equations, one for each node of the boundary and the interior. Afterwards, the n coefficients α_j , $j = 1, 2, \dots, n$, which appear in Equation (3), are determined.

Without loss of generality, the proposed methodology below refers to Poisson's equation,

$$(D(u) - f = \nabla^2 u - f = 0).$$

3.2. Matrix formulation. Because the basis functions do not fulfill any special condition, regardless of whether the Dirichlet boundary conditions are or are not homogeneous, Equation (3) is written for all boundary nodes:

$$\bar{\mathbf{u}} = \mathbf{C}_0 \boldsymbol{\alpha}, \quad (4)$$

where $\bar{\mathbf{u}}$ is a vector of n_b elements, including the nodal values of the prescribed variable u along $\partial\Omega$, \mathbf{C}_0 is a $n_b \times n$ matrix with elements $[\mathbf{C}_0]_{ij} = \phi_j(x_i, y_i)$, $i = 1, \dots, n_b$, $j = 1, \dots, n$, and $\boldsymbol{\alpha}$ is the vector of the n unknown coefficients appearing in Equation (3).

By taking the Laplacian of both parts in Equation (3), one arrives at the following approximation:

$$\nabla^2 \tilde{u}(x, y) = \sum_{j=1}^n \alpha_j \nabla^2 \phi_j(x, y).$$

The collocation method enforces the residual

$$r(x, y) = \nabla^2 \tilde{u}(x, y) - f(x, y), \quad (5)$$

to become zero at specific points (x_i, y_i) . In the proposed method, it is suggested that these points be chosen so as to coincide with the abovementioned n_I internal nodes. Therefore, by applying Equations

(5) and (6) at the internal nodes, one obtains:

$$\mathbf{r} = \mathbf{C}_2\boldsymbol{\alpha} - \bar{\mathbf{f}} = \mathbf{0}, \tag{6}$$

where \mathbf{C}_2 is an $n_I \times n$ matrix with elements $[\mathbf{C}_2]_{ij} = \nabla^2\phi_j(x_i, y_i), i = 1, \dots, n_I, j = 1, \dots, n$, \mathbf{r} is the vanishing vector of residuals, and $\bar{\mathbf{f}}$ is a vector of n_I elements that consists of the values of the functions $f(x, y)$ at the collocation points (x_i, y_i) in the interior.

Obviously, Equations (4) and (6) constitute a linear system of n equations with n unknowns,

$$\begin{bmatrix} \mathbf{C}_0 \\ \mathbf{C}_2 \end{bmatrix} \boldsymbol{\alpha} = \begin{Bmatrix} \bar{\mathbf{u}} \\ \bar{\mathbf{f}} \end{Bmatrix},$$

which can be easily solved in $\boldsymbol{\alpha}$.

3.3. Numerical implementation. A FORTRAN-77 code was developed on a usual PC Pentium IV. A subroutine was written for the automatic determination of the abovementioned $2(p + q)$ monomials involved in the boundary discretization, Equation (1). Then, two choices are available as follows. The first concerns the use of Lagrange-type interpolation ($(p - 1) \times (q - 1)$ terms: $x^i y^j; i = 0, 1, \dots, p, j = 0, 1, \dots, q$), and the second, the sequence of previously defined S_1, S_2 and S_3 sets (see Section 2.2). As we are concerned with second order problems, (Poisson’s equation) we have limited this subroutine only to the second derivatives in x and y .

4. Numerical results

The theory is elucidated by two examples taken from literature [Elansari et al. 2001], in which the exact solution is not of polynomial form. The quality of the numerical solution is evaluated in terms of an L_2 -norm, which is defined as follows:

$$L_2 = \frac{\sqrt{\int_{\Omega} (\tilde{u} - u_{\text{exact}})^2 d\Omega}}{\sqrt{\int_{\Omega} u_{\text{exact}}^2 d\Omega}} \times 100\%.$$

Both examples are defined on the square domain $\Omega = [0, 2]^2$ in \mathbb{R}^2 , and refer to the Poisson’s equation:

$$\nabla^2 u = f(x, y).$$

Example 1.

$$f(x, y) = -2 \sin(x) \sin(y).$$

In this case, the exact solution is

$$u(x, y) = \sin(x) \sin(y). \tag{7}$$

The Dirichlet boundary condition is calculated using Equation (7) and prescribed on the entire boundary. In the beginning, the solution is approximated by applying Coons interpolation in conjunction with only boundary data (Equation (1)). Then, one (S_1 -space), four (S_2 -space) and nine (S_3 -space) internal nodes were introduced. For the case of four internal nodes, two options were tested: the first using equidistant positions and the second using the locations occupied in the usual Gaussian quadrature (the

latter was initially suggested in one-dimensional problems [De Boor and Swartz 1973]). For the case of nine internal nodes, only equidistant locations were tested. In addition, for each boundary discretization (p), the corresponding $(p - 1)^2$ internal nodes, which also exist in a Lagrange-type finite element (that occupies the entire domain), are tested. The results of this example are shown in Table 1 and suggest the following:

- The bivariate Coons interpolation (Equation (1)) is incapable of approximating the solution and converges to an error norm L_2 about 13.2%.
- The introduction of only one internal node at the center of the domain induces severe improvement in the solution (L_2 reduces to about 2.2%).
- The introduction of four internal nodes causes a further reduction of L_2 to about 0.6%. In contrast to prior observations [Carey and Finlayson 1975; Carey and Oden 1983; Elansari et al. 2001], when the internal points are distributed in equal distances, the solution becomes slightly better than that using locations of Gaussian quadrature.
- The introduction of nine equidistantly distributed internal points causes a further improvement (0.04%).
- The locations of uniformly distributed points according to the Lagrange-type finite element lead to the best approximate solution tested.
- In the abovementioned case of using the set of monomials found in the Lagrange-type finite element, it was not possible to use more than nine segments per side ($p = q = 9$), due to truncation errors involved.
- When $p > 7$, the L_2 -norm does not further decrease. This finding is consistent with the practice of Szabó and Babuška [1991, p.355], who reduce the use of Legendre polynomials up to the seventh degree.

Example 2.

$$f(x, y) = 2e^{x+y}.$$

Now, the exact solution is

$$u(x, y) = e^{x+y} + e^y \sin x. \quad (8)$$

The Dirichlet boundary condition is calculated using Equation (8) and prescribed on the entire boundary. In an analogous way with Example 1, the results are shown in Table 2 and indicate a very similar quality. All remarks in the bullets of Example 1 are also valid here.

5. Discussion and conclusions

The global collocation method has been previously applied mainly to one-dimensional problems in conjunction with trigonometrical, Chebyshev, Legendre, and similar polynomials used in spectral methods. In the last cases, a complete space of monomials is hidden. For example, it was recently shown that either of Lagrange, Chebyshev, or Bernstein polynomials led to the same results with those obtained through the Taylor's series expansion [Provatidis 2007]. Moreover, the finite element method has intuitively used monomials related to truncated Taylor's series expansion and Pascal's triangle. Therefore, it is an

p	L_2 -norm (in %)					
	Number of monomials related to internal nodes (n_I)					
	0 Equation (1)	1 (S_1)	4 (S_2)		9 (S_3)	Lagrange-type $S^{p,q}(\Omega_{st}^{(q)})$
			Equidistantly	At Gauss points		
1	57.29	98.22	683.29	123.29	61.77	—
2	13.32	5.49	3.21	3.42	23.36	5.49
3	13.09	3.56	1.58	3.08	0.54	1.58
4	13.18	2.18	0.63	1.28	0.10	0.10
5	13.19	2.19	0.62	1.29	0.06	2.86E-02
6	13.18	2.17	0.63	1.24	0.04	1.31E-03
7	13.18	2.17	0.63	1.24	0.04	2.94E-04
8	13.18	2.17	0.63	1.24	0.04	5.06E-04
9	13.18	2.17	0.63	1.24	0.04	1.44E-02

Table 1. Example 1: accuracy of the proposed method for several boundary discretizations ($p = q$) and several monomials.

p	L_2 -norm (in %)					
	Number of monomials related to internal nodes (n_I)					
	0 Equation (1)	1 (S_1)	4 (S_2)		9 (S_3)	Lagrange-type $S^{p,q}(\Omega_{st}^{(q)})$
			Equidistantly	At Gauss points		
1	49.58	12.27	208.18	63.08	67.70	—
2	6.95	5.39	2.91	2.93	9.41	5.39
3	5.45	1.39	1.11	1.91	3.19E-01	1.11
4	5.58	1.25	0.34	0.69	1.05E-01	1.05E-01
5	5.58	1.27	0.33	0.69	3.43E-02	1.51E-02
6	5.58	1.26	0.34	0.64	2.83E-02	1.17E-03
7	5.58	1.26	0.34	0.64	2.92E-02	1.92E-04
8	5.58	1.26	0.34	0.64	2.93E-02	2.60E-04
9	5.58	1.26	0.34	0.64	2.93E-02	9.11E-03

Table 2. Example 2: accuracy of the proposed method for several boundary discretizations ($p = q$) and monomials.

old idea used to approximate the solution within a domain through monomials. However, difficulties in inverting the matrix of coefficients C_0 (see Equation (4)) have been extensively discussed in the 1960s. Zienkiewicz [1977, p.151] writes that “occasionally an inverse of C_0 may not exist and *always* considerable algebraic difficulty is experienced in obtaining an inverse in general terms suitable for all element geometries”.

Unlike the previous work mentioned above, we show here that instead of an intuitive choice of monomials, the well known bivariate Gordon–Coons transfinite interpolation can be used. Since this method reflects the extension of linear interpolation from a one- to a two-dimensional field, and it is based on the solid background of Computational Geometry, in the case of a smooth patch such as a rectangle, the invertability of C_0 is always anticipated.

We have shown here that a complete solution requires the use of internal nodes that should be generally located at equidistant locations like an imaginary uniform mesh. For a certain number of boundary discretizations, when progressively increasing the number of internal nodes up to $p = 7$ subdivisions, the solution monotonically improves. For $p > 7$, probably due to truncation errors, the solution becomes ill-conditioned and gives rise to a slightly increasing error norm (see, for example, the bottom of Table 1 and Table 2).

As mentioned in Section 1, the proposed collocation method can be applied also to nonrectangular domains. However, ongoing research shows that the method should be reformulated by replacing monomials with the global cardinal shape functions of which closed form expressions have been previously reported [Provatidis 2006a; 2006b; 2006c; 2006d]. In case of a boundary under partially Dirichlet and partially Neumann conditions, the procedure is straightforward, and analogous one-dimensional applications can be found in [Provatidis 2007] (both ends fixed, one fixed the other free). Finally, it is well known that one weakness of a global interpolation method is its inability to handle problems having discontinuous boundary conditions. Indeed, the proposed method is no exception.

In conclusion, the proposed method is a global collocation technique in which no domain or boundary integrals need to be computed and no least-squares procedure is required (at least for the Dirichlet conditions tested). Obviously, the extension of the proposed approach to other types of partial differential operators and/or three-dimensional problems is straightforward.

References

- [Botha and Pinder 1983] J. F. Botha and G. F. Pinder, *Fundamental concepts in the numerical solution of differential equations*, Wiley, New York, 1983.
- [Carey and Finlayson 1975] G. F. Carey and B. A. Finlayson, “Orthogonal collocation on finite elements”, *Chem. Eng. Sci.* **30** (1975), 587–596.
- [Carey and Oden 1983] G. F. Carey and J. T. Oden, *Finite elements: a second course*, vol. II, Prentice-Hall, Englewoods Cliffs, New Jersey, 1983.
- [Cavendish et al. 1976] J. C. Cavendish, W. J. Gordon, and C. A. Hall, “Ritz-Galerkin approximations in blending function spaces”, *Numer. Math.* **26** (1976), 155–178.
- [De Boor and Swartz 1973] C. De Boor and B. Swartz, “Collocation at Gaussian points”, *SIAM J. Numer. Anal.* **10** (1973), 582–606.
- [Diaz 1977] J. Diaz, “A collocation-Galerkin method for the two-point boundary-value problem using continuous piecewise polynomial spaces”, *SIAM J. Numer. Anal.* **14**:5 (1977), 844–858.

- [Elansari et al. 2001] M. Elansari, D. Quazar, and A. H.-D. Cheng, “Boundary solution of Poisson’s equation using radial basis function collocated on Gaussian quadrature nodes”, *Commun. Numer. Methods Eng.* **17** (2001), 455–464.
- [Farin 1990] G. Farin, *Curves and surfaces for computer aided geometric design: a practical guide*, Academic Press, Boston, 1990.
- [Finlayson 1972] B. A. Finlayson, *The method of weighted residuals and variational principles*, Academic Press, New York, 1972.
- [Frind and Pinder 1979] E. O. Frind and G. F. Pinder, “A collocation finite element method for potential problems in irregular domains”, *Int. J. Numer. Methods Eng.* **14** (1979), 681–701.
- [Gordon 1971] W. J. Gordon, “Blending functions methods of bivariate multivariate interpolation and approximation”, *SIAM J. Numer. Anal.* **8** (1971), 158–177.
- [Hayes 1980] L. J. Hayes, “An alternative-direction collocation method for finite element approximations on rectangles”, *Comput. Math. Appl.* **6** (1980), 45–50.
- [Houstis 1978] E. Houstis, “A collocation method for systems of nonlinear ordinary differential equations”, *J. Math. Anal. Appl.* **62** (1978), 24–37.
- [Lanczos 1938] C. Lanczos, “Trigonometric interpolation of empirical and analytical functions”, *J. Math. Phys.* **17** (1938), 123–199.
- [Provatidis 2006a] C. G. Provatidis, “Coons patch macroelements in two-dimensional parabolic problems”, *Appl. Math. Model.* **30**:4 (2006), 319–351.
- [Provatidis 2006b] C. G. Provatidis, “Free vibration analysis of two-dimensional structures using Coons patch macroelements”, *Finite Elem. Anal. Des.* **42**:6 (2006), 518–531.
- [Provatidis 2006c] C. G. Provatidis, “Three-dimensional Coons macroelements: application to eigenvalue and scalar wave propagation problems”, *Int. J. Numer. Methods Eng.* **65**:1 (2006), 111–134.
- [Provatidis 2006d] C. G. Provatidis, “Transient elastodynamic analysis of two-dimensional structures using Coons patch macroelements”, *Int. J. Solids Struct.* **43**:22–23 (2006), 6688–6706.
- [Provatidis 2007] C. G. Provatidis, “Free vibration analysis of elastic rods using global collocation”, *Archive of Applied Mechanics* (2007).
- [Ronto 1971] N. I. Ronto, “Application of the method of collocation to solve boundary value problems”, *Ukrainskii Matematicheskii Zhurnal* **23**:3 (1971), 415–421.
- [Russell and Shampine 1972] R. D. Russell and L. F. Shampine, “A collocation method for boundary value problems”, *Numer. Math.* **19** (1972), 1–28.
- [Szabó and Babuška 1991] B. Szabó and I. Babuška, *Finite element analysis*, John Wiley & Sons, Inc., New York, 1991.
- [Van Blerk and Botha 1993] J. J. Van Blerk and J. F. Botha, “Numerical solution of partial differential equations on curved domains by collocation”, *Numer. Meth. Part. D. E.* **9** (1993), 357–371.
- [Zienkiewicz 1977] O. C. Zienkiewicz, *The finite element method*, third ed., McGraw-Hill, London, 1977.

Received 18 Mar 2007. Revised 2 Aug 2007. Accepted 6 Aug 2007.

CHRISTOPHER G. PROVATIDIS: cprovat@central.ntua.gr
National Technical University of Athens, School of Mechanical Engineering, 9 Iroon Polytechniou Avenue,
GR-15773 Athens, Greece
<http://users.ntua.gr/cprovat>

SUBMISSION GUIDELINES

ORIGINALITY

Authors may submit manuscripts in PDF format on-line. Submission of a manuscript acknowledges that the manuscript is *original and has neither previously, nor simultaneously, in whole or in part, been submitted elsewhere*. Information regarding the preparation of manuscripts is provided below. Correspondence by email is requested for convenience and speed. For further information, write to:

Marie-Louise Steele
Division of Mechanics and Computation
Durand Building, Room 262
Stanford University
Stanford CA 94305

LANGUAGE

Manuscripts must be in English. A brief abstract of about 150 words or less must be included. The abstract should be self-contained and not make any reference to the bibliography. Also required are keywords and subject classification for the article, and, for each author, postal address, affiliation (if appropriate), and email address if available. A home-page URL is optional.

FORMAT

Authors are encouraged to use L^AT_EX and the standard article class, but submissions in other varieties of T_EX, and, exceptionally in other formats, are acceptable. Electronic submissions are strongly encouraged in PDF format only; after the refereeing process we will ask you to submit all source material.

REFERENCES

Bibliographical references should be listed alphabetically at the end of the paper and include the title of the article. All references in the bibliography should be cited in the text. The use of B^IB_T_EX is preferred but not required. Tags will be converted to the house format (see a current issue for examples), however, in the manuscript, the citation should be by first author's last name and year of publication, e.g. "as shown by Kramer, et al. (1994)". Links will be provided to all literature with known web locations and authors are encouraged to provide their own links on top of the ones provided by the editorial process.

FIGURES

Figures prepared electronically should be submitted in Encapsulated PostScript (EPS) or in a form that can be converted to EPS, such as GnuPlot, Maple, or Mathematica. Many drawing tools such as Adobe Illustrator and Aldus FreeHand can produce EPS output. Figures containing bitmaps should be generated at the highest possible resolution. If there is doubt whether a particular figure is in an acceptable format, the authors should check with production by sending an email to:

production@mathscipub.org

Each figure should be captioned and numbered so that it can float. Small figures occupying no more than three lines of vertical space can be kept in the text ("the curve looks like this:"). It is acceptable to submit a manuscript with all figures at the end, if their placement is specified in the text by means of comments such as "Place Figure 1 here". The same considerations apply to tables.

WHITE SPACE

Forced line breaks or page breaks should not be inserted in the document. There is no point in your trying to optimize line and page breaks in the original manuscript. The manuscript will be reformatted to use the journal's preferred fonts and layout.

PROOFS

Page proofs will be made available to authors (or to the designated corresponding author) at a web site in PDF format. Failure to acknowledge the receipt of proofs or to return corrections within the requested deadline may cause publication to be postponed.

Journal of Mechanics of Materials and Structures

Volume 3, Nº 1 January 2008

Effect of nonhomogeneity on the contact of an isotropic half-space and a rigid base with an axially symmetric recess SAKTI PADA BARIK, MRIDULA KANORIA AND PRANAY KUMAR CHAUDHURI	1
Estimating lever-type active multiple tuned mass dampers for structures under harmonic excitation CHUNXIANG LI AND BINGKANG HAN	19
Flexure of beams with an interlayer — symmetric beams with orthotropic adherends K. S. ALFREDSSON, T. A. BOGETTI, L. A. CARLSSON, J. W. GILLESPIE, JR. AND A. YIOURNAS	45
Energy-minimizing inclusion in an elastic plate under remote shear SHMUEL VIGDERGAUZ	63
Homogenization relations for elastic properties of two-phase composites using two-point statistical functions GHAZAL SAHELI, HAMID GARMESTANI AND ARUN GOKHALE	85
Dynamic analysis of banana fiber reinforced high-density polyethylene/poly (ϵ -caprolactone) composites RAGHVENDRA KUMAR MISRA, SANDEEP KUMAR, KUMAR SANDEEP AND ASHOK MISRA	107
Gradient reproducing kernel particle method ALIREZA HASHEMIAN AND HOSSEIN M. SHODJA	127
On the elastic moduli and compliances of transversely isotropic and orthotropic materials VLADO A. LUBARDA AND MICHELLE C. CHEN	153
Experimental investigations of spontaneous bimaterial interfacial fractures KAIWEN XIA, CARL-ERNST ROUSSEAU AND ARES ROSAKIS	173
A global collocation method for two-dimensional rectangular domains CHRISTOPHER G. PROVATIDIS	185



1559-3959(200801)3:1;1-D